# Mathematical modelling of Fast, High Volume Infiltration in poroelastic media using finite elements

Rahrah, M.

**DOI**
10.4233/uuid:45e88cc3-3802-4169-a916-8ff7d170506c

**Publication date**
2020

**Document Version**
Final published version

**Citation (APA)**
Rahrah, M. (2020). *Mathematical modelling of Fast, High Volume Infiltration in poroelastic media using finite elements*. https://doi.org/10.4233/uuid:45e88cc3-3802-4169-a916-8ff7d170506c

# Mathematical modelling of Fast, High Volume Infiltration in poroelastic media using finite elements

PROEFSCHRIFT

ter verkrijging van de graad van doctor
aan de Technische Universiteit Delft,
op gezag van de Rector Magnificus prof.dr.ir. T.H.J.J. van der Hagen,
voorzitter van het College voor Promoties,
in het openbaar te verdedigen op
dinsdag 3 november 2020 om 12:30 uur

door

Menel RAHRAH

Wiskundig ingenieur, Technische Universiteit Delft,
geboren te 's-Gravenhage, Nederland.

Dit proefschrift is goedgekeurd door de promotoren dr.ir. F.J. Vermolen en prof.dr.ir. C. Vuik.

Samenstelling promotiecommissie:

| | |
|---|---|
| Rector Magnificus | voorzitter |
| Prof.dr.ir. C. Vuik | Technische Universiteit Delft, promotor |
| Dr.ir. F.J. Vermolen | Technische Universiteit Delft, promotor |
| *Onafhankelijke leden:* | |
| Prof.dr. P.L.J. Zitha | Technische Universiteit Delft |
| Prof.dr.ir. G. Jongbloed | Technische Universiteit Delft |
| Prof.dr. I. Berre | Universitetet i Bergen, Noorwegen |
| Prof.dr. I.S. Pop | Universiteit Hasselt, België |
| Dr. C. Rodrigo | Universidad de Zaragoza, Spanje |
| Prof.dr.ir. C.W. Oosterlee | Technische Universiteit Delft, reservelid |

The research in this dissertation was supported by the Netherlands Organisation for Scientific Research (NWO), project number 13263, Fugro GeoServices B.V. and the members of the Foundation for Research and Development of Sustainable Infiltration Techniques (O2DIT).




Mathematical modelling of Fast, High Volume Infiltration in poroelastic media using finite elements
Dissertation at Delft University of Technology


ISBN 978-94-6380-979-5

Printed by: ProefschriftMaken || `www.proefschriftmaken.nl`.
An electronic version of this dissertation is available at `https://repository.tudelft.nl/`.

*Voor de dierbare die ons heeft verlaten,*
*mama, Makrem, Kerim en mijn*
*kleine wonder.*

# Contents

# Samenvatting

**Wiskundige modellering van Snelle, Hoog Volume Infiltratie in poro-elastische media met behulp van eindige elementen**

Menel Rahrah

Naarmate de vraag naar water wereldwijd toeneemt, zal de beschikbaarheid van zoetwater in veel regio's waarschijnlijk afnemen als gevolg van een veranderend klimaat, een toename van de wereldbevolking en veranderingen in landgebruik en energieopwekking. Anderzijds, voorspellen klimaatscenario's extreme perioden van regenval en droogte. Zware regenval leidt regelmatig tot overstromingen, schade aan de infrastructuur en tot erosie van de waardevolle bovengrond. Een eenvoudige en goedkope oplossing voor beide mondiale problemen is in opkomst: het opslaan van regenwater in natte perioden voor gebruik in droge perioden. Snelle, Hoog Volume Infiltratie (FHVI) is een recent ontdekte methode om, in perioden met extreme neerslag, snel grote hoeveelheden zoetwater in ondergrondse aquifers te infiltreren en werd oorspronkelijk ontdekt in de bouwsector. Dit onderzoek omvat de wiskundige modellering en de numerieke simulatie van FHVI in poro-elastische media met behulp van de eindige elementenmethode.

In Hoofdstuk 2 wordt de impact van mechanische trillingen en drukpulsen op de stroming door de poriën van een poreus medium onderzocht. In deze studie, wordt een axiale stroming als gevolg van een drukverschil gesimuleerd. Dit probleem wordt beschreven met behulp van Biot's poro-elasticiteitssysteem dat wordt opgelost door de continue Galerkin eindige elementenmethode gecombineerd met het impliciete Euler-schema. Bovendien worden Monte Carlo-simulaties uitgevoerd om de invloed van variatie in de invoerparameters op de modeloutput te kwantificeren. Allereerst, worden mechanische oscillaties toegepast als randvoorwaarde voor de vervorming van het poreuze medium. Uit de numerieke resultaten bleek dat de waterstroom wordt gestimuleerd door lopende golven die dezelfde richting hebben als de stroming. Vervolgens toonde het opleggen van een oscillerende mechanische spanning op de rand van het domein aan dat water sneller stroomt door poreuze media met grote korreldiameters en/of hoge initiële porositeiten. Ten slotte gaven de numerieke simulaties met drukpulsen aan dat de gepulseerde injectie een gunstig effect heeft op de waterstroom door poreuze media.

In Hoofdstuk 3 wordt de injectie van water in de watervoerende laag gesimuleerd, waarbij de vloeistof radiaal wegstroomt van het injectiefilter ten gevolge van een drukverschil. Deze studie bevat Monte Carlo-simulaties om de impact van variatie

in de bodemeigenschappen en de injectieparameters op de stroomsnelheid te kwantificeren. Verder worden twee verschillende injectiemethoden getest en met elkaar vergeleken om de beste methode voor regenwaterinfiltratie te bepalen. De numerieke simulaties wezen erop dat, ongeacht het type grond waarin de vloeistof wordt geïnjecteerd, gepulseerde injectie de hoeveelheid regenwater kan vergroten die snel in de ondergrond kan worden opgeslagen.

Het onderzoek naar de relatie tussen de permeabiliteit en de porositeit die in deze poro-elasticiteitssimulaties wordt gebruikt, begint in Hoofdstuk 4. De Kozeny-Carman vergelijking wordt meestal gebruikt om de permeabiliteit van het poreuze medium te bepalen uit de porositeit. Deze vergelijking stelt dat stroming door de poriën mogelijk is zolang de porositeit groter is dan nul. In tegenstelling tot de Kozeny-Carman relatie, uit discrete netwerkmodellen is bekend dat de vloeistof niet zal stromen als de porositeit kleiner wordt dan een bepaalde waarde groter dan nul. Deze waarden worden bepaald door de percolatiedrempels. Het verschil tussen de Kozeny-Carman vergelijking en de netwerk-geïnspireerde relatie, die gebaseerd is op de percolatietheorie, wordt onderzocht in dit hoofdstuk. Uit de numerieke resultaten kunnen we concluderen dat voor lage percolatiedrempels de netwerk-geïnspireerde relatie resulteert in hogere stroomsnelheden dan de Kozeny-Carman vergelijking. Bovendien wordt aangetoond dat de stroomsnelheid aanzienlijk verandert als functie van de percolatiedrempel, wat betekent dat de waterstroom afhangt van de topologie van de verbonden porieruimte. Voor hoge percolatiedrempels verschenen ongewenste oscillaties in de numerieke oplossing. Omdat we kunnen bewijzen dat de oplossing van Biot's model convergeert naar de oplossing van een zadelpuntprobleem voor kleine tijdstappen en een lage permeabiliteit en omdat de hoge percolatiedrempels snel leidt tot lokaal zeer lage permeabiliteiten, hebben we stabilisatie nodig in de eindige elementenbenadering.

Hoofdstuk 5 presenteert de toepasbaarheid van de netwerk-geïnspireerde relatie tussen de permeabiliteit en de porositeit op een driedimensionaal probleem. Dit probleem bestudeert de infiltratie van een vloeistof in het watervoerende pakket. Het sterkste kenmerk van de netwerk-geïnspireerde relatie hangt samen met het vermogen om de permeabiliteit goed te beschrijven in geval van lage porositeiten. Daarom wordt aan de rand van het domein een verticale mechanische spanning uitgeoefend om een grote dichtheid van de korrels te creëren, wat resulteert in een afname van de porositeit. Het doel van dit numerieke experiment is om de toepasbaarheid van deze microscopisch netwerk-geïnspireerde relatie op de driedimensionale macroschaal te analyseren.

Lineaire poro-elasticiteitstheorie, die werd gebruikt in de bovengenoemde simulaties, is een goed model voor zeer kleine vervormingen. De bekende theorie van grote vervormingen is daarentegen geschikter om poro-elasticiteitsproblemen met matige tot grote vervormingen op te lossen. Echter, het oplossen van dit niet-lineaire wiskundige model is complex en heeft hoge rekentijden. In Hoofdstuk 6 vergelijken we de benaderingen van de poro-elasticiteitstheorie met grote vervorming met die van de lineaire poro-elasticiteitstheorie voor de oplossing van een tweedimensionaal modelprobleem waarbij stroming door poreuze media wordt beschouwd. Bovendien wordt de impact van een vervormingsafhankelijke permeabiliteit volgens de Kozeny-Carman vergelijking onderzocht. De numerieke resultaten laten zien dat de fouten in de benaderingen voor de vervorming en het drukveld die worden verkregen met behulp van

de lineaire poro-elasticiteitstheorie voornamelijk te wijten zijn aan het ontbreken van de kinematische niet-lineariteit. Verder wordt de benaderingsfout in het drukveld groter als we een constante permeabiliteit gebruiken in plaats van een vervormingsafhankelijke permeabiliteit.

Omdat het moeilijk is om de samenstelling van een natuurlijke bodem te bepalen, wordt stroming door de poriën van de bodem meestal gemodelleerd uitgaande van een homogeen grondmengsel in plaats van een heterogeen mengsel. In Hoofdstuk 7 wordt het verschil tussen de waterstroom in een model met een heterogeen gelaagd poreus medium en een model met een homogeen poreus medium beschouwd om te onderzoeken of deze vereenvoudiging gerechtvaardigd is. De studie bevat simulaties met mechanische trillingen en drukpulsen. Bovendien worden Monte Carlo-simulaties uitgevoerd om de impact van variatie van modelparameters op de waterstroom te kwantificeren. De numerieke resultaten laten zien dat water twee keer zo snel door heterogene gelaagde poreuze media stroomt dan door homogene poreuze media.

In Hoofdstuk 8 wordt het verschil tussen een vloeistofstroom door een homogeen poreus medium en een macroscopisch-heterogeen poreus medium onderzocht door een bromide-tracer in een aquifer te injecteren. Gebaseerd op de combinatie van Biot's model en de advectie-dispersievergelijking, wordt een gekoppeld model voorgesteld dat stoftransport in een vervormbare grond beschrijft, rekening houdend met niet-lineaire permeabiliteit. De numerieke resultaten wezen erop dat een hogere waarde van de longitudinale dispersiviteit (d.w.z. een grotere microscopische heterogeniteit) resulteert in een grotere afstand die kan worden bereikt door de bromide-tracer en in hogere concentratiewaarden in de buurt van het injectiefilter. Verder worden hogere concentratiewaarden berekend in het heterogene gelaagde poreuze medium dan in het homogene poreuze medium.

# Summary

**Mathematical modelling of Fast, High Volume Infiltration in poroelastic media using finite elements**

Menel Rahrah

As demand for water increases across the globe, the availability of fresh water in many regions is likely to decrease due to a changing climate, an increase in human population and changes in land use and energy generation. On the other hand, climate scenarios predict extreme periods of drought and rainfall. Heavy rainfall regularly leads to flooding, damaging infrastructure, and to erosion of valuable top soil. A simple and cheap solution for both global problems is emerging: storing rainwater in wet periods for use in dry periods. Fast, High Volume Infiltration (FHVI) is a recently discovered method to quickly infiltrate high volumes of fresh water and it was originally discovered in the field of construction. This research entails the mathematical modelling and the numerical simulation of FHVI in poroelastic media using the finite element method.

In Chapter 2, an axial flow owing to a pressure difference is simulated to investigate the impact of mechanical vibrations and pressure pulses on the flow through the pores of a porous medium. This problem is described using Biot's poroelasticity system which is solved by the continuous Galerkin finite element method combined with the implicit Euler scheme. Furthermore, Monte Carlo simulations are performed to quantify the impact of variation in the input parameters on the model output. Firstly, soil vibrations are applied as oscillatory displacement boundary condition. Numerical results showed that the water flow is being stimulated by waves travelling in the same direction. Subsequently, applying an oscillating load on the boundary showed that water flows faster through porous media with large grain sizes and/or high initial porosities. Numerical simulations of pressure pulsing pointed out that pulsed injection has a beneficial effect on the water flow in porous media.

In Chapter 3, the injection of water into an aquifer is simulated where the fluid flows radially outward owing to a pressure difference. This study contains Monte Carlo simulations to quantify the impact of variation in the soil characteristics and the injection parameters on the flow rate. Furthermore, two different injection methods are tested and compared with each other in order to determine the best method for rainwater infiltration. Numerical simulations pointed out that, regardless of the type of soil into which the fluid is injected, by applying pulsed injection we can increase the amount of rainwater that can be stored quickly in the underground.

The investigation of the permeability-porosity relation that is used in these poroelasticity simulations is initiated in Chapter 4. The Kozeny-Carman equation is commonly used to determine the permeability of the porous medium from the porosity. This relation states that flow through the pores is possible as long as the porosity is larger than zero. In contrast, from discrete network models it is known that the fluid will stop flowing if the porosity becomes smaller than a certain value larger than zero, dictated by percolation thresholds. The difference between the Kozeny-Carman equation and the network-inspired relation that is based on the percolation theory, is investigated. From the numerical results we could conclude that for low percolation thresholds, the network-inspired relation results in higher flow rates than the Kozeny-Carman relation. In addition, it is shown that the flow rate changes significantly as a function of the percolation threshold which means that the water flow depends on the topology of the connected pore space. For high percolation thresholds, spurious oscillations appeared in the numerical solution. Since we can prove that the solution of Biot's model converges to the solution of a saddle point problem for small time steps and low permeability, we need stabilisation in the finite element approximation.

Chapter 5 presents the applicability of the network-inspired permeability-porosity relation on a three-dimensional problem. This problem studies the infiltration of a fluid into an aquifer. The strongest feature of the network-inspired approach is related to its capability to give a good description of the permeability in case of low porosities. Hence, on the top of the domain, a vertical mechanical load is applied in order to create a large density of the grains which results in a decrease of the porosity. The goal of this numerical experiment is to analyse the applicability of this microscopic network-inspired relation on the three-dimensional macro-scale.

Linear poroelasticity theory, which is used in the above-mentioned simulations, is a good model for very small deformations. On the other hand, the well-known large-deformation theory is more suitable to solve poroelasticity problems with moderate to large deformations. However, adopting this nonlinear mathematical model comes with a high computational complexity and cost. In Chapter 6, we compare the predictions of linear poroelasticity with those of large-deformation poroelasticity in the context of a two-dimensional model problem where flow through porous media is considered. In addition, the impact of introducing a deformation-dependent permeability according to the Kozeny-Carman equation is explored. The numerical results showed that the errors in the displacement and pressure fields that are obtained using the linear poroelasticity are primarily due to the lack of the kinematic nonlinearity. Furthermore, the error in the pressure field is amplified by incorporating a constant permeability rather than a deformation-dependent permeability.

Since it is hard to determine the composition of a natural soil, flow through the voids in the soil is usually modelled assuming a homogeneous soil mixture rather than a heterogeneous mixture. In Chapter 7, the difference between the flow of water in a model with a heterogeneous layered porous medium and a model with a homogeneous porous medium is explored, in order to investigate whether this simplification is justified. The study contains simulations with mechanical oscillations as well as pressure pulses. Furthermore, Monte Carlo simulations are performed to quantify the impact of variation of model parameters on the volumetric flow rate. From the numerical results, we could conclude that water flows twice as fast through heterogeneous layered porous media than through homogeneous porous media.

In Chapter 8, the difference between a fluid flow through a homogeneous porous medium and a macroscopic-heterogeneous porous medium is investigated by injecting a bromide tracer into an aquifer. Based on the combination of Biot's theory of linear poroelasticity and the advection-dispersion equation, a coupled model describing solute transport in a deforming soil is proposed, taking into account nonlinear permeability. The numerical results pointed out that a higher value of the longitudinal dispersivity (i.e. a larger microscopic heterogeneity) results in a larger distance that can be reached by the bromide tracer and in higher concentration values in the vicinity of the injection filter. Furthermore, higher concentration values are computed in the heterogeneous layered porous medium than in the homogeneous porous medium.

Chapter 1

# Introduction

## 1.1 Motivation

Access to fresh water is considered a universal human right [131]. However, climate change and the growing population and industrial activity put water resources worldwide under severe pressure [107]. This issue has already resulted in desiccation in large areas of the world and in a global freshwater crisis. For this reason, authorities, knowledge institutions and private companies collaborate closely to develop new approaches to the growing freshwater demand. On the other hand, climate scenarios predict extreme periods of drought and rainfall. Heavy rainfall regularly leads to flooding, damaging buildings and infrastructure, and to erosion of valuable top soil. Traditionally, during periods of heavy rainfall, the approach is to transport water quickly to surface waters and the sea in order to prevent flooding. However, a simple and cheap solution for both global problems is emerging: storing water in wet periods for use in dry periods. Especially the infiltration of large amounts of rainwater into the shallow subsurface can have great value for battling flooding and for the underground storage of fresh water. Groundwater is currently the primary freshwater supply source for approximately two billion people and the dependence on it will increase into the future [76]. A prerequisite for effective storing of rainwater in periods of extreme precipitation is that the water can be stored quickly. A new method to quickly infiltrate high volumes of fresh water has been discovered recently. We refer to this method as Fast, High Volume Infiltration (FHVI).

Another field in which FHVI constitutes a significant breakthrough is in construction, where this method was originally discovered. Building sites have to be pumped dry to enable construction. In the past, extracted water was often released into surface water. However, since the potential impact on the ecology is negative, new regulations prescribe that water should be returned to the ground. Conventionally, infiltration has to be applied at a certain distance from the pit, thereby affecting groundwater levels in a relatively large area. FHVI can be much closer to the pit, as the infiltrated water is rapidly transported away from the infiltration points. This means that the effect on groundwater levels is much smaller (see Figure 1.1). However, according to

preliminary research and findings, this infiltration method does not obey the classical Dupuit's law that is commonly used in hydrogeology, and it is currently impossible to predict its applicability. To describe this infiltration method, we consider a model for aquifers in which water is injected. The flow of water induces local deformations in the aquifer, which are described by a poroelastic formalism.

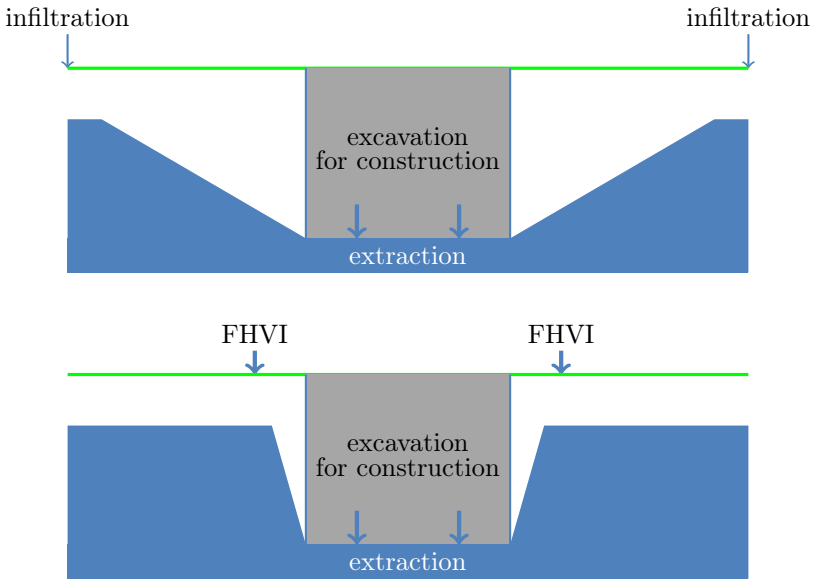


Figure 1.1: *A simplified scheme of a conventional infiltration (top) and FHVI (bottom). This scheme emphasises the difference between both infiltration techniques.*

In petroleum reservoirs, observations from the last 50 years suggest that seismic waves generated from earthquakes and passing trains may alter water and oil production. It has also been observed in some laboratory measurements and field applications that imposing harmonic signals into cores or reservoirs sometimes may induce higher fluid flow rates [97]. Further the fact that the pore pressure may undergo variations under the influence of seismic waves is well known to geotechnical engineers [11]. In addition, laboratory experiments have shown that ultrasonic radiation can considerably increase the rate of flow of a liquid through a porous medium [1]. Furthermore, Davidson et al. [42] performed experiments in a wide range of configurations, grain sizes, viscosities and flow factors, showing that high-amplitude pressure pulsing or mechanical excitation of a saturated porous medium under a pressure gradient increases the flow rate of the liquid along the direction of the flow gradient. Based on the experimental results, they concluded that flow rate enhancement occurred for all liquids, and for all the grain sizes that were tested.

The research problems we address in the present dissertation is how to mathematically model FHVI and to investigate whether during FHVI, oscillatory and pulsating forces that are induced by large injection rates increase the amount of water that can be injected into an aquifer.

## 1.2 Background

Porous media consist of a structure phase (the skeleton) and a viscous fluid phase, flowing through connected pores. The connected porous space is the space through which the fluid actually flows and whose two points can be joined by a path lying entirely within it so that the fluid phase remains continuous there. The matrix is composed of both a solid part and a possible occluded porosity, whether saturated or not, but through which no filtration occurs. The connected porosity is the ratio of the volume of the connected porous space to the total volume. A saturated porous medium is composed of a porous solid material, the connected porous space of which is fully saturated by a viscous fluid. Poroelasticity involves fluid flow in porous media that are elastic and can deform when subjected to external forces and to variations in pressure of the saturating fluid. Moreover, poromechanical deformations are poroelastic when they are controlled by the reversible storage and release of elastic energy. In deformable porous materials such as soils, rocks and tissues, the flow of the pore fluid and the deformation of the solid matrix are tightly coupled to each other.

Poroelasticity theory was originally developed to study several geophysical applications [61, 68, 91]. In the last few decades, the mechanics of porous media has been of great interest due to its potential application in many geological and biological systems across a wide range of scales such as civil engineering [22, 52, 95, 116, 122, 127] with applications including flow in porous media [34, 55], energy and environmental technologies [37, 49, 69, 109, 111, 140], materials science [85] and biophysics [50, 92], where poromechanics plays an important role in modelling bones and soft tissues [3, 41, 120] and the macroscopic processes in a human lung [133], and it is the dominant mechanism underlying plant motion [45]. In physical chemistry, poromechanical processes include mass and heat transfer [144]. Additionally, poromechanics has been studied intensely in geophysics, in the context of consolidation of aquifers [96, 104] and in the context of enhanced oil and gas recovery [9, 110, 124].

### 1.2.1 Poroelasticity equations

The theory of poroelasticity has been largely successful in modelling poromechanical behaviour in relatively simple systems. It forms a simplified mixture theory where a complex fluid-structure interaction problem is replaced by a superposition of both components, each of them representing a fraction of the complete material. Assuming only a poroelastic medium with intrinsically incompressible solid and fluid constituents, a poromechanical problem is described mathematically by a coupled system of two partial differential equations: the momentum balance equation which governs the solid deformation, and the mass balance equation which governs the fluid flow. This continuum theory is fundamentally limited by the high complexity and in most cases also unknown geometry of porous media on the micro-scale as well as our limited understanding of the pore-scale interactions between the fluid and the solid. Hence, a fully resolved model is nearly impossible to obtain, but most of the times also not necessary to answer important questions.

The theory of poroelasticity originally emerged in soil mechanics with the work of Terzaghi [128]. Based on Terzaghi's findings, a theory of porous materials fully filled with a viscous fluid was presented by Biot [16]. In the following years, Biot

extended his work to anisotropic materials [17] and later to poroviscoelasticity [18]. Biot gave a complete theory about poroelasticity that describes the behaviour of fluid-filled porous materials undergoing deformation in the infinitesimal deformation range. Assuming that the solid material is linearly elastic, the classical theory of linear poroelasticity developed by Biot [84, 135] can be used to analyse the coupled interaction between fluid flow and matrix deformation. The classical theory of linear poroelasticity captures this coupling by describing the mechanical behaviour of a porous medium using a linear elastic formulation for the solid matrix, and Darcy's law for the fluid flow through the matrix. These theories mentioned above are quasi-static theories, i.e., no inertia effects have been taken into account. Furthermore, in Biot's theory a fully saturated material is considered, hence an elastic skeleton with a statistical distribution of the interconnected pores is considered.

The classical theory of linear poroelasticity is a good model for infinitesimal deformations of the solid, but it becomes increasingly inappropriate for moderate to large deformations. Since many real systems feature large deformations, such as damage, fractures or swelling, that lead to a strongly nonlinear coupling between the pore structure and the fluid flow [50, 109], it is important to consider the complete poroelasticity theory without linearisation. In the well-known theory of large-deformation poroelasticity, fluid flow is described by Darcy's law and mass conservation, and matrix deformation is described by Biot's constitutive relations and nonlinear elasticity.

### 1.2.2 Permeability-porosity relationschips

For the description of different physical processes, such as consolidation, it is of a pivotal importance to have a valid estimation of permeability. The permeability of porous media is usually expressed as a function of some physical properties of the interconnected pore system such as porosity. One of the first published relations introduced by Hazen [59], relates the hydraulic conductivity of a porous medium to the characteristic particle diameter, the maximum diameter of the finest 10% of the grains in that solid medium, using an empirical coefficient. The applicability of the Hazen relation is limited to a small range of characteristic particle diameters, which, together with the variability of the empirical coefficient, make it unsuitable for general use.

Although it is natural to assume that the permeability depends on the porosity, it is not simple to formulate satisfactory theoretical models for the relation between them, mainly due to the complexity of the connected pore space. The most widely used permeability-porosity relationships is the Kozeny-Carman relation, which was originally published in [75] and was later modified in [35]. This relation assumes that the connectivity of a porous space does not vary in time, either by assuming a pore space that stays fully connected or by taking the effective porosity initially and assuming no loss of connectivity. Therefore, the Kozeny-Carman relation assumes that flow through the porous medium is possible as long as the porosity is nonzero. Hence, this relation is not capable of predicting blocking of the flow if the porosity is too low in some parts of the porous medium leading to poorly connected porous media, as is shown by Mostaghimi et al. [93]. Moreover, it is empirically proven that the permeability decreases dramatically with decreasing porosity [15], indicating that the Kozeny-Carman relation is less accurate at low porosities. To improve the behaviour

of this relation for small values of the porosity, Mavko and Nur [88] incorporated a simple porosity adjustment into the Kozeny-Carman relation, by taking the percolation threshold into account. This approach resulted in a better prediction of the permeability for low porosities. However, in the study of Mavko and Nur the percolation threshold was chosen empirically to give a good fit for the experimental data. Another approach to take into account the percolation threshold was presented by Porter et al. [99], based on the work of Koltermann and Gorelick [72], who adapted the Kozeny-Carman equation to represent bimodal grain-size mixtures.

In the literature, the relationship between the permeability and the porosity is also derived using upscaling-based approaches, in case the underlying pore geometry of a representative elementary volume is prescribed [112]. Application of these approaches provides a link from the micro- to macroscopic behaviour of the material and allows the derivation of effective properties. Starting from mathematical models at the pore scale, such as the Stokes equation for fluid flow, an averaging procedure is performed in order to derive effective models. Possible averaging methods that may be applied to these equations are volume averaging [139] and two-scale asymptotic expansion [10]. The effective permeability tensor is given as the integral over solutions of auxiliary cell problems which are defined on the representative elementary volume. Upscaling methods directly enable calculating the full, potentially anisotropic, permeability tensor and one only needs the geometric information in terms of a representative elementary volume as input [112]. In contrast, well-established relations such as the Kozeny-Carman equation relate the porosity to a scalar permeability coefficient. Another upscaling method is the fast marching method (FMM), that is employed by Sharifi et al. [114] as an efficient tool for permeability upscaling. Their approach is based on the minimisation of the difference between dynamic behaviours of fine-scale and up-scaled reservoir models that is provided by the FMM.

### 1.2.3 Numerical procedure

The equations describing poroelastic flow and deformation are derived from the principles of conservation of fluid mass and the balance of forces on the porous matrix. These equations can be solved either iteratively or simultaneously as a fully coupled system. In the fully coupled method the equations of flow and soil mechanics are solved simultaneously at each time step. The iterative coupling method solves the pore fluid flow variables and the mechanical variables independently and sequentially. The iterative coupling between the fluid pressure and the mechanical deformations is then performed at the end of each time step [81]. A widely used approach in coupling the flow and the mechanics in porous media iteratively, is the fixed stress split iterative algorithm [25, 71, 90]. The monolithic approach is consistent and rigorous, because the fluid flow and the mechanics equations are solved simultaneously on the same discretised grid [61]. Consequently, the coupled poroelasticity model requires intensive computation. However, the fully coupled method is more efficient in poroelasticity problems with strong hydromechanical coupling [43]. Hence, the monolithic approach for solving the quasi-static poroelasticity equations is adopted in this study.

Since it is difficult to obtain analytical solutions for poroelasticity problems, solving these problems relies mainly on numerical methods. In particular, numerical methods are necessary to solve poromechanical problems with large deformation since

these systems are inherently nonlinear. Solving the poroelasticity equations has been attracting attention from the scientific computing community [63, 94, 138], and references therein. More recent work can be found in [51, 62, 63, 102, 121]. The classical poroelasticity equations have been solved by Luo et al. [83] using the finite volume method combined with a nonlinear multigrid method. In addition, stabilised finite difference methods using central differences on staggered grids are used by Gaspar et al. [53, 54] to solve Biot's model. However, the numerical solution of the two-dimensional poroelasticity equations is usually approached using finite element methods [8, 79, 98]. Hence, in this dissertation, numerical models have been developed to solve the poroelasticity equations following the continuous Galerkin (CG) finite element method.

The linear poroelastic equations are often solved in a two-field formulation with the solid skeleton displacements and the fluid pressures as primary variables. From these variables the fluid flux can be recovered [94, 141]. However, since a differential operator is acting on the fluid pressure, the flow is of a lower accuracy than the pressure in the two-field approach. Hence, a three-field formulation with the displacement, fluid flux and pressure as primary variables [13] is used in many applications of the poroelastic equations in which the flow of the fluid through the medium is of primary interest. This avoids the need for post-processing to calculate the fluid flux and allows physically meaningful boundary conditions to be applied when modelling the interaction between a fluid and a poroelastic structure [6]. A clear disadvantage of the three-field formulation is the increased number of degrees of freedom of the linear system arising from the finite element discretisation. The simplicity of the displacement-pressure two-field formulation is attractive and hence pursued by this dissertation.

When using the finite element method to solve the two-field poroelastic equations, the main challenge is to ensure convergence of the method and to prevent numerical instabilities. These instabilities often manifest themselves in the form of localised spurious oscillations in the pressure field, when seeking to approximate steep pressure gradients in the solution. The nonphysical pressure oscillations are especially observed in finite element calculations of poroelastic problems involving low-permeable media [102] and in problems with Dirichlet pressure boundary conditions such as Terzaghi's problem [94, 141]. It has been proved that this problem is caused by the saddle point structure in the poroelasticity equations leading to a violation of the Ladyzhenskaya-Babuska-Brezzi (LBB) inf-sup stability condition (see Chapter 4). Solving this problem requires a stable mixed element pair [57] such as the popular Taylor-Hood element, that employs one order higher interpolation for the displacement compared to the fluid pressure [125]. When using equal-order interpolations of displacement and pressure field, these oscillations can be alleviated and, in some cases, completely eliminated by using stabilisation techniques [123, 129, 134, 141]. Various stabilisation schemes have been developed, including the Brezzi-Pitkäranta scheme [31], the Galerkin least-squares approach [66], the variational multiscale method [65], the polynomial pressure projection technique [19, 44], and the pressure stabilisation procedure [2, 108].

## 1.3 Dissertation objectives

The aim of this dissertation is to model the infiltration method FHVI mathematically and to investigate whether during FHVI, oscillatory and pulsating forces that are induced by large injection rates increase the amount of water that can be injected into an aquifer. The research objectives are defined as follows:

- Construct a methodology to investigate the impact of mechanical vibrations and pressure pulses on the flow through porous media and to quantify the impact of variation in the input parameters on the model output using Monte Carlo simulations;
- Investigate the applicability of the permeability-porosity relation based on the percolation theory on poroelasticity problems;
- Develop a finite element solver for linear and nonlinear poroelasticity problems, which will be used to compare the predictions of linear poroelasticity with those of large-deformation poroelasticity;
- Explore the difference between the fluid flow in a model with a homogeneous porous medium and the same fluid flow through a heterogeneous layered porous medium.

## 1.4 Dissertation outline

The rest of this dissertation is organised as follows:

- In Chapter 2, an axial flow is simulated to investigate the impact of mechanical vibrations and pressure pulses on the flow through the pores of a porous medium. Furthermore, Monte Carlo simulations are performed to quantify the impact of variation in the input parameters on the model output.
- In Chapter 3, the injection of water into an aquifer is simulated where the fluid flows radially outward owing to a pressure difference. This study contains Monte Carlo simulations to quantify the impact of variation in the soil characteristics and the injection parameters on the flow rate. Furthermore, two different injection methods are tested and compared with each other in order to determine the best method for rainwater infiltration.
- Chapter 4 analyses the permeability-porosity relation that is used in the poroelasticity simulations. Therefore, the difference between the Kozeny-Carman equation and the network-inspired relation that is based on the percolation theory, is investigated. In addition, the convergence of the solution of Biot's model to the solution of a saddle point problem for small time steps and low permeability is proven.
- In Chapter 5 the applicability of the microscopic network-inspired permeability-porosity relation on a three-dimensional macro-scale problem is presented. This problem studies the infiltration of a fluid into an aquifer.

- In Chapter 6, the predictions of linear poroelasticity with those of nonlinear poroelasticity are compared. In addition, the impact of introducing a deformation-dependent permeability according to the Kozeny-Carman equation is explored.
- Chapter 7 presents the difference between the water flow in a model with a heterogeneous layered porous medium and a model with a homogeneous porous medium. The study contains simulations with mechanical oscillations as well as pressure pulses. Furthermore, Monte Carlo simulations are performed to quantify the impact of variation of model parameters on the flow rate.
- In Chapter 8, the difference between a fluid flow through a homogeneous porous medium and a macroscopic-heterogeneous porous medium is investigated by injecting a bromide tracer into an aquifer. Based on the combination of Biot's theory of linear poroelasticity and the advection-dispersion equation, a coupled model describing solute transport in a deforming soil is proposed, taking into account nonlinear permeability.

Chapter 2

# Monte Carlo assessment of the impact of oscillatory and pulsating boundary conditions

*Stress and water injection induce deformations and changes in pore pressure in the soil. The interaction between the mechanical deformations and the flow of water induces a change in porosity and permeability, which results in nonlinearity. To investigate this interaction and the impact of mechanical vibrations and pressure pulses on the flow rate through the pores of a porous medium under a pressure gradient, a poroelastic model is proposed. In this chapter, a Galerkin finite element method is applied for solving the quasi-static Biot's consolidation problem for poroelasticity, considering nonlinear permeability. Space discretisation using Taylor-Hood elements is considered, and the implicit Euler scheme for time stepping is used. Furthermore, Monte Carlo simulations are performed to quantify the impact of variation in the parameters on the model output. Numerical results show that pressure pulses and soil vibrations in the direction of the flow increase the amount of water that can be injected into a deformable fluid-saturated porous medium.*

This chapter is based on the journal article:

M. Rahrah and F. Vermolen. Monte Carlo Assessment of the Impact of Oscillatory and Pulsating Boundary Conditions on the Flow Through Porous Media. *Transp. Porous Med.*, 123(1):125 – 146, 2018.

## 2.1 Introduction



Our aim is to investigate whether during Fast, High Volume Infiltration (FHVI), large injection rates induce an oscillatory or a pulsating force near the injection point and whether induced vibrations increase the amount of water that can be injected into an aquifer. In this chapter, we tackle the second question by investigating the impact of soil vibrations and pressure pulses on the effective transmigration of water through the pores of the soil. For this purpose, a tube filled with a deformable fluid-saturated porous medium is simulated, into which water is injected. In the current chapter, Biot's consolidation model for poroelasticity [16, 17] is used to determine the local deformation of the porous medium as a result of the injection of water. Darcy's law [64] is used in Biot's model to describe the fluid flow, while linear elasticity of the porous medium determines the local deformations as a result of the vibrations. More precisely, we use in this chapter a simplistic Hookean representation of the deformation of the soil.

In this study, a finite element method based on Taylor-Hood elements, with linear and quadratic basis functions, has been developed for solving the system of incompressible poroelasticity equations. This method is commonly used for flow problems modelled by (Navier-)Stokes equations. Furthermore, the fully coupled scheme was employed which involves solving the coupled governing equations of flow and geomechanics simultaneously at every time step. In this manuscript, we consider a nonlinear relation between the permeability and the dilatation. Subsequently, to quantify the impact of variation of model parameters such as Young's modulus, the oscillatory modes and the injection pressure pulses, we further present results from an uncertainty quantification. This uncertainty quantification is used to quantify the propagation of uncertainty in the input data. Such uncertainty quantifications have been applied in biomedical mathematics [73] and in geomechanics [82], where an uncertainty quantification is carried out by modelling the permeability as a stochastic field parameter.

The rest of this chapter is organised as follows: Section 2.2 describes Biot's consolidation model. Section 2.3 presents the numerical experiments that are used to demonstrate the impact of oscillatory and pulsating boundary conditions on the volumetric flow rate. In Section 2.4, the numerical method is formulated. Here, the weak form of the partial differential equations is derived and the Galerkin finite element approximations are described. Section 2.5 presents some of our numerical experiments and results. Lastly, in Section 2.6 the conclusions and some suggestions for further work are given.

## 2.2 Governing equations

Sand and gravel layers (aquifers) are not rigid, but constitute an elastic matrix, if the deformations are very small. To be able to determine the local displacement of the skeleton of the porous medium, as well as the fluid flow through the pores, after injection of water, the model provided by Biot's theory of linear poroelasticity with single-phase flow is used [16, 17]. In this model, flow in porous media is combined with mechanical deformations of the soil into which water is injected. Furthermore,

Darcy's law [64] and infinitesimal strain theory [26] are used to describe the fluid flow and the local displacements, respectively. Note that this is an approximation if the displacements and the strains are large.

### 2.2.1 Biot's partial differential equations



The quasi-static Biot model for soil consolidation describes the time-dependent interaction between the displacement of the solid matrix and the pressure of the fluid. We assume the porous medium to be linearly elastic, homogeneous, isotropic and saturated by an incompressible Newtonian fluid. According to Biot's theory, the consolidation process satisfies the following system of equations [2, 36, 135]:

$$\text{mechanical balance:} \quad -\nabla \cdot \boldsymbol{\sigma}' + (\nabla p + \rho g \mathbf{e}_z) = \mathbf{0}; \tag{2.1}$$

$$\text{constitutive equation:} \quad \boldsymbol{\sigma}' = \lambda tr(\boldsymbol{\varepsilon})\mathbf{I} + 2\mu\boldsymbol{\varepsilon}; \tag{2.2}$$

$$\text{compatibility condition:} \quad \boldsymbol{\varepsilon}(\mathbf{u}) = \frac{1}{2}(\nabla \mathbf{u} + \nabla \mathbf{u}^T); \tag{2.3}$$

$$\text{Darcy's law:} \quad \mathbf{v} = -\frac{\kappa}{\eta}(\nabla p + \rho g \mathbf{e}_z); \tag{2.4}$$

$$\text{continuity equation:} \quad \frac{\partial}{\partial t}(\nabla \cdot \mathbf{u}) + \nabla \cdot \mathbf{v} = 0, \tag{2.5}$$

where $\boldsymbol{\sigma}'$ and $\boldsymbol{\varepsilon}$ are the effective stress and strain tensors for the porous medium, $p$ is the pore pressure, $\rho$ is the density of water, $g$ is the gravitational acceleration, $\lambda$ and $\mu$ are the Lamé coefficients, $\mathbf{u}$ is the displacement vector of the porous medium, $\mathbf{v}$ is the percolation fluid velocity relative to the porous medium, $\kappa$ is the permeability of the porous medium and $\eta$ is the dynamic viscosity of the fluid.

### 2.2.2 Permeability and porosity relations

In the physical problem presented here, we will focus on the interaction between the mechanical deformations and the flow of water. Therefore, we consider the spatial dependency of the porosity and the permeability. We calculate the porosity using a procedure outlined by Tsai et al. [130]. Their derivation is based on the mass balance of solids in saturated porous media:

$$\frac{\partial[(1-\theta)\rho_s]}{\partial t} + \nabla \cdot [(1-\theta)\rho_s \frac{\partial \mathbf{u}}{\partial t}] = 0, \tag{2.6}$$

where $\theta$ is the porosity and $\rho_s$ is the density of the solid skeleton. Assuming that $\rho_s$ is constant and that $\mathbf{u}$ is sufficiently smooth to interchange the order of differentiation with respect to time and space, we get

$$\frac{\partial \theta}{\partial t} + \nabla\theta \cdot \frac{\partial \mathbf{u}}{\partial t} = (1-\theta)\frac{\partial}{\partial t}(\nabla \cdot \mathbf{u}). \tag{2.7}$$

By Tsai et al. [130], it is assumed that $|\frac{\partial \theta}{\partial t}| \gg |\nabla\theta \cdot \frac{\partial \mathbf{u}}{\partial t}|$; herewith, they arrive at

$$\frac{\partial \theta}{\partial t} = (1-\theta)\frac{\partial}{\partial t}(\nabla \cdot \mathbf{u}). \tag{2.8}$$

From this equation, we get

$$\theta(\mathbf{x},t) = 1 - \frac{1-\theta_0}{\exp(\nabla\cdot\mathbf{u})}, \tag{2.9}$$

2

with $\theta_0$ the initial porosity. Note that the above relation differs from the one of Tsai et al. [130], where in Eq. (2.8) they used a linearisation. By not applying this linearisation, we think that our approach is slightly more accurate. The permeability $\kappa$ is determined using the Kozeny-Carman equation [136]

$$\kappa(\mathbf{x},t) = \frac{d_s^2}{180}\frac{\theta^3}{(1-\theta)^2}, \tag{2.10}$$

where $d_s$ is the mean grain size of the soil. As a result of the dependency of the permeability on the mechanical deformations, problem (2.1)-(2.5) becomes nonlinear.

## 2.3 The set-up of the model

In this section, we will use Eqs. (2.1)-(2.5) to describe the flow pattern of water in a tube filled with a poroelastic material, after the injection of water into the left end of the tube. The situation is as shown in Figure 2.1a. We assume that the gravity-induced contribution to the flow of water is much smaller than the other contributions, which yields that the flow is axisymmetric, hence $\frac{\partial}{\partial\hat{\theta}}(.) = 0$ in which $\hat{\theta}$ is the azimuthal coordinate. Therefore, it is sufficient to determine the solution for a fixed azimuth (for example, the grey region in Figure 2.1a). The computational domain $\Omega$ is thus a rectangular two-dimensional surface with cylindrical coordinates $(x, r)$, as depicted in Figure 2.1b.

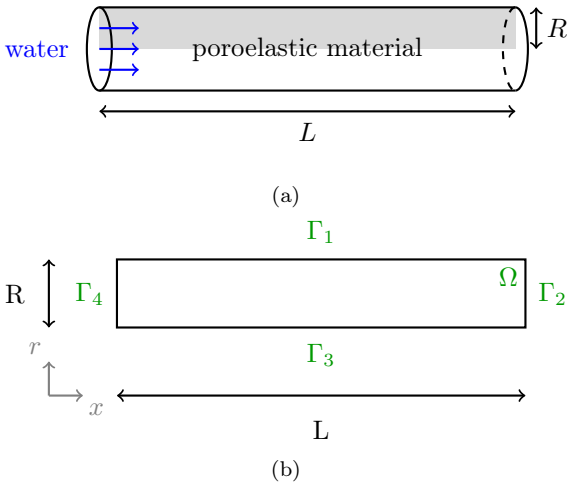


Figure 2.1: *Sketch of the set-up for the tube problem: (top) physical problem and (bottom) numerical discretisation. Taking advantage of the symmetry of geometry and boundary conditions, only the grey region is discretised.*

In order to solve this problem, Biot's consolidation model is applied on the computational domain $\Omega$, with two spatial dimensions $\mathbf{x} = (x, r)$ and with $t$ denoting time:

$$\begin{aligned} -\mu\tilde{\Delta}\mathbf{u} - (\lambda+\mu)\nabla(\nabla\cdot\mathbf{u}) + \nabla p = \mathbf{0} \quad &\text{for} \quad \mathbf{x}\in\Omega,\ t>0; \\ \frac{\partial}{\partial t}(\nabla\cdot\mathbf{u}) - \nabla\cdot(\frac{\kappa}{\eta}\nabla p) = 0 \quad &\text{for} \quad \mathbf{x}\in\Omega,\ t>0, \end{aligned} \tag{2.11}$$

where $\tilde{\Delta}$ is the vector Laplacian

$$\tilde{\Delta} = \begin{pmatrix} \Delta & 0 \\ 0 & \Delta \end{pmatrix}, \tag{2.12}$$

where $\Delta$ represents the Laplace operator. To complete the formulation of a well-posed problem, appropriate boundary and initial conditions are specified in Sections 2.3.1 and 2.3.2.

### 2.3.1 Water flow in a vibrating tube

To investigate the effect of vibrations on the water flow in the tube, we present two numerical experiments in this section. In these experiments, several ways of imposing vibrations are described, whereafter the effect on the volumetric flow rate at the right end of the tube is determined. In all problems, a tube of length $L$ and initial radius $R$ is considered. Furthermore, we assume that the casing of the tube is deformable, so that $R = R(x,t)$ holds. The poroelastic material in the tube is assumed to be isotropic and homogeneous.

**Effect of an oscillating casing of the tube on the flow** In this problem, a tube is considered with a frictionless, impermeable casing on which transverse waves are imposed (as shown in Figure 2.2).

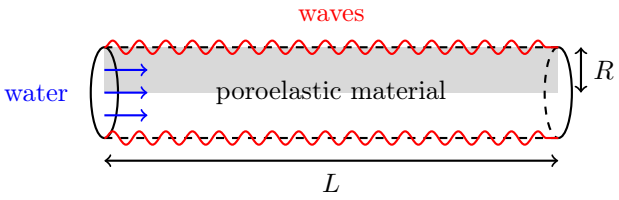


Figure 2.2: *Illustration of the waves imposed on the casing of the tube.*

Water is injected at a constant pressure into the soil through the left side surface ($x = 0$), while the right side surface ($x = L$) is kept at an ambient pressure at all times. Furthermore, filters are placed along the side surfaces to prevent that the grains exit the tube. More precisely, the boundary conditions for this problem are

given as follows:

$$\frac{\kappa}{\eta}\nabla p \cdot \mathbf{n} = 0 \quad \text{on} \quad \mathbf{x} \in \Gamma_1 \cup \Gamma_3; \tag{2.13a}$$

$$p = 0 \quad \text{on} \quad \mathbf{x} \in \Gamma_2; \tag{2.13b}$$

$$p = p_{pump} \quad \text{on} \quad \mathbf{x} \in \Gamma_4; \tag{2.13c}$$

$$(\boldsymbol{\sigma}'\mathbf{n}) \cdot \mathbf{t} = 0 \quad \text{on} \quad \mathbf{x} \in \Gamma; \tag{2.13d}$$

$$\mathbf{u} \cdot \mathbf{n} = u_{vib} \quad \text{on} \quad \mathbf{x} \in \Gamma_1; \tag{2.13e}$$

$$\mathbf{u} \cdot \mathbf{n} = 0 \quad \text{on} \quad \mathbf{x} \in \Gamma_2 \cup \Gamma_3; \tag{2.13f}$$

$$\mathbf{u} \cdot \mathbf{n} \leq 0 \quad \text{on} \quad \mathbf{x} \in \Gamma_4, \tag{2.13g}$$

where $\Gamma = \Gamma_1 \cup \Gamma_2 \cup \Gamma_3 \cup \Gamma_4$, $\mathbf{t}$ is the unit tangent vector at the boundary, $\mathbf{n}$ is the outer normal vector, $u_{vib}$ is a prescribed boundary displacement due to the vibrations and $p_{pump}$ is a prescribed boundary pore pressure due to the injection of water. Figure 2.1b shows the definition of the boundary segments. Note that the boundary conditions on boundary segment $\Gamma_3$ are required by the definition of symmetry. The variational inequality in condition (2.13g) accounts for the fact that the grains cannot exit the tube through boundary segment $\Gamma_4$. More specifically, condition (2.13g) states

$$\mathbf{u} \cdot \mathbf{n} \leq 0 \text{ and } (\boldsymbol{\sigma}'\mathbf{n}) \cdot \mathbf{n} = 0 \quad \text{or} \quad \mathbf{u} \cdot \mathbf{n} = 0. \tag{2.14}$$

This boundary condition could also be used on boundary segment $\Gamma_2$. However, in this case it is possible that $(\boldsymbol{\sigma}'\mathbf{n}) \cdot \mathbf{n} = 0$ on both boundary segments $\Gamma_2$ and $\Gamma_4$. Then, there is no Dirichlet boundary condition for the horizontal displacement (in the $x$-direction). This leads to a degenerate elliptic operator for the displacement $\mathbf{u}$, which could make the problem ill-posed. Initially, the following condition is fulfilled:

$$\mathbf{u}(\mathbf{x}, 0) = 0 \quad \text{for} \quad \mathbf{x} \in \Omega. \tag{2.15}$$

As mentioned earlier, transverse waves are imposed for the boundary displacement $u_{vib}$, represented by

$$u_{vib}(x, t) = \gamma \sin\left(\frac{2\pi}{\lambda_w}(x - vt)\right), \tag{2.16}$$

with $\gamma$ the amplitude of the wave, $\lambda_w$ the wavelength and $v$ the phase velocity. Note that for $v < 0$ the wave is travelling to the left, while for $v > 0$ the wave is travelling to the right.

**Effect of a vibrating imposed load on the flow** While in the previous section the vibrations were imposed as an oscillating casing of the tube, in this section the effect of an oscillating load applied on the casing is analysed. Accordingly, the boundary condition for the mechanical deformation on $\Gamma_1$ becomes

$$(\boldsymbol{\sigma}'\mathbf{n}) \cdot \mathbf{n} = \sigma'_{vib} \quad \text{on} \quad \mathbf{x} \in \Gamma_1, \tag{2.17}$$

with $\sigma'_{vib}$ is an oscillating vertical load. Similar to the previous section, transverse waves are used for the oscillating load

$$\sigma'_{vib}(x, t) = \gamma_\sigma \sin\left(\frac{2\pi}{\lambda_{w,\sigma}}(x - v_\sigma t)\right). \tag{2.18}$$

On $t = 0$, the initial condition (2.15) is fulfilled.

### 2.3.2 Pulsed injection

Instead of applying mechanical vibrations on the displacement, we can also investigate the effect of a pulsed injection of water into the left end of the tube. In this case, the prescribed boundary pore pressure $p_{pump}$ caused by the injection of water will have a pulsating behaviour rather than being constant. Hence, for the boundary conditions for the mechanical deformation on $\Gamma_1$ and for the water pressure on $\Gamma_4$ holds

$$p = p_{pump}(t) \quad \text{on} \quad \mathbf{x} \in \Gamma_4; \qquad \mathbf{u} \cdot \mathbf{n} = 0 \quad \text{on} \quad \mathbf{x} \in \Gamma_1, \tag{2.19}$$

with $p_{pump}(t)$ represented by the Heaviside step function

$$\mathcal{H}(t) = \begin{cases} 0 & t < 0 \\ 1/2 & t = 0 \\ 1 & t > 0 \end{cases}. \tag{2.20}$$

A rectangular pulse wave with period $T_p$ and pulse time $\tau$ can now be defined as

$$p_{pump}(t) = p_{max} \sum_{k=0}^{N_p} (\mathcal{H}(t - kT_p) - \mathcal{H}(t - kT_p - \tau)), \tag{2.21}$$

where $p_{max}$ is the maximum injection pressure and $N_p$ is the number of periods. An example of a rectangular pulse is shown in Figure 2.3. Furthermore, the initial condition (2.15) is fulfilled.

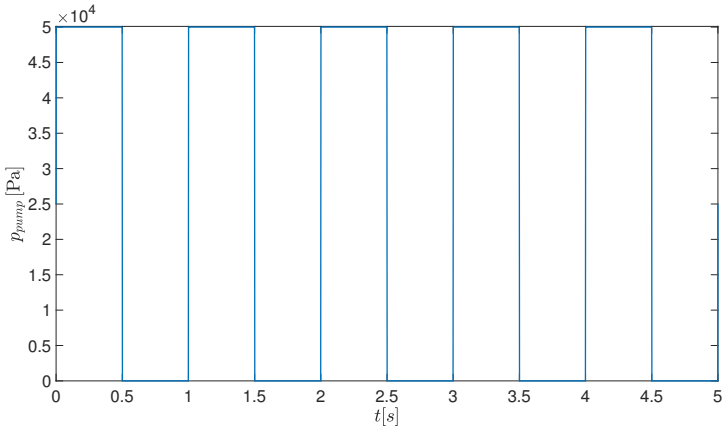


Figure 2.3: *A visualisation of a rectangular pulse with* $p_{max} = 5.0 \cdot 10^4\,\text{Pa}$, $\tau = 0.5\,\text{s}$ *and* $T_p = 1.0\,\text{s}$.

## 2.4 Numerical method

In this section, we outline the numerical procedures used to discretise the poroelastic model presented in Section 2.2 and to solve the resulting coupled fluid/solid finite-dimensional problem. The weak form of the governing equations will be derived and

discretised using a continuous Galerkin finite element approach with displacements and fluid pressures as primary variables. The suitability of the proposed methodology to model flow through elastic, saturated porous media will be demonstrated using the illustrative numerical examples described in the previous section.



### 2.4.1 Weak formulation

To present the variational formulation of these problems, we first introduce the appropriate function spaces. Let $L^2(\Omega)$ be the Hilbert space of square integrable scalar-valued functions $f$ on $\Omega$ defined in cylinder coordinates $(x, r)$ as

$$L^2(\Omega) = \{f : \Omega \to \mathbb{R} : \int_\Omega |f|^2 \, r \, d\Omega < \infty\}, \tag{2.22}$$

with inner product

$$(f, g) = \int_\Omega fgr \, d\Omega. \tag{2.23}$$

Let $H^1(\Omega)$ denote the subspace of $L^2(\Omega)$ of functions with first derivatives in $L^2(\Omega)$. We further introduce the function space

$$\mathscr{Q} = \{q \in H^1(\Omega) : q = 0 \text{ on } \Gamma_2 \text{ and } q = p_{pump} \text{ on } \Gamma_4\} \tag{2.24}$$

for all the problems that we consider. Subsequently, we use the function spaces

$$\mathscr{W} = \{\mathbf{w} \in (H^1(\Omega))^2 : \mathbf{w} \cdot \mathbf{n} = u_{vib} \text{ on } \Gamma_1 \text{ and } \mathbf{w} \cdot \mathbf{n} = 0 \text{ on } \Gamma_2\} \tag{2.25}$$

and

$$\mathscr{W}_0 = \{\mathbf{w} \in (H^1(\Omega))^2 : \mathbf{w} \cdot \mathbf{n} = 0 \text{ on } \Gamma_1 \cup \Gamma_2\} \tag{2.26}$$

for the problems with boundary conditions as stated in Eqs. (2.13) and (2.19), respectively. For the problem with boundary conditions (2.17), we introduce

$$\mathscr{W} = \{\mathbf{w} \in (H^1(\Omega))^2 : \mathbf{w} \cdot \mathbf{n} = 0 \text{ on } \Gamma_2\}. \tag{2.27}$$

Furthermore, we consider the bilinear forms [100]

$$a(\mathbf{u}, \mathbf{w}) = \lambda(\nabla \cdot \mathbf{u}, \nabla \cdot \mathbf{w}) + 2\mu \sum_{i,j=1}^{n_d} (\epsilon_{ij}(\mathbf{u}), \epsilon_{ij}(\mathbf{w})); \tag{2.28}$$

$$b(p, q) = \sum_{i=1}^{n_d} (\frac{\kappa}{\eta} \frac{\partial p}{\partial x_i}, \frac{\partial q}{\partial x_i}), \tag{2.29}$$

with $n_d$ the spatial dimension of the problem. The variational formulation in cylinder coordinates $(x, r)$ for problem (2.11) with boundary and initial conditions (2.13)-(2.15) and also for problem (2.11) with initial and boundary conditions (2.15) and (2.19) consists of the following, using the notation $\dot{\mathbf{u}} = \frac{\partial \mathbf{u}}{\partial t}$:

For each $t > 0$, find $(\mathbf{u}(t), p(t)) \in (\mathscr{W} \times \mathscr{Q})$ and $(\mathbf{u}(t), p(t)) \in (\mathscr{W}_0 \times \mathscr{Q})$ such that

$$a(\mathbf{u}(t), \mathbf{w}) - (p(t), \nabla \cdot \mathbf{w}) = h(\mathbf{w}) \qquad \forall \mathbf{w} \in \mathscr{W}_0; \tag{2.30}$$

$$(\nabla \cdot \dot{\mathbf{u}}(t), q) + b(p(t), q) = 0 \qquad \forall q \in \mathscr{Q}_0, \tag{2.31}$$

with the initial condition $\mathbf{u}(0) = \mathbf{0}$, and where

$$h(\mathbf{w}) = -p_{pump} \int_{\Gamma_4} \mathbf{w} \cdot \mathbf{n}\ r\ d\Gamma; \tag{2.32}$$

$$\mathscr{Q}_0 = \{q \in H^1(\Omega) : q = 0 \text{ on } \Gamma_2 \cup \Gamma_4\}. \tag{2.33}$$



The variational formulation for problem (2.11) in cylinder coordinates $(x, r)$ with initial and boundary conditions (2.15) and (2.17) consists of the following:

For each $t > 0$, find $(\mathbf{u}(t), p(t)) \in (\mathscr{W} \times \mathscr{Q})$ such that

$$a(\mathbf{u}(t), \mathbf{w}) - (p(t), \nabla \cdot \mathbf{w}) + c(p(t), \mathbf{w}) = h(\mathbf{w}) + g(\mathbf{w}) \qquad \forall \mathbf{w} \in \mathscr{W}; \tag{2.34}$$

$$(\nabla \cdot \dot{\mathbf{u}}(t), q) + b(p(t), q) = 0 \qquad \forall q \in \mathscr{Q}_0, \tag{2.35}$$

with the initial condition $\mathbf{u}(0) = \mathbf{0}$, and where

$$c(p, \mathbf{w}) = \int_{\Gamma_1} p\ \mathbf{w} \cdot \mathbf{n}\ r\ d\Gamma; \tag{2.36}$$

$$g(\mathbf{w}) = \int_{\Gamma_1} \sigma'_{vib}\ \mathbf{w} \cdot \mathbf{n}\ r\ d\Gamma. \tag{2.37}$$

### 2.4.2 Finite element discretisation

Problems (2.30)-(2.33) and (2.34)-(2.37) are solved by applying the finite element method, with triangular Taylor-Hood elements [28, 70, 113]. Let $\mathscr{P}_h^k \subset H^1(\Omega)$ be a function space of piecewise polynomials on $\Omega$ of degree $k$. Hence, we define finite element approximations for $\mathscr{W}$ and $\mathscr{Q}$ as $\mathscr{W}_h^k = \mathscr{W} \cap (\mathscr{P}_h^k \times \mathscr{P}_h^k)$ with basis

$$\{\boldsymbol{\phi}_i = (\phi_i, \phi_i) \in (\mathscr{W}_h^k \times \mathscr{W}_h^k) : i = 1, \ldots, n_u\}$$

and $\mathscr{Q}_h^{k'} = \mathscr{Q} \cap \mathscr{P}_h^{k'}$ with basis $\{\psi_j \in \mathscr{Q}_h^{k'} : j = 1, \ldots, n_p\}$, respectively [2, 100]. Subsequently, we approximate the functions $\mathbf{u}(t)$ and $p(t)$ with functions $\mathbf{u}_h(t) \in \mathscr{W}_h^k$ and $p_h(t) \in \mathscr{Q}_h^{k'}$, defined as

$$\mathbf{u}_h(t) = \sum_{i=1}^{n_u} \mathbf{u}_i(t)\boldsymbol{\phi}_i, \quad p_h(t) = \sum_{j=1}^{n_p} p_j(t)\psi_j, \tag{2.38}$$

in which the Dirichlet boundary conditions are imposed. Then, the semi-discrete Galerkin approximation of problem (2.30)-(2.33) is defined as follows:

For each $t > 0$, find functions $(\mathbf{u}_h(t), p_h(t)) \in (\mathscr{W}_h^k \times \mathscr{Q}_h^{k'})$ and $(\mathbf{u}_h(t), p_h(t)) \in (\mathscr{W}_{0h}^k \times \mathscr{Q}_h^{k'})$ such that

$$a(\mathbf{u}_h(t), \mathbf{w}_h) - (p_h(t), \nabla \cdot \mathbf{w}_h) = h(\mathbf{w}_h) \qquad \forall \mathbf{w}_h \in \mathscr{W}_{0h}^k; \tag{2.39}$$

$$(\nabla \cdot \dot{\mathbf{u}}_h(t), q_h) + b(p_h(t), q_h) = 0 \qquad \forall q_h \in \mathscr{Q}_{0h}^{k'}, \tag{2.40}$$

and for $t = 0$: $\mathbf{u}_h(0) = \mathbf{0}$.

Simultaneously, discretisation in time is applied using the backward Euler method. Let $\Delta t$ be the time step size and define a time grid $\{t_m = m\Delta t : m \in \mathbb{N}\}$, then the discrete Galerkin scheme of (2.39)-(2.40) is formulated as follows:

For $m \geq 1$, find $(\mathbf{u}_h^m, p_h^m) \in (\mathscr{W}_h^k \times \mathscr{Q}_h^{k'})$ and $(\mathbf{u}_h^m, p_h^m) \in (\mathscr{W}_{0h}^k \times \mathscr{Q}_h^{k'})$ such that

$$a(\mathbf{u}_h^m, \mathbf{w}_h) - (p_h^m, \nabla \cdot \mathbf{w}_h) = h(\mathbf{w}_h) \qquad \forall \mathbf{w}_h \in \mathscr{W}_{0h}^k; \tag{2.41}$$

$$(\nabla \cdot \mathbf{u}_h^m, q_h) + \Delta t \; b(p_h^m, q_h) = (\nabla \cdot \mathbf{u}_h^{m-1}, q_h) \qquad \forall q_h \in \mathscr{Q}_{0h}^{k'}, \tag{2.42}$$



while for $m = 0$: $\quad \mathbf{u}_h^0 = \mathbf{0}$.

The discrete Galerkin scheme for problem (2.34)-(2.37) is derived similarly. These discrete Galerkin schemes are solved using triangular Taylor-Hood elements. The displacements are spatially approximated by quadratic basis functions, whereas continuous piecewise linear approximation is used for the pressure field. We remark that the Taylor-Hood elements are suitable as a stable approach for this problem. However, spurious oscillations are diminished but not completely removed for small time steps. To fully remove the nonphysical oscillations, one may use the stabilisation techniques as considered by Aguilar et al. [2]. The numerical investigations are carried out using the matrix-based software package MATLAB (version R2011b). At each time step, we solve Eqs. (2.41)-(2.42) as a fully coupled system, where we use the permeability from the previous time step. After having obtained the numerical approximations for $\mathbf{u}$ and $p$, we update the porosity using Eq. (2.9). Subsequently, the Kozeny-Carman relation (2.10) is used to calculate the permeability. The new value for the permeability is then used for the next time step. An iterative method is not used in this approach because of efficiency and since no instability was observed in our results. In order to use Eq. (2.9), we determine the dilatation

$$\nabla \cdot \mathbf{u}_h^m = \frac{\partial u_{x,h}^m}{\partial x} + \frac{1}{r}\frac{\partial (r u_{r,h}^m)}{\partial r}, \tag{2.43}$$

using the numerical solution $\mathbf{u}_h = (u_{x,h}, u_{r,h})$ at time $t_m$. The spatial derivatives in the dilatation

$$\omega_1^m = \frac{\partial u_{x,h}^m}{\partial x} \quad \text{and} \quad \omega_2^m = \frac{1}{r}\frac{\partial (r u_{r,h}^m)}{\partial r}, \tag{2.44}$$

are then computed by applying the finite element method. Firstly, we introduce the functions $d \in L^2(\Omega)$ and we define the finite element approximation as $\mathscr{D}_h^k = L^2(\Omega) \cap \mathscr{P}_h^k$ with basis $\{\xi_i \in \mathscr{D}_h^k : i = 1, \ldots, n_u\}$. Secondly, we approximate the function $\omega_1^m$ with the function $\omega_{1,h}^m \in \mathscr{D}_h^k$, defined as

$$\omega_{1,h}^m = \sum_{i=1}^{n_u} \omega_{1,i}^m \xi_i. \tag{2.45}$$

Hence, the discrete Galerkin scheme is given by

For $m \geq 1$, find $\omega_{1,h}^m \in \mathscr{D}_h^k$ such that

$$(\omega_{1,h}^m, d_h) = (\frac{\partial u_{x,h}^m}{\partial x}, d_h) \quad \forall d_h \in \mathscr{D}_h^k.$$

The discrete Galerkin scheme for the function $\omega_2^m$ is derived similarly. In these finite element schemes, the spatial derivatives are approximated by quadratic basis functions. For the integrals in the element matrices and the element vectors, exact integration is used. Regarding accuracy, our numerical experiments showed that this

strategy produced sufficiently reliable results. We note that improvements of the accuracy can be obtained using gradient recovery techniques which yield superconverging behaviour [147]. The aim of this study is to investigate the impact of oscillatory and pulsating boundary conditions on the volumetric flow rate at the right end of the tube. We compute the volumetric flow rate at the right boundary segment, using the velocity field as described by Darcy's law (2.4). To compute the velocity field for post-processing issues, the finite element method is applied analogously to the computation of the derivatives of the displacements, combined with piecewise linear approximation and exact integration.



## 2.5 Numerical results

In this section, we discuss the solution results for the discrete Galerkin approximation of the quasi-two-dimensional problems that are presented in Section 2.3. The simulation domain is a rectangle with length 1.0 m and width 10 cm (see Figure 2.1b). The domain is discretised using a 101 by 11 regular triangular grid, which provides sufficient resolution according to a mesh refinement study. The chosen values for the material properties of the porous medium are given in Table 2.1, where $\lambda$ and $\mu$ are related to Young's modulus $E$ and Poisson's ratio $\nu$ by [2]:

$$\lambda = \frac{\nu E}{(1+\nu)(1-2\nu)}, \quad \mu = \frac{E}{2(1+\nu)}.$$

Table 2.1: *An overview of the values of the material properties and the parameters of the model.*

| Property | Symbol | Value | Unit |
|---|---|---|---|
| Young's modulus | $E$ | $10^7$ | Pa |
| Poisson's ratio | $\nu$ | 0.3 | - |
| Fluid viscosity | $\eta$ | $1.307 \cdot 10^{-3}$ | Pa · s |
| Initial porosity | $\theta_0$ | 0.375 | - |
| Mean grain size | $d_s$ | $0.2 \cdot 10^{-3}$ | m |
| Pump pressure | $p_{pump}$ | $0.5 \cdot 10^5$ | Pa |

The values in Table 2.1 are chosen based on discussions with experts from engineering and consultancy company Fugro GeoServices B.V. and on the literature [142].

### 2.5.1 The impact of an oscillating casing of the tube on the water flow

In order to obtain some insight into the impact of an oscillating casing of the tube on the water flow, we present an overview of the simulation results in Figures 2.4 and 2.5. In this simulation, water is injected into the soil at a constant pump pressure equal to 0.5 bar. As a consistency check, we start with the simulation results for

problem (2.41)-(2.42) without any vibrations, i.e. $u_{vib} = 0$. The simulated pressure, fluid velocity, permeability and displacement profiles are provided in Figure 2.4.

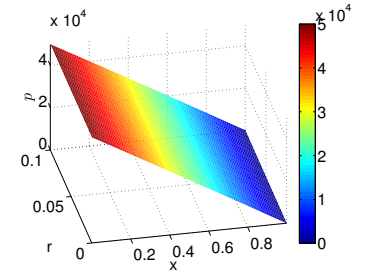


(a) Numerical solution for the pressure.

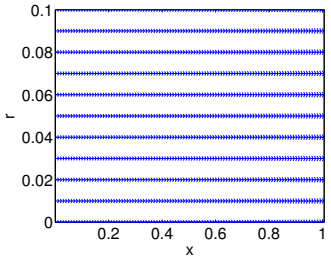


(b) Numerical solution for the fluid velocity.

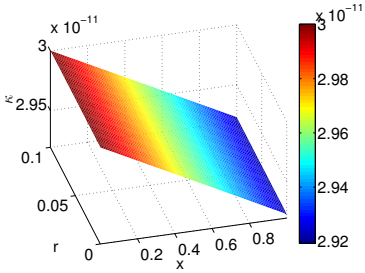


(c) Numerical solution for the permeability.

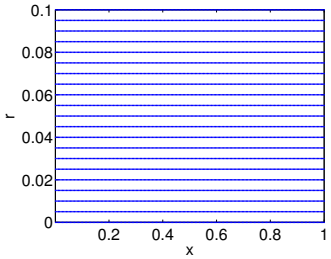


(d) The positions of the mesh points after subjecting them to the calculated displacement vector **u**.

Figure 2.4: *Numerical solutions for the pressure, the fluid velocity, the permeability and the displacement, without vibrations, at time* $t = 5$ *using a constant time step size* $\Delta t = 0.1$. *The values of the remaining parameters are as depicted in Table 2.1.*

As shown in Figure 2.4, the simulated pressure is almost linear and the behaviour of the fluid velocity is completely horizontal. This means that the injected water flows in a horizontal direction through the tube from the left end of the tube to the right end. Mechanically, the deformations in the porous medium are negligible, other than a small shift of the grains to the right, as a result of the force exerted on the grains by the injected water. As a result of this small shift of the grains and the assumption that the grains cannot exit the tube, we expect a higher grain density near the right end. Consequently, the permeability will linearly decrease towards the right end of the tube, as depicted in Figure 2.4c. In Figure 2.5, the numerical solutions are shown for a test case of problem (2.41)-(2.42) with vibrations. In this test case, a transverse wave (2.16) travelling to the right is chosen as prescribed boundary displacement $u_{vib}$, with $\gamma = 1\,\text{cm}$, $\lambda_w = 1\,\text{m}$ and $v = 1\,\text{m/s}$.

In contrast to the pressure shown in Figure 2.4a, the numerical solution for the pressure in the problem with vibrations is no longer linear, but shows an oscillatory behaviour, as depicted in Figure 2.5a. The vibrations also provide an oscillatory profile in the permeability, as shown in Figure 2.5c. In this figure, we can see that the permeability decreases when the grains are pressed together by the vibration, while

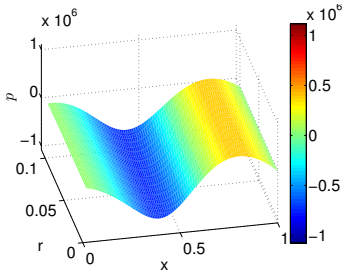


(a) Numerical solution for the pressure.

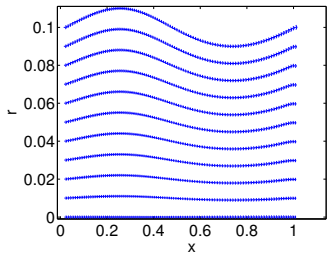


(b) Numerical solution for the fluid velocity.

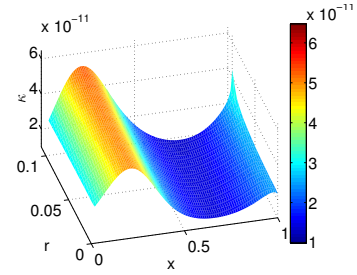


(c) Numerical solution for the permeability.

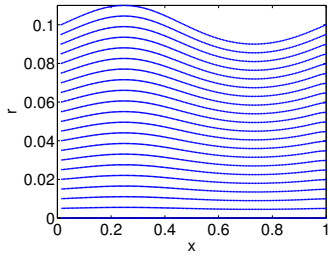


(d) The positions of the mesh points after subjecting them to the calculated displacement vector $\mathbf{u}$.

Figure 2.5: *Numerical solutions for the pressure, the fluid velocity, the permeability and the displacement, at time* $t = 5$ *using a constant time step size* $\Delta t = 0.1$. *For the vibrations a travelling wave to the right is chosen as prescribed boundary displacement* $u_{vib}$, *with* $\gamma = 1\,\text{cm}$, $\lambda_w = 1\,\text{m}$ *and* $v = 1\,\text{m/s}$. *The values of the remaining parameters are as depicted in Table 2.1.*

it increases when the grains are pulled apart. The simulation results in Figures 2.4 and 2.5 show an impact of the vibrations, imposed on the casing, on the water flow. However, by only looking at these results, the impact of vibrations on the amount of water that flows through the tube stays unmeasurable. For this reason, the impact of the vibrations and pulses on the water flow is defined in this chapter as the impact on the volumetric flow rate $Q$ at the right end of the tube. In Figure 2.6, two graphs are presented that sketch the behaviour of the volumetric flow rate over time at the right end of the tube. In these simulations, the aforementioned test cases are used. For the test case without vibrations, the time average of the volumetric flow rate $\overline{Q}$ over the time interval $(0, 5]$ is equal to $6.86 \cdot 10^{-5}\,\text{m}^3/\text{s}$. For the test case with imposed vibrations, the time average of the volumetric flow rate $\overline{Q}$ over the time interval $(0, 5]$ is equal to $9.69 \cdot 10^{-4}\,\text{m}^3/\text{s}$. Thus, the percentage change $\overline{Q}_{\%}$ of the time average of the volumetric flow rate as result of the imposed vibration is 1311.7%. Based on these test cases, we can conclude that the volumetric flow rate at the right end of the tube increases as a result of the imposed vibrations on the casing, as depicted in Figure 2.6. We finally note that the area enclosed by the $Q$-curve and the $t$-axis represents the total amount of water that flows out of the domain over a certain period.

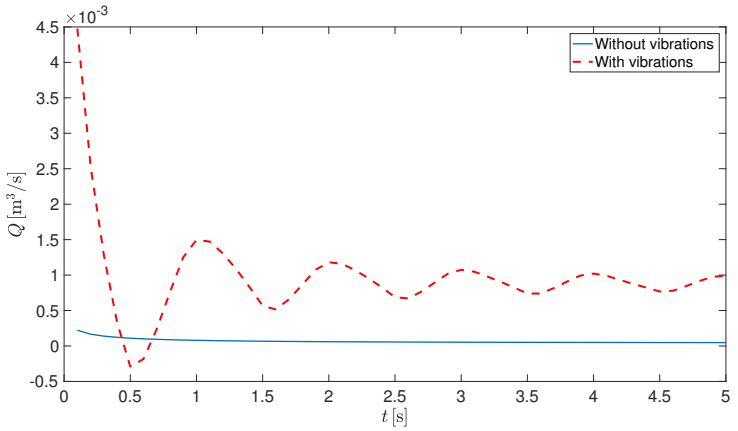


Figure 2.6: *The volumetric flow rate at the right end of the tube over time, using a constant time step size* $\Delta t = 0.1$. *The continuous line represents the volumetric flow rate for the test case without vibrations. The dashed line represents the volumetric flow rate for the test case with vibrations, in which for the vibrations a travelling wave to the right is chosen, with* $\gamma = 1\,\mathrm{cm}$, $\lambda_w = 1\,\mathrm{m}$ *and* $v = 1\,\mathrm{m/s}$. *The values of the remaining parameters are as depicted in Table 2.1.*

### Monoparametric variation

In this section, we will investigate the impact of the transverse waves (2.16) on the flow of water. Furthermore, the contributions of the variations in the values of the vibration characteristics to the volumetric flow rate are quantified by assigning a range of possible values to the parameters: $\gamma$, $\lambda_w$ and $v$. Firstly, a monoparametric variation is applied whereby the values of the parameters are varied one by one, within ranges of possible values. In Figure 2.7, the volumetric flow rate at the right end of the tube is depicted over time after applying a monoparametric variation in the values of the vibration characteristics $\gamma$, $\lambda_w$ and $v$. For the variation, the following ranges of possible values are chosen:

$$\gamma \in [0, 1, 5, 10] \cdot 10^{-3}, \quad \lambda_w \in [1/4, 1/2, 1], \quad v \in [-2.0, -1.0, -0.5, 0.5, 1.0, 2.0].$$

In the generations of the simulation results presented in Figure 2.7, the time step size $\Delta t$ is determined using the formula $\Delta t = \frac{1}{8f}$, in which $f$ is the frequency computed by

$$f = \frac{|v|}{\lambda_w}. \tag{2.46}$$

In case variation is applied to the values of $\lambda_w$ or $v$, the maximum value of $f$ is used to determine the time step size. Figure 2.7a indicates that an increase in the amplitude of the imposed wave, with fixed wavelength and phase velocity, results in an increase in the volumetric flow rate. However, an increase in the wavelength, with fixed amplitude and phase velocity, leads to a decrease in the volumetric flow rate, as shown in Figure 2.7b. Figure 2.7c indicates that an increase in the phase velocity magnitude $|v|$, with fixed amplitude and wavelength, leads to a larger impact on the flow rate.

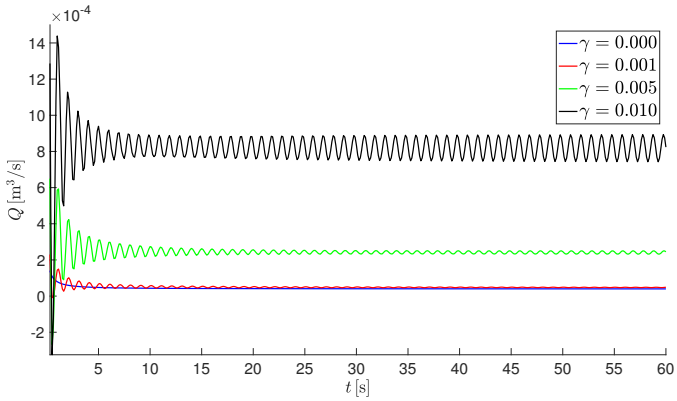


(a) The flow rate over time, after applying variation in the values of $\gamma$. The other vibration characteristics are $\lambda_w = 1$ and $v = 1$.

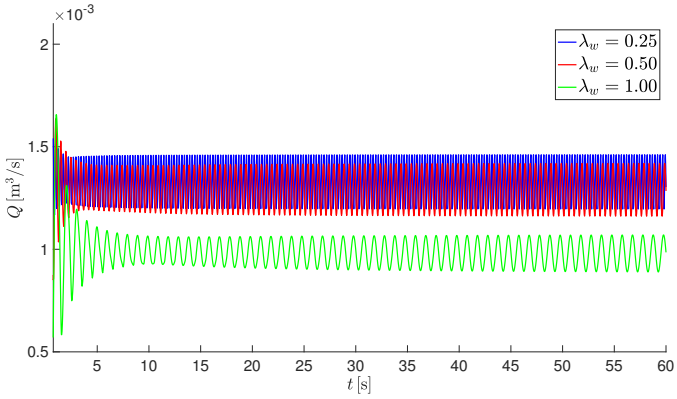


(b) The flow rate over time, after applying variation in the values of $\lambda_w$. The other vibration characteristics are $\gamma = 0.01$ and $v = 1$.

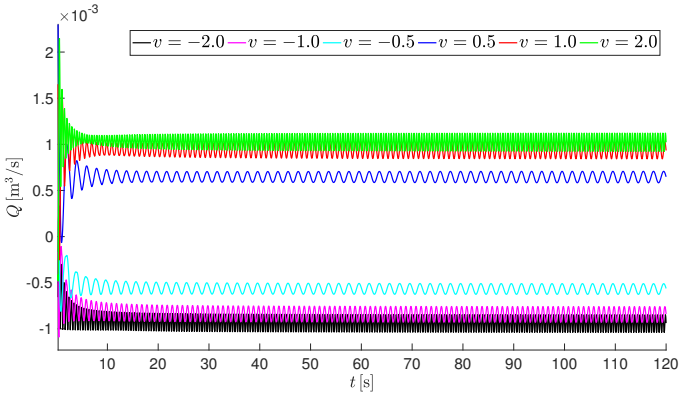


(c) The flow rate over time, after applying variation in the values of $v$. The other vibration characteristics are $\gamma = 0.01$ and $\lambda_w = 1$.

Figure 2.7: *The volumetric flow rate profiles at the right end of the tube over time, after applying a monoparametric variation in the values of $\gamma$, $\lambda_w$ and $v$.*

Furthermore, assigning positive values to the phase velocity $v$ (corresponding with transverse waves travelling to the right) results in positive volumetric flow rate profiles. Assigning negative values to the phase velocity $v$ (corresponding with transverse waves travelling to the left) produces negative volumetric flow rates. As expected, the water flow, which is directed to the right, is stimulated by waves travelling in the same direction. However, waves travelling in the opposite direction counteract the flow, resulting in negative volumetric flow rates. In fact, the negative volumetric flow rates are a result of the force applied by the oppositely directed waves that is larger than the pump pressure. At a higher pump pressure, the effect of these waves on the volumetric flow rate is smaller, as illustrated in Figure 2.8.

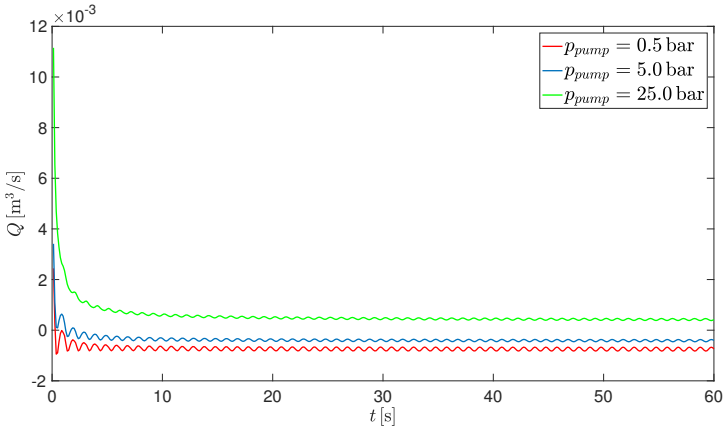


Figure 2.8: *The volumetric flow rate at the right end of the tube over time for different values of the pump pressure $p_{pump}$, using a constant time step size $\Delta t = 0.1$. In all test cases, a travelling wave to the left is chosen as prescribed boundary displacement $u_{vib}$, with $\gamma = 1\,\mathrm{cm}$, $\lambda_w = 1\,\mathrm{m}$ and $v = -1\,\mathrm{m/s}$.*

### Multiparametric variation

In the previous section, the contributions of the variations in the values of the vibration characteristics to the volumetric flow rate were quantified by applying a monoparametric variation where the values of the parameters are varied one by one, within ranges of possible values. As we choose to fix a number of parameter values each time, we are not able to draw any conclusions from this monoparametric variation. In this section, a multiparametric variation is applied to the values of the vibration characteristics. Multiparametric variation means that all possible combinations of the values of these parameters are considered, in which the values are selected from sets of possible values. In Figure 2.9, the time average of the volumetric flow rate at the right end of the tube is depicted after applying a multiparametric variation to the values of the vibration characteristics $\gamma$, $\lambda_w$ and $v$. For the variation, the following sets of possible values are chosen:

$$\begin{gathered}\gamma \in [2, 4, 6, 8, 10] \cdot 10^{-3}, \quad \lambda_w \in [1/4, 1/3, 1/2, 1], \\ v \in [-2.0, -1.0, -0.5, 0.5, 1.0, 2.0].\end{gathered} \tag{2.47}$$

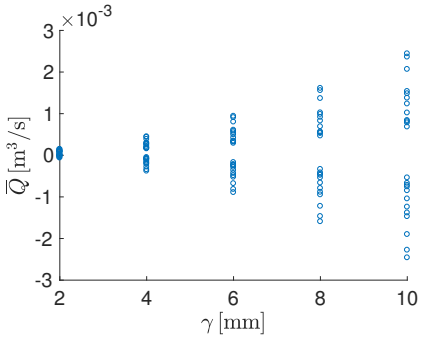


(a) The time average of the volumetric flow rate as function of $\gamma$.

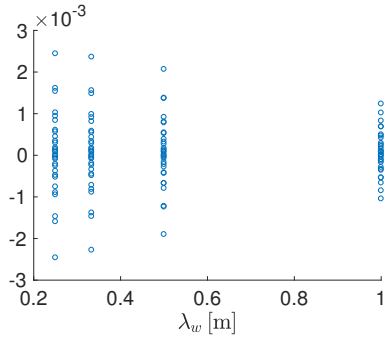


(b) The time average of the volumetric flow rate as function of $\lambda_w$.

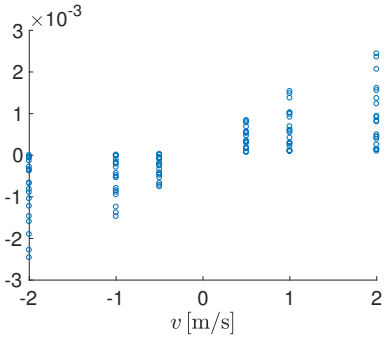


(c) The time average of the volumetric flow rate as function of $v$.

Figure 2.9: *Scatter plots of the time average of the volumetric flow rate over the time interval* $(0, 60]$*, after applying a multiparametric variation to the values of the parameters* $\gamma$*,* $\lambda_w$ *and* $v$*. For the vibrations, transverse waves* (2.16) *are used as prescribed boundary displacement* $u_{vib}$*, with* $\gamma \in [2, 4, 6, 8, 10]$ mm*,* $\lambda_w \in [1/4, 1/3, 1/2, 1]$ m *and* $v \in [-2.0, -1.0, -0.5, 0.5, 1.0, 2.0]$ m/s*.*

Figure 2.9a shows that an increase in the amplitude of the imposed wave leads to a larger impact on the time average of the volumetric flow rate $\overline{Q}$. However, an increase in the wavelength results in a smaller impact on $\overline{Q}$, as shown in Figure 2.9b. In both figures, we observe a mirroring across a line near the horizontal axis. Values of $\overline{Q}$ above the mirror line correspond with positive values of the phase velocity, while values of $\overline{Q}$ bellow the mirror line correspond with negative values of $v$, as can be concluded from Figure 2.9c. Furthermore, Figure 2.9c shows that an increasing phase velocity magnitude $|v|$ leads to a larger impact on $\overline{Q}$. In addition, we observe in Figure 2.9c that for $v < 0$ some of the values of $\overline{Q}$ are positive, these values correspond with small values of the amplitude. In this case, the pump pressure is larger than the force applied by the oppositely directed waves, which results in positive volumetric flow rates. Note that these results are consistent with the results from the previous section.

### Monte Carlo method

The sets of values (2.47) used in the previous section are not covering all possible values for the vibration characteristics. Hence, instead of varying the parameter values using sets of predetermined values, we can also sample them from probability distributions. In this section, Monte Carlo method is applied to the values of the vibration characteristics using samples from uniform distributions with chosen boundaries. In Figure 2.10, the time average of the volumetric flow rate is depicted after applying Monte Carlo simulations to the values of the vibration characteristics $\gamma$, $\lambda_w$ and $v$. For the simulations, 300 samples from the following uniform distributions are generated:

$$\gamma \sim \mathcal{U}(0.001, 0.01), \quad \lambda_w \sim \mathcal{U}(1/4, 1), \quad v \sim \mathcal{U}(-2, 2). \tag{2.48}$$

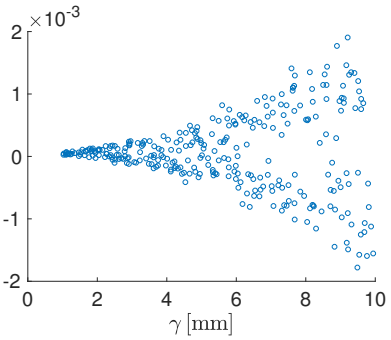


(a) The time average of the volumetric flow rate as function of $\gamma$.

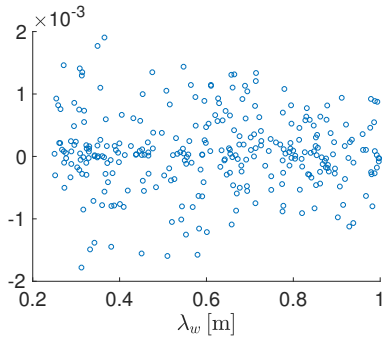


(b) The time average of the volumetric flow rate as function of $\lambda_w$.

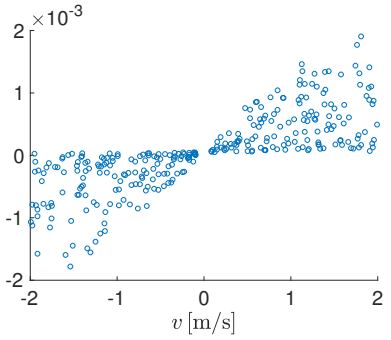


(c) The time average of the volumetric flow rate as function of $v$.

Figure 2.10: *Scatter plots of the time average of the volumetric flow rate over the time interval* $(0, 70.86]$*, after applying Monte Carlo simulations to the values of* $\gamma$*,* $\lambda_w$ *and* $v$*. For the vibrations transverse waves* (2.16) *are used as prescribed boundary displacement* $u_{vib}$*, with* $\gamma \sim \mathcal{U}(1, 10)$ mm*,* $\lambda_w \sim \mathcal{U}(1/4, 1)$ m *and* $v \sim \mathcal{U}(-2, 2)$ m/s*.*

Similar to the results shown in Figure 2.9, Figures 2.10a and 2.10b indicate that an increase in the amplitude leads to a larger impact on $\overline{Q}$. While an increase in the wavelength results in a smaller impact on $\overline{Q}$. Furthermore, Figure 2.10c shows that an increasing fase velocity magnitude $|v|$ leads to a larger impact on $\overline{Q}$. From

the formula for the frequency and Figure 2.10, we can conclude that large amplitudes and high frequencies lead to high volumetric flow rates for $v > 0$. In Table 2.2, the Pearson correlation coefficients are given together with the associated $p$-values. From this table we can conclude that the vibration characteristics $\gamma$ and $v$ have the most impact on the time average of the volumetric flow rate.

Table 2.2: *The Pearson correlation coefficients together with the associated p-values. A p-value less than 0.05 means that the two paired sets of data are most probably related, at the significance level 0.05.*

| | $corr(\gamma, \overline{Q})$ | | $corr(\lambda_w, \overline{Q})$ | | $corr(v, \overline{Q})$ | |
|---|---|---|---|---|---|---|
| | $v > 0$ | $v < 0$ | $v > 0$ | $v < 0$ | $v > 0$ | $v < 0$ |
| $r$ | 0.82 | −0.81 | −0.09 | 0.07 | 0.40 | 0.47 |
| $p$ | $< 0.05$ | $< 0.05$ | 0.27 | 0.39 | $< 0.05$ | $< 0.05$ |

To measure the real impact of the transverse waves (2.16) on the water flow, the percentage change $\overline{Q}_{\%}$ of the time average of the volumetric flow rates as result of the imposed vibrations is determined by the formula

$$\overline{Q}_{\%} = \frac{\overline{Q} - \overline{Q}_0}{\overline{Q}_0} \cdot 100, \tag{2.49}$$

where $\overline{Q}_0$ is the time average of the volumetric flow rate in the test case without vibrations. The percentage change $\overline{Q}_{\%}$ of the time average $\overline{Q}$, that is computed after applying the above described Monte Carlo method (see Figure 2.10), is depicted as function of $\gamma$ in Figure 2.11.

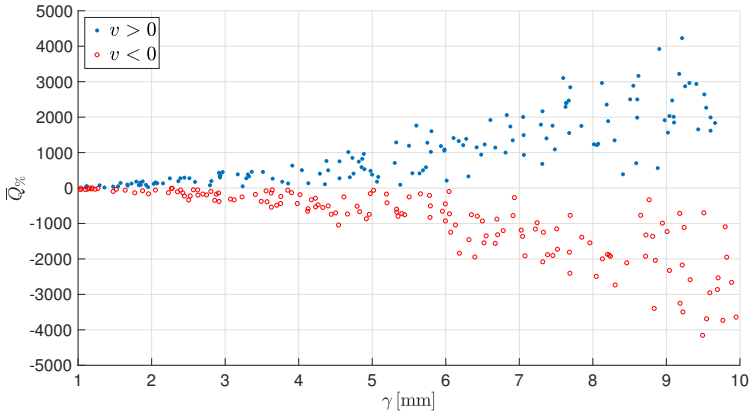


Figure 2.11: *Scatter plot of the percentage change* $\overline{Q}_{\%}$ *over the time interval* $(0, 70.86]$ *as function of* $\gamma$*, after applying Monte Carlo method to the values of* $\gamma$*,* $\lambda_w$ *and* $v$*.*

Figure 2.11 shows that, for $v > 0$, the volumetric flow rate at the right end of the tube increases as a result of the imposed vibrations on the casing. For vibrations

with a large amplitude and a high frequency, the time average of the volumetric flow rate can become as large as 42 times the time average of the volumetric flow rate in the test case without vibrations. While the smallest percentage change in the volumetric flow rate as cause of the vibrations is equal to 6.0%. On the other hand, for $v < 0$, all vibrations lead to a negative percentage change $\overline{Q}_{\%}$, even the vibrations with small values of the amplitude $\gamma$. Given the probability space $(\Omega_p, \mathcal{F}, P)$, with sample space $\Omega_p$ (which is the set of all possible outcomes), the set of events $\mathcal{F}$ (where each event is a set with zero or more outcomes), and the probability $P$, with $P : \mathcal{F} \to [0, 1]$, we can compute the cumulative distribution function. In Figure 2.12, the histogram and the cumulative distribution function of the percentage change $\overline{Q}_{\%}$ are presented. Since 51% of the sampled values of $v$ are negative, we see in Figure 2.12 that $P(\overline{Q}_{\%} \leq 0) \approx 0.51$. Furthermore, using the probability space we can compute the probabilities that the percentage change is greater than 100%: $P(\overline{Q}_{\%} \geq 100) \approx 0.43$ and $P(\overline{Q}_{\%} \geq 100 | v > 0) \approx 0.89$.

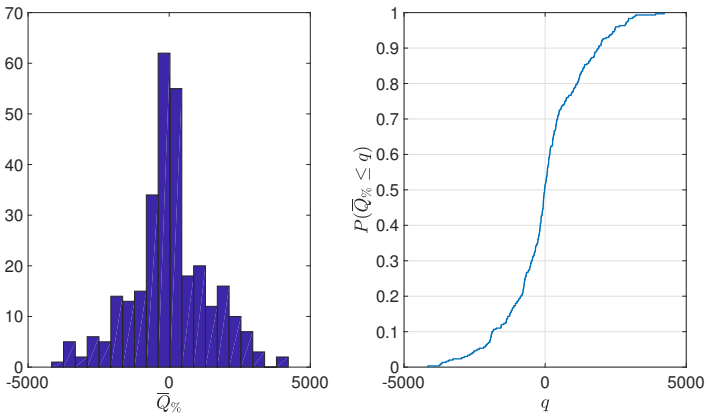


Figure 2.12: *The histogram and the cumulative distribution function of the percentage change*

### 2.5.2 The impact of a vibrating load on the water flow

In this section, the impact of a vibrating load, which is applied on the casing of the tube, on the water flow is investigated. This numerical experiment makes it possible to analyse the contributions of the variations in the values of the porous medium properties to the volumetric flow rate. These contributions are quantified by assigning a range of possible values to the parameters: $E$, $\nu$, $\theta_0$ and $d_s$. For this purpose, four types of soil are distinguished: clay, silt, sand and gravel. In the literature, there is a large consensus that the Kozeny-Carman equation (2.10) applies to sands but not to clays [38]. Therefore, this experiment is only applied to sand and gravel.

#### Monte Carlo method for sand and gravel

Monte Carlo method is applied to the values of the material properties of sand and gravel, using samples of uniform distributions with boundaries found in the litera-

ture [56, 117]. As the values within these boundaries are all equally likely to occur, we have chosen to use uniform distributions instead of another frequently used distributions like the log-normal distribution. In Figures 2.13 and 2.14, the time average of the volumetric flow rate at the right end of the tube is depicted after applying Monte Carlo simulations to the values of the material properties $E$, $\nu$, $\theta_0$ and $d_s$. For sand, 300 samples from the following uniform distributions are generated:

$$E \sim \mathcal{U}(30 \cdot 10^6, 50 \cdot 10^6), \quad \nu \sim \mathcal{U}(0.15, 0.40), \quad \theta_0 \sim \mathcal{U}(0.26, 0.46), \\ d_s \sim \mathcal{U}(0.05 \cdot 10^{-3}, 2.00 \cdot 10^{-3}), \tag{2.50}$$

while for gravel, 300 samples from these uniform distributions are generated:

$$E \sim \mathcal{U}(80 \cdot 10^6, 160 \cdot 10^6), \quad \nu \sim \mathcal{U}(0.30, 0.40), \quad \theta_0 \sim \mathcal{U}(0.23, 0.38), \\ d_s \sim \mathcal{U}(2 \cdot 10^{-3}, 50 \cdot 10^{-3}). \tag{2.51}$$

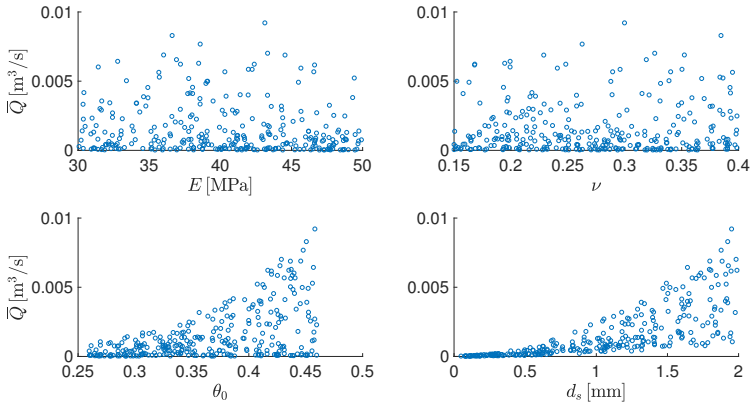


Figure 2.13: *Scatter plots of* $\overline{Q}$ *over the time interval* $(0, 25]$*, after applying Monte Carlo simulations to the values of the material properties of sand using the ranges* (2.50)*. For the vibrations transverse waves* (2.18) *are used as prescribed vertical load* $\sigma'_{vib}$*, with* $\gamma_\sigma = 10^4\,\mathrm{Pa}$*,* $\lambda_{w,\sigma} = 1/4\,\mathrm{m}$ *and* $v_\sigma = 1\,\mathrm{m/s}$*.*

Figures 2.13 and 2.14 show that water flows faster through porous media with large mean grain sizes or high initial porosities, after imposing a vibrating load on the casing. On the other hand, these figures show that the volumetric flow rate is invariant under variation in the values of Young's modulus and Poisson's ratio. This can also be concluded from the values of the Pearson correlation coefficients given in Table 2.3.

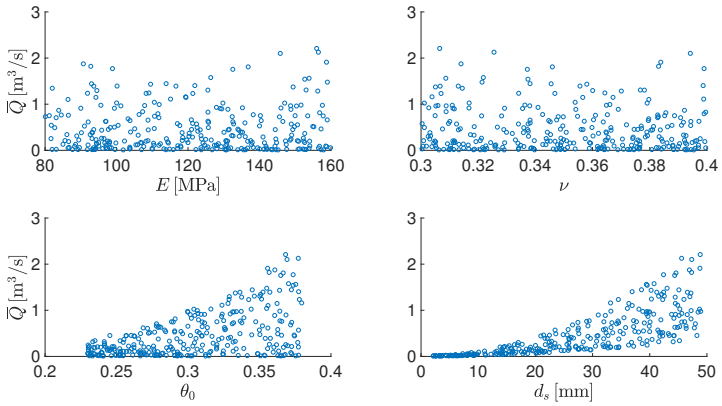


Figure 2.14: *Scatter plots of* $\overline{Q}$ *over the time interval* $(0, 25]$*, after applying Monte Carlo simulations to the values of the material properties of gravel using the ranges* (2.51)*. For the vibrations transverse waves* (2.18) *are used as prescribed vertical load* $\sigma'_{vib}$*, with* $\gamma_\sigma = 10^4\,\text{Pa}$*,* $\lambda_{w,\sigma} = 1/4\,\text{m}$ *and* $v_\sigma = 1\,\text{m/s}$*.*

Table 2.3: *The Pearson correlation coefficients together with the associated p-values.*

| | $corr(E, \overline{Q})$ | | $corr(\nu, \overline{Q})$ | | $corr(\theta_0, \overline{Q})$ | | $corr(d_s, \overline{Q})$ | |
|---|---|---|---|---|---|---|---|---|
| | sand | gravel | sand | gravel | sand | gravel | sand | gravel |
| $r$ | $-0.11$ | 0.05 | 0.05 | $-0.06$ | 0.52 | 0.52 | 0.75 | 0.77 |
| $p$ | 0.07 | 0.43 | 0.39 | 0.30 | $< 0.05$ | $< 0.05$ | $< 0.05$ | $< 0.05$ |

### 2.5.3 The impact of a pulsed injection on the water flow

Based on over 160 laboratory tests, Dusseault [46] demonstrated the beneficial effects of pressure pulsing on the water flow in porous media. To theoretically examine his findings, we investigated the impact of a pulsed injection of water, into the left end of the tube, on the water flow. The results of this research are presented in this section. In addition, the contributions of the variations in the values of the pulse wave characteristics to the volumetric flow rate are analysed. These contributions are examined by applying Monte Carlo method to the pulse wave period $T_p$ and the relative pulse time $\tilde{\tau}$, defined as $\tilde{\tau} = \frac{\tau}{T_p}$, with $\tau$ the pulse time (see Formula (2.21)). Subsequently, in order to be able to draw reliable conclusions about the impact of pressure pulsing on the volumetric flow rate, we compare the volumetric flow rate caused by the pulsed injection with the volumetric flow rate by a constant pump pressure $p_{pump}$. In this comparison, the percentage change $\overline{Q}_\%$ of the time average of the volumetric flow rate $\overline{Q}$ is used, determined by

$$\overline{Q}_\% = \frac{\overline{Q} - \overline{Q}_C}{\overline{Q}_C} \cdot 100, \tag{2.52}$$

where $\overline{Q}_C$ is the time average of the volumetric flow rate caused by a constant pump pressure. In each simulation, the constant pump pressure is chosen equal to the total pump pressure over time by pulsed injection. Hence, for a particular relative pulse time $\tilde{\tau}$, the constant pump pressure is computed by $p_{pump} = \tilde{\tau} p_{max}$. In Figure 2.15, the percentage change in the time average of the volumetric flow rate at the right end of the tube is depicted after applying Monte Carlo simulations to the values of the pulse wave characteristics $T_p$ and $\tilde{\tau}$. For the simulation, 300 samples from the following uniform distributions are generated:

$$T_p \sim \mathcal{U}(0.5, 4), \quad \tilde{\tau} \sim \mathcal{U}(0.1, 0.9). \tag{2.53}$$

In the generations of the simulation results presented in Figure 2.15, the time step size $\Delta t$ is determined by $\Delta t = \frac{T_p}{20}$. As variation is applied to the values of $T_p$, the minimum value of $\Delta t$ is used as time step size.

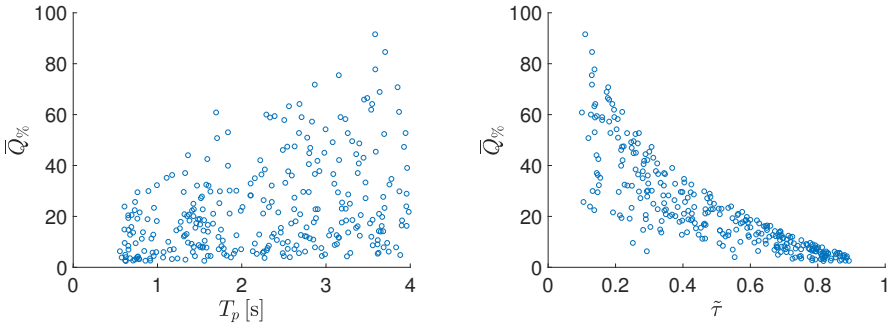


(a) $\overline{Q}_{\%}$ as function of $T_p$.

(b) $\overline{Q}_{\%}$ as function of $\tilde{\tau}$.

Figure 2.15: *Scatter plots of the percentage change* $\overline{Q}_{\%}$ *of the time average of the volumetric flow rate over the time interval* $(0, 20]$*, after applying Monte Carlo method to the values of* $T_p$ *and* $\tilde{\tau}$ *using the distributions* (2.53)*. For the pump pressure, pulse waves* (2.21) *are used with* $p_{max} = 0.5 \cdot 10^5$ Pa.

Figure 2.15 shows that pressure pulsing with small relative pulse times $\tilde{\tau}$ leads to a major increase in the volumetric flow rate, while it increases slightly by increasing the pulse period $T_p$. This can also be confirmed by the Pearson correlation coefficients and the $p$-values given in Table 2.4.

Table 2.4: *The Pearson correlation coefficients together with the associated p-values.*

| | $corr(T_p, \overline{Q})$ | $corr(\tilde{\tau}, \overline{Q})$ |
|---|---|---|
| $r$ | 0.38 | $-0.83$ |
| $p$ | $< 0.05$ | $< 0.05$ |

In Figure 2.16, the histogram and the cumulative distribution function of the percentage change $\overline{Q}_{\%}$ are depicted. Since $P(\overline{Q}_{\%} \leq 0) = 0$, we can conclude from Figures 2.15 and 2.16 that pulsed injection has a beneficial effect on the water flow in porous media.

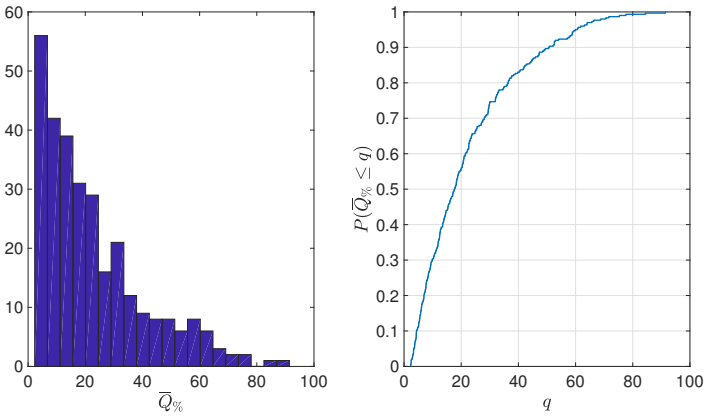


Figure 2.16: *The histogram and the cumulative distribution function of the percentage change.*

## 2.6 Discussion and conclusions

In this study, the poroelasticity system with nonlinear permeability is solved using the Galerkin finite element method based on Taylor-Hood elements, combined with a backward Euler time integration. The study contains simulations with oscillatory force boundary conditions as well as pressure pulses. Furthermore, to quantify the impact of variation of model parameters such as Young's modulus, the oscillatory modes and the injection pressure pulses, a probabilistic approach is carried out.

To begin with, soil vibrations are applied on the casing of a tube as oscillatory displacement boundary condition. Numerical results showed that large amplitudes and high frequencies of the imposed mechanical vibrations lead to high-volumetric flow rates for positive values of the phase velocity, corresponding with transverse waves travelling to the right. Therefore, the flow rate at the right end of the tube increased as a result of the imposed mechanical vibrations. On the other hand, for negative values of the phase velocity, corresponding with waves travelling to the left, the vibrations lead to a decrease in the volumetric flow rate at the right end of the tube. As expected, the water flow, which is directed to the right, is stimulated by waves travelling in the same direction, while waves travelling in the opposite direction counteract the flow, resulting in negative volumetric flow rates in case the force applied by the oppositely directed waves is larger than the pump pressure. In this chapter, these effects have been quantified. Subsequently, applying an oscillating load on the casing of the tube showed that water flows faster through porous media with large grain sizes and/or high initial porosities. On the other hand, variation in the values of Young's modulus and Poisson's ratio indicated that these parameters do not have a large impact on the volumetric flow rate. Numerical simulations of pressure pulsing pointed out that injection pulses with small relative pulse times lead to a major increase in the volumetric flow rate, while an increasing pulse period results in a slight increase in the flow rate. Most importantly, we can conclude that pulsed injection has a beneficial effect on the water flow in porous media.

In the current chapter, we use a "brute-force" Monte Carlo simulation procedure. Doing simulations with thousands of samples can reduce the Monte Carlo error. However, as in our case each sample simulation takes about two hours, we instead adopted 300 samples. In recent studies [40], multilevel Monte Carlo methods (MLMC) have been applied to various systems, such as groundwater flow. These MLMC methods are characterised by the advantage that relatively few simulations are needed at high mesh resolutions, whereas one performs large numbers of simulations at lower resolutions. The MLMC methods are therefore thought to be a suitable candidate for future applications.



In conclusion, pressure pulses and soil vibrations in the direction of the flow increase the amount of water that can be injected into a tube filled with a deformable fluid-saturated porous medium. However, to elucidate the underlying mechanisms of FHVI, the injection of water into an aquifer should be simulated. In addition, further research should be carried out to examine the validity and applicability of the Kozeny-Carman equation especially for the problems in which vibrations can lead to very large gradients of the porosity and permeability in the soil. Furthermore, it is important to note that the model we are currently using is based on the assumption that the displacements and the strains are small. For this reason, we used Hooke's law and the assumption that the strain tensor is only determined by the deformation gradient (and its transpose), while higher-order terms are neglected. However, as the mechanical vibrations can lead to large strains and displacements, it is probably more realistic to use a morphoelastic model or another plasticity model for soil. The treatment of large deformations would imply nonlinear terms. For the morphoelastic model, for example, an additional nonlinear time-dependent equation would have to be solved, which would increase the computational complexity. Since the purpose of this study is to investigate how vibrations can influence the fluid flow using uncertainty quantification, these nonlinear terms are neglected and the model is kept simple and cheap from a computational point of view. In Chapter 6 and in [105], the accuracy of Biot's linear poroelasticity model in approximating the solutions of poroelasticity problems with moderate to large deformations is investigated.

Chapter 3

# Uncertainty quantification in injection and soil characteristics

*As demand for water increases across the globe, the availability of fresh water in many regions is likely to decrease due to a changing climate, an increase in human population and changes in land use and energy generation. Many of the world's freshwater sources are being drained faster than they are being replenished. To solve this problem, new techniques are developed to improve and optimise renewable groundwater sources, which are an increasingly important water supply source globally. One of this emerging techniques is rainwater storage in the subsurface. In this chapter, different methods for rainwater infiltration are presented. Furthermore, Monte Carlo simulations are performed to quantify the impact of variation in the soil characteristics and the infiltration parameters on the infiltration rate. Numerical results show that injection pulses may increase the amount of water that can be injected into an aquifer.*

This chapter is based on the article:

M. Rahrah and F. Vermolen. Uncertainty Quantification in Injection and Soil Characteristics for Biot's Poroelasticity Model. In *European Conference on Numerical Mathematics and Advanced Applications ENUMATH 2017*, pages 645 – 652. Springer, 2019.

## 3.1 Introduction

During rainwater infiltration, different injection methods could be used. Our aim is to investigate the impact of these injection methods on the percolation fluid velocity of the injected water into an aquifer. Two injection methods are considered in this chapter: constant injection and pulsed injection. Furthermore, to be able to determine the fluid flow through the pores of the aquifer, taking into account the local displacement of the skeleton of the porous medium, Biot's model for poroelasticity [16] is used in this study. In addition, the impact of uncertainty in the soil characteristics and in the injection parameters is quantified using Monte Carlo techniques and statistical analysis.



The poroelasticity equations are often solved using finite element methods [79, 87]. In this study, a finite element method based on Taylor-Hood elements, with linear and quadratic basis functions, has been developed for solving the system of incompressible poroelasticity equations. We remark that the Taylor-Hood elements are suitable as a stable approach for this problem. Spurious oscillations are diminished but not completely removed for small time steps. To fully remove the nonphysical oscillations, one may use the stabilisation techniques as considered in [108].

The rest of this chapter is organised as follows: In Section 3.2 the considered model equations are presented, including the employed permeability model. The numerical experiments for the different methods for rainwater infiltration are described in Section 3.3. Section 3.4 discusses the numerical results and some concluding remarks are reported in Section 3.5.

## 3.2 Governing equations

Assuming that the deformations are very small, the model provided by Biot's theory of linear poroelasticity with single-phase flow [16] is used to determine the local displacement of the skeleton of a porous medium, as well as the fluid flow through the pores. We assume that the deformable fluid-saturated porous medium has a linearly elastic solid matrix and is saturated by an incompressible Newtonian fluid. The solid matrix is assumed to be fully connected. Let $\Omega \subset \mathbb{R}^3$ denote the domain occupied by the porous medium with boundary $\Gamma$, and $\mathbf{x} = (x, y, z) \in \Omega$. Furthermore, $t$ denotes time, belonging to a half-open time interval $I = (0, T]$, with $T > 0$.

The initial boundary value problem for the consolidation process of a fluid flow in a deformable porous medium is stated as follows [2, 135]:

$$\text{equilibrium equations:} \quad -\nabla \cdot \boldsymbol{\sigma}' + (\nabla p + \rho g \mathbf{e}_z) = \mathbf{0} \qquad \text{on } \Omega \times I; \tag{3.1a}$$

$$\text{continuity equation:} \quad \frac{\partial}{\partial t}(\nabla \cdot \mathbf{u}) + \nabla \cdot \mathbf{v} = 0 \qquad \text{on } \Omega \times I, \tag{3.1b}$$

where $\boldsymbol{\sigma}'$ and $\mathbf{v}$ are defined by the following equations

$$\text{Biot's constitutive equations:} \quad \boldsymbol{\sigma}' = \lambda(\nabla \cdot \mathbf{u})\mathbf{I} + \mu(\nabla \mathbf{u} + \nabla \mathbf{u}^T); \tag{3.2}$$

$$\text{Darcy's law:} \quad \mathbf{v} = -\frac{\kappa}{\eta}(\nabla p + \rho g \mathbf{e}_z). \tag{3.3}$$

In the above relations, $\boldsymbol{\sigma}'$, $p$, $\rho$, $g$, $\mathbf{u}$, $\mathbf{v}$, $\lambda$ and $\mu$; $\kappa$ and $\eta$ respectively, denote the effective stress tensor for the porous medium, the pore pressure, the fluid density, the gravitational acceleration, the displacement vector of the porous medium, Darcy's velocity, the Lamé coefficients, the permeability of the porous medium, and the fluid viscosity. To complete the formulation of a well-posed problem, appropriate boundary and initial conditions are specified in Section 3.3.

In this study, we focus on the interaction between the mechanical deformations and the fluid flow during an infiltration process. Therefore, we consider the spatial dependency of the porosity and the permeability of the porous medium. The permeability can be determined using the Kozeny-Carman equation [136]

$$\kappa(\mathbf{x},t) = \frac{d_s^2}{180}\frac{\theta(\mathbf{x},t)^3}{(1-\theta(\mathbf{x},t))^2}, \tag{3.4}$$

where $d_s$ is the mean grain size of the soil and the porosity $\theta$ is computed from the displacement vector using the porosity-dilatation relation (see [130])

$$\theta(\mathbf{x},t) = 1 - \frac{1-\theta_0}{\exp(\nabla\cdot\mathbf{u})}, \tag{3.5}$$

with $\theta_0$ the initial porosity, which is treated in the current chapter as a given constant in each sample computation. Problem (3.1) is solved as a fully coupled system. At each time step, after having obtained the numerical approximations for $\mathbf{u}$ and $p$, we update the porosity using Eq. (3.5). Subsequently, the Kozeny-Carman relation (3.4) is used to calculate the permeability. The new value for the permeability is then used for the next time step.

## 3.3 Problem formulation

The infiltration of a fluid through a filter into an aquifer is shown in Figure 3.1a. We assume that the flow pattern is axisymmetric, hence for the azimuthal coordinate $\hat{\theta}$ holds $\frac{\partial}{\partial\hat{\theta}}(.) = 0$. Therefore, we determine the solution for a fixed azimuth. The computational domain $\Omega$ is an L-shaped two-dimensional surface with cylindrical coordinates $\mathbf{r} = (r, z)$, as depicted in Figure 3.1b. In order to solve this problem, Biot's consolidation model, as described in Section 3.2, is applied on the computational domain $\Omega$ with radius $R$ and height $H$. The fluid is injected into the soil through a filter placed on boundary segment $\Gamma_3$.

The fluid injection can be described by two different boundary conditions: the volumetric flow rate is prescribed at the injection filter (Neumann boundary condition for the pore pressure $p$) or the boundary pore pressure caused by the injection of the fluid is prescribed at boundary segment $\Gamma_3$ (Dirichlet boundary condition for the pore pressure $p$). Furthermore, the injection tube (boundary segments $\Gamma_2$, $\Gamma_3$ and $\Gamma_4$) is fitted with a casing (boundary segments $\Gamma_2$ and $\Gamma_4$) and a perforated section (boundary segment $\Gamma_3$) to prevent loose material from entering and potentially clogging the injection tube.

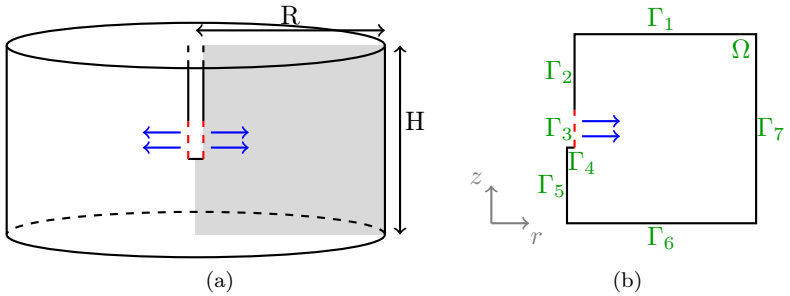


Figure 3.1: *Sketch of the set-up for the aquifer problem: (left) physical problem and (right) numerical discretisation. Taking advantage of the symmetry of geometry and boundary conditions, only the grey region is discretised.*

### 3.3.1 Prescribed injection volumetric flow rate

First, we start by prescribing the injection of a fluid into the soil through a filter (boundary segment $\Gamma_3$) using the volumetric flow rate. More precisely, the boundary conditions for this problem are given as follows:

$$p = \rho g(H - z) \quad \text{on} \quad \mathbf{r} \in \Gamma_1 \cup \Gamma_6 \cup \Gamma_7; \tag{3.6a}$$

$$\frac{\kappa}{\eta}(\nabla p + \rho g \mathbf{e}_z) \cdot \mathbf{n} = 0 \quad \text{on} \quad \mathbf{r} \in \Gamma_2 \cup \Gamma_4 \cup \Gamma_5; \tag{3.6b}$$

$$\frac{\kappa}{\eta}\nabla p \cdot \mathbf{n} = \frac{Q_{in}(t)}{2\pi R_f L_f} \quad \text{on} \quad \mathbf{r} \in \Gamma_3; \tag{3.6c}$$

$$\boldsymbol{\sigma}'\mathbf{n} = \mathbf{0} \quad \text{on} \quad \mathbf{r} \in \Gamma_1 \cup \Gamma_6; \tag{3.6d}$$

$$(\boldsymbol{\sigma}'\mathbf{n}) \cdot \mathbf{t} = 0 \quad \text{on} \quad \mathbf{r} \in \Gamma_2 \cup \Gamma_3 \cup \Gamma_4 \cup \Gamma_5; \tag{3.6e}$$

$$\mathbf{u} \cdot \mathbf{n} \leq 0 \quad \text{on} \quad \mathbf{r} \in \Gamma_2 \cup \Gamma_3 \cup \Gamma_4; \tag{3.6f}$$

$$\mathbf{u} \cdot \mathbf{n} = 0 \quad \text{on} \quad \mathbf{r} \in \Gamma_5; \tag{3.6g}$$

$$\mathbf{u} = \mathbf{0} \quad \text{on} \quad \mathbf{r} \in \Gamma_7, \tag{3.6h}$$

where $\mathbf{t}$ is the unit tangent vector at the boundary, $\mathbf{n}$ the outward unit normal vector and $Q_{in}$ is a prescribed injection volumetric flow rate due to the injection of the fluid through a filter with radius $R_f$ and length $L_f$. Figure 3.1b shows the definition of the boundary segments. Note that the boundary conditions on boundary segment $\Gamma_5$ appear as a result of symmetry. Initially, the following condition is fulfilled:

$$\mathbf{u}(\mathbf{r}, 0) = 0 \quad \text{for} \quad \mathbf{r} \in \Omega. \tag{3.7}$$

To infiltrate a fluid into the soil, several injection methods can be used. In this chapter, we present two different injection methods in order to investigate the impact of the injection on the water flow in an aquifer.

**Constant injection volumetric flow rate** We start with the simulation of problem (3.1) with a constant injection volumetric flow rate $Q_{in,c}(t) = Q_{in,c}$. Note that the injection rate is continuous over time.

**Pulsed injection** In this method, the prescribed injection volumetric flow rate will have a pulsing behaviour rather than being constant. In this case, the injection volumetric flow rate is represented by a combination of the Heaviside step functions

$$\mathcal{H}(t) = \begin{cases} 0 & t < 0 \\ 1/2 & t = 0 \\ 1 & t > 0 \end{cases}. \tag{3.8}$$

A rectangular pulse wave with period $T_Q$ and pulse time $\tau_Q$ is defined as

$$Q_{in,p}(t) = \gamma_Q \sum_{k=0}^{N_Q} (\mathcal{H}(t - kT_Q) - \mathcal{H}(t - kT_Q - \tau_Q)), \tag{3.9}$$

where $\gamma_Q$ is the maximum injection volumetric flow rate and $N_Q$ is the number of periods. Note that the injection rate contains discontinuities over time.

### 3.3.2 Prescribed pump pressure

Another way to describe the fluid injection is by considering a prescribed pump pressure at the injection filter. Hence, we use a Dirichlet boundary condition for the pore pressure on boundary segment $\Gamma_3$. Accordingly, the boundary condition for the pore pressure on $\Gamma_3$ becomes

$$p = \rho g(H - z) + p_{pump}(t) \quad \text{on} \quad \mathbf{r} \in \Gamma_3, \tag{3.10}$$

where $p_{pump}$ is a prescribed pump pressure. On $t = 0$, the initial condition (3.7) is fulfilled. Similar to the previous section, two different injection methods to infiltrate a fluid into the soil are presented, in order to investigate the impact of the injection on the water flow in an aquifer.

**Constant pump pressure** We start with the simulation of problem (3.1) with a constant pump pressure $p_{pump,c}(t) = p_{pump,c}$. Note that the injection pressure is continuous over time.

**Pulsed pump pressure** In this method, the prescribed pump pressure will have a pulsing behaviour rather than being constant. In this case, the pump pressure is represented by a rectangular pulse wave with period $T_p$ and pulse time $\tau_p$, defined as

$$p_{pump,p}(t) = p_{max} \sum_{k=0}^{N_p} (\mathcal{H}(t - kT_p) - \mathcal{H}(t - kT_p - \tau_p)), \tag{3.11}$$

where $p_{max}$ is the maximum injection pressure and $N_p$ is the number of periods. Note that the injection pressure contains discontinuities over time.

## 3.4 Numerical results

The Galerkin finite element method [113], with triangular Taylor-Hood elements, is employed for the solution of the discretised quasi-two-dimensional problem (3.1). The displacements are spatially approximated by quadratic basis functions, whereas a continuous piecewise linear approximation is used for the pressure field. For the time integration, the backward Euler method is applied. The numerical investigations are carried out using the matrix-based software package MATLAB (version R2011b).



The computational domain is an L-shaped surface with radius $R = 5.0\,\mathrm{m}$, height $H = 5.0\,\mathrm{m}$, filter radius $R_f = 20.0\,\mathrm{cm}$ and filter length $L_f = 1.0\,\mathrm{m}$. The filter is placed between $z = 2$ and $z = 3$. The domain is discretised using a regular triangular grid, with $\Delta r = \Delta z = 0.1$. Mesh refinement did not yield any significant changes of the numerical solution. In addition, values for some model parameters have been chosen based on the literature (see Table 3.1).

Table 3.1: *An overview of the values of the model parameters.*

| Property | Symbol | Value | Unit |
|---|---|---|---|
| Fluid viscosity | $\eta$ | $1.307 \cdot 10^{-3}$ | $\mathrm{Pa \cdot s}$ |
| Fluid density | $\rho$ | 1000 | $\mathrm{kg/m^3}$ |
| Gravitational acceleration | $g$ | 9.81 | $\mathrm{m/s^2}$ |

Furthermore, the Lamé coefficients $\lambda$ and $\mu$ are related to Young's modulus $E$ and Poisson's ratio $\nu$ by [2]:

$$\lambda = \frac{\nu E}{(1+\nu)(1-2\nu)} \quad \text{and} \quad \mu = \frac{E}{2(1+\nu)}. \tag{3.12}$$

In this chapter, we will investigate the impact of two different injection methods on the flow of water. This impact is defined in this chapter as the impact on the time average of the volumetric flow rate $\overline{Q}_{out}$ at a distance $R - R_f$ from the injection filter. Subsequently, the Monte Carlo method is applied to the values of the soil characteristics $E$, $\nu$, $\theta_0$ and $d_s$, using samples of uniform distributions with boundaries found in the literature [89]. Hence, for these simulations, 300 samples from the following uniform distributions are generated:

$$\begin{gathered} E \sim \mathcal{U}(30 \cdot 10^6, 160 \cdot 10^6), \quad \nu \sim \mathcal{U}(0.15, 0.40), \quad \theta_0 \sim \mathcal{U}(0.23, 0.46), \\ d_s \sim \mathcal{U}(0.05 \cdot 10^{-3}, 50.0 \cdot 10^{-3}). \end{gathered} \tag{3.13}$$

In the generations of the simulation results, the time step size $\Delta t$ is determined by

$$\Delta t = \frac{T_i}{10}, \tag{3.14}$$

where $i \in \{Q, p\}$.

### 3.4.1 Numerical results using a prescribed volumetric flow rate

To quantify the difference between a pulsed injection and a constant injection of water into an aquifer, the contributions of the variations in the values of the pulse wave characteristics to the volumetric flow rate are analysed. These contributions are examined by applying Monte Carlo method to $\gamma_Q$, $T_Q$ and the relative pulse time $\tilde{\tau}$, defined as (see Formula (3.9))

$$\tilde{\tau} = \frac{\tau_Q}{T_Q}. \tag{3.15}$$



The number of periods $N_Q$ is equal to five in all simulations. In each simulation, the constant injection velocity is chosen equal to the total pulsed injection velocity over time, in order to be able to draw reliable conclusions. Hence, the constant injection velocity is computed by

$$Q_{in,c} = \tilde{\tau}\gamma_Q. \tag{3.16}$$

For the simulations, 300 samples from the following uniform distributions are generated:

$$\gamma_Q \sim \mathcal{U}(10/3600, 40/3600), \quad T_Q \sim \mathcal{U}(1, 10), \quad \tilde{\tau} \sim \mathcal{U}(0.1, 0.9). \tag{3.17}$$

Let '$p$' be an abbreviation for pulsed injection and '$c$' for constant injection. The Pearson correlation coefficients $r_i$, with $i \in \{p, c\}$, are presented together with the associated $p_i$-values in Table 3.2.

Table 3.2: *The Pearson correlation coefficients together with the associated p-values. A p-value less than* 0.05 *means that the two paired sets of data are most probably related, at the significance level* 0.05.

| | $r_p$ | $p_p$ | $r_c$ | $p_c$ |
|---|---|---|---|---|
| $corr(E, \overline{Q}_{out})$ | 0.09 | 0.11 | 0.10 | 0.10 |
| $corr(\nu, \overline{Q}_{out})$ | 0.05 | 0.36 | 0.07 | 0.21 |
| $corr(\theta_0, \overline{Q}_{out})$ | 0.01 | 0.94 | 0.01 | 0.85 |
| $corr(d_s, \overline{Q}_{out})$ | 0.10 | 0.10 | 0.09 | 0.13 |
| $corr(\gamma_Q, \overline{Q}_{out})$ | 0.31 | $< 0.05$ | 0.28 | $< 0.05$ |
| $corr(T_Q, \overline{Q}_{out})$ | $-0.69$ | $< 0.05$ | $-0.66$ | $< 0.05$ |
| $corr(\tilde{\tau}, \overline{Q}_{out})$ | 0.45 | $< 0.05$ | 0.49 | $< 0.05$ |

From Table 3.2 we can conclude that, for both injection methods, the variation in the soil characteristics does not have a large impact on the numerical results, while variation in the injection parameters influence the time average of the volumetric flow rate at a distance $R - R_f$ from the injection filter significantly. Furthermore, the results in Table 3.2 show that injection pulses with small pulse periods $T_Q$ lead to a major increase in the volumetric flow rate $\overline{Q}_{out}$, while $\overline{Q}_{out}$ increases slightly by increasing the relative pulse time $\tilde{\tau}$ and the maximum injection velocity $\gamma_Q$. These conclusions can also be confirmed by the scatter plots shown in Figure 3.2.

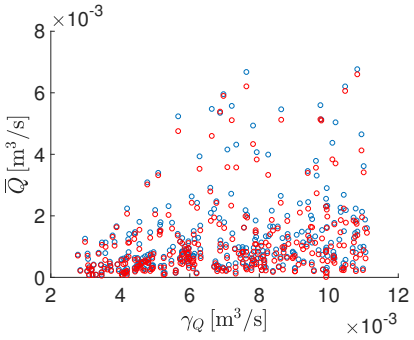


(a) The time average of the volumetric flow rate as function of $\gamma_Q$.

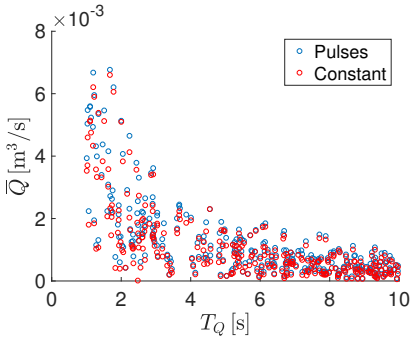


(b) The time average of the volumetric flow rate as function of $T_Q$.

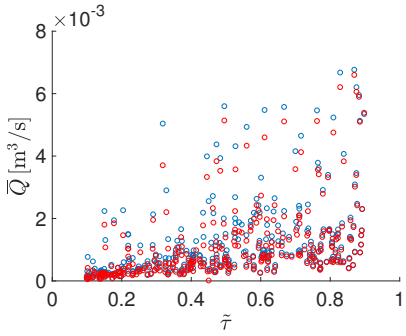


(c) The time average of the volumetric flow rate as function of $\tilde{\tau}$.

Figure 3.2: *Scatter plots of the time average of the volumetric flow rate, after applying Monte Carlo simulations to the values of $\gamma_Q$, $T_Q$ and $\tilde{\tau}$.*

To compare the injection methods, the percentage change $\overline{Q}_{\%}$ of the time average of the volumetric flow rate $\overline{Q}_{out}$ is used, determined by

$$\overline{Q}_{\%} = \frac{\overline{Q}_{out,p} - \overline{Q}_{out,c}}{\overline{Q}_{out,c}} \cdot 100, \tag{3.18}$$

where $\overline{Q}_{out,c}$ and $\overline{Q}_{out,p}$ are the time averages of the volumetric flow rate as result of the constant injection and the pulsed injection respectively. In Figure 3.3, the histogram and the cumulative distribution function of the percentage change $\overline{Q}_{\%}$ are presented. Since $P(\overline{Q}_{\%} > 0) \approx 0.98$, we can conclude that the pulsed injection has a beneficial effect on the water flow in an aquifer, with a maximal percentage change of 105.7%.

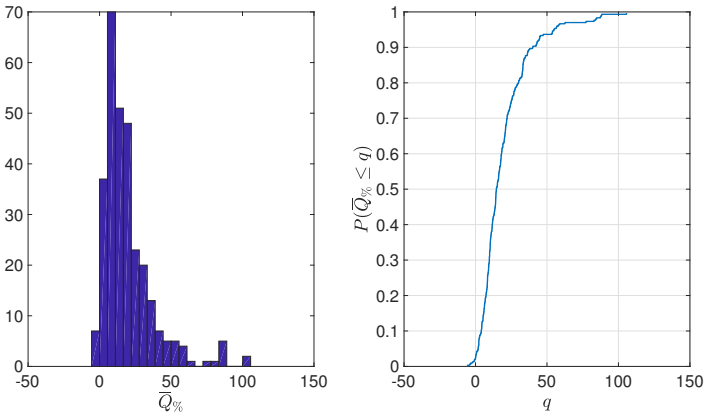


Figure 3.3: *The histogram and the cumulative distribution function of the percentage change $\overline{Q}_{\%}$ of the time average of the volumetric flow rate.*

### 3.4.2 Numerical results using a prescribed pore pressure

The low impact of the soil characteristics on $\overline{Q}_{out}$, as indicated in the previous section, may be attributed to boundary condition (3.6c). In this section, we will investigate whether prescribing the pore pressure pressure on the filter instead of the volumetric flow rate will change this significance. In addition, the contributions of the variations in the values of the pulse wave characteristics to the volumetric flow rate at a distance $R - R_f$ from the injection filter are analysed by applying Monte Carlo simulations to $p_{max}$, $T_p$ and the relative pulse time $\tilde{\tau}$ as defined in (3.15). For these simulations, 300 samples from the following uniform distributions are generated:

$$p_{max} \sim \mathcal{U}(0.1 \cdot 10^5, 2 \cdot 10^5), \quad T_p \sim \mathcal{U}(1, 10), \quad \tilde{\tau} \sim \mathcal{U}(0.1, 0.9). \tag{3.19}$$

In each simulation, the constant pump pressure is chosen equal to the total pump pressure over time by pulsed injection. Hence, for a particular relative pulse time $\tilde{\tau}$, the constant pump pressure is computed by

$$p_{pump} = \tilde{\tau} p_{max}. \tag{3.20}$$

Similarly to the previous section, the number of periods $N_p$ is equal to five in all simulations. In Figure 3.4, the time average of the volumetric flow rate at the right end of the tube is depicted after applying Monte Carlo simulations to the values of the material properties $E$, $\nu$, $\theta_0$ and $d_s$, using the uniform distributions given in (3.13).

From Figure 3.4, we can conclude that water flows faster through porous media with large mean grain sizes or high initial porosities. On the other hand, these results indicate that the volumetric flow rate is invariant under variation in the values of Young's modulus and Poisson's ratio. This can also be concluded from the values of the Pearson correlation coefficients given in Table 3.3. Note that these conclusions are in agreement with the results presented in Section 2.5.2.

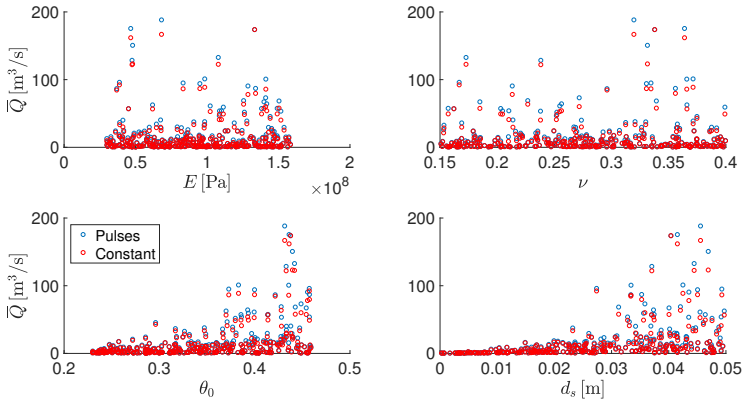


Figure 3.4: *The histogram and the cumulative distribution function of the percentage change $\overline{Q}_{\%}$ of the time average of the volumetric flow rate.*

Table 3.3: *The Pearson correlation coefficients together with the associated p-values. A p-value less than* 0.05 *means that the two paired sets of data are most probably related, at the significance level* 0.05.

| | $r_p$ | $p_p$ | $r_c$ | $p_c$ |
|---|---|---|---|---|
| $corr(E, \overline{Q}_{out})$ | 0.02 | 0.79 | 0.01 | 0.88 |
| $corr(\nu, \overline{Q}_{out})$ | 0.04 | 0.48 | 0.04 | 0.45 |
| $corr(\theta_0, \overline{Q}_{out})$ | 0.43 | $< 0.05$ | 0.42 | $< 0.05$ |
| $corr(d_s, \overline{Q}_{out})$ | 0.45 | $< 0.05$ | 0.44 | $< 0.05$ |
| $corr(p_{max}, \overline{Q}_{out})$ | 0.34 | $< 0.05$ | 0.34 | $< 0.05$ |
| $corr(T_p, \overline{Q}_{out})$ | $-0.12$ | $< 0.05$ | $-0.12$ | $< 0.05$ |
| $corr(\tilde{\tau}, \overline{Q}_{out})$ | 0.23 | $< 0.05$ | 0.25 | $< 0.05$ |

From the results presented in Table 3.3 and the scatter plots shown in Figure 3.5, we can also conclude that pressure pulses with large relative pulse times $\tilde{\tau}$ and maximum injection pressures $p_{max}$ lead to an increase in the volumetric flow rate $Q_{out}$. However, in contrast with the results in the previous section, the scatter plot in Figure 3.5b points out that the pulse period $T_p$ does not have a significant impact on the volumetric flow rate $Q_{out}$.

To compare the injection methods, the percentage change $\overline{Q}_{\%}$ of the time average of the volumetric flow rate $\overline{Q}_{out}$ is used, as defined in (3.18). In Figure 3.6, the histogram and the cumulative distribution function of the percentage change $\overline{Q}_{\%}$ are presented. With these numerical results we come to a similar conclusion as in the previous section, namely that pressure pulses have a beneficial effect on the storage of rainwater in the shallow subsurface.

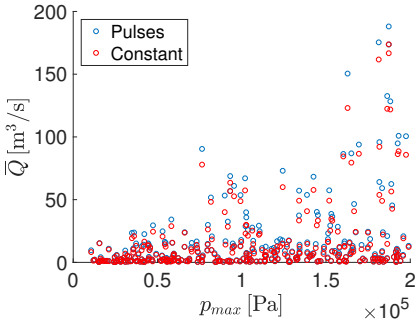


(a) The time average of the volumetric flow rate as function of $p_{max}$.

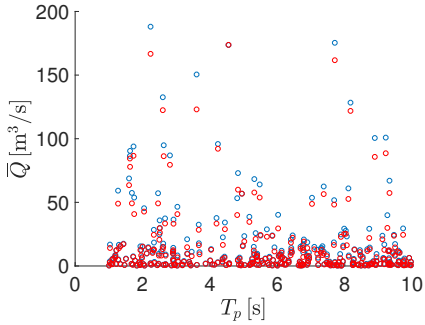


(b) The time average of the volumetric flow rate as function of $T_p$.

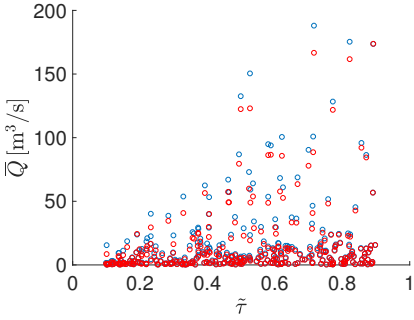


(c) The time average of the volumetric flow rate as function of $\tilde{\tau}$.

Figure 3.5: *Scatter plots of the time average of the volumetric flow rate, after applying Monte Carlo simulations to the values of $p_{max}$, $T_p$ and $\tilde{\tau}$.*

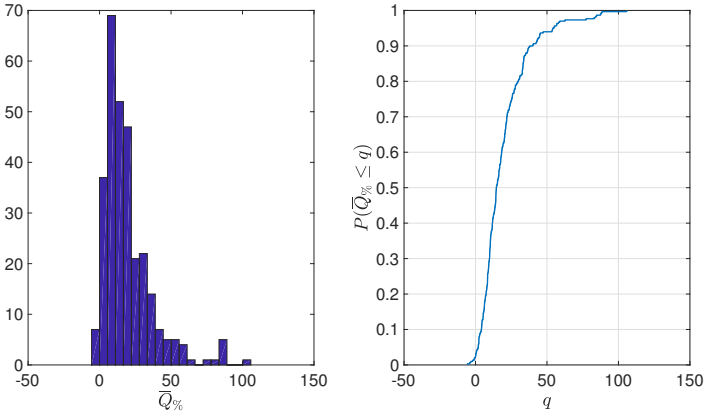


Figure 3.6: *The histogram and the cumulative distribution function of the percentage change $\overline{Q}_{\%}$ of the time average of the volumetric flow rate.*

## 3.5 Discussion and conclusions

In this work, a numerical model for the quasi-static Biot's consolidation problem for poroelasticity has been developed, considering nonlinear permeability. The model is discretised by a continuous Galerkin finite element method based on Taylor-Hood elements, combined with the implicit Euler scheme for time stepping. The study contains Monte Carlo simulations to quantify the impact of variation in the soil characteristics and the injection parameters on the time average of the volumetric flow rate at a particular distance from the injection filter. Furthermore, two injection methods: a pulsed injection and a constant injection, are tested and compared with each other in order to determine the best infiltration method that can be used for the storage of rainwater in the shallow subsurface. Finally, two different types boundary conditions are considered to describe the fluid injection.



To reduce the Monte Carlo error, simulations should be performed with thousands of samples. However, as in our case each sample simulation takes more than one hour, we instead adopted 300 samples. Another approach is to use Multilevel Monte Carlo methods [40]. By applying these methods, relatively few simulations are needed at high mesh resolutions, whereas one performs large numbers of simulations at lower resolutions.

The first boundary condition that we used is a Neumann boundary condition for the pore pressure, where the volumetric flow rate is prescribed at the injection filter. The numerical simulations of pulsed injection pointed out that injection pulses with small pulse periods lead to a major increase in the volumetric flow rate, while an increasing relative pulse time and maximum injection velocity result in a slight increase in the flow rate. On the other hand, variation in the values of the soil characteristics indicated that these parameters do not have a large impact on the volumetric flow rate. On the contrary, numerical simulations using Dirichlet boundary conditions, in which the boundary pore pressure caused by the injection of the fluid is prescribed, indicated that water flows faster through porous media with large mean grain sizes or high initial porosities. On the other hand, the results indicated that the volumetric flow rate is invariant under variation in the values of Young's modulus and Poisson's ratio. In addition, pressure pulses with large relative pulse times and maximum injection pressures lead to an increase in the volumetric flow rate. However, the numerical results pointed out that the pulse period does not have a significant impact on the volumetric flow rate.

Most importantly, we can conclude that, regardless of the type of soil into which we inject, by applying pulsed injection we can increase the amount of rainwater that can be stored quickly in the underground.

Chapter 4

# Network-inspired versus Kozeny-Carman based permeability-porosity relations

*Water injection in an aquifer induces deformations in the soil. These mechanical deformations give rise to a change in porosity and permeability, which results in nonlinearity of the mathematical problem. Assuming that the deformations are very small, the model provided by Biot's theory of linear poroelasticity is used to determine the local displacement of the skeleton of a porous medium, as well as the fluid flow through the pores. In this continuum scale model, the Kozeny-Carman equation is commonly used to determine the permeability of the porous medium from the porosity. The Kozeny-Carman relation states that flow through the pores is possible at a certain location as long as the porosity is larger than zero at this location in the aquifer. However, from network models it is known that percolation thresholds exist, indicating that the permeability will be equal to zero if the porosity becomes smaller than these thresholds. In this chapter, the relationship between permeability and porosity is investigated. A new permeability-porosity relation, based on the percolation theory, is derived and compared with the Kozeny-Carman relation. The strongest feature of the new approach is related to its capability to give a good description of the permeability in case of low porosities. However, with this network-inspired approach small values of the permeability are more likely to occur. Since we show that the solution of Biot's model converges to the solution of a saddle point problem for small time steps and low permeability, we need stabilisation in the finite element approximation.*

This chapter is based on the article:

M. Rahrah, L. Lopez-Peña, F. Vermolen, and B. Meulenbroek. Network-inspired versus Kozeny-Carman based permeability-porosity relations applied to Biot's poroelasticity model. *Journal of Mathematics in Industry*, 10:19, 2020.

## 4.1 Introduction

The Kozeny-Carman equation is based on only having spherical grains in the porous medium, whereas these grains can have various shapes. In this sense, the Kozeny-Carman relation represents a limit case. Another limit case is the assumption that the voids between the grains are represented by straight channels. In this study, we briefly introduce a new approach for the permeability that is derived on a micro-scale network model. At the pore-scale, this network model offers a detailed description of the porous medium [14]. The current modelling framework deals with the latter limit case, and can be used for general network topologies (such as rectangular, triangular and cubic arrangements of the channels). In contrast with the Kozeny-Carman equation, the new network-inspired approach yields that the permeability is nonzero only if the porosity is larger than a specific percolation threshold, that depends on the topology of the network. This means that the new approach may give a better prediction of the permeability in physics problems where abrupt changes in the porous medium occur resulting in a loss of connectivity of the connected pore space. In addition, the current model provides a computational framework to determine the percolation threshold for any given network with straight channels, which implies that there is no need for fitting on the basis of experiments if the network topology is known. This numerically determined threshold value agrees very well with the known values of the percolation thresholds from the literature. The new permeability-porosity approach is derived from percolation theory, which is a branch of probability that describes the effects of randomness arising from the porous media structure [32].



In percolation theory, the nodes of the network are called sites and the edges are called bonds. This leads to two approaches: site percolation and bond percolation. In this chapter, we consider the bond percolation approach, whose basic idea can be explained as follows. Consider a network such as shown in Figure 4.1. Whether a bond is open or closed depends on a certain probability and it is independent of the neighbouring bonds. If one bond is open and the nearest neighbours are closed, it is said that a 1-cluster is formed. If two adjacent bonds are open, they form a 2-cluster and so on. If the probability $p$ of a bond being open increases, then larger clusters are created. There exists a critical probability at which the first cluster that spans the entire network from the inlet to the outlet is obtained. For infinite networks, this critical probability is well defined and it is called the percolation threshold $p_c$ [14].

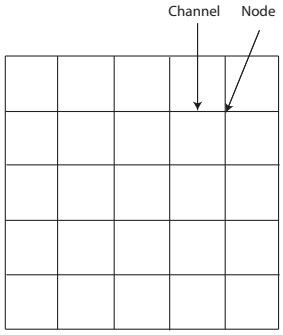


Figure 4.1: *An illustration of a rectangular network.*

Some macroscopic properties of porous media are mainly determined by the connectivity of the pore system [14]. Hence, it is possible to find a relation between the permeability of a porous medium and the percolation properties using the network model. For instance, if each of the open bonds conducts a fluid and there exists a cluster that spans the network from the inlet to the outlet, then a volumetric flow is possible through the network. By adding more open bonds to the cluster, the volumetric flow through the network may increase. Since the number of open bonds represents the porosity of the network, it is possible to find a relation between the volumetric flow and the porosity [7, 143]. In addition, Darcy's law gives a relationship between the permeability of the porous medium and the volumetric flow. As a result, a relation between the permeability and the porosity can be derived.

The applicability of these permeability-porosity relations will be demonstrated using two illustrative numerical examples. The three-dimensional analogue can be found in the next chapter and in [106]. In these two-dimensional examples, flow of an incompressible fluid through a linearly elastic, saturated porous medium is modelled, using the classical theory of linear poroelasticity. Originally developed by Biot [16], poroelasticity theory assumes a superposition of solid and fluid components and couples the mechanical deformation of a porous solid with fluid flow through its internal structure. This approach is valid in the infinitesimal deformation range. Poroelasticity problems exist widely in the real world, making this theory of a great interest due to its applicability in various branches of science and engineering (see e.g. [12, 39, 104, 118, 120]).



In order to investigate the difference between the Kozeny-Carman approach and the equation based on the percolation theory, the boundary conditions in both academic poroelasticity examples are chosen such that a decrease in porosity is realised in some parts of the computational domain. This decrease in porosity will lead in both relations to a decrease in the permeability of the porous medium. When using the finite element method to solve the poroelastic equations, it is well known that the numerical solution of these equations may exhibit nonphysical oscillations in the pressure field for low permeabilities and short time steps [57, 132]. In Section 4.5.1, we will prove that under these conditions, the resulting finite element discretisation approaches saddle point problems. Hence, a considerate numerical methodology in terms of possible spurious oscillations is needed. Therefore, a Galerkin finite element method based on Taylor-Hood elements has been developed, combined with the stabilisation technique proposed in [2, 108]. Another stabilised finite element method is employed by Wan [134], Korsawe and Starke [74] and Tchonkova et al. [126], based on the Galerkin least-squares method.

The rest of this chapter is organised as follows: In Section 4.2, a detailed description of the model is presented. In addition, the considered permeability-porosity relations are derived in Section 4.3. Subsequently, two numerical experiments are described in Section 4.4. To solve these numerical experiments, the applied numerical algorithm is provided in Section 4.5. In this section, the convergence of the solution of Biot's model to the solution of a saddle point problem for small time steps and low permeability is proven. The simulation results are presented in Section 4.6 and finally, these results are discussed in Section 4.7.

## 4.2 Governing equations

The model provided by Biot's theory of linear poroelasticity with single-phase flow [16] is used in this study to determine the local displacement of the grains of a porous medium and the fluid flow through the pores, assuming that the deformations are very small. The fluid-saturated porous medium has a linearly elastic solid matrix and is saturated by an incompressible Newtonian fluid. Let $\Omega \subset \mathbb{R}^2$ denote the computational domain with boundary $\Gamma$, and $\mathbf{x} = (x, y) \in \Omega$. Furthermore, $t$ denotes time, belonging to a half-open time interval $I = (0, T]$, with $T > 0$. The initial boundary value problem for the consolidation process of an incompressible fluid flow in a deformable porous medium is stated as follows [2, 135]:

$$-\nabla \cdot \boldsymbol{\sigma}' + \nabla p = \mathbf{0} \text{ on } \Omega \times I; \tag{4.1a}$$

$$\frac{\partial}{\partial t}(\nabla \cdot \mathbf{u}) + \nabla \cdot \mathbf{v} = 0 \text{ on } \Omega \times I, \tag{4.1b}$$



where $\boldsymbol{\sigma}'$ and $\mathbf{v}$ are defined by the following equations

$$\boldsymbol{\sigma}' = \lambda \mathrm{tr}(\boldsymbol{\varepsilon})\mathbf{I} + 2\mu\boldsymbol{\varepsilon}; \tag{4.2}$$

$$\boldsymbol{\varepsilon} = \frac{1}{2}(\nabla \mathbf{u} + \nabla \mathbf{u}^T); \tag{4.3}$$

$$\mathbf{v} = -\frac{\kappa}{\eta}\nabla p. \tag{4.4}$$

In the above relations, $\boldsymbol{\sigma}'$ and $\boldsymbol{\varepsilon}$ denote the effective stress and strain tensors, $p$ the pore pressure, $\mathbf{u}$ the displacement vector, $\mathbf{v}$ Darcy's velocity, $\lambda$ and $\mu$ the Lamé coefficients; $\kappa$ the permeability of the porous medium and $\eta$ the fluid viscosity. The parameter values used in this chapter are given in Table 4.5. In addition, appropriate boundary and initial conditions are specified in Section 4.4.

## 4.3 The permeability-porosity relations

In this study, we consider the spatial dependency of the porosity and the permeability of the porous medium. The porosity $\theta$ is computed from the displacement vector using the porosity-dilatation relation (see [103, 130])

$$\theta(\mathbf{x}, t) = 1 - \frac{1 - \theta_0}{\exp(\nabla \cdot \mathbf{u})}, \tag{4.5}$$

with $\theta_0$ the initial porosity. Subsequently, the permeability can be determined using the Kozeny-Carman equation [136]

$$\kappa(\mathbf{x}, t) = \frac{d_s^2}{180} \frac{\theta(\mathbf{x}, t)^3}{(1 - \theta(\mathbf{x}, t))^2}, \tag{4.6}$$

where $d_s$ is the mean grain size of the soil. The Kozeny-Carman relation assumes that the permeability becomes zero if and only if the porosity also becomes zero. A new approach for the relation between the porosity and the permeability is inspired by the fluid flow through a network, where the fluid flows into the edges (channels) of

the network. The network-inspired relation takes into account that a certain number of the channels are removed randomly, therefore the fluid cannot flow through those particular channels causing an alteration in the permeability and the porosity of the network. The number of removed channels increases from 1% of the total number of channels to 100%. For a certain number of removed channels, there are no connected paths anymore between the inlet and the outlet. In this case, the fluid will stop flowing and the permeability will be expected to become zero. For an arbitrary network topology, the network-inspired relation states:

$$\kappa(\mathbf{x}, t) = \begin{cases} 0 & \theta < \hat{\theta} \\ \frac{\theta - \hat{\theta}}{\theta_0 - \hat{\theta}} \kappa_0 & \theta \geq \hat{\theta} \end{cases}, \tag{4.7}$$

where $\kappa_0$ is the initial permeability. The percolation threshold porosity $\hat{\theta} = p_c \theta_0$, represents the minimal porosity needed to have connection via voids or channels from one end to the other, and is dependent on the topology of the network. For $\hat{\theta} = 0.5\theta_0$, the normalised permeability for the network-inspired relation and the Kozeny-Carman relation is depicted in Figure 4.2 as function of the normalised porosity. In the coming section, we will show how the permeability-porosity relation (4.7) is derived using a network model.



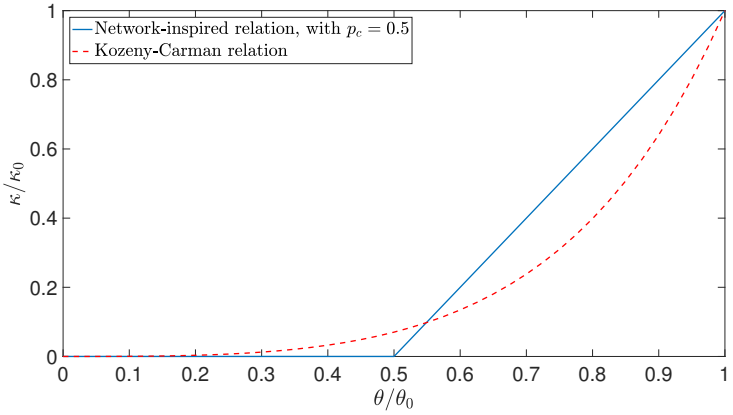


Figure 4.2: *The normalised permeability as function of the normalised porosity for the Kozeny-Carman relation and the network-inspired relation, with* $\hat{\theta} = 0.5\theta_0$.

### 4.3.1 The network-inspired permeability-porosity relation

In this section, we explain the procedure followed to obtain the network-inspired permeability-porosity relation. According to Balberg [7] and Wong [143], it is possible to obtain a relation between the number of open bonds (or channels) in the network $N_o$ and the flow rate through the network $Q$. This relation is determined by a power law as follows:

$$Q \propto (N_o - \hat{N})^b \quad \text{for} \quad N_o > \hat{N}, \tag{4.8}$$

in which $\hat{N}$ is the number of bonds corresponding with the percolation threshold porosity and $b$ is an exponent that can be determined by theory or via computer simulations. A similar relation between the permeability $\kappa$ and the porosity $\theta$ will be obtained in this section.

First, we consider a network with all channels open and with a pressure gradient $\Delta p$ imposed over the horizontal direction of the network. Second, we assume that mass conservation holds in each node of the network $n_i$, hence

$$\sum_{j \in S_i} q_{ij} = 0, \tag{4.9}$$

where $S_i = \{j \mid \text{node } n_j \text{ is adjacent to node } n_i\}$, and $q_{ij}$ is the flow rate in the channels connected to node $n_i$. This flow rate is given by the Poiseuille flow



$$q_{ij} = \frac{\pi r^4}{8\eta l} \Delta p_{ij}, \tag{4.10}$$

where $r$ and $l$ are the radius and the length of a channel between two neighbouring nodes, respectively, and $\Delta p_{ij}$ is the pressure drop.

A linear system for the pressure $p_i$ in each node arises from substituting Eq. (4.10) in Eq. (4.9). This system is solved via a direct method and, subsequently, the flow rate in each channel is computed via Eq. (4.10). Finally, the flow rate through the network $Q$ is computed by the summation of the flow rates in the channels that are connected with the outlet of the network. After this, we randomly close the channels, starting with 1% of the total number of channels in the network until that 100% of the channels is closed. In each stage, 500 simulations are performed and in each simulation, the linear system for the pressure is solved and the flow rate through the network is computed. From the computed flow rate $Q$, the permeability of the network can be determined using Darcy's law

$$\kappa = -\frac{Q}{A} \frac{\eta L}{\Delta p}, \tag{4.11}$$

where $A$ is the cross-sectional area of the network and $L$ is the length over which the pressure gradient is taking place. In addition, there is a direct relation between the porosity of the network and the volume of the open channels $V_o$

$$\theta = \frac{V_o}{V_t} \theta_0, \tag{4.12}$$

in which $V_t$ is the total volume of the channels. This procedure yields a relation between the permeability and the porosity of the network. In the coming sections, this procedure will be demonstrated for three two-dimensional networks: rectangular, triangular and triangular unstructured.

**Rectangular network**

We start by describing the results obtained for a rectangular network (see Figure 4.1). In this case, we use a network with $N_x = 100$ horizontal nodes and $N_y = 60$ vertical

nodes. We computed the fraction of closed channels $f_c = V_c/V_t$, that is needed to obtain a normalised permeability $\kappa_n = \kappa/\kappa_0$ such that $k_i - 0.05 < \kappa_n < k_i + 0.05$, where $k_i \in \{0.1, 0.2, \ldots, 0.9\}$. In Figure 4.3, the histograms for $k_i = 0.1$, $k_i = 0.5$ and $k_i = 0.9$ are shown. The mean $\bar{\mu}$ and the standard deviation $\sigma$ of the distribution of $f_c$ depend on the normalised permeability $\kappa_n$ as presented in Table 4.1.

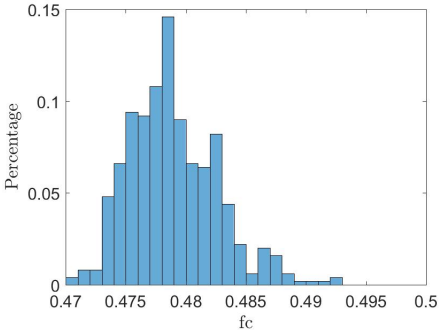


(a) The histogram of the fraction $f_c$ that satisfies $0.05 < \kappa_n < 0.15$.

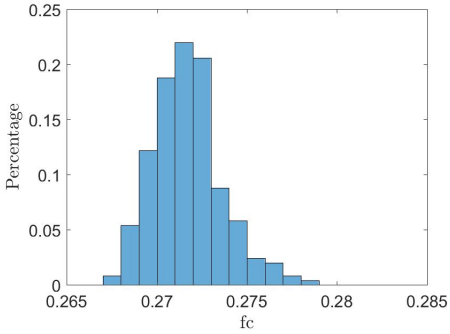


(b) The histogram of the fraction $f_c$ that satisfies $0.45 < \kappa_n < 0.55$.

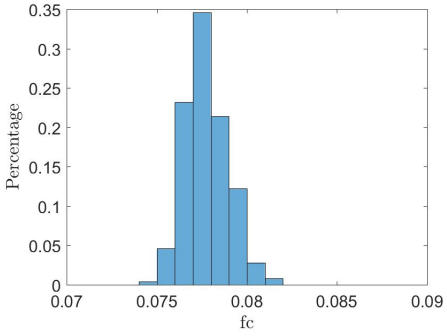


(c) The histogram of the fraction $f_c$ that satisfies $0.85 < \kappa_n < 0.95$.

Figure 4.3: *The histograms of the fraction of closed channels $f_c$ for the rectangular network.*

Table 4.1: *The mean $\bar{\mu}$ and the standard deviation $\sigma$ of the distribution of $f_c$ for the rectangular network.*

| | $\bar{\mu}$ | $\sigma$ |
|---|---|---|
| $0.05 < \kappa_n < 0.15$ | 0.4789 | 0.0037 |
| $0.15 < \kappa_n < 0.25$ | 0.4188 | 0.0026 |
| $0.25 < \kappa_n < 0.35$ | 0.3678 | 0.0023 |
| $0.35 < \kappa_n < 0.45$ | 0.3195 | 0.0022 |
| $0.45 < \kappa_n < 0.55$ | 0.2717 | 0.0019 |
| $0.55 < \kappa_n < 0.65$ | 0.2240 | 0.0018 |
| $0.65 < \kappa_n < 0.75$ | 0.1760 | 0.0016 |
| $0.75 < \kappa_n < 0.85$ | 0.1273 | 0.0014 |
| $0.85 < \kappa_n < 0.95$ | 0.0777 | 0.0012 |



**Triangular network**

In this section, we present the results obtained with a triangular network as shown in Figure 4.4. The number of nodes in the horizontal direction $N_x = 100$ and the number of nodes in the vertical direction $N_y = 60$. The coordination number of the interior nodes is eight or four (see Figure 4.4). In Figure 4.5, the histograms for $k_i = 0.1$, $k_i = 0.5$ and $k_i = 0.9$ are depicted. In addition, the values of the mean $\bar{\mu}$ and the standard deviation $\sigma$ of the distribution of $f_c$ are presented in Table 4.2.

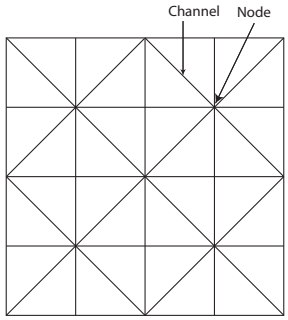


Figure 4.4: *An illustration of a triangular network.*

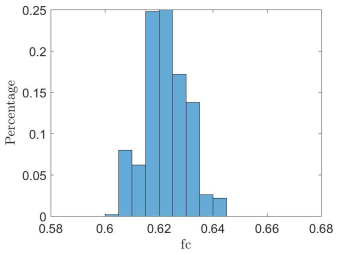


(a) The histogram of the fraction $f_c$ that satisfies $0.05 < \kappa_n < 0.15$.

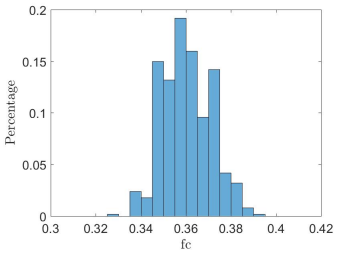


(b) The histogram of the fraction $f_c$ that satisfies $0.45 < \kappa_n < 0.55$.

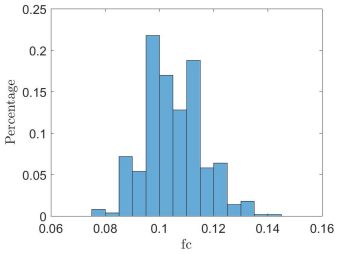


(c) The histogram of the fraction $f_c$ that satisfies $0.85 < \kappa_n < 0.95$.

Figure 4.5: *The histograms of the fraction of closed channels $f_c$ for the triangular network.*

Table 4.2: *The mean $\bar{\mu}$ and the standard deviation $\sigma$ of the distribution of $f_c$ for the triangular network.*

| | $\bar{\mu}$ | $\sigma$ |
|---|---|---|
| $0.05 < \kappa_n < 0.15$ | 0.6226 | 0.0077 |
| $0.15 < \kappa_n < 0.25$ | 0.5522 | 0.0086 |
| $0.25 < \kappa_n < 0.35$ | 0.4882 | 0.0099 |
| $0.35 < \kappa_n < 0.45$ | 0.4240 | 0.0102 |
| $0.45 < \kappa_n < 0.55$ | 0.3604 | 0.0105 |
| $0.55 < \kappa_n < 0.65$ | 0.2975 | 0.0108 |
| $0.65 < \kappa_n < 0.75$ | 0.2333 | 0.0111 |
| $0.75 < \kappa_n < 0.85$ | 0.1687 | 0.0104 |
| $0.85 < \kappa_n < 0.95$ | 0.1052 | 0.0103 |

### Triangular unstructured network

Finally, we present the results obtained with a triangular unstructured network such as shown in Figure 4.6. The total number of nodes in this network is 6921. The histograms of the fraction of closed channels for some values of the normalised permeability are depicted in Figure 4.7. Moreover, in Table 4.3, the values of the mean $\bar{\mu}$ and the standard deviation $\sigma$ of the distribution of $f_c$ are given.

This method is also used to compute $f_c$ for $\kappa_n = 0$. The mean $\bar{\mu}$ of the smallest

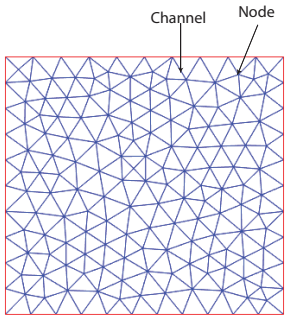


Figure 4.6: *An illustration of a triangular unstructured network.*



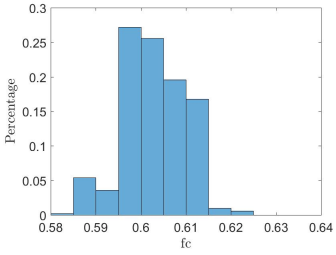


(a) The histogram of the fraction $f_c$ that satisfies $0.05 < \kappa_n < 0.15$.

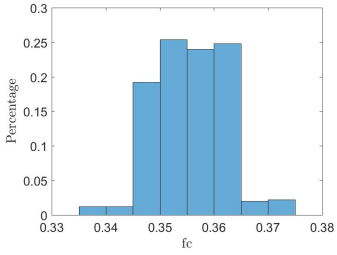


(b) The histogram of the fraction $f_c$ that satisfies $0.45 < \kappa_n < 0.55$.

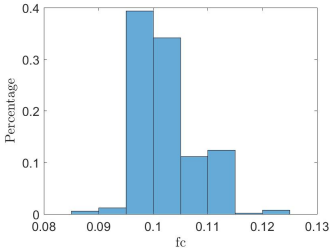


(c) The histogram of the fraction $f_c$ that satisfies $0.85 < \kappa_n < 0.95$.

Figure 4.7: *The histograms of the fraction of closed channels $f_c$ for the triangular unstructured network.*

value of $f_c$ for which holds $\kappa_n = 0$ is depicted in Table 4.4. Since $\theta/\theta_0 = 1 - f_c$, we observe from the results obtained with the different networks that the permeability becomes zero for porosities below a certain threshold. These percolation thresholds are different for the different networks used in this study, as can be seen in Table 4.4. The values are in good agreement with the literature [119]. We also observe that, for all three networks, the relation between the permeability and the porosity exhibits an almost linear increase for values of the porosity larger than the percolation threshold. Moreover, the slope of these linear lines depends on the percolation threshold and hence on the network topology. The normalised permeabilities, for the different

Table 4.3: *The mean $\bar{\mu}$ and the standard deviation $\sigma$ of the distribution of $f_c$ for the triangular unstructured network.*

| | $\bar{\mu}$ | $\sigma$ |
|---|---|---|
| $0.05 < \kappa_n < 0.15$ | 0.6030 | 0.0066 |
| $0.15 < \kappa_n < 0.25$ | 0.5385 | 0.0062 |
| $0.25 < \kappa_n < 0.35$ | 0.4773 | 0.0059 |
| $0.35 < \kappa_n < 0.45$ | 0.4168 | 0.0063 |
| $0.45 < \kappa_n < 0.55$ | 0.3555 | 0.0062 |
| $0.55 < \kappa_n < 0.65$ | 0.2938 | 0.0063 |
| $0.65 < \kappa_n < 0.75$ | 0.2308 | 0.0061 |
| $0.75 < \kappa_n < 0.85$ | 0.1667 | 0.0059 |
| $0.85 < \kappa_n < 0.95$ | 0.1024 | 0.0049 |



network topologies used in this chapter and for the Kozeny-Carman equation, are depicted in Figure 4.8.

Table 4.4: *The percolation threshold for different network topologies.*

| Network type | $f_c$ | $p_c$ |
|---|---|---|
| Rectangular | 0.5065 | 0.4935 |
| Triangular | 0.6768 | 0.3232 |
| Triangular unstructured | 0.6562 | 0.3438 |

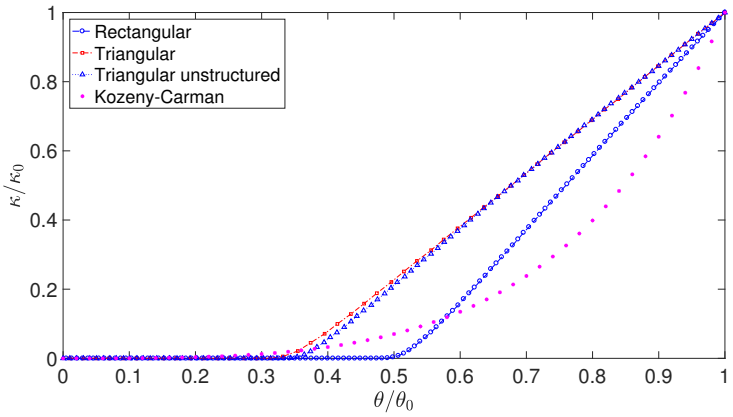


Figure 4.8: *The network-inspired versus Kozeny-Carman based permeability-porosity relations.*

## 4.4 Problem formulation

The following numerical experiments are designed to study the different relations for the porosity and the permeability. In both experiments, the boundary conditions are chosen such that a decrease in porosity is realised in some parts of the computational domain.

### 4.4.1 Problem with high pump pressure

In this numerical experiment, the infiltration of an incompressible fluid through a filter into a two-dimensional area is considered, as shown in Figure 4.9. During the infiltration, a high pump pressure is used to inject water into the porous medium. Leading to a compression of the material against the rigid right boundary $\Gamma_4$.



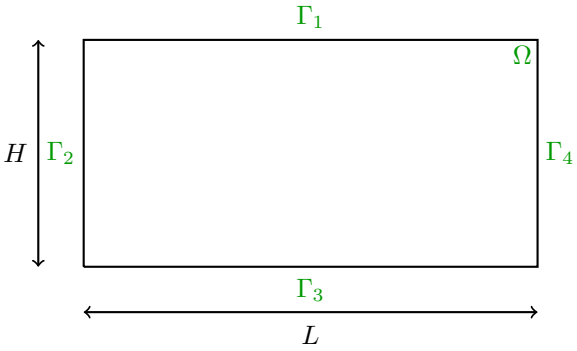


Figure 4.9: *Sketch of the set-up for the two-dimensional problem with high pump pressure.*

The computational domain $\Omega$ is a two-dimensional rectangular surface with Cartesian coordinates $\mathbf{x} = (x, y)$. In order to solve this problem, Biot's consolidation model, as described in Section 4.2, is applied on the computational domain $\Omega$ with width $L$ and height $H$. The fluid is injected into the soil through a filter placed on boundary segment $\Gamma_2$. More precisely, the boundary conditions for this problem are given as follows:

$$\frac{\kappa}{\eta}\nabla p \cdot \mathbf{n} = 0 \quad \text{on} \quad \mathbf{x} \in \Gamma_1 \cup \Gamma_3; \tag{4.13a}$$

$$p = p_{pump} \quad \text{on} \quad \mathbf{x} \in \Gamma_2; \tag{4.13b}$$

$$p = 0 \quad \text{on} \quad \mathbf{x} \in \Gamma_4; \tag{4.13c}$$

$$(\boldsymbol{\sigma}'\mathbf{n}) \cdot \mathbf{t} = 0 \quad \text{on} \quad \mathbf{x} \in \Gamma_1 \cup \Gamma_3 \cup \Gamma_4; \tag{4.13d}$$

$$\mathbf{u} \cdot \mathbf{n} = 0 \quad \text{on} \quad \mathbf{x} \in \Gamma_1 \cup \Gamma_3 \cup \Gamma_4; \tag{4.13e}$$

$$\boldsymbol{\sigma}'\mathbf{n} = \mathbf{0} \quad \text{on} \quad \mathbf{x} \in \Gamma_2, \tag{4.13f}$$

where $\mathbf{t}$ is the unit tangent vector at the boundary, $\mathbf{n}$ the outward unit normal vector and $p_{pump}$ is a prescribed high pump pressure due to the injection of the fluid. Figure 4.9 shows the definition of the boundary segments. Initially, the following

condition is imposed:

$$\mathbf{u}(\mathbf{x}, 0) = 0 \quad \text{for} \quad \mathbf{x} \in \Omega. \tag{4.14}$$

### 4.4.2 Squeeze problem

The infiltration of a fluid through a filter into a rectangular two-dimensional area is shown in Figure 4.10. In this numerical experiment, the porous medium is squeezed by applying a vertical load on the middle of the top and bottom edges of the domain.

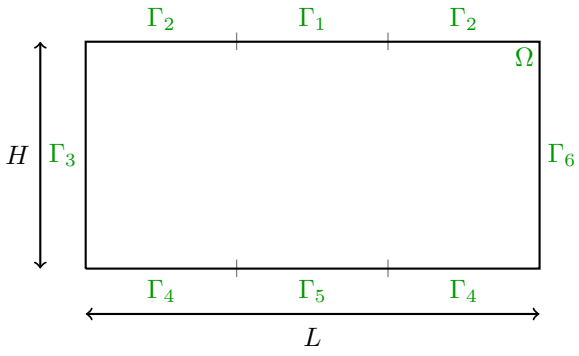


Figure 4.10: *Sketch of the set-up for the two-dimensional squeeze problem.*

This problem is solved using Biot's consolidation model, that is applied on the computational domain $\Omega$ with width $L$ and height $H$. The fluid is injected into the soil through a filter placed on boundary segment $\Gamma_3$. The boundary conditions for this problem are given as follows:

$$\frac{\kappa}{\eta}\nabla p \cdot \mathbf{n} = 0 \quad \text{on} \quad \mathbf{x} \in \Gamma_1 \cup \Gamma_2 \cup \Gamma_4 \cup \Gamma_5; \tag{4.15a}$$

$$p = p_{pump} \quad \text{on} \quad \mathbf{x} \in \Gamma_3; \tag{4.15b}$$

$$p = 0 \quad \text{on} \quad \mathbf{x} \in \Gamma_6; \tag{4.15c}$$

$$\boldsymbol{\sigma}'\mathbf{n} = (0, -\sigma_0')^T \quad \text{on} \quad \mathbf{x} \in \Gamma_1; \tag{4.15d}$$

$$\boldsymbol{\sigma}'\mathbf{n} = \mathbf{0} \quad \text{on} \quad \mathbf{x} \in \Gamma_2 \cup \Gamma_3 \cup \Gamma_4; \tag{4.15e}$$

$$\boldsymbol{\sigma}'\mathbf{n} = (0, \sigma_0')^T \quad \text{on} \quad \mathbf{x} \in \Gamma_5; \tag{4.15f}$$

$$\mathbf{u} = \mathbf{0} \quad \text{on} \quad \mathbf{x} \in \Gamma_6, \tag{4.15g}$$

where $\mathbf{t}$ is the unit tangent vector at the boundary, $\mathbf{n}$ the outward unit normal vector, $p_{pump}$ is a prescribed pump pressure due to the injection of the fluid and $\sigma_0'$ is the intensity of a uniform vertical load. Figure 4.10 shows the definition of the boundary segments. Initially, the following condition is imposed:

$$\mathbf{u}(\mathbf{x}, 0) = 0 \quad \text{for} \quad \mathbf{x} \in \Omega. \tag{4.16}$$

## 4.5 Numerical method

To present the variational formulation of problem (4.1), we first introduce the appropriate function spaces. Let $L^2(\Omega)$ be the Hilbert space of square integrable scalar-valued functions, with inner product $(f,g) = \int_\Omega fg \; d\Omega$. And let $H^1(\Omega)$ denote the subspace of $L^2(\Omega)$ of functions with first derivatives in $L^2(\Omega)$. We further introduce the function spaces

$$\mathscr{W}(\Omega) = \{\mathbf{w} \in (H^1(\Omega))^2 : (\mathbf{w}\cdot\mathbf{n})|_{\Gamma_1\cup\Gamma_3\cup\Gamma_4} = 0\}; \tag{4.17}$$

$$\mathscr{Q}(\Omega) = \{q \in H^1(\Omega) : q|_{\Gamma_2} = p_{pump} \text{ and } q|_{\Gamma_4} = 0\}. \tag{4.18}$$

In addition, we consider the bilinear forms

$$a(\mathbf{u},\mathbf{w}) = \lambda(\nabla\cdot\mathbf{u}, \nabla\cdot\mathbf{w}) + 2\mu\sum_{i,j=1}^{2}(\epsilon_{ij}(\mathbf{u}), \epsilon_{ij}(\mathbf{w})); \tag{4.19}$$

$$b(p,\mathbf{w}) = (p, \nabla\cdot\mathbf{w}); \tag{4.20}$$

$$c(p,q) = \sum_{i=1}^{2}(\frac{\kappa}{\eta}\frac{\partial p}{\partial x_i}, \frac{\partial q}{\partial x_i}). \tag{4.21}$$

The variational formulation for poroelasticity problem (4.1) with boundary and initial conditions (4.13)-(4.14), consists of the following, using the notation $\dot{\mathbf{u}} = \frac{\partial \mathbf{u}}{\partial t}$:

Find $(\mathbf{u}(t), p(t)) \in (\mathscr{W}\times\mathscr{Q})$ such that

$$a(\mathbf{u}(t),\mathbf{w}) - b(p(t),\mathbf{w}) = h(\mathbf{w}) \qquad \forall \mathbf{w}\in\mathscr{W}; \tag{4.22a}$$

$$b(q,\dot{\mathbf{u}}(t)) + c(p(t),q) = 0 \qquad \forall q\in\mathscr{Q}_0, \tag{4.22b}$$

with the initial condition $\mathbf{u}(0) = \mathbf{0}$, and where

$$h(\mathbf{w}) = -p_{pump}\int_{\Gamma_2}\mathbf{w}\cdot\mathbf{n}\; d\Gamma;$$

$$\mathscr{Q}_0(\Omega) = \{q\in H^1(\Omega) : q|_{\Gamma_2\cup\Gamma_4} = 0\}.$$

Subsequently, problem (4.22) is solved by applying the finite element method. Let $\mathscr{P}_h^k \subset H^1(\Omega)$ be a function space of piecewise polynomials on $\Omega$ of degree $k$. Hence, we define finite element approximations for $\mathscr{W}$ and $\mathscr{Q}$ as $\mathscr{W}_h^k = \mathscr{W}\cap(\mathscr{P}_h^k\times\mathscr{P}_h^k)$ with basis $\{\boldsymbol{\phi}_i = (\phi_i,\phi_i) \in (\mathscr{W}_h^k\times\mathscr{W}_h^k) : i = 1,\dots,n_u\}$ and $\mathscr{Q}_h^{k'} = \mathscr{Q}\cap\mathscr{P}_h^{k'}$ with basis $\{\psi_j \in \mathscr{Q}_h^{k'} : j = 1,\dots,n_p\}$, respectively [2]. Afterwards, we approximate the functions $\mathbf{u}(t)$ and $p(t)$ with functions $\mathbf{u}_h(t)\in\mathscr{W}_h^k$ and $p_h(t)\in\mathscr{Q}_h^{k'}$, defined as

$$\mathbf{u}_h(t) = \sum_{i=1}^{n_u}\mathbf{u}_i(t)\boldsymbol{\phi}_i, \quad p_h(t) = \sum_{j=1}^{n_p}p_j(t)\psi_j, \tag{4.23}$$

in which the Dirichlet boundary conditions are imposed. Simultaneously, discretisation in time is applied using the backward Euler method. Let $\Delta t$ be the time step size and define a time grid $\{t_m = m\Delta t : m\in\mathbb{N}\}$, then the discrete Galerkin scheme of (4.22) is formulated as follows:

For $m \geq 1$, find $(\mathbf{u}_h^m, p_h^m) \in (\mathscr{W}_h^k \times \mathscr{Q}_h^{k'})$ such that

$$a(\mathbf{u}_h^m, \mathbf{w}_h) - b(p_h^m, \mathbf{w}_h) = h(\mathbf{w}_h) \qquad \forall \mathbf{w}_h \in \mathscr{W}_h^k; \tag{4.24}$$

$$b(q_h, \mathbf{u}_h^m) + \Delta t c(p_h^m, q_h) = b(q_h, \mathbf{u}_h^{m-1}) \; \forall q_h \in \mathscr{Q}_{0h}^{k'}, \tag{4.25}$$

while for $m = 0$: $\mathbf{u}_h^0 = \mathbf{0}$. The discrete Galerkin scheme for problem (4.1) with boundary and initial conditions (4.15)-(4.16) is derived similarly.

In the network-inspired relation (4.7), the permeability is equal to zero for $\theta \in [0, \hat{\theta}]$. Hence for high percolation thresholds, is it more likely that the permeability goes to zero. In the next section, the convergence of problem (4.1) to a saddle point problem when $\kappa$ goes to zero is proven.

### 4.5.1 Convergence to a saddle point problem

In this section, we will prove that the solution of the variational formulation (4.22) converges to the solution of the related saddle point problem as $\Delta t\kappa \to 0$, both in the continuous as in the discrete system. Since we are interested in the case $\Delta t\kappa \to 0$, we can assume without loss of generality that $\kappa$ is bounded and that it fulfils the following relation (see Figure 4.8):

$$\kappa(\mathbf{x}, t) = \kappa_{max} f(\theta), \tag{4.26}$$

where $\kappa_{max} > 0$ is constant and $f(\theta) \in [0, 1]$. Consequently, define the bilinear form

$$c_\theta(p, q) = \sum_{i=1}^{2} \left(\frac{f(\theta)}{\eta} \frac{\partial p}{\partial x_i}, \frac{\partial q}{\partial x_i}\right), \tag{4.27}$$

and define $\widetilde{\mathbf{u}} = \mathbf{u}^m - \mathbf{u}^{m-1}$, which gives $\mathbf{u}^m = \widetilde{\mathbf{u}} + \mathbf{u}^{m-1}$. This transformation results in the following variational formulation:

For $m \geq 1$, find $(\widetilde{\mathbf{u}}, p^m) \in (\mathscr{W} \times \mathscr{Q})$ such that

$$(\mathcal{P}_{\Delta t\kappa}) \coloneqq \begin{cases} a(\widetilde{\mathbf{u}}, \mathbf{w}) - b(p^m, \mathbf{w}) = g(\mathbf{u}, \mathbf{w}) & \forall \mathbf{w} \in \mathscr{W}; \\ b(q, \widetilde{\mathbf{u}}) + \Delta t \kappa_{max} c_\theta(p^m, q) = 0 & \forall q \in \mathscr{Q}_0, \end{cases}$$

where $g(\mathbf{u}, \mathbf{w}) = h(\mathbf{w}) - a(\mathbf{u}^{m-1}, \mathbf{w})$. The well-posedness of this problem has been analysed in [115, 145].

Using the inequality $|2ab| \leq (a^2 + b^2)$ for $a, b \in \mathbb{R}$, we can show that

$$\begin{aligned} \left|c_\theta(p^m, q)\right| &\leq \frac{1}{2\eta} \left[\sum_{i=1}^{2} \left(\frac{\partial p^m}{\partial x_i}, \frac{\partial p^m}{\partial x_i}\right) + \sum_{i=1}^{2} \left(\frac{\partial q}{\partial x_i}, \frac{\partial q}{\partial x_i}\right)\right] \\ &\leq \frac{1}{2\eta} (\|p^m\|_{H^1(\Omega)}^2 + \|q\|_{H^1(\Omega)}^2) < \infty, \end{aligned} \tag{4.28}$$

where the second inequality is a result of the definition of the $H^1$-norm

$$\|p\|_{H^1(\Omega)}^2 = (p, p) + \sum_{i=1}^{2} \left(\frac{\partial p}{\partial x_i}, \frac{\partial p}{\partial x_i}\right). \tag{4.29}$$

Furthermore, define the spaces $\mathscr{R}(\Omega) = \{q \in L^2(\Omega) : q|_{\Gamma_2} = p_{pump} \text{ and } q|_{\Gamma_4} = 0\}$ and $\mathscr{R}_0(\Omega) = \{q \in L^2(\Omega) : q|_{\Gamma_2 \cup \Gamma_4} = 0\}$. Hence, assuming that $\Delta t \kappa_{max} \to 0$, the variational formulation becomes:

For $m \geq 1$, find $(\widetilde{\mathbf{u}}_0, p_0^m) \in (\mathscr{W} \times \mathscr{R})$ such that

$$(\mathcal{P}_0) := \begin{cases} a(\widetilde{\mathbf{u}}_0, \mathbf{w}) - b(p_0^m, \mathbf{w}) = g(\mathbf{u}, \mathbf{w}) & \forall \mathbf{w} \in \mathscr{W}; \\ b(q, \widetilde{\mathbf{u}}_0) = 0 & \forall q \in \mathscr{R}_0. \end{cases}$$

Brenner and Scott [30] showed, using Korn's inequality, that the bilinear form $a(\mathbf{u}, \mathbf{w})$ is coercive in $\mathscr{W}$. In addition, the bilinear form $b(p, \mathbf{w})$ satisfies the inf-sup condition on $(\mathscr{W} \times \mathscr{R})$ as proven in [29]. The continuity of both bilinear forms follows from the Cauchy-Schwarz inequality. Hence, from Brezzi's splitting theorem [29] we can conclude that a unique solution exists for problem $(\mathcal{P}_0)$. This problem is referred to as a saddle point problem. We assume that our domain allows classical solutions to exist for problem $(\mathcal{P}_0)$, and as a result the solution of this problem is in the spaces $(\mathscr{W} \times \mathscr{Q})$. Then we prove that solutions to $(\mathcal{P}_{\Delta t\kappa})$ converge to solutions of $(\mathcal{P}_0)$, which illustrates that the solutions of $(\mathcal{P}_{\Delta t\kappa})$ inherit the saddle point structure of $(\mathcal{P}_0)$.

4

**Theorem 4.5.1.** The solution of $(\mathcal{P}_{\Delta t\kappa})$ converges to the solution of $(\mathcal{P}_0)$ for

$$\Delta t \kappa_{max} \to 0.$$

*Proof.* Subtracting $(\mathcal{P}_0)$ from $(\mathcal{P}_{\Delta t\kappa})$ yields

$$a(\widetilde{\mathbf{u}} - \widetilde{\mathbf{u}}_0, \mathbf{w}) - b(p^m - p_0^m, \mathbf{w}) = 0 \qquad \forall \mathbf{w} \in \mathscr{W}; \tag{4.30a}$$

$$b(q, \widetilde{\mathbf{u}} - \widetilde{\mathbf{u}}_0) + \Delta t \kappa_{max} c_\theta(p^m, q) = 0 \qquad \forall q \in \mathscr{Q}_0. \tag{4.30b}$$

Take $\mathbf{w} = \widetilde{\mathbf{u}} - \widetilde{\mathbf{u}}_0$ in (4.30a), hence we get

$$a(\widetilde{\mathbf{u}} - \widetilde{\mathbf{u}}_0, \widetilde{\mathbf{u}} - \widetilde{\mathbf{u}}_0) - b(p^m - p_0^m, \widetilde{\mathbf{u}} - \widetilde{\mathbf{u}}_0) = 0. \tag{4.31}$$

Using (4.30b) and the bilinearity of the form $c_\theta(p, q)$ gives

$$a(\widetilde{\mathbf{u}} - \widetilde{\mathbf{u}}_0, \widetilde{\mathbf{u}} - \widetilde{\mathbf{u}}_0) + \Delta t \kappa_{max} c_\theta(p^m, p^m) = \Delta t \kappa_{max} c_\theta(p^m, p_0^m). \tag{4.32}$$

From the coercivity of $a(\mathbf{u}, \mathbf{w})$ and the definition of $c_\theta(p, q)$, we can state that

$$0 \leq a(\widetilde{\mathbf{u}} - \widetilde{\mathbf{u}}_0, \widetilde{\mathbf{u}} - \widetilde{\mathbf{u}}_0) + \Delta t \kappa_{max} c_\theta(p^m, p^m) \tag{4.33a}$$

$$= \Delta t \kappa_{max} c_\theta(p^m, p_0^m) < \infty, \tag{4.33b}$$

where the last inequality follows from (4.28). Let $\Delta t \kappa_{max} \to 0$, then follows that $a(\widetilde{\mathbf{u}} - \widetilde{\mathbf{u}}_0, \widetilde{\mathbf{u}} - \widetilde{\mathbf{u}}_0) \to 0$. Consequently, the coercivity of $a(\mathbf{u}, \mathbf{w})$ implies that $\widetilde{\mathbf{u}} \to \widetilde{\mathbf{u}}_0$ as $\Delta t \kappa_{max} \to 0$. Therefore, we have $a(\widetilde{\mathbf{u}} - \widetilde{\mathbf{u}}_0, \mathbf{w}) \to 0$ for all $\mathbf{w} \in \mathscr{W}$. Subsequently, this last result together with Eq. (4.30a) lead to $b(p^m - p_0^m, \mathbf{w}) \to 0$. Hence, we can conclude that $p^m \to p_0^m$ as $\Delta t \kappa_{max} \to 0$. □

Numerically, the discrete Galerkin scheme (4.24)-(4.25) can be expressed as a linear equations system

$$(\mathcal{P}^D_{\Delta t\kappa}) := \begin{cases} A\mathbf{u}^m - B^T \mathbf{p}^m & = \mathbf{h}, \\ B\mathbf{u}^m + \Delta t \kappa_{max} C \mathbf{p}^m & = B\mathbf{u}^{m-1}, \end{cases}$$

with $\mathbf{u} = (\mathbf{u}_1, \mathbf{u}_2, \ldots, \mathbf{u}_{n_u})$ and $\mathbf{p} = (p_1, p_2, \ldots, p_{n_p})$. The matrix $A \in \mathbb{R}^{2n_u \times 2n_u}$ is the symmetric positive definite elasticity matrix, $B \in \mathbb{R}^{n_p \times 2n_u}$ the divergence matrix and $C \in \mathbb{R}^{n_p \times n_p}$ is the diffusive matrix. The vector $\mathbf{h}$ is the right-hand side vector with components $\mathbf{h}_i = h(\boldsymbol{\phi}_i), i = 1, \ldots, n_u$. Initially, $\mathbf{u}^0 = \mathbf{0}$. For $\Delta t \kappa_{max} \to 0$, we have

$$(\mathcal{P}_0^D) \coloneqq \begin{cases} A\mathbf{u}_0^m - B^T \mathbf{p}_0^m & = \mathbf{h}, \\ B\mathbf{u}_0^m & = B\mathbf{u}_0^{m-1}. \end{cases}$$

**Theorem 4.5.2.** The solution of $(\mathcal{P}_{\Delta t\kappa}^D)$ converges to the solution of $(\mathcal{P}_0^D)$ as

$$\Delta t \kappa_{max} \to 0.$$

*Proof.* The convergence proof in the discrete problem is similar to the continuous problem. Hence, it is sufficient to show that $a(\mathbf{u}, \mathbf{w})$ is coercive in $\mathscr{W}_h^k$. Since $\mathscr{W}_h^k \subset \mathscr{W}$, the coercivity property is automatically verified in the discrete case. □



Since Biot's poroelasticity problem converges to the related saddle point problem as $\Delta t\kappa \to 0$, the Taylor-Hood elements can be used to solve this problem numerically. These elements represent finite element pairs that satisfy the inf-sup condition for the saddle point problem [21, 48]. Although the inf-sup condition and the coercivity and boundedness of bilinear form $a(\mathbf{u}, \mathbf{w})$ warrant existence and uniqueness of the finite element solution, the inf-sup condition is not sufficient for reliable numerical solutions of Biot's problem (4.1). Since for low permeabilities and/or small time steps, the approximation to the pressure exhibits nonphysical oscillations due to loss of the M-matrix property, as shown in [2]. In order to improve the monotonicity properties of the finite element scheme and to obtain oscillation free approximations of the pressure, the stabilisation procedure outlined in [2, 108] is applied in this study. Therefore, a stabilisation term is added to the continuity equation in Biot's model with stabilisation parameter $\beta = \frac{\sqrt{\Delta x^2 + \Delta y^2}}{4(\lambda + 2\mu)}$.

## 4.6 Numerical results

The Galerkin finite element method, with triangular Taylor-Hood elements [103, 113], is adopted to solve the discretised quasi-two-dimensional problem (4.1). The displacements are spatially approximated by quadratic basis functions, whereas a continuous piecewise linear approximation is used for the pressure field. From the system of equations (4.1) and the boundary conditions (4.13) it is obvious that this two-dimensional problem is symmetrical in the $y$-direction and that it can be reduced to a one-dimensional problem. Aguilar et al. [2] solved this one-dimensional problem analytically and showed that the finite element method with Taylor-Hood elements gives accurate numerical results. For the time integration, the backward Euler method is applied. The numerical investigations are carried out using the matrix-based software package MATLAB (version R2015a).

The computational domain is a rectangular surface with width $L = 2.0\,\mathrm{m}$ and height $H = 1.0\,\mathrm{m}$. The domain is discretised using a regular triangular grid, with $\Delta x = \Delta y = 0.02$. In addition, values for some model parameters have been chosen based on the literature (see Table 4.5).

Table 4.5: *An overview of the values of the model parameters.*

| Property | Symbol | Value | Unit |
|---|---|---|---|
| Young's modulus | $E$ | $35 \cdot 10^6$ | Pa |
| Poisson's ratio | $\nu$ | 0.3 | - |
| Fluid viscosity | $\eta$ | $1.307 \cdot 10^{-3}$ | Pa · s |
| Initial porosity | $\theta_0$ | 0.4 | - |
| Mean grain size | $d_s$ | $0.2 \cdot 10^{-3}$ | m |
| Pump pressure | $p_{pump}$ | $50 \cdot 10^5$ / $5 \cdot 10^5$ | Pa |
| Uniform load | $\sigma_0'$ | $3 \cdot 10^6$ | $N/m^2$ |



Furthermore, the Lamé coefficients $\lambda$ and $\mu$ are related to Young's modulus $E$ and Poisson's ratio $\nu$ by

$$\lambda = \frac{\nu E}{(1+\nu)(1-2\nu)}, \quad \mu = \frac{E}{2(1+\nu)}. \tag{4.34}$$

The impact of the permeability-porosity relation on the water flow is defined in this study as the impact on the time average of the volumetric flow rate $\overline{Q}_{out}$ at a distance $L$ from the injection filter. The initial permeability $\kappa_0$ used in Eq. (4.7) is computed by the Kozeny-Carman relation (4.6), in order to have a reliable comparison between the two relations. In the generations of the simulation results, the time step size is chosen to be $\Delta t = 0.5$.

### 4.6.1 Numerical results for the problem with high pump pressure

In order to obtain some insight into the impact of a high pump pressure on the water flow, we present an overview of the simulation results in Figures 4.11 - 4.13. In these simulations, water is injected into the soil at a constant pump pressure of 50 bar. The simulated fluid velocity, permeability and porosity profiles that have been obtained using the Kozeny-Carman relation are provided in Figure 4.11, while the simulated results that have been obtained using the network-inspired relation with $p_c = 0.3232$, corresponding with a triangular structured network, are provided in Figure 4.12. In Figure 4.13, the simulated results that have been obtained using the network-inspired relation with $p_c = 0.4935$, corresponding with a rectangular network, are depicted.

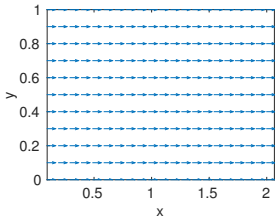


(a) Numerical solution for the fluid velocity.

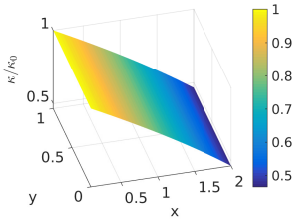


(b) Numerical solution for the permeability.

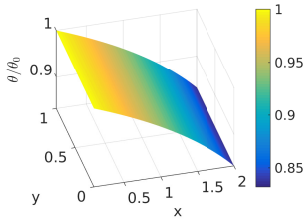


(c) Numerical solution for the porosity.

Figure 4.11: *Numerical solutions for the fluid velocity, the permeability and the porosity, at time $t = 300$, obtained using the Kozeny-Carman relation.*

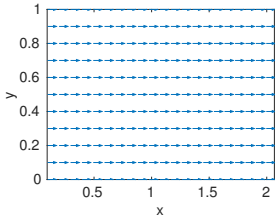


(a) Numerical solution for the fluid velocity.

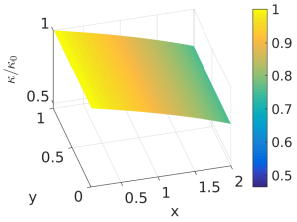


(b) Numerical solution for the permeability.

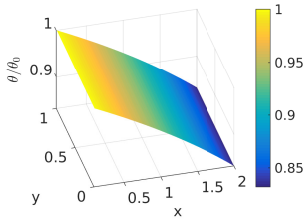


(c) Numerical solution for the porosity.

Figure 4.12: *Numerical solutions for the fluid velocity, the permeability and the porosity, at time $t = 300$, obtained using the network-inspired relation with $p_c = 0.3232$.*

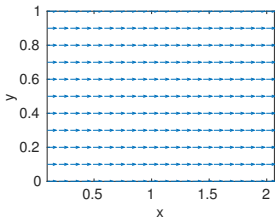


(a) Numerical solution for the fluid velocity.

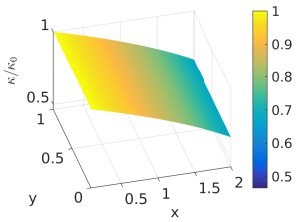


(b) Numerical solution for the permeability.

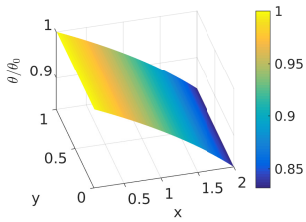


(c) Numerical solution for the porosity.

Figure 4.13: *Numerical solutions for the fluid velocity, the permeability and the porosity, at time $t = 300$, obtained using the network-inspired relation with $p_c = 0.4935$.*

As shown in these figures, the injected water flows in the horizontal direction through the domain from the inlet to the outlet. Furthermore, the magnitude of the velocity $|v|$ in the inlet is larger than in the outlet. This change in $|v|$ can be explained by the permeability profiles shown in Figures 4.11b-4.13b. In these figures we observe that the permeability decreases almost linearly from the inlet to the outlet. In addition, the permeability obtained using the Kozeny-Carman relation exhibits a larger decrease than the permeabilities obtained with the network-inspired model. The normalised permeability using the Kozeny-Carman relation decreases from 1 to

0.4659, while the normalised permeabilities for the network-inspired relation decrease from 1 to 0.7519 and from 1 to 0.6684 for the triangular structured and the rectangular network respectively. This behaviour is clarified by Figure 4.8 and Figures 4.11c-4.13c. Due to boundary condition (4.13e), the values of the normalised porosity in all three cases are almost the same in the outlet and are equal to 0.8321. In Figure 4.8, we see that for this value of the porosity, the normalised permeability is the lowest for the Kozeny-Carman relation and the highest for the network-inspired relation derived from the triangular structured network. This explains the difference in decrease in the permeability profiles.

In Figure 4.14, the time average of the volumetric flow rate $\overline{Q}_{out}$ is depicted for different values of the percolation threshold. As expected from Figure 4.8, for low percolation thresholds the network-inspired relation results in higher flow rates than the Kozeny-Carman relation. Furthermore, the flow rate changes significantly as a function of the percolation threshold. Hence the water flow depends on the topology of the network. The negative values of the flow rate $\overline{Q}_{out}$ for the large values of the percolation threshold from the network-inspired relation are caused by violation of the M-matrix property that gives loss of monotonicity of the numerical solution. To demonstrate this, the problem is solved for a coarser grid $\Delta x = \Delta y = 0.04$, as shown in Figure 4.15. In this figure, it becomes even worse, and we observe spurious oscillations for the network-inspired relation for percolation thresholds larger than 0.85 approximately. The reason for this behaviour is that for large values of the percolation threshold, the permeability goes to zero very soon. Therefore, even the used stabilisation did not diminish the nonphysical oscillations. Probably a stronger stabilisation will alleviate these spurious oscillations. This was behind the scope of the current chapter.

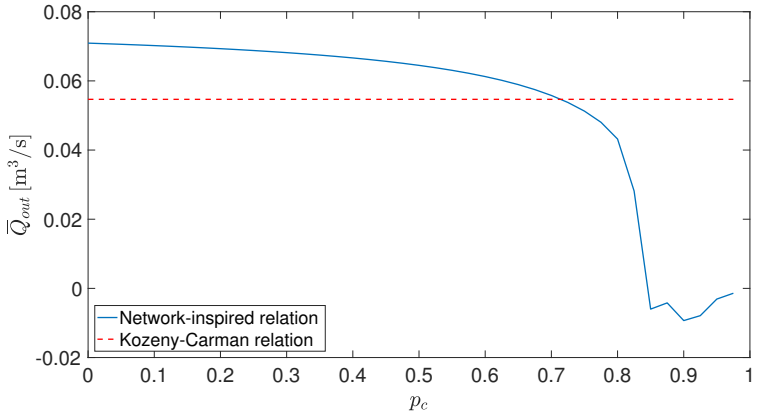


Figure 4.14: *The time average of the volumetric flow rate* $\overline{Q}_{out}$ *as a function of the percolation threshold* $p_c$*, using* $\Delta x = \Delta y = 0.02$.

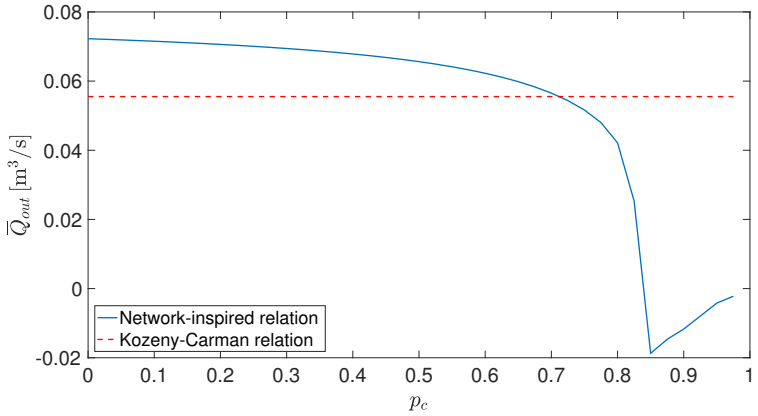


Figure 4.15: *The time average of the volumetric flow rate* $\overline{Q}_{out}$ *as a function of the percolation threshold* $p_c$*, using* $\Delta x = \Delta y = 0.04$.



### 4.6.2 Numerical results for the squeeze problem

The impact of the imposed vertical load on boundary segments $\Gamma_1$ and $\Gamma_5$ is shown in Figures 4.16 - 4.18, using the Kozeny-Carman relation and the network-inspired relation respectively. In these simulations, water is injected into the porous medium at a constant pump pressure equal to 5.0 bar. The simulated fluid velocity, permeability and porosity profiles that are obtained using the Kozeny-Carman relation are provided in Figure 4.16, while the simulated results that are obtained using the network-inspired relation with $p_c = 0.3232$, corresponding with a triangular structured network, are provided in Figure 4.17. In Figure 4.18, the simulated results that are obtained using the network-inspired relation with $p_c = 0.4935$, corresponding with a rectangular network, are depicted.

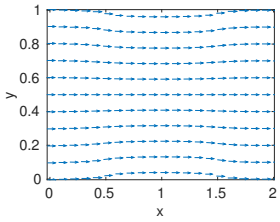


(a) Numerical solution for the fluid velocity.

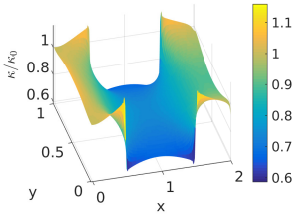


(b) Numerical solution for the permeability.

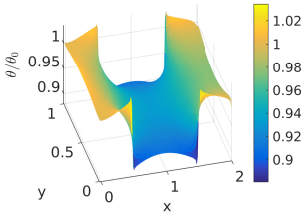


(c) Numerical solution for the porosity.

Figure 4.16: *Numerical solutions for the fluid velocity, the permeability and the porosity, at time $t = 300$, obtained using the Kozeny-Carman relation.*



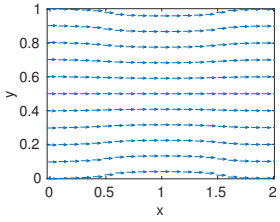


(a) Numerical solution for the fluid velocity.

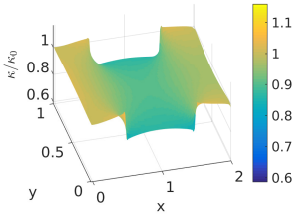


(b) Numerical solution for the permeability.

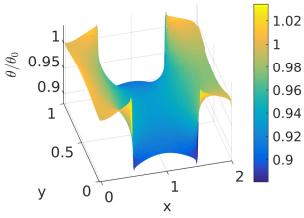


(c) Numerical solution for the porosity.

Figure 4.17: *Numerical solutions for the fluid velocity, the permeability and the porosity, at time $t = 300$, obtained using the network-inspired relation with $p_c = 0.3232$.*

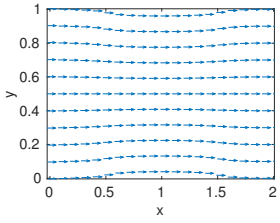


(a) Numerical solution for the fluid velocity.

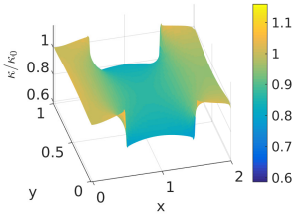


(b) Numerical solution for the permeability.

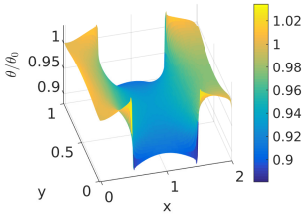


(c) Numerical solution for the porosity.

Figure 4.18: *Numerical solutions for the fluid velocity, the permeability and the porosity, at time $t = 300$, obtained using the network-inspired relation with $p_c = 0.4935$.*

In Figures 4.16a-4.18a, the impact of the imposed vertical load on the computational domain is shown. The magnitude of the velocity is small near the boundary segments where the vertical load is applied and large in the middle near the symmetry axis $y = H/2$. In the outlet, the magnitude of the velocity is maximal near the upper and lower boundary segments and decreases towards the symmetry axis. In all three cases, the fluid flows mainly in the horizontal direction. In the region where the load is imposed, the domain is squeezed, resulting in a larger density of the grains. This leads

to a lower porosity in this region, with minimum values 0.8809, 0.8811 and 0.8810 for the Kozeny-Carman relation, the triangular structured network-inspired relation and the rectangular network-inspired relation respectively. The abrupt transition in the boundary condition between boundary segments $\Gamma_1$ and $\Gamma_2$ (and between $\Gamma_4$ and $\Gamma_5$), which results in a discontinuous force, results in a small numerical artefact at the location of these transitions. As expected from Figure 4.8 and the minimum values for the porosities, the decrease in permeability by the Kozeny-Carman relation, as shown in Figure 4.16b, is larger than the decrease in the porosities obtained using the network-inspired relation, Figures 4.17b and 4.18b.

In Figure 4.19, the time average of the volumetric flow rate $\overline{Q}_{out}$ is depicted for different values of the percolation threshold. Similarly to the high pump pressure problem, the flow rates for small values of the percolation threshold using the network-inspired relation are higher than the flow rates obtained using the Kozeny-Carman relation. In addition, we observe that the flow rate depends significantly on the percolation threshold and hence on the topology of the network for high percolation thresholds.



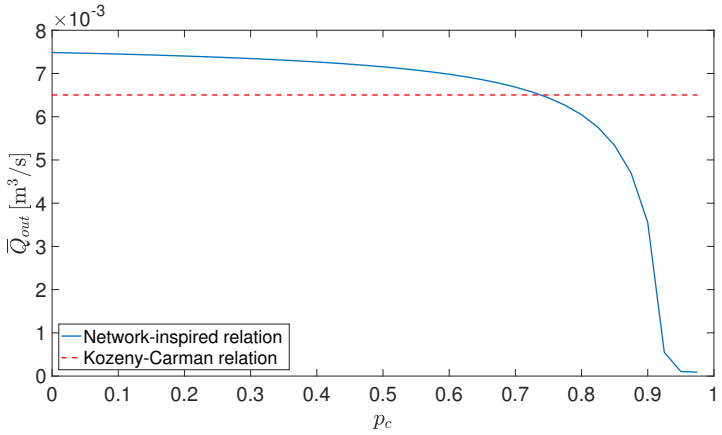


Figure 4.19: *The time average of the volumetric flow rate $\overline{Q}_{out}$ as a function of the percolation threshold $p_c$.*

## 4.7 Discussion and conclusions

In this chapter, the network-inspired permeability-porosity relation is applied on two two-dimensional poroelasticity problems. This numerical experiment is designed in order to analyse the applicability of this microscopic relation on the macro-scale. Furthermore, we compare the results obtained with the network-inspired relation to the Kozeny-Carman relation which is often used in these physical problems. In the first problem, a high pump pressure is imposed in the inlet of a porous medium package. This high pressure forces the grains to move towards the outlet. In the second problem the package is squeezed by applying a load on the middle of the top and bottom edges of the domain. The purpose of considering these two-dimensional

poroelasticity problems is to create a large density of the grains in the computational domain which results in a decrease of the porosity. In these problems, Biot's model for poroelasticity is used to determine the water pressure and the displacements of the grains that are needed to compute the porosity. From the porosity the permeability is determined either by the network-inspired relation or by the Kozeny-Carman relation. Depending on the topology, three different percolation thresholds, corresponding with a rectangular network ($p_c = 0.4935$), triangular structured network ($p_c = 0.3232$) and triangular unstructured network ($p_c = 0.3438$), are distinguished. However, since the topology of macro-scale porous media is not known, computations are also performed with percolation thresholds in the interval $[0, 0.975]$ to investigate the influence of the percolation threshold (and hence the topology of the porous medium) on the flow rate.



First, the problems are solved with the Kozeny-Carman relation, the network-inspired relation based on the triangular structured network and the relation based on the rectangular network. From the numerical results we conclude that the permeability obtained using the Kozeny-Carman relation exhibits a larger decrease than the permeabilities obtained with the network-inspired relations, which is clarified by Figure 4.8. In contrast, the porosity profile is not affected significantly by the selected permeability-porosity relation. Second, the time average of the volumetric flow rate was computed for percolation thresholds in the interval $[0, 0.975]$. For low percolation thresholds the network-inspired relation results in higher flow rates than the Kozeny-Carman relation, as expected from Figure 4.8. In addition, it is shown that the flow rate changes significantly as a function of the percolation threshold which means that the water flow depends on the topology of the network. For high percolation thresholds, spurious oscillations appeared due to the violation of the M-matrix property in the discretisation matrix that resulted from the convergence of Biot's problem to the related saddle point problem, as proven in Section 4.5.1. The results for these percolation thresholds could be improved by using a finer grid.

For the studied problems and the set of parameters chosen, we noticed that the applied permeability-porosity relations result in small changes in the porosity while a major change is realised in the permeability profiles. A possible explanation for this behaviour is that the relation between the velocity field and the change of the displacements in time as stated in Eq. (4.1b), is not strong enough to lead to significant changes in the porosity profile.

Chapter 5

# A three-dimensional poroelasticity model using a network-inspired porosity-permeability relation

*Compressing a porous material or injecting fluid into a porous material can induce changes in the pore space, leading to a change in porosity and permeability. In a continuum scale PDE model, such as Biot's theory of linear poroelasticity, the Kozeny-Carman equation is commonly used to determine the permeability of the porous medium from the porosity. The Kozeny-Carman relation assumes that there will be flow through the porous medium at a certain location as long as the porosity is larger than zero at this location. In contrast, from discrete network models it is known that percolation thresholds larger than zero exist, indicating that the fluid will stop flowing if the average porosity becomes smaller than a certain value dictated by these thresholds. In this study, the difference between the Kozeny-Carman equation and the equation based on the percolation theory, is investigated considering a three-dimensional poroelasticity problem.*

This chapter is based on the article:

M. Rahrah, F. J. Vermolen, L. A. Lopez-Peña, and B. J. Meulenbroek. A Poroelasticity Model Using a Network-Inspired Porosity-Permeability Relation. In *Progress in Industrial Mathematics at ECMI 2018*, pages 83 – 88. Springer, 2019.

## 5.1 Introduction

Having a good estimation of permeability is of a pivotal importance for the description of different physical processes. However, mainly due to the complexity of the connected pore space, it has been very difficult to formulate satisfactory theoretical models for the relation between the porosity and the permeability. One of the most largely used methods remains the Kozeny-Carman approach. In this study, we briefly introduce a new approach for the permeability that is derived on a micro-scale network model. We refer to this approach as the network-inspired relation. The Kozeny-Carman relation assumes that the pore space is fully connected, therefore, flow through the porous medium is possible as long as the average porosity is larger than zero. In contrast, the new network-inspired approach states that the permeability is positive only if the porosity is larger than a specific percolation threshold, that depends on the topology of the network. As application, we consider the flow of an incompressible fluid through a poroelastic porous medium.

The rest of this chapter is organised as follows: In Section 5.2 the considered model equations are presented, including the employed porosity-permeability relations. Section 5.3 presents the numerical experiment that is used to demonstrate the applicability of the network-inspired permeability-porosity relation on a three-dimensional problem. The numerical results of this experiment are shown in Section 5.4 and lastly, the conclusions are given in Section 5.5.



## 5.2 Governing equations

The model provided by Biot's theory of linear poroelasticity with single-phase flow [16] is used in this study to determine the local displacement of the grains of a porous medium and the fluid flow through the pores, assuming that the deformations are very small. We assume that the fluid-saturated porous medium has a linearly elastic solid matrix and is saturated by an incompressible Newtonian fluid. Let $\Omega \subset \mathbb{R}^3$ denote the computational domain with boundary $\Gamma$, and $\mathbf{x} = (x, y, z) \in \Omega$. Furthermore, $t$ denotes time, belonging to a half-open time interval $I = (0, T]$, with $T > 0$. The initial boundary value problem of an incompressible fluid flow in a deformable porous medium in the two-field $(\mathbf{u}/p)$ formulation, where $\mathbf{u}$ and $p$ are the unknown functions, is stated as follows [135]:

$$\text{equilibrium equations:} \quad -\nabla \cdot \boldsymbol{\sigma}' + (\nabla p + \rho g \mathbf{e}_z) = \mathbf{0} \qquad \text{on } \Omega \times I; \tag{5.1a}$$

$$\text{continuity equation:} \quad \frac{\partial}{\partial t}(\nabla \cdot \mathbf{u}) + \nabla \cdot \mathbf{v} = 0 \qquad \text{on } \Omega \times I, \tag{5.1b}$$

where $\boldsymbol{\sigma}'$ and $\mathbf{v}$ are defined by the following equations

$$\text{Biot's constitutive equations:} \quad \boldsymbol{\sigma}' = \lambda(\nabla \cdot \mathbf{u})\mathbf{I} + \mu(\nabla \mathbf{u} + \nabla \mathbf{u}^T); \tag{5.2}$$

$$\text{Darcy's law:} \quad \mathbf{v} = -\frac{\kappa}{\eta}(\nabla p + \rho g \mathbf{e}_z). \tag{5.3}$$

Here, $\boldsymbol{\sigma}'$ denotes the effective stress tensor, $p$ the pore pressure, $\rho$ the fluid density, $g$ the gravitational acceleration, $\mathbf{u}$ the displacement vector, $\mathbf{v}$ Darcy's velocity, $\lambda$ and $\mu$ the Lamé coefficients; $\kappa$ the permeability of the porous medium and $\eta$ the fluid

viscosity. In addition, appropriate boundary and initial conditions are specified in Section 5.3.

### 5.2.1 The porosity-permeability relations

In this study, we consider the spatial dependency of the porosity and the permeability of the porous medium. The porosity $\theta$ is computed from the displacement vector using the porosity-dilatation relation (see [103, 130])

$$\theta(\mathbf{x}, t) = 1 - \frac{1 - \theta_0}{\exp(\nabla \cdot \mathbf{u})}, \tag{5.4}$$

with $\theta_0$ the initial porosity. Subsequently, the permeability can be determined using the Kozeny-Carman equation [136]

$$\kappa(\mathbf{x}, t) = \frac{d_s^2}{180} \frac{\theta(\mathbf{x}, t)^3}{(1 - \theta(\mathbf{x}, t))^2}, \tag{5.5}$$

where $d_s$ is the mean grain size of the soil. The Kozeny-Carman relation assumes that the permeability becomes zero if and only if the porosity also becomes zero. A new approach for the relation between the porosity and the permeability is inspired by the fluid flow through the edges (channels) of a network. In a network with a random topology, the network-inspired porosity-permeability relation states:

$$\kappa(\mathbf{x}, t) = \begin{cases} 0 & \theta \leq \hat{\theta} \\ \frac{\theta - \hat{\theta}}{\theta_0 - \hat{\theta}} \kappa_0 & \theta > \hat{\theta} \end{cases}, \tag{5.6}$$

where $\kappa_0$ is the initial permeability computed using the Kozeny-Carman relation and $\hat{\theta}$ the percolation threshold, which represents the minimal porosity needed to have connection via voids or channels from one end to the other. This percolation threshold depends on the topology of the network. The normalised permeability $\kappa/\kappa_0$ obtained using both relations as function of the normalised porosity $\theta/\theta_0$, is depicted in Figure 5.1.

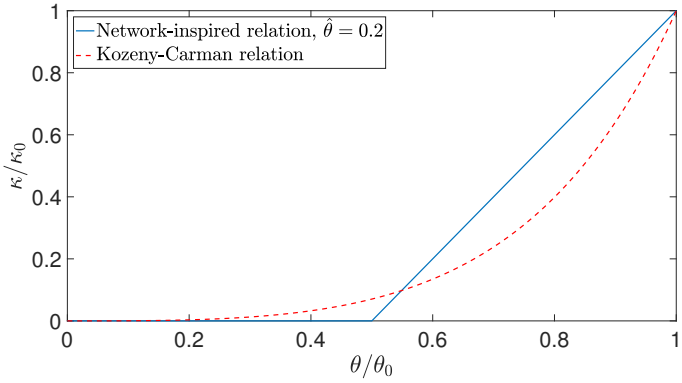


Figure 5.1: *The normalised permeability as function of the normalised porosity.*

## 5.3 Problem formulation

The following numerical experiment is designed to study the different relations for the porosity and the permeability. As shown in Figure 5.2, the infiltration of a fluid into a porous medium is studied. In addition, a vertical load is applied on a part of the top edge of the domain, in order to create a region with a high density of the grains which will emphasise the difference between the porosity-permeability relations. We assume that the flow pattern is axisymmetric. Therefore, we determine the solution for a fixed azimuth. Hence, the computational domain $\Omega$ is an L-shaped two-dimensional surface with cylindrical coordinates $\mathbf{r} = (r, z)$ and boundary $\Gamma$.

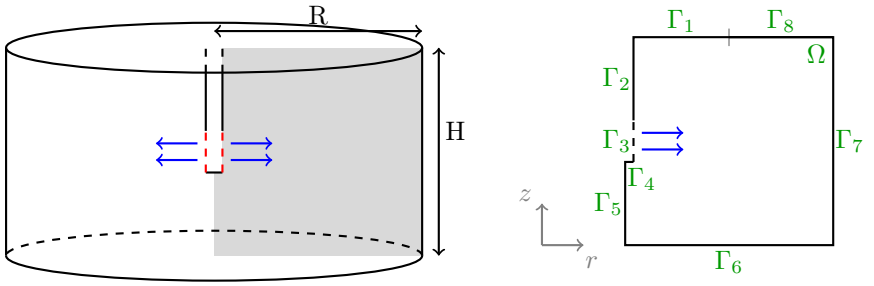


Figure 5.2: *Sketch of the set-up for the aquifer problem: (left) physical problem and (right) numerical discretisation. Taking advantage of the symmetry of geometry and boundary conditions, only the grey region is discretised.*

The fluid is injected into the soil through a filter placed on boundary segment $\Gamma_3$, using a pump pressure. The vertical load is applied on boundary segment $\Gamma_8$. Furthermore, the injection tube is fitted with a casing (boundary segments $\Gamma_2$ and $\Gamma_4$) and a perforated section (boundary segment $\Gamma_3$) to prevent loose material from entering and potentially clogging the injection tube. More precisely, the boundary conditions for this problem are given as follows:

$$\frac{\kappa}{\eta}(\nabla p + \rho g \mathbf{e}_z) \cdot \mathbf{n} = 0 \quad \text{on} \quad \mathbf{r} \in \Gamma \setminus \Gamma_3 \cup \Gamma_7; \tag{5.7a}$$

$$p = \rho g(H - z) + p_{pump} \quad \text{on} \quad \mathbf{r} \in \Gamma_3; \tag{5.7b}$$

$$p = \rho g(H - z) \quad \text{on} \quad \mathbf{r} \in \Gamma_7; \tag{5.7c}$$

$$\boldsymbol{\sigma}'\mathbf{n} = \mathbf{0} \quad \text{on} \quad \mathbf{r} \in \Gamma_1 \cup \Gamma_7; \tag{5.7d}$$

$$\mathbf{u} \cdot \mathbf{n} \leq 0 \quad \text{on} \quad \mathbf{r} \in \Gamma_2 \cup \Gamma_3 \cup \Gamma_4; \tag{5.7e}$$

$$(\boldsymbol{\sigma}'\mathbf{n}) \cdot \mathbf{t} = 0 \quad \text{on} \quad \mathbf{r} \in \Gamma \setminus \Gamma_1 \cup \Gamma_7 \cup \Gamma_8; \tag{5.7f}$$

$$\mathbf{u} \cdot \mathbf{n} = 0 \quad \text{on} \quad \mathbf{r} \in \Gamma_5 \cup \Gamma_6; \tag{5.7g}$$

$$\boldsymbol{\sigma}'\mathbf{n} = (0, -\sigma_0')^T \quad \text{on} \quad \mathbf{r} \in \Gamma_8, \tag{5.7h}$$

where $\mathbf{t}$ and $\mathbf{n}$ are the unit tangent and the outward normal vectors. Further, $p_{pump}$ is a prescribed pump pressure and $\sigma_0'$ is the intensity of a uniform vertical load. Note that the boundary conditions on boundary segment $\Gamma_5$ appear as a result of symmetry. The initial condition is $\mathbf{u}(\mathbf{r}, 0) = 0$ for $\mathbf{r} \in \Omega$.

## 5.4 Numerical results

To solve the discretised problem of (5.1), the Galerkin finite element method with triangular Taylor-Hood elements [103], is adopted. Quadratic basis functions are used for the approximation of the displacements, while the pressure field is approximated by continuous piecewise linear functions. In addition, the backward Euler method is applied for the time integration. The computational domain is an L-shaped surface with radius $R = 1.0\,\text{m}$, height $H = 2.0\,\text{m}$, filter radius $R_f = 10.0\,\text{cm}$ and filter length $L_f = 1.0\,\text{m}$. The filter is placed between $z = 0.5$ and $z = 1.5$, while the vertical load is applied between $r = 0.5$ and $r = 1.0$. The domain is discretised using a regular triangular grid, with $\Delta r = \Delta z = 0.05$. The time step size is chosen to be $\Delta t = 0.5$. Furthermore, values for some model parameters have been chosen (see Table 5.1).

Table 5.1: *An overview of the values of the model parameters.*

| Property | Symbol | Value | Unit |
|---|---|---|---|
| Young's modulus | $E$ | $35 \cdot 10^6$ | Pa |
| Poisson's ratio | $\nu$ | 0.3 | - |
| Fluid viscosity | $\eta$ | $1.307 \cdot 10^{-3}$ | $\text{Pa} \cdot \text{s}$ |
| Fluid density | $\rho$ | 1000 | $\text{kg/m}^3$ |
| Gravitational acceleration | $g$ | 9.81 | $\text{m/s}^2$ |
| Initial porosity | $\theta_0$ | 0.4 | - |
| Mean grain size | $d_s$ | $314 \cdot 10^{-6}$ | m |
| Pump pressure | $p_{pump}$ | $10^5$ | Pa |
| Uniform load | $\sigma_0'$ | $10^7$ | $\text{N/m}^2$ |

The Lamé coefficients $\lambda$ and $\mu$ are related to Young's modulus $E$ and Poisson's ratio $\nu$ by: $\lambda = \frac{\nu E}{(1+\nu)(1-2\nu)}$ and $\mu = \frac{E}{2(1+\nu)}$. The impact of the porosity-permeability relations on the fluid flow is defined in this study as the impact on the time average of the volumetric flow rate $\overline{Q}$ at a distance $R - R_f$ from the injection filter. We compute the volumetric flow rate using the velocity field as described by Darcy's law (5.3). The velocity field is obtained from the gradient of the pressure $\nabla p$ by applying the finite element method with piecewise linear approximation. For the Kozeny-Carman relation as well as for the network-inspired relation, $\overline{Q}$ is depicted in Figure 5.3 as a function of the percolation threshold. In this figure, $\overline{Q}$ is normalised by dividing on the time average of the volumetric flow rate obtained by the Kozeny-Carman relation $\overline{Q}_{KC}$. As expected from Figure 5.1, for low percolation thresholds the network-inspired relation results in higher flow rates than the Kozeny-Carman relation. In addition, the flow rate changes significantly as a function of the percolation threshold. Hence, the fluid flow depends on the topology of the connected pore space.

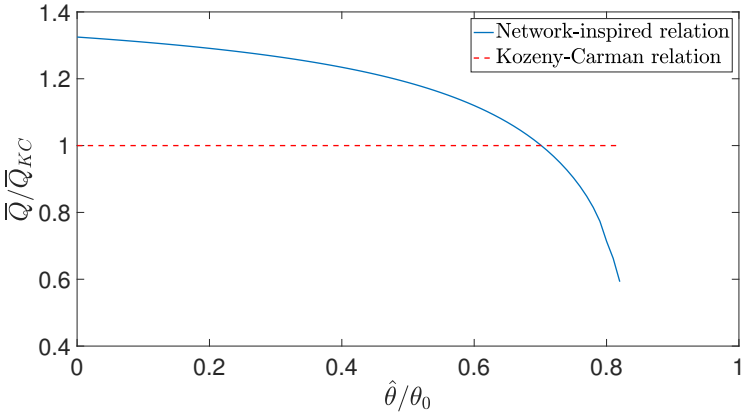


Figure 5.3: *The time average of the volumetric flow rate $\overline{Q}$ as a function of the percolation threshold $\hat{\theta}$.*

## 5.5 Discussion and conclusions

In this study, a three-dimensional poroelasticity problem is designed in order to analyse the applicability of the microscopic network-inspired porosity-permeability relation on the macro-scale. Furthermore, the results obtained with this relation are compared with the Kozeny-Carman relation, which is often used for this type of physical problems. To determine the displacements of the grains that are needed to compute the porosity, Biot's model for poroelasticity is used. Since the topology of macro-scale porous media is not known, computations are performed with different values of the percolation threshold. The numerical results indicate that for low percolation thresholds the network-inspired relation results in higher flow rates than the Kozeny-Carman relation, as expected from Figure 5.1. In addition, it is shown that the flow rate changes significantly as a function of the percolation threshold which means that the water flow depends on the topology of the connected pore space.

Chapter 6

# A moving finite element framework for fast infiltration in nonlinear poroelastic media

*Poroelasticity theory can be used to analyse the coupled interaction between fluid flow and porous media (matrix) deformation. The classical theory of linear poroelasticity captures this coupling by combining Terzaghi's effective stress with a linear continuity equation. Linear poroelasticity is a good model for very small deformations; however, it becomes less accurate for moderate to large deformations. On the other hand, the theory of large-deformation poroelasticity combines Terzaghi's effective stress with a nonlinear continuity equation. In this chapter, we present a finite element solver for linear and nonlinear poroelasticity problems on triangular meshes based on the displacement-pressure two-field model. We then compare the predictions of linear poroelasticity with those of large-deformation poroelasticity in the context of a two-dimensional model problem where flow through elastic, saturated porous media, under applied mechanical oscillations, is considered. In addition, the impact of introducing a deformation-dependent permeability according to the Kozeny-Carman equation is explored. We computationally show that the errors in the displacement and pressure fields that are obtained using the linear poroelasticity are primarily due to the lack of the kinematic nonlinearity. Furthermore, the error in the pressure field is amplified by incorporating a constant permeability rather than a deformation-dependent permeability.*

This chapter is based on the journal article:

M. Rahrah and F. Vermolen. A moving finite element framework for fast infiltration in nonlinear poroelastic media. *Comput. Geosci.*, 2020.

## 6.1 Introduction

A saturated porous medium is composed of a porous solid material, fully saturated by a viscous fluid, flowing through connected pores. In deformable porous materials such as soils, rocks and tissues, the flow of the pore fluid and the deformation of the solid matrix are tightly coupled to each other. Poromechanics involves fluid flow in porous media that can deform when subjected to external forces and to variations in pressure of the saturating fluid. Moreover, poromechanical deformations are poroelastic when they are controlled by the reversible storage and release of elastic energy.

In the last few decades, the mechanics of porous media has been of great interest due to its potential application in many geological and biological systems across a wide range of scales such as civil engineering [22, 34, 52, 55, 95, 116, 122, 127], energy and environmental technologies [37, 49, 69, 109, 111, 140], material science [85] and biophysics [50, 92], where poromechanics plays an important role in modelling bones and soft tissues [3, 41, 120]. In physical chemistry, poromechanical processes include mass and heat transfer [144]. Additionally, poromechanics has been studied intensely in geophysics, in the context of consolidation of aquifers [96, 104] and in the context of enhanced oil or gas recovery [9, 110, 124]. Our current main motivation is related to the development of a comprehensive model for fluid injection into a monolayer of soil particles subjected to surface mechanical oscillations. Therein, we include dynamic effects, especially a time and space dependent porosity and permeability.

Due to the high complexity and the unknown geometry of porous media, a fully resolved model is nearly impossible to obtain. Classically, in the theory of linear poroelasticity [16, 135], fluid flow is described by Darcy's law and fluid mass conservation, and matrix deformation is described by Terzaghi's effective stress and linear elasticity. This theory is originally emerged in soil mechanics with the work of Terzaghi [128], but its general statement was given by Biot [16, 18] using an elastic formulation for the solid matrix and Darcy's law for the fluid flow. This approach, as formulated in Biot's consolidation model [16], is valid for infinitesimal deformations of the solid. However, it becomes increasingly inappropriate for moderate to large deformations. The well-known theory of large-deformation poroelasticity [84] combines Darcy's law with Terzaghi's effective stress and nonlinear elasticity in a rigorous kinematic framework, leading to a strongly nonlinear coupling between the pore structure and the fluid flow [50, 109]. Another nonlinear poroelasticity model that takes large deformations into account is considered in [23]. In this model, the mechanical deformation follows the Saint Venant-Kirchhoff constitutive law for hyperelastic solid materials and the fluid compressibility in the fluid equation is assumed to be nonlinear. In the current chapter, the fluid phase is assumed to be incompressible and a linear stress-strain constitutive law is considered.

In this chapter, we propose finite element methods for the resolution of the governing equations both in the theory of linear poroelasticity as in the large-deformation poroelasticity. The fluid-mass balance equation is discretised in time by a backward Euler scheme. The resulting system of nonlinearly coupled equations is solved by a standard Picard iterative procedure, which is linearly convergent. In the literature, this system is also solved by Newton's method [23], which is quadratically convergent. The drawbacks of the Newton-Raphson method are that the method is only locally convergent and that the computation of derivatives is needed. Another valu-

able alternative to Picard's method is the L-scheme [23, 24]. The L-method is robust and linearly convergent, and does not involve the computation of any derivatives. Moreover, the convergence rate does not depend on the mesh size. Only a relatively mild constraint on the time step size is required when the hydraulic conductivity is not taken constant [80]. The L-scheme contains a constant parameter $L > 0$ which mimics the Jacobian from Newton iteration. However, in order to determine the parameter $L$, for any given problem, it is necessary to use apriorily derived convergence estimates [33]. In the current chapter, Picard's iterative method is used since it is easy to understand and to implement and since it does not involve the computation of derivatives or unknown parameters. Furthermore, monolithic approaches for solving the quasi-static two-field poroelasticity equations are adopted. Another approach that is widely used in coupling the flow and the mechanics in porous media is the fixed-stress split method [25], which falls within the class of segregated approaches. This method can be combined with a linearisation scheme for the nonlinear poroelasticity models (see [24] where the L-scheme is used for the linearisation).

To assess the accuracy of aforementioned constitutive laws and the performance of finite element methods presented herein, we consider a two-dimensional simulation. The obtained numerical results from both linear and nonlinear poroelasticity theories are compared with each other. The research problem we address in the present chapter is for which applied mechanical oscillations it is sufficient to solve the linear poroelasticity model, which is computationally cheaper and simpler to solve.

The rest of this chapter is organised as follows: In Section 6.2 the considered constitutive equations are summarised, including the employed permeability model. Section 6.3 presents a two-dimensional numerical example that is used to demonstrate the difference between the linear and nonlinear poroelasticity models. In Section 6.4, the nonlinear equations are discretised and the finite elements are combined with the first-order implicit Euler temporal discretisation to establish a solver for linear and nonlinear poroelasticities on triangular meshes, which couples the solid displacement and fluid pressure in a monolithic system. Furthermore, the nonlinear equation systems are solved using a Picard iterative method. Section 6.5 discusses the numerical results and some concluding remarks are reported in Section 6.6.



## 6.2 Governing equations

In the following, we briefly recall the equations governing the problem of a porous material subjected to oscillating mechanical deformations characterised by displacements $\mathbf{u}$ of the solid skeleton.

We consider a two-phase mixture composed of an elastic solid matrix whose voids are continuous and completely saturated by an incompressible Newtonian fluid. In this study, it is further assumed that the porous material is in an initial state of hydraulic and mechanical equilibrium, gravitational body force remains constant and the matrix grains are incompressible. Let $\Omega_t \subset \mathbb{R}^3$ denote a bounded domain occupied by a homogeneous and isotropic elastic body with boundary $\Gamma_t$ and $\mathbf{x} = (x, y, z) \in \Omega_t$. Denote by $\Omega_0$ the reference domain corresponding to the poroelastic medium in the initial state and $\Omega_t$ the deformed domain. Furthermore, $t$ denotes time, belonging to a half-open time interval $I = (0, T]$, with $T > 0$. To determine the local displacement

of the skeleton of a porous medium as well as the fluid flow through the pores, the poroelastic equations with single-phase flow can be expressed as [84]

$$-\nabla \cdot \boldsymbol{\sigma}' + (\nabla p + \rho \mathbf{g}) = \mathbf{0} \text{ on } \Omega_t \times I; \tag{6.1a}$$

$$\nabla \cdot \frac{D\mathbf{u}}{Dt} + \nabla \cdot \mathbf{v}_f = 0 \text{ on } \Omega_t \times I, \tag{6.1b}$$

where $\boldsymbol{\sigma}'$ and $\mathbf{v}_f$ are defined by the following equations

$$\text{Stress-strain constitutive law:} \quad \boldsymbol{\sigma}' = \lambda \text{tr}(\boldsymbol{\varepsilon})\mathbf{I} + 2\mu\boldsymbol{\varepsilon}; \tag{6.2}$$

$$\text{Darcy's law:} \quad \mathbf{v}_f = -\frac{\kappa}{\eta}(\nabla p + \rho \mathbf{g}), \tag{6.3}$$

where $\boldsymbol{\sigma}'$ is Terzaghi's effective stress tensor for the porous medium, $p$ is the fluid pressure, $\rho$ is the fluid density, $\mathbf{g}$ is the gravitational acceleration vector, $\mathbf{u}$ is the solid displacement vector, $\mathbf{v}_f$ is Darcy's velocity, $\lambda$ and $\mu$ are the Lamé constants; $\boldsymbol{\varepsilon}$ is the effective strain tensor, $\kappa$ is the permeability of the porous medium and $\eta$ is the fluid viscosity. Note that in Eq. (6.1b) we have used the material derivative, which reads as

$$\frac{D}{Dt}(\cdot) = \frac{\partial}{\partial t}(\cdot) + \mathbf{v}_s \cdot \nabla(\cdot), \tag{6.4}$$

where

$$\mathbf{v}_s = \left.\frac{\partial \mathbf{u}}{\partial t}\right|_{\Omega_0}, \tag{6.5}$$

is the solid velocity. This system needs to be complemented by appropriate boundary and initial conditions that will be specified in Section 6.3.

In the infinitesimal deformation range, corresponding to the assumptions that $\|\mathbf{u}\| \ll 1$ and $\|\partial \mathbf{u}/\partial \mathbf{x}\| \ll 1$, the model provided by Biot's theory of linear poroelasticity [16] is used

$$-\nabla \cdot \boldsymbol{\sigma}' + (\nabla p + \rho \mathbf{g}) = \mathbf{0} \text{ on } \Omega_t \times I; \tag{6.6a}$$

$$\nabla \cdot \frac{\partial \mathbf{u}}{\partial t} + \nabla \cdot \mathbf{v}_f = 0 \text{ on } \Omega_t \times I. \tag{6.6b}$$

In the finite deformation range, the deformations are not very small and cannot be neglected. Hence, the poroelastic equations with single-phase flow are expressed as

$$-\nabla \cdot \boldsymbol{\sigma}' + (\nabla p + \rho \mathbf{g}) = \mathbf{0} \text{ on } \Omega_t \times I; \tag{6.7a}$$

$$\nabla \cdot \frac{\partial \mathbf{u}}{\partial t} + \nabla \cdot (\nabla \mathbf{u}\ \mathbf{v}_s) + \nabla \cdot \mathbf{v}_f = 0 \text{ on } \Omega_t \times I. \tag{6.7b}$$

Furthermore, for the solid skeleton, we consider linear and nonlinear constitutive laws for the relationship between strain and displacement. Assuming that the solid deforms elastically, these relationships are quasi-static and reversible. Hencky elasticity is a nonlinear hyperelastic model that is based on a logarithmic strain measure and provides good agreement for the elastic behaviour of a wide variety of materials under moderate to large deformations [4, 58]. The Hencky strain tensor can be written as [84]

$$\boldsymbol{\varepsilon}_N = \frac{1}{2}\ln(\mathbf{F}\mathbf{F}^T), \tag{6.8}$$

where $\mathbf{F} = (\mathbf{I} - \nabla \mathbf{u})^{-1}$ is the deformation gradient tensor, with $\mathbf{I}$ denoting the identity tensor. The natural logarithm $\ln(\cdot)$ is computed in each element of the tensor $\mathbf{F}\mathbf{F}^T$. On the other hand, assuming that the porous material is linearly elastic, the linear strain tensor can be defined by

$$\boldsymbol{\varepsilon}_L = \frac{1}{2}(\nabla \mathbf{u} + \nabla \mathbf{u}^T). \tag{6.9}$$

Considering Hencky elasticity law (6.8) combined with nonlinear poroelasticity (6.7) is the most appropriate model for moderate to large deformations. However, this model is computationally expensive. According to Auton and MacMinn [5], using nonlinear poroelasticity (6.7) combined with linear elasticity (6.9) offers a good compromise between accuracy, robustness and computational efficiency, demonstrating the same qualitative behaviour as the fully nonlinear model. Hence, in this chapter, we adopt linear elasticity (6.9) for all models: $\boldsymbol{\varepsilon} = \boldsymbol{\varepsilon}_L$.

In addition, we assume that the solid and fluid phases are individually incompressible, such that deformation occurs only through rearrangement of the solid skeleton with corresponding changes in the local porosity. This is then likely to alter the permeability of the material. The deformation-dependent permeability can be determined using the Kozeny-Carman equation [136]

$$\kappa(\mathbf{x}, t) = \frac{d_s^2}{180} \frac{\theta(\mathbf{x}, t)^3}{(1 - \theta(\mathbf{x}, t))^2}, \tag{6.10}$$

where $d_s$ is the mean grain size of the soil and the porosity $\theta$ is computed from the displacement vector using the porosity-dilatation relation (see [103, 130])

$$\theta(\mathbf{x}, t) = 1 - \frac{1 - \theta_0}{\exp(\nabla \cdot \mathbf{u})}, \tag{6.11}$$

with $\theta_0$ the initial uniform porosity. In this study, the term porosity refers to the entire connected porosity.

Since in linear poroelasticity it is assumed that the deformations are infinitesimal, this model is in the literature often combined with constant permeability. In this study, we consider three models: linear poroelasticity, where Eqs. (6.6) are used, combined with constant permeability $\kappa(\mathbf{x}, t) = \kappa(\mathbf{x}, 0)$ which we abbreviate as $(L_C)$, linear poroelasticity combined with the Kozeny-Carman equation $(L_{KC})$ and nonlinear poroelasticity, where Eqs. (6.7) are used, combined with the Kozeny-Carman equation $(N_{KC})$.

## 6.3 Numerical experiment

This section presents a numerical example that verifies the proposed finite element formulation and highlights the differences between the infinitesimal deformation and the finite deformation regimes in a poromechanical problem. In this example, we consider the effect of applied mechanical oscillations with small and large amplitudes.

In this problem, a poroelastic medium is instantaneously subjected to uniform boundary pressure on the left boundary. As soon as the boundary pressure is applied, excess pore pressure develops inside the domain, and so, the pore fluid starts

to drain through the right boundary. The boundary pressure is maintained constant throughout. Figure 6.1 illustrates the set-up of the problem. We consider a rectangular domain with initial width $L$ and initial height $H$. At the top of the domain, an oscillating mechanical deformation is applied. No-flow conditions are imposed on the top and bottom boundaries. The material is assumed to be fully saturated and free of gravitational forces throughout.

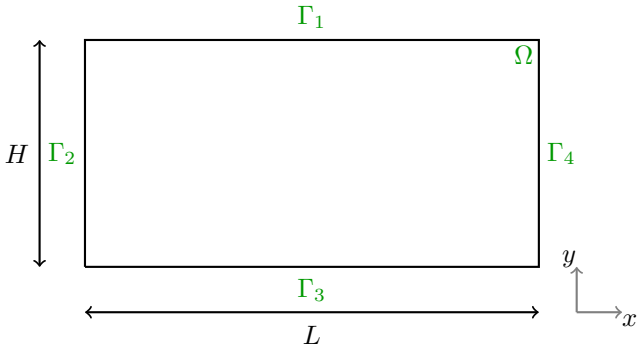


Figure 6.1: *Sketch of the set-up for the two-dimensional problem.*

The boundary conditions for this problem are as follows:

$$\frac{\kappa}{\eta}\nabla p \cdot \mathbf{n} = 0 \quad \text{on} \quad \mathbf{x} \in \Gamma_1 \cup \Gamma_3; \tag{6.12a}$$

$$p = p_{pump} \quad \text{on} \quad \mathbf{x} \in \Gamma_2; \tag{6.12b}$$

$$p = 0 \quad \text{on} \quad \mathbf{x} \in \Gamma_4; \tag{6.12c}$$

$$\mathbf{u} = (0, u_{vib})^T \quad \text{on} \quad \mathbf{x} \in \Gamma_1; \tag{6.12d}$$

$$\boldsymbol{\sigma}'\mathbf{n} = \mathbf{0} \quad \text{on} \quad \mathbf{x} \in \Gamma_2 \cup \Gamma_4; \tag{6.12e}$$

$$\mathbf{u} \cdot \mathbf{n} = 0 \quad \text{on} \quad \mathbf{x} \in \Gamma_3; \tag{6.12f}$$

$$(\boldsymbol{\sigma}'\mathbf{n}) \cdot \mathbf{t} = 0 \quad \text{on} \quad \mathbf{x} \in \Gamma_3, \tag{6.12g}$$

where $\mathbf{t}$ is the unit tangent vector at the boundary, $\mathbf{n}$ the outward unit normal vector and $p_{pump}$ is a prescribed pump pressure. Figure 6.1 shows the definition of the boundary segments. Initially, the following condition is fulfilled:

$$\mathbf{u}(\mathbf{x}, 0) = \mathbf{0} \quad \text{for} \quad \mathbf{x} \in \Omega_0. \tag{6.13}$$

For the boundary displacement $u_{vib}$, a standing wave is considered, represented by

$$u_{vib}(x,t) = -\gamma \cos\left(\frac{\pi}{2L}(x - L)\right) \cos\left(\frac{\pi}{2\Delta t}(t - \Delta t)\right), \tag{6.14}$$

with $\gamma$ the amplitude of the oscillation and $\Delta t$ the time increment.

## 6.4 Numerical procedure

In this section, we outline the numerical procedures used to discretise the poroelastic models presented in Section 6.2 and to solve the resulting coupled fluid/solid finite-

dimensional problem. The weak form of the governing equations will be derived and discretised using a continuous Galerkin finite element approach with displacements and fluid pressures as primary variables. The suitability of the proposed methodology to model flow through elastic, saturated porous media under finite deformations will be demonstrated using the illustrative numerical example described in the previous section.

### 6.4.1 Weak formulation

We present a finite element framework for Eqs. (6.6) and (6.7), using the continuously deforming domain $\Omega_t$ with initially $\Omega_t = \Omega_0$. Firstly, we introduce the appropriate function spaces. Let $L^2(\Omega_t)$ be the Hilbert space of square integrable scalar-valued functions on $\Omega_t$ defined as $L^2(\Omega_t) = \{f : \Omega_t \to \mathbb{R} : \int_{\Omega_t} |f|^2 \, d\Omega_t < \infty\}$, with inner product $(f, g) = \int_{\Omega_t} fg \, d\Omega_t$. Let $H^1(\Omega_t)$ denote the subspace of $L^2(\Omega_t)$ of functions with first derivatives in $L^2(\Omega_t)$. Subsequently, we define the function spaces $\mathscr{Q} = \{q \in H^1(\Omega_t) : q|_{\Gamma_2} = p_{pump} \text{ and } q|_{\Gamma_4} = 0\}$ and $\mathscr{W} = \{\mathbf{w} \in (H^1(\Omega_t))^2 : \mathbf{w}|_{\Gamma_1} = (0, u_{vib})^T \text{ and } (\mathbf{w} \cdot \mathbf{n})|_{\Gamma_3} = 0\}$. Furthermore, we consider the bilinear forms [102]

$$
\begin{aligned}
a(\mathbf{u}, \mathbf{w}) &= \lambda(\nabla \cdot \mathbf{u}, \nabla \cdot \mathbf{w}) + 2\mu \sum_{i,j=1}^{2} (\epsilon_{ij}(\mathbf{u}), \epsilon_{ij}(\mathbf{w})); \\
b(p, \mathbf{w}) &= (p, \nabla \cdot \mathbf{w}); \\
c(p, q) &= \sum_{i=1}^{2} (\frac{\kappa}{\eta} \frac{\partial p}{\partial x_i}, \frac{\partial q}{\partial x_i}).
\end{aligned}
$$

Using the notation $\dot{\mathbf{u}} = \partial \mathbf{u}/\partial t$, the variational formulation for Eqs. (6.6) with boundary and initial conditions (6.12)-(6.13) consists of the following:

Find $(\mathbf{u}(\mathbf{x}, t), p(\mathbf{x}, t)) \in (\mathscr{W} \times \mathscr{Q})$ such that

$$
\begin{aligned}
a(\mathbf{u}, \mathbf{w}) - b(p, \mathbf{w}) &= h(\mathbf{w}) \qquad \forall \mathbf{w} \in \mathscr{W}_0; & \text{(6.15a)} \\
b(q, \dot{\mathbf{u}}) + c(p, q) &= 0 \qquad \forall q \in \mathscr{Q}_0, & \text{(6.15b)}
\end{aligned}
$$

with the initial condition $\mathbf{u}(0) = \mathbf{0}$, and where

$$
\begin{aligned}
h(\mathbf{w}) &= -p_{pump} \int_{\Gamma_2} \mathbf{w} \cdot \mathbf{n} \, d\Gamma; \\
\mathscr{W}_0(\Omega_0) &= \{\mathbf{w} \in (H^1(\Omega_0))^2 : \mathbf{w}|_{\Gamma_1} = \mathbf{0} \text{ and } (\mathbf{w} \cdot \mathbf{n})|_{\Gamma_3} = 0\}; \\
\mathscr{Q}_0(\Omega_0) &= \{q \in H^1(\Omega_0) : q|_{\Gamma_2 \cup \Gamma_4} = 0\}.
\end{aligned}
$$

In this work, we use the implicit Euler method for the discretisation in time, which is unconditionally stable and commonly used in the computational poromechanics literature. Let us denote by $\Delta t = t_m - t_{m-1}$ the time increment from time $t_{m-1}$ to $t_m$ and add the superscripts $(\cdot)^{m-1}$ and $(\cdot)^m$ to denote respective values at these time instances. After applying this method we get:

For $m \geq 1$, find $(\mathbf{u}^m(\mathbf{x}), p^m(\mathbf{x})) \in (\mathscr{W} \times \mathscr{Q})$ such that

$$
\begin{aligned}
a(\mathbf{u}^m, \mathbf{w}) - b(p^m, \mathbf{w}) &= h(\mathbf{w}) \qquad \forall \mathbf{w} \in \mathscr{W}_0; & \text{(6.16)} \\
b(q, \mathbf{u}^m) + \Delta t \; c(p^m, q) &= b(q, \mathbf{u}^{m-1}) \quad \forall q \in \mathscr{Q}_0, & \text{(6.17)}
\end{aligned}
$$

while for $m = 0$: $\mathbf{u}^0 = \mathbf{0}$. At each time step, we solve the equations as a fully coupled system.

Now we derive the variational formulation for Eq. (6.7b), first we multiply this equation by a basis function $q \in \mathscr{Q}_0$, and integrate the result over $\Omega_t$, to get

$$\int_{\Omega_t} \left[ \nabla \cdot \frac{\partial \mathbf{u}}{\partial t} + \nabla \cdot (\nabla \mathbf{u}\ \mathbf{v}_s) + \nabla \cdot \mathbf{v}_f \right] q \ d\Omega_t = 0. \tag{6.18}$$

First, we introduce $\mathbf{J} = [\nabla \mathbf{u} - (\nabla \cdot \mathbf{u})\mathbf{I}]\mathbf{v}_s + \mathbf{v}_f$, then using Clairaut's theorem on equality of mixed partials for $C^2$-functions over time and position, we obtain

$$\int_{\Omega_t} \left[ \frac{\partial}{\partial t}(\nabla \cdot \mathbf{u}) + \nabla \cdot (\mathbf{v}_s \nabla \cdot \mathbf{u}) + \nabla \cdot \mathbf{J} \right] q \ d\Omega_t = 0. \tag{6.19}$$

The definition of the material derivative (6.4) gives

$$\int_{\Omega_t} \left[ \frac{D}{Dt}(\nabla \cdot \mathbf{u}) + (\nabla \cdot \mathbf{v}_s)(\nabla \cdot \mathbf{u}) + \nabla \cdot \mathbf{J} \right] q \ d\Omega_t = 0. \tag{6.20}$$

According to Dziuk and Elliott [47], it holds that $\frac{Dq}{Dt} = 0$ for the Lagrangian basis functions that we will use in this study. Hence, we get using the definition of the material derivative (6.4)

$$\int_{\Omega_t} \left[ \frac{\partial}{\partial t}[(\nabla \cdot \mathbf{u})q] + \mathbf{v}_s \cdot \nabla[(\nabla \cdot \mathbf{u})q] + (\nabla \cdot \mathbf{v}_s)(\nabla \cdot \mathbf{u})q + (\nabla \cdot \mathbf{J})q \right] d\Omega_t = 0. \tag{6.21}$$



The divergence theorem gives

$$\int_{\Omega_t} \nabla \cdot [\mathbf{v}_s(\nabla \cdot \mathbf{u})q] d\Omega_t = \int_{\partial\Omega_t} \mathbf{v}_s(\nabla \cdot \mathbf{u})q \cdot \mathbf{n} \ d\Gamma_t. \tag{6.22}$$

Furthermore, from Reynolds' theorem, it follows

$$\int_{\Omega_t} \frac{\partial}{\partial t}[(\nabla \cdot \mathbf{u})q] \ d\Omega_t = \frac{d}{dt} \int_{\Omega_t} (\nabla \cdot \mathbf{u})q \ d\Omega_t - \int_{\partial\Omega_t} (\nabla \cdot \mathbf{u})q \ \mathbf{v}_s \cdot \mathbf{n} \ d\Gamma_t. \tag{6.23}$$

This results into

$$\frac{d}{dt} \int_{\Omega_t} (\nabla \cdot \mathbf{u})q \ d\Omega_t + \int_{\Omega_t} (\nabla \cdot \mathbf{J})q \ d\Omega_t = 0. \tag{6.24}$$

Applying the divergence theorem again yields

$$\frac{d}{dt} \int_{\Omega_t} (\nabla \cdot \mathbf{u})q \ d\Omega_t - \int_{\Omega_t} \mathbf{J} \cdot \nabla q \ d\Omega_t + \int_{\partial\Omega_t} \mathbf{J}q \cdot \mathbf{n} \ d\Gamma_t = 0. \tag{6.25}$$

From boundary conditions (6.12) it follows, using the definition of $\mathbf{J}$, that

$$\frac{d}{dt} \int_{\Omega_t} (\nabla \cdot \mathbf{u})q \ d\Omega_t + \int_{\Omega_t} [(\nabla \cdot \mathbf{u})\mathbf{I} - \nabla \mathbf{u}]\mathbf{v}_s \cdot \nabla q \ d\Omega_t - \int_{\Omega_t} \mathbf{v}_f \cdot \nabla q \ d\Omega_t = 0. \tag{6.26}$$

After applying the implicit Euler method for the temporal discretisation of $\mathbf{v}_s$

$$\mathbf{v}_s^m = \frac{\partial \mathbf{u}^m}{\partial t} \approx \frac{\mathbf{u}^m - \mathbf{u}^{m-1}}{\Delta t}, \tag{6.27}$$

it follows that

$$\int_{\Omega_t} (\nabla \cdot \mathbf{u}^m) q^m \, d\Omega_t - \int_{\Omega_t} [(\nabla \cdot \mathbf{u}^m)\mathbf{I} - \nabla \mathbf{u}^m](\mathbf{u}^m - \mathbf{u}^{m-1}) \cdot \nabla q^m \, d\Omega_t - \tag{6.28}$$
$$- \Delta t \int_{\Omega_t} \mathbf{v}_f^m \cdot \nabla q^m \, d\Omega_t = \int_{\Omega_{t-\Delta t}} (\nabla \cdot \mathbf{u}^{m-1}) q^{m-1} \, d\Omega_t.$$

We thus obtain, for each time step, a nonlinear system to be solved using an iterative scheme. Nonlinear algebraic system (6.28) can be solved by Picard's iterative procedure, where the subscripts $(\cdot)_{k-1}$ and $(\cdot)_k$ denote the values of the previous and the current iterations respectively. In addition, we choose the initial guess $\mathbf{u}_0^m = \mathbf{u}^{m-1}$ and the stopping criterion $\frac{\|\mathbf{u}_k - \mathbf{u}_{k-1}\|}{\|\mathbf{u}_k\|} + \frac{\|p_k - p_{k-1}\|}{\|p_k\|} \leq 10^{-5}$, to get

$$\int_{\Omega_t} (\nabla \cdot \mathbf{u}_k^m) q_{k-1}^m \, d\Omega_t - \int_{\Omega_t} [(\nabla \cdot \mathbf{u}_k^m)\mathbf{I} - \nabla \mathbf{u}_k^m](\mathbf{u}_{k-1}^m - \mathbf{u}^{m-1}) \cdot \nabla q_{k-1}^m \, d\Omega_t - \tag{6.29}$$
$$- \Delta t \int_{\Omega_t} \mathbf{v}_{f,k}^m \cdot \nabla q_{k-1}^m \, d\Omega_t = \int_{\Omega_{t-\Delta t}} (\nabla \cdot \mathbf{u}^{m-1}) q^{m-1} \, d\Omega_t.$$

Picard's iterative scheme is also applied for solving the models that use the Kozeny-Carman equation. Thus, after having obtained the numerical approximation for the displacement in the previous iteration $\mathbf{u}_{k-1}$, we update the porosity using Eq. (6.11). Subsequently, the Kozeny-Carman relation (6.10) is used to calculate the permeability in the current iteration $k$.

### 6.4.2 Finite element formulation

Equations (6.15) and Eqs. (6.15a) and (6.29) are solved by applying the finite element method, with triangular Taylor-Hood elements [28]. Regarding spatial discretisation, the displacement field is approximated using finite elements with quadratic basis functions, whereas continuous piecewise linear approximation is used for the pressure field. Time discretisation of the above dynamical equations is performed by using the implicit Euler method.

Let $\mathscr{P}_h^l \subset H^1(\Omega_t)$ be a function space of piecewise polynomials on $\Omega_t$ of degree $l$. Hence, we define finite element approximations for $\mathscr{W}$ and $\mathscr{Q}$ as $\mathscr{W}_h^l = \mathscr{W} \cap (\mathscr{P}_h^l \times \mathscr{P}_h^l)$ with basis $\{\boldsymbol{\phi}_i = (\phi_i, \phi_i) \in (\mathscr{W}_h^l \times \mathscr{W}_h^l) : i = 1, \ldots, n_u\}$ and $\mathscr{Q}_h^{l'} = \mathscr{Q} \cap \mathscr{P}_h^{l'}$ with basis $\{\psi_j \in \mathscr{Q}_h^{l'} : j = 1, \ldots, n_p\}$, respectively. Subsequently, we introduce a spatial approximation for the functions $\mathbf{u}(\mathbf{x}, t)$ and $p(\mathbf{x}, t)$, writing this in the form

$$\mathbf{u}_h(\mathbf{x}, t) = \sum_{i=1}^{n_u} \mathbf{u}_i(t) \boldsymbol{\phi}_i(\mathbf{x}), \quad p_h(\mathbf{x}, t) = \sum_{j=1}^{n_p} p_j(t) \psi_j(\mathbf{x}), \tag{6.30}$$

in which the Dirichlet boundary conditions are imposed. When a continuously deforming grid is used, each trial function is time-dependent due to the motion of the grid. Hence, the finite-element trial solution is of the form

$$\mathbf{u}_h(\mathbf{x}, t) = \sum_{i=1}^{n_u} \mathbf{u}_i(t) \boldsymbol{\phi}_i(\mathbf{x}(t), t), \quad p_h(\mathbf{x}, t) = \sum_{j=1}^{n_p} p_j(t) \psi_j(\mathbf{x}(t), t). \tag{6.31}$$

For the mesh points, it holds $\mathbf{x}(t) = \mathbf{x}_0 + \mathbf{u}(t)$, where $\mathbf{x}_0$ are the coordinates of the reference domain $\Omega_0$.

## 6.5 Numerical results

The Galerkin finite element method with triangular Taylor-Hood elements is employed for the solution of the discretised quasi-two-dimensional problems (6.6) and (6.7). The numerical investigations are carried out using the matrix-based software package MATLAB (version R2017a). The computational domain is a rectangular surface with initial width $L = 1.0\,\mathrm{m}$ and initial height $H = 1.0\,\mathrm{m}$. The domain is discretised using a regular triangular grid, with $\Delta x = \Delta y = 1/200$. Mesh refinement did not yield any significant changes of the numerical solution. In addition, the hydraulic and mechanical properties used in the simulation can be found in Table 6.1. The solid material properties are characteristic of an unconsolidated, sandy formation.

Table 6.1: *An overview of the values of physical properties used in the simulation.*

| Property | Symbol | Value | Unit |
|---|---|---|---|
| Elasticity modulus | $E$ | $35 \cdot 10^6$ | Pa |
| Poisson's ratio | $\nu$ | 0.3 | - |
| Mean grain size | $d_s$ | $0.2 \cdot 10^{-3}$ | m |
| Initial porosity | $\theta_0$ | 0.4 | - |
| Fluid viscosity | $\eta$ | $1.307 \cdot 10^{-3}$ | Pa · s |
| Pump pressure | $p_{pump}$ | $5 \cdot 10^5$ | Pa |



Furthermore, the Lamé constants $\lambda$ and $\mu$ in Eq. (6.2) are related to elasticity modulus $E$ and Poisson's ratio $\nu$ by:

$$\lambda = \frac{\nu E}{(1+\nu)(1-2\nu)}, \mu = \frac{E}{2(1+\nu)}. \tag{6.32}$$

The suitability of the proposed methodology to model flow through elastic porous media under infinitesimal and finite deformations is investigated in this study by means of the $L^2$-norm of the computed displacements $\|\mathbf{u}\|$ and pressure field $\|p\|$. Subsequently, to compare the results from the different models, we compute the percentage change as follows:

$$\|\mathbf{u}\|_{\%,AB} = \frac{\|\mathbf{u}_A\| - \|\mathbf{u}_B\|}{\|\mathbf{u}_B\|} \cdot 100, \tag{6.33}$$

where $A$ and $B$ are two different models from the three models considered in this study: $L_C$, $L_{KC}$ and $N_{KC}$. In the generations of the simulation results, the time increment is chosen to be $\Delta t = 0.1$.

In order to obtain some insight into the impact of the applied mechanical oscillations on the solid displacements and the fluid pressure, we present an overview of the simulation results in Figures 6.2 and 6.3. In these simulations, water is injected into the soil at a constant pump pressure of 5 bar. We start with the simulation results for the nonlinear model ($N_{KC}$) without any oscillations applied, i.e. $\gamma = 0$. The simulated pressure and displacement profiles are provided in Figures 6.2a and 6.2b. Mechanically, the deformations in the porous medium are negligible, other than a small shift of the grains to the right, as a result of the force exerted on the grains by the injected water. As shown in Figure 6.2b, the simulated pressure is almost linear.

This means that the injected water flows in a horizontal direction through the domain from the left to the right boundary. In Figures 6.2c and 6.2d, the numerical solutions at $t = 0.9$ are shown for the nonlinear model using applied oscillations with $\gamma = 0.1$.

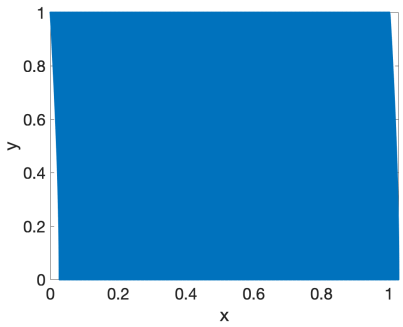


(a) Positions of the mesh points after subjecting them to the calculated displacement vector $\mathbf{u}$, $\gamma = 0$.

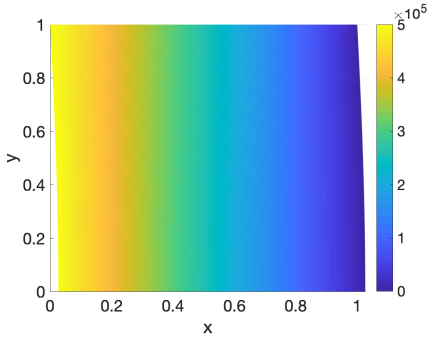


(b) Numerical solution for the pressure, $\gamma = 0$.

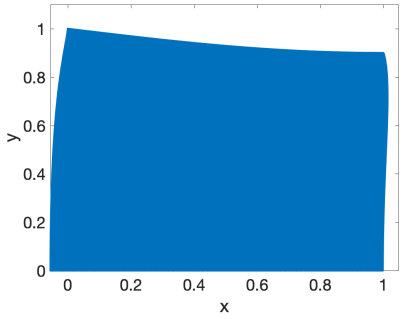


(c) Positions of the mesh points after subjecting them to the calculated displacement vector $\mathbf{u}$, $\gamma = 0.1$.

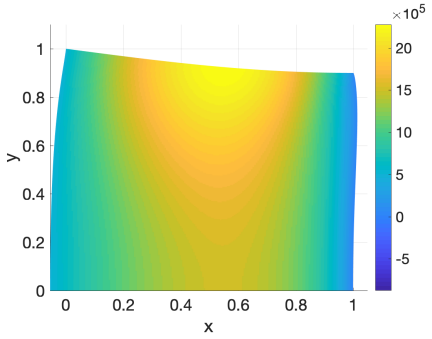


(d) Numerical solution for the pressure, $\gamma = 0.1$.

Figure 6.2: *Numerical solutions for the pressure and the displacement at time* $t = 0.9$.

Figures 6.2c and 6.2d show the impact of the applied oscillations, imposed on the top of the domain, on the water flow. In contrast to the pressure shown in Figure 6.2b, the numerical solution for the pressure in the problem with oscillations is no longer linear, but shows an oscillatory behaviour, as depicted in Figure 6.2d. In this figure, we can see that the fluid pressure increases when the grains are pressed together by the applied oscillation. The norm of the simulated displacement and pressure profiles that have been obtained using an applied oscillation with $\gamma = 0$ (no oscillation) are depicted in Figures 6.3a and 6.3b, while the simulated results that have been obtained using an applied oscillation with $\gamma = 0.1$ are provided in Figures 6.3c and 6.3d.

In Figures 6.3a and 6.3b, the behaviours of the displacement and pressure fields as function of the time, without applied oscillations, are shown. The difference between the linear models $L_C$ and $L_{KC}$ is negligibly small in the displacement field, while this difference is more visible in the pressure field for small times. This is a consequence

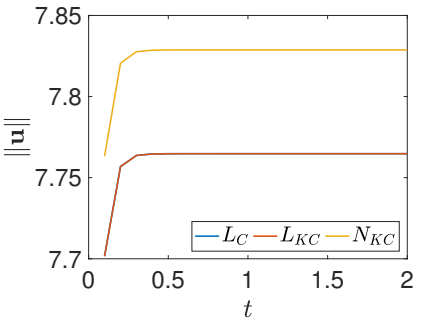


(a) The norm of the displacement, $\gamma = 0$.

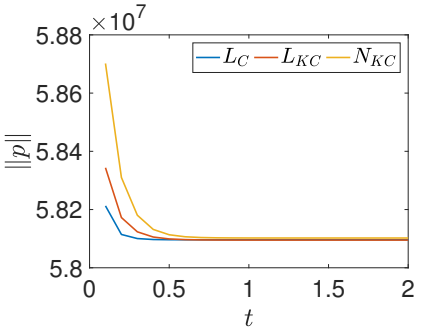


(b) The norm of the pressure, $\gamma = 0$.

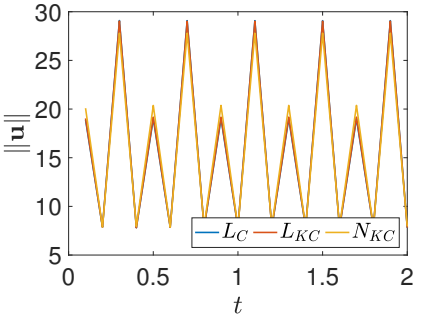


(c) The norm of the displacement, $\gamma = 0.1$.

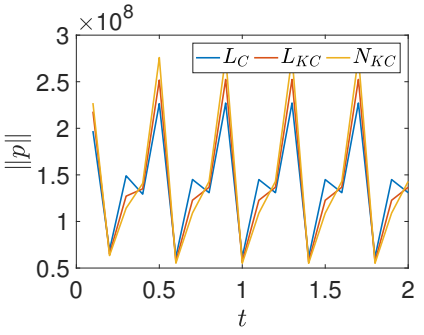


(d) The norm of the pressure, $\gamma = 0.1$.

Figure 6.3: *The norm of the simulated displacement* $\|\mathbf{u}\|$ *and pressure profiles* $\|p\|$ *as function of the time* $t$.

of the different permeability relationships that are used in these models and that have more effect on the pressure field than on the solid deformations. Over time, the difference between the three models becomes smaller in the pressure field. However, the value of the norm of the displacement as a result of the nonlinear model is larger than the norm of the displacements in the linear models. Hence, for larger times, the nonlinearity has more effect on the displacement than on the pressure field. This is also expected from Eqs. (6.6) and (6.7). The impact of the applied mechanical oscillation is shown in Figures 6.3c and 6.3d, where we notice an oscillatory behaviour in the displacement and pressure profiles. In these figures, we notice more similarity in the results of the three models for the displacement than for the fluid pressure. Furthermore, it is clear that the applied oscillation, which has an amplitude equal to 10% of the height of the domain, has a larger impact on the results than the adopted mathematical models.

The percentage change (6.33) in the norms of the simulated displacement $\|\mathbf{u}\|_{\%}$ and pressure $\|p\|_{\%}$ is depicted in Figures 6.4 and 6.5, for different values of the amplitude of the applied oscillations.

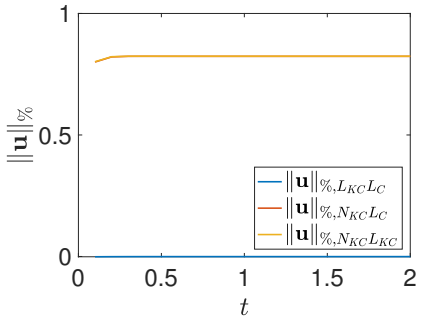


(a) The percentage change in the norm of the displacement, $\gamma = 0$.

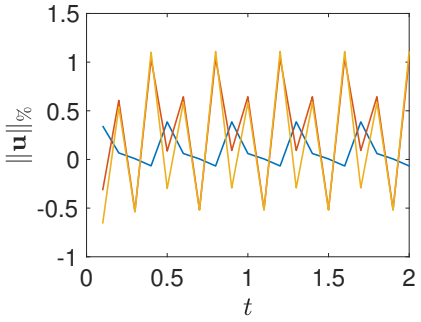


(b) The percentage change in the norm of the displacement, $\gamma = 0.04$.

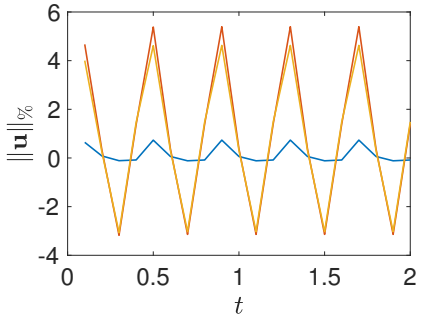


(c) The percentage change in the norm of the displacement, $\gamma = 0.08$.

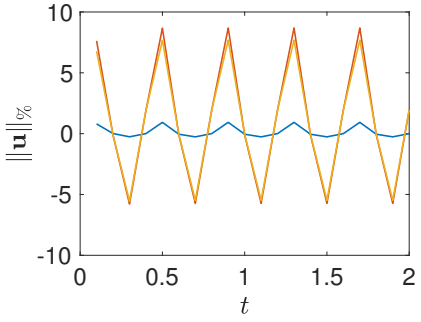


(d) The percentage change in the norm of the displacement, $\gamma = 0.12$.

Figure 6.4: *The percentage change in the norm of the simulated displacement* $\|\mathbf{u}\|_{\%}$ *as function of the time* $t$.

When comparing the linear models in Figures 6.4 and 6.5, we notice that the impact of the Kozeny-Carman relation on the displacement is small, whereas this impact on the fluid pressure field becomes larger with increasing amplitude of the applied oscillation. The reason for this behaviour is that the permeability relationship is directly related to the pressure through Eq. (6.3). Moreover, the influence of the deformations on the porosity (see Eq. (6.11)), and thus on the Kozeny-Carman permeability, is greater for larger deformations. In addition, the comparison between the linear and the nonlinear models both combined with Kozeny-Carman equation leads to the conclusion that the nonlinearity has a larger impact on the displacement field more than the permeability relationship. In contrast, the pressure field is more influenced by the permeability relation that is used than the nonlinearity in the models. In the extrema, the percentage change between the nonlinear model and the linear model with constant permeability is as large as the percentage change between the linear models and the percentage change between the nonlinear model and the linear model combined with the Kozeny-Carman relation.

Picard's iterative scheme is used to solve the nonlinear poroelasticity model ($N_{KC}$). For the previous values of the amplitude of the applied oscillations, the number of

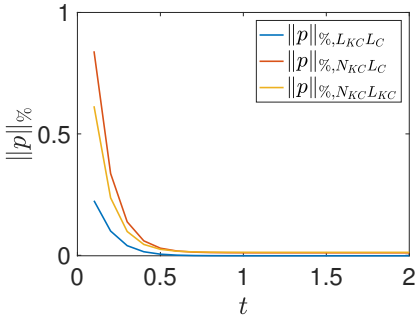


(a) The percentage change in the norm of the pressure, $\gamma = 0$.

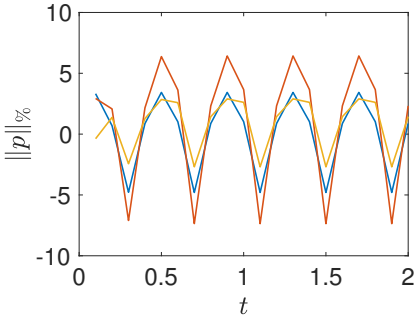


(b) The percentage change in the norm of the pressure, $\gamma = 0.04$.

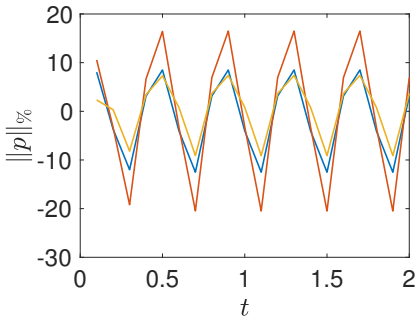


(c) The percentage change in the norm of the pressure, $\gamma = 0.08$.

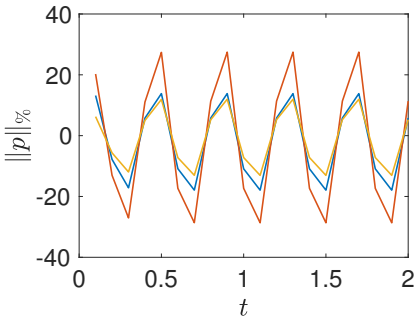


(d) The percentage change in the norm of the pressure, $\gamma = 0.12$.

Figure 6.5: *The percentage change in the norm of the simulated pressure* $\|p\|_{\%}$ *as function of the time* $t$.

iterations per time step as function of the time $t$ is depicted in Figure 6.6. It can be seen from Figure 6.6 that the number of Picard iterations stabilises with time and depends mildly on the magnitude of $\gamma$.

The aim of this study was to quantify the amplitudes for which the linear poroelasticity model is accurate enough and demonstrates the same qualitative behaviour as the nonlinear poroelasticity model. As expected, for small applied mechanical oscillations, the difference between the linear and the nonlinear models is small both in the displacement as in the pressure fields. In Table 6.2, the upper limits of the absolute values of the percentage change for the different models are depicted.

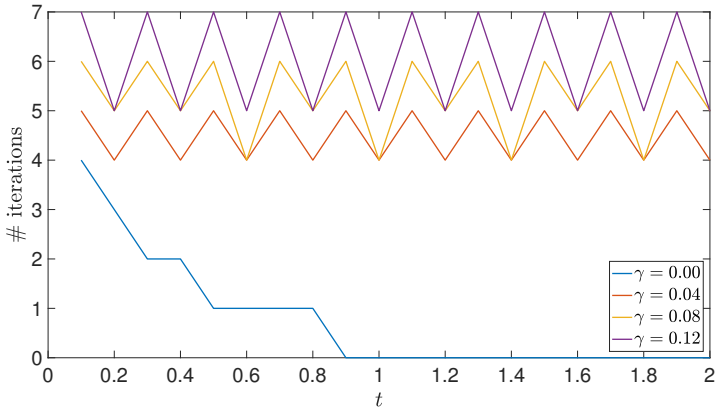


Figure 6.6: *The number of iterations per time step as function of the time $t$, for different values of the amplitude $\gamma$.*

Table 6.2: *The upper limits of the absolute values of the percentage change.*

| $\gamma$ [m] | $\|\mathbf{u}\|_{\%,N_{KC}L_{KC}}$ | $\|\mathbf{u}\|_{\%,N_{KC}L_{C}}$ | $\|p\|_{\%,N_{KC}L_{KC}}$ | $\|p\|_{\%,N_{KC}L_{C}}$ |
|---|---|---|---|---|
| 0.00 | 0.8242 | 0.8236 | 0.6140 | 0.8402 |
| 0.01 | 0.8889 | 0.9045 | 0.3345 | 0.7937 |
| 0.02 | 1.2588 | 1.2373 | 1.0128 | 2.2942 |
| 0.03 | 1.6468 | 1.4731 | 1.8968 | 4.2280 |
| 0.04 | 1.1095 | 1.0415 | 2.8980 | 7.3587 |
| 0.05 | 1.1938 | 1.6926 | 4.7570 | 11.6912 |
| 0.06 | 2.5034 | 3.1282 | 6.4628 | 15.1482 |
| 0.07 | 3.6431 | 4.3453 | 7.8815 | 18.0029 |
| 0.08 | 4.6264 | 5.3951 | 9.1113 | 20.4882 |
| 0.09 | 5.4970 | 6.3267 | 10.2152 | 22.7376 |
| 0.10 | 6.2852 | 7.1733 | 11.2296 | 24.8238 |
| 0.11 | 7.0107 | 7.9559 | 12.1755 | 26.7877 |
| 0.12 | 7.6857 | 8.6876 | 13.0655 | 28.6535 |

For instance, given an applied oscillation with an amplitude $\gamma = 0.08$ (8% of the height of the domain), an accuracy of 10% can be obtained in both the displacement and the pressure fields using the linear poroelasticity model combined with Kozeny-Carman equation. However, this accuracy can only be obtained using the linear model combined with constant permeability for applied oscillations with an amplitude of 0.04 or smaller. For applied mechanical oscillations with amplitudes larger than $\gamma = 0.12$, the nonlinear poroelasticity model becomes unstable resulting in negative porosities. Hence, we will not consider these oscillations in this chapter.

## 6.6 Discussion and conclusions

In this work, we have developed a mathematical model for fluid injection into a monolayer of soil particles subjected to surface mechanical oscillations, based on the two-field model (solid displacement and fluid pressure). This two-field mixed formulation is employed to calculate the solid displacement and the fluid pressure directly, in a monolithic system. In addition, we have included dynamic effects, such as a time- and space-dependent porosity and permeability. Firstly, we have summarised the governing equations both in the theory of linear poroelasticity as in the large-deformation poroelasticity. Subsequently, we have presented a finite element solver for the linear and nonlinear poroelasticity models, combined with constant and deformation-dependent permeability. This solver is developed on a triangular mesh and relies on quadratic basis functions for the discretisation of the displacement in elasticity and the continuous piecewise linear approximation for discretisation of pressure in Darcy's flow. These spatial discretisations are combined with the backward Euler temporal discretisation of the fluid-mass balance equation. For the nonlinear poroelasticity equation, a weak formulation based on the motion of the solid was first presented, then linearisation of the resulting nonlinear coupled equation systems has been made using a standard Picard iterative procedure, which is subsequently implemented in a finite element code that is based on Taylor-Hood elements. The suitability of the proposed methodology to model flow through elastic, saturated porous media under finite deformations is demonstrated using an illustrative numerical example. In this example, injection of a fluid into a two-dimensional fully saturated porous medium is considered, assuming that the solid material is subjected to surface mechanical oscillations with different amplitude sizes and that the fluid and solid constituents are individually incompressible.



Linear poroelasticity is a good model for very small deformations, besides that it is a simple model to solve and is computationally cheap. On the other hand, the well-known large-deformation theory is more suitable to solve poroelasticity problems with moderate to large deformations. However, adopting this nonlinear mathematical model increases the computational complexity and cost, especially because the basis functions in the finite element code have to be updated in every iteration within the time integration. For this reason, the two-dimensional numerical example is used in this study to investigate the accuracy of the linear poroelasticity model for applied mechanical oscillations with different sizes. In addition, the impact of introducing a deformation-dependent permeability according to the Kozeny-Carman equation is explored.

The numerical example is solved using mechanical oscillations with amplitudes in the range $[0, 0.12]$ corresponding with $[0, 12]\%$ of the height of the domain. For solving this physical problem, three different mathematical models are considered: linear poroelasticity combined with constant permeability ($L_C$), linear poroelasticity combined with the Kozeny-Carman equation ($L_{KC}$) and nonlinear poroelasticity combined with the Kozeny-Carman equation ($N_{KC}$). Since the nonlinear poroelasticity model was unstable for applied mechanical oscillations with amplitudes larger than 0.12, resulting in negative porosities, we did not do any simulations for larger oscillations. In order to remove the nonphysical behaviour, one could analyse the improvement of the initial condition for the Picard iteration scheme of the displace-

ment by the use of the linear model. As an alternative, one could investigate the performance of different time-integration schemes and time stepping. Another aspect is that, in the current work, we first applied time integration, followed by the finite element discretisation and finally the Picard method was implemented. One could reverse the order between the application of the finite element discretisation and Picard's method and investigate whether this reversal gives any improvement of the results. On the other hand, we could also analyse whether the model would actually predict these negative porosities and look whether the model (in terms of the Kozeny-Carman relation (6.10) and in the wake of Eq. (6.11)) is entirely appropriate for this regime.

Firstly, by considering the numerical example without applied oscillations, we have shown that the nonlinearity has more effect on the displacement than on the pressure field. This is a consequence of the nonlinearity in the displacement that can be seen in Eqs. (6.7). On the contrary, the impact of including a deformation-dependent permeability was larger on the pressure field than on the solid deformations. The reason for this behaviour is that the permeability relationship is directly related to the pressure through Darcy's law (6.3). Secondly, the impact of the applied mechanical oscillation was investigated by applying standing waves on the top surface of the solid matrix. From the numerical results, we noticed that the oscillatory behaviour was visible in the displacement and pressure profiles. Moreover, the differences between the three models $(L_C)$, $(L_{KC})$ and $(N_{KC})$ are small for small applied oscillations, while these differences become larger by an increasing amplitude of the applied oscillation. Hence, the errors in the simulated displacement and pressure as a result of solving the linear poroelasticity model in the finite-deformation range increase when we choose applied oscillations with large amplitudes. The difference between the linear models can be explained by the impact of the large deformations on the porosity, which in turn has a larger impact on the Kozeny-Carman permeability. While this influence is not taken into account in the linear model combined with constant permeability.



In summary, for the studied problem and the set of parameters chosen, the use of the linear poroelasticity model for solving physical problems with finite deformations results in errors in the displacement and pressure fields that are mainly the consequence of the lack of the kinematic nonlinearity. To reduce these errors, especially in the pressure field, the linear poroelasticity model can preferably be combined with a deformation-dependent permeability, such as the Kozeny-Carman relationship.

Chapter 7

# Fluid flow through homogeneous versus heterogeneous layered porous media

*All natural soils are heterogeneous mixtures. To determine the composition of soil, laboratory tests and field experiments are needed. However, since these tests and experiments can only been performed on a limited number of locations in the soil, flow through the voids in a soil is usually modelled assuming a homogeneous soil mixture rather than a heterogeneous mixture. In this chapter, we investigated whether this simplification is justified by exploring the difference between the flow of water in a model with a heterogeneous layered porous medium and a model with a homogeneous porous medium. The study contains simulations with oscillatory force boundary conditions as well as pressure pulses. Furthermore, Monte Carlo simulations are performed to quantify the impact of variation of model parameters on the volumetric flow rate. From the numerical results, we could conclude that water flows twice as fast through heterogeneous layered porous media than through homogeneous porous media.*

## 7.1 Introduction

Soil is a mixture of broken rocks and minerals, living organisms, and decaying organic matter called humus [137]. A homogeneous mixture is a solid, liquid or gaseous mixture that has the same proportions of its components throughout a given sample. In contrast, a heterogeneous mixture is not uniform in composition, but proportions of its components vary throughout the sample [60]. According to this definition, all natural soils are heterogeneous mixtures, because no two nature soil samples will have the exact proportions of its inherent components.

Simulations of groundwater flow in heterogeneous porous aquifers require a detailed knowledge of the spatial distribution of aquifer parameters. In most cases, this information cannot easily be obtained at acceptable expenses. In general, subsurface investigation techniques are applied only at borehole locations, and the parameter values measured have to be regionalised in order to obtain continuous parameter fields. For this reason, aquifers are usually simulated as homogeneous mixtures. Similarly, in all the models that we considered in this dissertation, the porous medium is assumed to be homogeneous. In this chapter, we will investigate whether this simplification is justified by exploring the difference between the flow of water in a model with a heterogeneous layered porous medium and a model with a homogeneous porous medium. This difference will be quantified in this study by the impact of mechanical oscillations and pressure pulses on the water flow through the porous medium. In these investigations, we make use of the results from laboratory tests and field experiments to describe the soil layers. For the homogeneous porous medium, the values of the soil characteristics are obtained by averaging the values of the different layers. Note that the heterogeneous layered model is unrealistic on the assumption that the soil consists of homogeneous horizontal layers, since the heterogeneities may be arranged in an entirely different way.



The rest of this chapter is organised as follows: In Section 7.2 the considered model equations are given, including the employed porosity-permeability relation. The numerical experiments with homogeneous and heterogeneous layered porous media are described in Section 7.3. The simulation results from these models are presented in Section 7.4 and, lastly, some concluding remarks are reported in Section 7.5.

## 7.2 Governing equations

The model provided by Biot's theory of linear poroelasticity with single-phase flow is used to determine the local displacement of the skeleton of a porous medium, as well as the fluid flow through the pores. The initial boundary value problem for the consolidation process of a fluid flow in a deformable porous medium is stated as follows:

$$\text{equilibrium equations:} \quad -\nabla\cdot\boldsymbol{\sigma}' + (\nabla p + \rho g \mathbf{e}_z) = \mathbf{0} \qquad \text{on } \Omega\times I; \tag{7.1a}$$

$$\text{continuity equation:} \quad \frac{\partial}{\partial t}(\nabla\cdot\mathbf{u}) + \nabla\cdot\mathbf{v} = 0 \qquad \text{on } \Omega\times I, \tag{7.1b}$$

where $\boldsymbol{\sigma}'$ and $\mathbf{v}$ are defined by the following equations

$$\text{Biot's constitutive equations:} \quad \boldsymbol{\sigma}' = \lambda(\nabla \cdot \mathbf{u})\mathbf{I} + \mu(\nabla \mathbf{u} + \nabla \mathbf{u}^T); \tag{7.2}$$

$$\text{Darcy's law:} \quad \mathbf{v} = -\frac{\kappa}{\eta}(\nabla p + \rho g \mathbf{e}_z). \tag{7.3}$$

In the above relations, $\boldsymbol{\sigma}'$, $p$, $\rho$, $g$, $\mathbf{u}$, $\mathbf{v}$, $\lambda$ and $\mu$; $\kappa$ and $\eta$ respectively, denote the effective stress tensor for the porous medium, the pore pressure, the fluid density, the gravitational acceleration, the displacement vector of the porous medium, Darcy's velocity, the Lamé coefficients, the permeability of the porous medium, and the fluid viscosity. The permeability can be determined using the Kozeny-Carman equation

$$\kappa(\mathbf{x}, t) = \frac{d_s^2}{\alpha} \frac{\theta(\mathbf{x}, t)^3}{(1 - \theta(\mathbf{x}, t))^2}, \tag{7.4}$$

where $d_s$ is the mean grain size of the soil, $\alpha$ is a parameter related to the shape of the grains and the porosity $\theta$ is computed from the displacement vector using the porosity-dilatation relation

$$\theta(\mathbf{x}, t) = 1 - \frac{1 - \theta_0}{\exp(\nabla \cdot \mathbf{u})}, \tag{7.5}$$

with $\theta_0$ the initial porosity.

## 7.3 Problem formulation

The infiltration of a fluid through a filter into an aquifer is shown in Figure 7.1a. We assume that the flow pattern is axisymmetric, hence we determine the solution for a fixed azimuth. The computational domain $\Omega$ is an L-shaped two-dimensional surface with cylindrical coordinates $\mathbf{r} = (r, z)$, as depicted in Figure 7.1b.



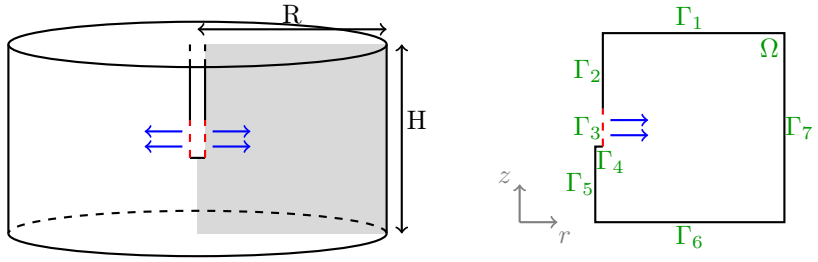


Figure 7.1: *Sketch of the set-up for the aquifer problem: (left) physical problem and (right) numerical discretisation.*

The fluid is injected into the soil through a filter placed on boundary segment $\Gamma_3$. Furthermore, the injection tube (boundary segments $\Gamma_2$, $\Gamma_3$ and $\Gamma_4$) is fitted with a casing (boundary segments $\Gamma_2$ and $\Gamma_4$) and a perforated section (boundary segment $\Gamma_3$) to prevent loose material from entering and potentially clogging the injection

tube. More precisely, the boundary conditions for this problem are given as follows:

$$p = \rho g(H - z) \quad \text{on} \quad \mathbf{r} \in \Gamma_1 \cup \Gamma_6 \cup \Gamma_7; \tag{7.6a}$$

$$\frac{\kappa}{\eta}(\nabla p + \rho g \mathbf{e}_z) \cdot \mathbf{n} = 0 \quad \text{on} \quad \mathbf{r} \in \Gamma_2 \cup \Gamma_4 \cup \Gamma_5; \tag{7.6b}$$

$$p = \rho g(H - z) + p_{pump} \quad \text{on} \quad \mathbf{r} \in \Gamma_3; \tag{7.6c}$$

$$\boldsymbol{\sigma}'\mathbf{n} = \mathbf{0} \quad \text{on} \quad \mathbf{r} \in \Gamma_1 \cup \Gamma_6; \tag{7.6d}$$

$$(\boldsymbol{\sigma}'\mathbf{n}) \cdot \mathbf{t} = 0 \quad \text{on} \quad \mathbf{r} \in \Gamma_2 \cup \Gamma_3 \cup \Gamma_4 \cup \Gamma_5; \tag{7.6e}$$

$$\mathbf{u} \cdot \mathbf{n} \leq 0 \quad \text{on} \quad \mathbf{r} \in \Gamma_2 \cup \Gamma_4; \tag{7.6f}$$

$$\mathbf{u} \cdot \mathbf{n} = u_{vib} \quad \text{on} \quad \mathbf{r} \in \Gamma_3; \tag{7.6g}$$

$$\mathbf{u} \cdot \mathbf{n} = 0 \quad \text{on} \quad \mathbf{r} \in \Gamma_5; \tag{7.6h}$$

$$(\boldsymbol{\sigma}'\mathbf{n}) \cdot \mathbf{n} = 0 \quad \text{on} \quad \mathbf{r} \in \Gamma_7; \tag{7.6i}$$

$$\mathbf{u} \cdot \mathbf{t} = 0 \quad \text{on} \quad \mathbf{r} \in \Gamma_7, \tag{7.6j}$$

where $p_{pump}$ is a prescribed pump pressure used to inject the fluid through a filter with radius $R_f$ and length $L_f$ and $u_{vib}$ is an imposed mechanical oscillation on boundary segment $\Gamma_3$. Initially, the following condition is fulfilled:

$$\mathbf{u}(\mathbf{r}, 0) = 0 \quad \text{for} \quad \mathbf{r} \in \Omega. \tag{7.7}$$

From laboratory tests and field experiments we got a description of the soil layers (see Table 7.1) and the values of the hydraulic conductivity $K$, the initial porosity $\theta_0$ and the main grain size $d_s$ (see Table 7.2). From the hydraulic conductivity we compute the initial permeability using the formula:

$$\kappa_0 = K \frac{\eta}{\rho g}. \tag{7.8}$$



Subsequently, we determine the value of $\alpha$ in the Kozeny-Carman equation for every soil layer by

$$\alpha = \frac{d_s^2}{\kappa_0} \frac{\theta_0^3}{(1 - \theta_0)^2}. \tag{7.9}$$

Table 7.1: *A description of the soil layers from laboratory tests.*

| $z$ [m] | Layer description |
|---|---|
| 24.7 - 25.0 | Sand, moderately fine, moderately silty, weakly gravelly, light grey |
| 24.4 - 24.7 | Sand, moderately fine, weakly silty, weakly gravelly, remnants debris, remains of roots, grey |
| 23.5 - 24.4 | Sand, moderately fine, weakly silty, grey |
| 22.5 - 23.5 | Sand, moderately fine, weakly silty, weakly gravelly, grey |
| 22.0 - 22.5 | Sand, moderately coarse, weakly silty, grey |
| 19.5 - 22.0 | Sand, very coarse, weakly silty, grey |
| 18.5 - 19.5 | Sand, moderately fine, weakly silty, grey |
| 16.5 - 18.5 | Sand, moderately coarse, weakly silty, grey |
| 15.5 - 16.5 | Sand, very coarse, weakly silty, weakly gravelly, grey |
| 15.0 - 15.5 | Sand, extremely coarse, weakly silty, very gravelly, grey |
| 14.5 - 15.0 | Sand, very coarse, weakly silty, chunks of clay, grey |
| 14.0 - 14.5 | Sand, very coarse, weakly silty, very gravelly, brown-grey |
| 13.5 - 14.0 | Sand, very coarse, weakly silty, weakly gravelly, grey |
| 13.0 - 13.5 | Sand, extremely coarse, weakly silty, very gravelly, brown-grey |
| 12.5 - 13.0 | Sand, very coarse, weakly silty, weakly gravelly, grey |
| 12.0 - 12.5 | Sand, extremely coarse, weakly silty, very gravelly, grey |
| 11.5 - 12.0 | Sand, very coarse, weakly silty, weakly gravelly, grey |
| 11.0 - 11.5 | Sand, extremely coarse, weakly silty, moderately gravelly, grey |
| 10.5 - 11.0 | Sand, extremely coarse, weakly silty, moderately gravelly, grey |
| 10.0 - 10.5 | Sand, very coarse, weakly silty, moderately gravelly, grey |
| 9.5 - 10.0 | Sand, extremely coarse, weakly silty, weakly gravelly, grey |
| 8.5 - 9.5 | Sand, moderately coarse, weakly silty, weakly gravelly, grey |
| 7.5 - 8.5 | Sand, very coarse, weakly silty, moderately gravelly, grey |
| 7.0 - 7.5 | Sand, extremely coarse, weakly silty, very gravelly, grey |
| 6.5 - 7.0 | Sand, very coarse, weakly silty, weakly gravelly, brown |
| 5.5 - 6.5 | Sand, extremely coarse, weakly silty, very gravelly, brown |
| 0.0 - 5.5 | Sand, extremely coarse, weakly silty, very gravelly, brown |

Young's modulus $E$ and Poisson's ratio $\nu$, that are used to compute the values of the Lamé coefficients, are derived from the book Foundation analysis and design [27]. In this book, intervals are given for these parameters (see Table 7.3). In addition, the Lamé coefficients $\lambda$ and $\mu$ are related to Young's modulus $E$ and Poisson's ratio $\nu$ by

$$\lambda = \frac{\nu E}{(1+\nu)(1-2\nu)} \quad \text{and} \quad \mu = \frac{E}{2(1+\nu)}. \tag{7.10}$$

Table 7.2: *The values of the hydraulic conductivity $K$, the initial porosity $\theta_0$ and the main grain size $d_s$ from laboratory tests and field experiments.*

| $z$ [m] | $K$ [m/s] | $d_s$ [$\mu$m] | $\theta_0$ |
|---|---|---|---|
| 24.7 - 25.0 | $1.6 \cdot 10^{-4}$ | 295 | 0.390 |
| 24.4 - 24.7 | $1.6 \cdot 10^{-4}$ | 295 | 0.390 |
| 23.5 - 24.4 | $6.5 \cdot 10^{-5}$ | 217 | 0.436 |
| 22.5 - 23.5 | $1.6 \cdot 10^{-4}$ | 295 | 0.390 |
| 22.0 - 22.5 | $6.5 \cdot 10^{-5}$ | 217 | 0.436 |
| 19.5 - 22.0 | $5.9 \cdot 10^{-5}$ | 308 | 0.376 |
| 18.5 - 19.5 | $9.7 \cdot 10^{-5}$ | 219 | 0.422 |
| 16.5 - 18.5 | $9.7 \cdot 10^{-5}$ | 219 | 0.422 |
| 15.5 - 16.5 | $9.8 \cdot 10^{-5}$ | 415 | 0.347 |
| 15.0 - 15.5 | $1.4 \cdot 10^{-4}$ | 563 | 0.403 |
| 14.5 - 15.0 | $8.6 \cdot 10^{-5}$ | 542 | 0.355 |
| 14.0 - 14.5 | $8.6 \cdot 10^{-5}$ | 542 | 0.355 |
| 13.5 - 14.0 | $9.8 \cdot 10^{-5}$ | 415 | 0.347 |
| 13.0 - 13.5 | $1.6 \cdot 10^{-4}$ | 570 | 0.384 |
| 12.5 - 13.0 | $9.8 \cdot 10^{-5}$ | 415 | 0.347 |
| 12.0 - 12.5 | $1.4 \cdot 10^{-4}$ | 563 | 0.403 |
| 11.5 - 12.0 | $9.8 \cdot 10^{-5}$ | 415 | 0.347 |
| 11.0 - 11.5 | $1.8 \cdot 10^{-4}$ | 456 | 0.399 |
| 10.5 - 11.0 | $3.1 \cdot 10^{-4}$ | 479 | 0.382 |
| 10.0 - 10.5 | $1.0 \cdot 10^{-4}$ | 379 | 0.379 |
| 9.5 - 10.0 | $4.6 \cdot 10^{-5}$ | 505 | 0.387 |
| 8.5 - 9.5 | $1.6 \cdot 10^{-4}$ | 295 | 0.390 |
| 7.5 - 8.5 | $1.7 \cdot 10^{-4}$ | 397 | 0.422 |
| 7.0 - 7.5 | $1.0 \cdot 10^{-3}$ | 672 | 0.386 |
| 6.5 - 7.0 | $1.8 \cdot 10^{-4}$ | 314 | 0.375 |
| 5.5 - 6.5 | $2.2 \cdot 10^{-4}$ | 657 | 0.374 |
| 0.0 - 5.5 | $2.3 \cdot 10^{-4}$ | 719 | 0.376 |



Table 7.3: *The values of Young's modulus $E$ and Poisson's ratio $\nu$.*

| Type of soil | $E$ [MPa] | $\nu$ |
|---|---|---|
| Loess | $15 - 60$ | 0.1 - 0.3 |
| Sand | $10 - 81$ | 0.3 - 0.4 |
| Sand and gravel | $50 - 200$ | 0.3 - 0.4 |
| Sandy clay | $25 - 250$ | 0.2 - 0.3 |

In the model with the homogeneous porous medium, the values of the soil characteristics are obtained by averaging the values of the different soil layers. Assume that we have two soil layers 1 and 2 in parallel with thicknesses $h_1$ and $h_2$, permeabilities $\kappa_1$ and $\kappa_2$ and cross-sectional areas $A_1$ and $A_2$ respectively. Since the layers are in

parallel, the total flow rate through both layers is equal to the sum of the flow rates across individual soil layers, hence the following expression can be derived

$$Q = Q_1 + Q_2. \tag{7.11}$$

Using Darcy's law (7.3), the total flow rate is given by

$$Q = -\frac{\kappa_h}{\eta}\nabla p(A_1 + A_2). \tag{7.12}$$

Substituting Eq. (7.12) in Eq. (7.11) and using Darcy's law (7.3) for the individual layers gives

$$-\frac{\kappa_h}{\eta}\nabla p(A_1 + A_2) = -\frac{\kappa_1}{\eta}\nabla pA_1 - \frac{\kappa_2}{\eta}\nabla pA_2. \tag{7.13}$$

Assuming that the width of each layer is identical, the average permeability of both layers can be computed by

$$\kappa_h = \frac{h_1\kappa_1 + h_2\kappa_2}{h_1 + h_2}. \tag{7.14}$$

Hence, the general expression for the average permeability of a parallel layered formation with $N$ layers is

$$\kappa_h = \frac{\sum_{i=1}^{N} h_i\kappa_i}{\sum_{i=1}^{N} h_i}. \tag{7.15}$$

For the porosity of a parallel layered formation with $N$ layers holds

$$\theta_h = \frac{\sum_{i=1}^{N} V_i\theta_i}{\sum_{i=1}^{N} V_i}, \tag{7.16}$$

where $V$ is the volume of the layer. For the grain size, the median $D50$ of the layers is used.



### 7.3.1 Mechanical oscillations

We start with the simulation of problem (7.1) with a constant pump pressure $p_{pump}$ and an imposed mechanical oscillations on boundary segment $\Gamma_3$. These mechanical oscillations are induced by the injection of water through the filter. For the boundary displacement $u_{vib}$ standing waves are used, represented by

$$u_{vib}(\mathbf{r}, t) = \left| \gamma \sin\left(\frac{\pi(z - z_{fs})}{L_f}\right) \cos\left(\frac{\pi t}{2\Delta t}\right) \right|, \tag{7.17}$$

where $\gamma$ is the amplitude of the wave, $z_{fs}$ is the $z$-coordinate of the lower end of the filter, and $\Delta t$ is the time step size.

### 7.3.2 Pulsed injection

In this numerical experiment, the prescribed pump pressure will have a pulsing behaviour rather than being constant. In this case, the pump pressure is represented by

a combination of the Heaviside step functions. A rectangular pulse wave with period $T_p$ and pulse time $\tau$ is defined as

$$p_{pump}(t) = p_{b1}\mathcal{H}(t) + (p_{b2} - p_{b1}) \sum_{k=0}^{N_p} [\mathcal{H}(t - kT_p) - \mathcal{H}(t - kT_p - \tau)], \tag{7.18}$$

where the pump pressure is pulsing between $p_{b1}$ and $p_{b2}$, and $N_p$ is the number of periods. The boundary conditions are as follows

$$p = \rho g(H - z) \quad \text{on} \quad \mathbf{r} \in \Gamma_1 \cup \Gamma_6 \cup \Gamma_7; \tag{7.19a}$$

$$\frac{\kappa}{\eta}(\nabla p + \rho g \mathbf{e}_z) \cdot \mathbf{n} = 0 \quad \text{on} \quad \mathbf{r} \in \Gamma_2 \cup \Gamma_4 \cup \Gamma_5; \tag{7.19b}$$

$$p = \rho g(H - z) + p_{pump}(t) \quad \text{on} \quad \mathbf{r} \in \Gamma_3; \tag{7.19c}$$

$$\boldsymbol{\sigma}'\mathbf{n} = \mathbf{0} \quad \text{on} \quad \mathbf{r} \in \Gamma_1 \cup \Gamma_6; \tag{7.19d}$$

$$(\boldsymbol{\sigma}'\mathbf{n}) \cdot \mathbf{t} = 0 \quad \text{on} \quad \mathbf{r} \in \Gamma_2 \cup \Gamma_3 \cup \Gamma_4 \cup \Gamma_5; \tag{7.19e}$$

$$\mathbf{u} \cdot \mathbf{n} \leq 0 \quad \text{on} \quad \mathbf{r} \in \Gamma_2 \cup \Gamma_3 \cup \Gamma_4; \tag{7.19f}$$

$$\mathbf{u} \cdot \mathbf{n} = 0 \quad \text{on} \quad \mathbf{r} \in \Gamma_5; \tag{7.19g}$$

$$(\boldsymbol{\sigma}'\mathbf{n}) \cdot \mathbf{n} = 0 \quad \text{on} \quad \mathbf{r} \in \Gamma_7; \tag{7.19h}$$

$$\mathbf{u} \cdot \mathbf{t} = 0 \quad \text{on} \quad \mathbf{r} \in \Gamma_7. \tag{7.19i}$$

## 7.4 Numerical results

In this section, we discuss the solution results for the Galerkin finite element method, with triangular Taylor-Hood elements [113], that are employed for the solution of the discretised quasi-two-dimensional problems that are presented in Section 7.3. The displacements are spatially approximated by quadratic basis functions, whereas a continuous piecewise linear approximation is used for the pressure field. For the time integration, the backward Euler method is applied. The numerical investigations are carried out using the matrix-based software package MATLAB (version R2011b).



The computational domain is an L-shaped surface with radius $R = 5.0\,\text{m}$, height $H = 25.0\,\text{m}$, filter radius $R_f = 10.0\,\text{cm}$ and filter length $L_f = 2.0\,\text{m}$. The filter is placed between $z = z_{fs} = 5.5$ and $z = 7.5$. The domain is discretised using a regular triangular grid, with $\Delta r = 0.1$ and $\Delta z = 0.25$. In addition, values for some model parameters have been chosen based on the literature (see Table 7.4).

Table 7.4: *An overview of the values of the model parameters.*

| Property | Symbol | Value | Unit |
|---|---|---|---|
| Fluid viscosity | $\eta$ | $1.307 \cdot 10^{-3}$ | $\text{Pa} \cdot \text{s}$ |
| Fluid density | $\rho$ | 1000 | $\text{kg/m}^3$ |
| Gravitational acceleration | $g$ | 9.81 | $\text{m/s}^2$ |

### 7.4.1 Numerical results for the problem with mechanical oscillations

In this section, we will investigate the impact of the standing waves (7.17) on the flow of water in the homogeneous and in the heterogeneous layered porous media. The impact of the injection methods on the water flow is defined in this study as the impact on the time average of the volumetric flow rate $\overline{Q}$ at a distance $R - R_f$ from the injection filter. In these simulations, water is injected into the soil at a constant pump pressure equal to 5.0 bar. Furthermore, as the exact values of Young's modulus $E$ and Poisson's ratio $\nu$ are unknown, we will apply the Monte Carlo method and draw samples for these values, using 300 samples of uniform distributions with characteristics that are presented in Table 7.3 and as corresponding with the soil type in each layer. To quantify the impact of the variation in the values of Young's modulus $E$ and Poisson's ratio $\nu$ and as a consistency check, we start with the simulation results for the problem with boundary conditions (7.6) and without any oscillations, i.e. $u_{vib} = 0$. The time average of the volumetric flow rate after applying the Monte Carlo simulations to the values of Young's modulus and Poisson's ratio are provided in the histograms in Figure 7.2. In the generations of the simulation results, the time step size is chosen to be $\Delta t = 0.5$.

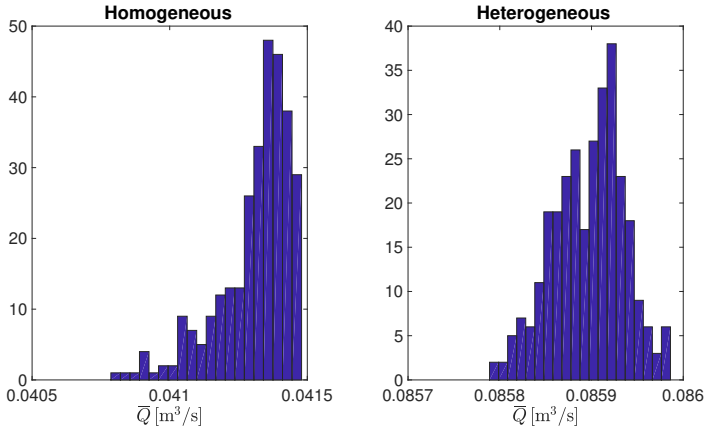


Figure 7.2: *The histogram of the time average of the volumetric flow rate over the time interval (0, 150], without oscillations and after applying Monte Carlo simulations to the values of Young's modulus and Poisson's ratio.*

Figure 7.2 shows that variation in the values of Young's modulus and Poisson's ratio leads to a small variation in the simulation results, in both the homogeneous and the heterogeneous layered model. The change in the time average of the volumetric flow rate in the homogeneous model, due to this variation, is maximally 1.70% while the change in the heterogeneous model is 0.23% maximal. Furthermore, this figure presents the difference between the porous media. From these results, we can conclude that water flows two times faster through heterogeneous layered porous media than through homogeneous porous media, in case there are no external imposed body forces.

In the problem with oscillations, the Monte Carlo method is applied to the values of the amplitude of the oscillations using samples of uniform distributions with chosen boundaries. In Figure 7.3, the time average of the volumetric flow rate is depicted after applying Monte Carlo simulations to the values of the oscillation characteristic $\gamma$. For the simulations, 300 samples from the following uniform distribution are generated:

$$\gamma \sim \mathcal{U}(0.05, 0.10).$$

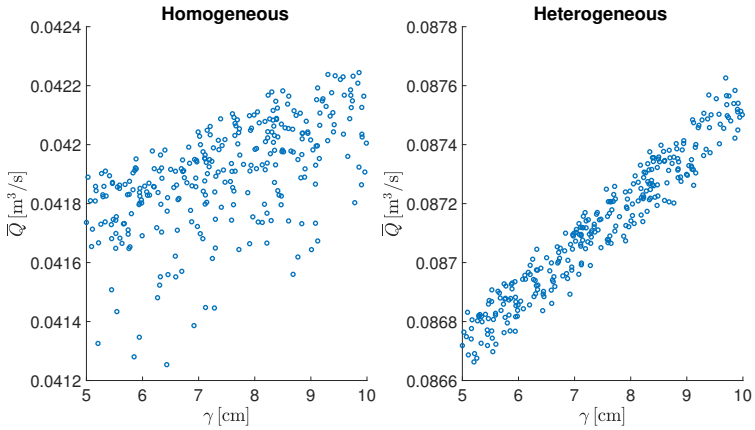


Figure 7.3: *Scatter plots of the time average of the volumetric flow rate over the time interval* $(0, 150]$*, after applying Monte Carlo simulations to the values of* $\gamma$*,* $E$ *and* $\nu$*. For the oscillations, standing waves* (7.17) *are used as prescribed boundary displacement* $u_{vib}$*, with* $\gamma \sim \mathcal{U}(5, 10)$ cm.

7

Figure 7.3 indicates that an increase in the amplitude of the imposed standing waves leads to an increase in the time average of the volumetric flow rate $\overline{Q}$. Moreover, this impact is larger on the water flow in the heterogeneous layered porous medium than the water flow in the homogeneous porous medium. In Table 7.5, the Pearson correlation coefficients are given together with the associated $p$-values. The notation $\overline{Q}_h$ is used for the time average of the volumetric flow rate in the homogeneous model and $\overline{Q}_l$ indicates the time average of the volumetric flow rate in the heterogeneous layered porous medium. From this table, we can conclude that $\gamma$ and $\overline{Q}_l$ are almost perfectly positively linearly related, since $corr(\gamma, \overline{Q}_l)$ is almost equal to 1. Furthermore, the correlation seems stronger for the heterogeneous case than for the homogeneous case.

Table 7.5: *The Pearson correlation coefficients and the associated p-values.* $p < 0.05$ *means that the two sets of data are most probably related, with significance level 0.05.*

| | $corr(\gamma, \overline{Q}_h)$ | $corr(\gamma, \overline{Q}_l)$ |
|---|---|---|
| $r$ | 0.58 | 0.97 |
| $p$ | $< 0.05$ | $< 0.05$ |

To measure the impact of the standing waves (7.17) on the water flow, the percentage change $\overline{Q}_{\%}$ of the time average of the volumetric flow rates as result of the imposed oscillations is determined by the formula

$$\overline{Q}_{\%} = \frac{\overline{Q} - \overline{Q}_0}{\overline{Q}_0} \cdot 100, \tag{7.20}$$

where $\overline{Q}_0$ is the time average of the volumetric flow rate in the test case without oscillations. The percentage change $\overline{Q}_{\%}$ of the time average $\overline{Q}$, that is computed after applying the Monte Carlo method, is depicted as function of $\gamma$ in Figure 7.4.

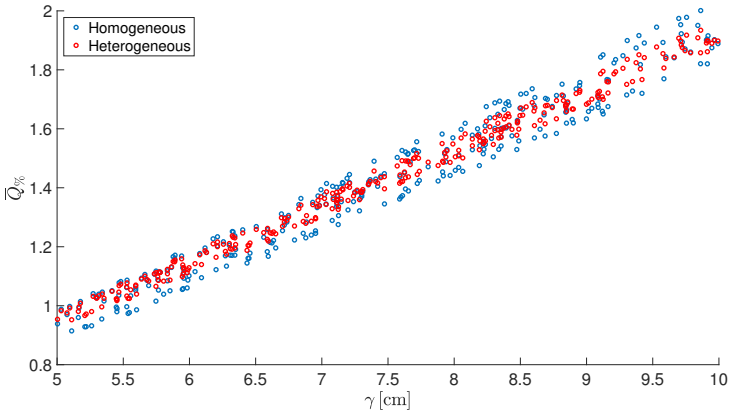


Figure 7.4: *Plots of the percentage change $\overline{Q}_{\%}$ over the time interval $(0, 150]$ as function of $\gamma$, after applying Monte Carlo method to the values of $\gamma$, $E$ and $\nu$.*

Figure 7.4 confirms that the impact of the imposed mechanical oscillations is larger on the flow through heterogeneous layered porous media. However, the change in the volumetric flow rate due to these oscillations is not significant, since the maximal percentage change $\overline{Q}_{\%}$ is 2.0%.



### 7.4.2 Numerical results for the problem with pulsed injection

Instead of imposing a mechanical oscillation, the pulsing behaviour of the pump pressure will be investigated in this section. Simultaneously, the Monte Carlo method will be applied to the values of Young's modulus $E$ and Poisson's ratio $\nu$. In addition, the contributions of the variations in the values of the pulse wave characteristics to the volumetric flow rate are analysed. These contributions are examined by applying the Monte Carlo method to the pulse wave period $T_p$ and the relative pulse time $\tilde{\tau}$, defined as $\tilde{\tau} = \frac{\tau}{T_p}$, with $\tau$ the pulse time (see Formula (7.18)). Subsequently, in order to be able to draw reliable conclusions about the impact of pressure pulsing on the volumetric flow rate, we compare the volumetric flow rate caused by the pulsed injection with the volumetric flow rate stimulated by a constant pump pressure $p_{pump,c}$. In each simulation, the constant pump pressure is chosen equal to the total pump pressure over time by pulsed injection. Hence, for a particular relative pulse time $\tilde{\tau}$,

the constant pump pressure is computed by

$$p_{pump,c} = \tilde{\tau} p_{b2} + (1 - \tilde{\tau}) p_{b1}. \tag{7.21}$$

In Figure 7.5, the time average of the volumetric flow rate at a distance $R - R_f$ from the injection filter is depicted after applying Monte Carlo simulations to the values of the pulse wave characteristics $T_p$ and $\tilde{\tau}$ and to the values of Young's modulus $E$ and Poisson's ratio $\nu$. For the simulation, 300 samples are randomly generated from the following datasets:

$$T_p \in \{60, 120, \ldots, 1800\}, \quad \tilde{\tau} \in \{0.1, 0.2, \ldots, 0.9\}. \tag{7.22}$$

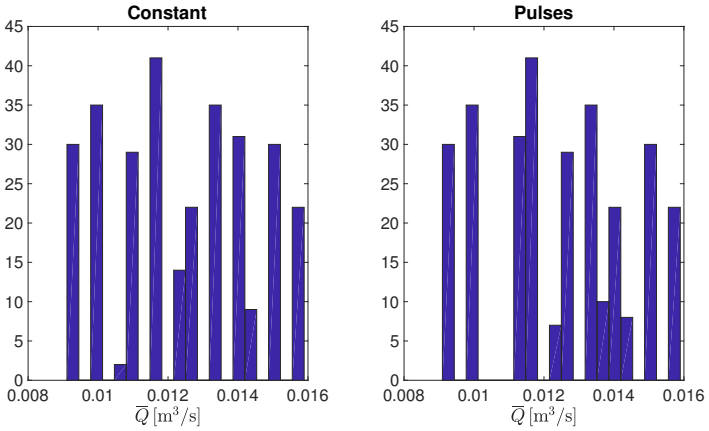


(a) Homogeneous porous medium.

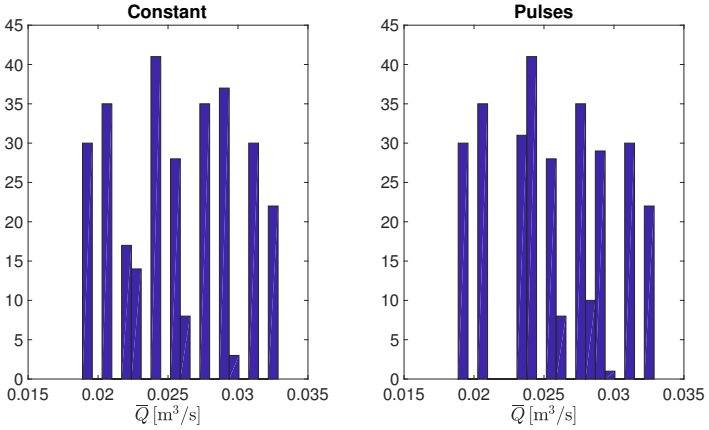


(b) Heterogeneous layered porous medium.

Figure 7.5: *The histogram of the time average of the volumetric flow rate after 10 pulsing periods, after applying Monte Carlo simulations to the values of $T_p$, $\tilde{\tau}$ using datasets* (7.22) *and to the values of $E$ and $\nu$. For the pump pressure, pulse waves* (7.18) *are used with $p_{b1} = 1.0 \cdot 10^5$ Pa and $p_{b2} = 2.0 \cdot 10^5$ Pa.*

In the generations of the simulation results presented in Figure 7.5, the time step size $\Delta t$ is determined by $\Delta t = \frac{T_p}{10}$. The number of periods $N_p$ is equal to 10 and the pump pressure is pulsing between $p_{b1} = 1.0 \cdot 10^5$ Pa and $p_{b2} = 2.0 \cdot 10^5$ Pa. Similarly to the mechanical oscillations problem, Figure 7.5 illustrates that the water flow rate at a distance $R - R_f$ from the injection filter is in average two times higher through heterogeneous layered porous media than through homogeneous porous media. More importantly, Figure 7.5 reveals that pulsed injection does not lead to a higher water flow rate in both models, in contrast with the results obtained in Chapter 3. The difference in simulation results can be a consequence of the different pulse waves that we have used in these problems. In the current problem with a homogeneous porous medium, we are using rectangular pulse waves that are pulsing between two positive pump pressure values $p_{b1} > 0$ and $p_{b2} > 0$. However, the pump pressure in Chapter 3 pulses between $p_{b1} = 0$ and $p_{b2} = p_{max} > 0$.

To measure the real impact of pulsed injection on the fluid flow and to compare both pulsed and constant injection methods, the percentage of the change $\overline{Q}_{\%}$ of the time average of the volumetric flow rate $\overline{Q}$ is used, which is determined by

$$\overline{Q}_{\%} = \frac{\overline{Q} - \overline{Q}_C}{\overline{Q}_C} \cdot 100, \tag{7.23}$$

where $\overline{Q}_C$ is the time average of the volumetric flow rate stimulated by a constant pump pressure. In Figure 7.6, the percentage of the change of the time average of the volumetric flow rate is depicted as function of $T_p$ and $\tilde{\tau}$, for both the homogeneous and the heterogeneous layered porous media.

Figure 7.6 provides insights into the impact of the variations in the values of the pulse wave characteristics to the volumetric flow rate. Firstly, this figure shows that the volumetric flow rate remains invariant while varying the values of the pulse period $T_p$. Secondly, it reveals that for small values of the relative pulse time $\tilde{\tau}$ the percentage change of the time average of the volumetric flow rate is negative. This means that the constant pump pressure results in higher flow rates than the pulsed injection for these values of the relative pulse time. Even though, the percentage change the volumetric flow rate in the homogeneous porous medium is positive in 82.3% of the simulations. While 84.3% of the simulations in the heterogeneous layered model provides a positive percentage change. Hence, we can conclude that pulsed injection has a beneficial effect on the water flow in porous media. However, the increase in volumetric flow rate due to the pump pressure pulses is insignificant. In both homogeneous and heterogeneous models, this increase is in 90% of the simulations less than 0.07%. In 10% of the simulation, the increase is between 3.8% and 4.0%.

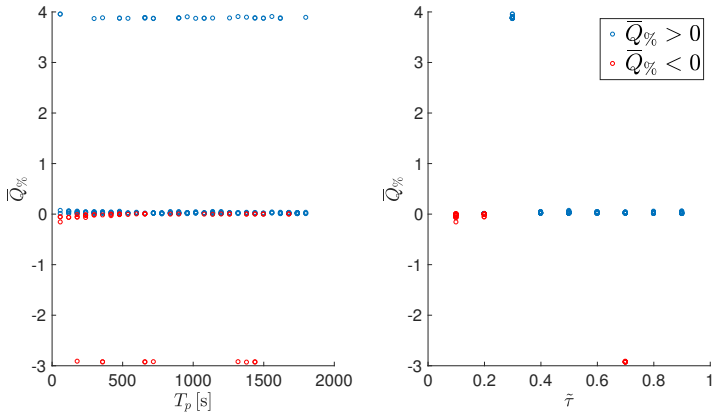


(a) Homogeneous porous medium.

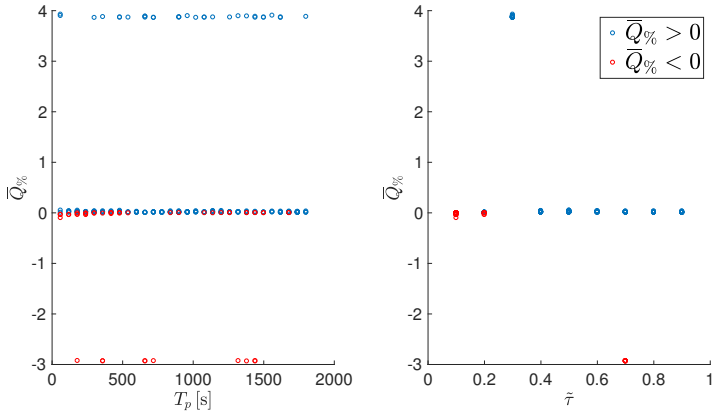


(b) Heterogeneous layered porous medium.

Figure 7.6: *Scatter plots of the percentage of the change* $\overline{Q}_{\%}$ *of the time average of the volumetric flow rate after 10 pulsing periods, after applying Monte Carlo simulations to the values of* $T_p$ *and* $\tilde{\tau}$ *using datasets* (7.22) *and to the values of* $E$ *and* $\nu$*. For the pump pressure, pulse waves* (7.18) *are used with* $p_{b1} = 1.0{\cdot}10^5$ Pa *and* $p_{b2} = 2.0{\cdot}10^5$ Pa.

## 7.5 Discussion and conclusions

All natural soils are heterogeneous mixtures of broken rocks and minerals, living organisms, and humus. To determine the composition of soil, laboratory tests and field experiments are needed. However, since these tests and experiments can only been performed on a limited number of locations in the soil, flow through the voids in a soil is usually modelled assuming a homogeneous soil mixture rather than a heterogeneous mixture. In this work, we investigated whether this simplification is justified by exploring the difference between the flow of water in a model with a heterogeneous layered porous medium and a model with a homogeneous porous medium. For this purpose, two three-dimensional physical problems are considered, describing the in-

filtration of a fluid through a filter into an aquifer. In the first simulated problem, the infiltration is stimulated by a constant pump pressure. Furthermore, mechanical oscillations, that are assumed to be induced by the injection of water, are imposed on the infiltration boundary. In the second numerical experiment, the prescribed pump pressure has a pulsing behaviour rather than being constant. To describe this behaviour, rectangular pulse waves are used with different periods and pulse times.

These problems are solved using Biot's theory of linear poroelasticity with single-phase flow, considering nonlinear permeability. The model is discretised by a continuous Galerkin finite element method based on Taylor-Hood elements, combined with the implicit Euler scheme for time stepping. The study contains simulations with oscillatory force boundary conditions as well as pressure pulses. Furthermore, Monte Carlo simulations are performed to quantify the impact of variation of model parameters such as Young's modulus, the oscillatory modes and the injection pressure pulses on the volumetric flow rate at a particular distance from the injection filter.

We started by performing Monte Carlo simulations to the values of Young's modulus and Poisson's ratio, on the first problem without imposing mechanical oscillations nor pressure pulses. The numerical results of that variation in the values of Young's modulus and Poisson's ratio indicated that these parameters do not have a large impact on the volumetric flow rate. After applying mechanical oscillations on the infiltration boundary in the form of standing waves with different amplitudes, the numerical results showed that an increase in the amplitude leads to an increase in the volumetric flow rate. Moreover, this impact is larger on the water flow in the heterogeneous layered porous medium than on the water flow in the homogeneous porous medium. However, the change in the volumetric flow rate due to these oscillations is not significant, since the maximal percentage change is 2.0%. Finally, numerical simulations of pressure pulsing pointed out that injection pulses does not lead to a higher water flow rate, regardless of the type of soil into which we inject. However, if pressure pulses are preferable to a constant pump pressure, large pulse times must be selected in order to increase the water outflow.

Most importantly, we can conclude that water flows twice as fast through heterogeneous layered porous media than through homogeneous porous media, in all problems tested.

**Acknowledgements** We would like to sincerely thank engineering and consultancy company Fugro GeoServices B.V. for providing us with the measurements of the laboratory tests and the field experiments.

Chapter 8

# Tracer dispersion through deforming heterogeneous and homogeneous porous media

*The detection of preferential flow paths and the characterisation of their hydraulic properties are important for the development of hydrogeological models in aquifers. Tracer tests offer the possibility to efficiently investigate the aquifer properties and the preferential flow pathways of the fluid injected into an aquifer. In this chapter, we investigate the preferential flow paths of a fluid by injecting a tracer into a heterogeneous layered porous medium and a homogeneous porous medium. For simulating this problem, a tracer model is considered, using bromide as a tracer for water flow. Based on the combination of Biot's theory of linear poroelasticity and the advection-dispersion equation, a coupled model describing solute transport in deforming soil is proposed, taking into account nonlinear permeability. The numerical results point out that a higher value of the longitudinal dispersivity (i.e. a larger microscopic heterogeneity) results in a larger distance that can be reached by the bromide tracer and in higher concentration values in the vicinity of the injection filter. Furthermore, higher concentration values are computed in the heterogeneous layered porous medium than in the homogeneous porous medium.*

## 8.1 Introduction

The objective of this dissertation is describing the flow paths of an incompressible Newtonian fluid through the pores of a linear elastic porous medium. Tracer tests offer the possibility to efficiently investigate the aquifer properties and the spreading of both nonreactive and reactive solutes in groundwater. Hence it is possible to investigate the preferential flow pathways and travel times in aquifers, surface waters and the unsaturated zone, by marking the fluid by a tracer at a specific location along the expected flow path. Tracer testing can be performed under forced or natural hydraulic gradient conditions; and at field-scales and laboratory. Due to lacking information on the aquifer transport behaviour, tracer tests very often even become a prerequisite to obtain reliable transport model predictions. A typical example is the identification of the main transport path of contaminants within natural attenuation studies [20]. A summary of some recent developments in the field of tracer testing and tracer based aquifer investigations can be found in [101], in this chapter the importance and advantages of tracer testing are emphasised.

In this chapter the tracer model will be considered, where a tracer is injected in the porous medium. Based on the combination of Biot's consolidation theory and solute transport theory, a three-dimensional coupled model describing solute transport in deforming soil has been proposed, taking into account the effect of consolidation on solute transport processes. In this study, a bromide ($Br^-$) is used as a tracer for water flow. Bromide was selected as a tracer because it does not react with the porous medium.

The rest of this chapter is organised as follows: A coupled model describing solute transport in deforming soil is proposed in Section 8.2, based on the combination of Biot's theory of linear poroelasticity and the advection-dispersion equation. Section 8.3 describes the numerical experiments. In Section 8.4, the numerical method is formulated. Here, the weak form of the partial differential equations is derived and the Galerkin finite element approximations are described. Section 8.5 discusses the numerical results and, lastly, some concluding remarks and suggestions for further work are reported in Section 8.6.



## 8.2 Governing equations

In this study, we assume that the deformations are very small. Hence, the model provided by Biot's theory of linear poroelasticity with single-phase flow [16] is used to determine the local displacement of the skeleton of a porous medium, as well as the fluid flow through the pores. We assume that the porous medium is a linear elastic continuum and that it is saturated by a Newtonian fluid. The solid matrix is assumed to be elastic and fully connected and the pore water is assumed to be incompressible. In addition, we assume that the fluid flow obeys Darcy's law and that the soil is in an isotropic condition. Let $\Omega \subset \mathbb{R}^3$ denote the domain occupied by the porous medium with boundary $\Gamma$, and $\mathbf{x} = (x, y, z) \in \Omega$. Furthermore, $t$ denotes time, belonging to a half-open time interval $I = (0, T]$, with $T > 0$. Biot's three-dimensional consolidation

theory is described as follows [2, 135]:

$$\text{equilibrium equations:} \quad -\nabla \cdot \boldsymbol{\sigma}' + (\nabla p + \rho g \mathbf{e}_z) = \mathbf{0} \qquad \text{on } \Omega \times I; \tag{8.1a}$$

$$\text{continuity equation:} \quad \frac{\partial}{\partial t}(\nabla \cdot \mathbf{u}) + \nabla \cdot \mathbf{v} = 0 \qquad \text{on } \Omega \times I, \tag{8.1b}$$

where $\boldsymbol{\sigma}'$ and $\mathbf{v}$ are defined by the following equations

$$\text{Biot's constitutive equations:} \quad \boldsymbol{\sigma}' = \lambda tr(\boldsymbol{\varepsilon})\mathbf{I} + 2\mu\boldsymbol{\varepsilon}; \tag{8.2}$$

$$\text{Darcy's law:} \quad \mathbf{v} = -\frac{\kappa}{\eta}(\nabla p + \rho g \mathbf{e}_z). \tag{8.3}$$

In the above relations, $\boldsymbol{\sigma}'$, $p$, $\rho$, $g$, $\mathbf{u}$, $\mathbf{v}$, $\lambda$ and $\mu$; $\boldsymbol{\varepsilon}$, $\kappa$ and $\eta$ respectively, denote the effective stress tensor for the porous medium, the pore pressure, the fluid density, the gravitational acceleration, the displacement vector of the porous medium, Darcy's velocity, the Lamé coefficients, the effective strain tensor, the permeability of the porous medium, and the fluid viscosity. To complete the formulation of a well-posed problem, appropriate boundary and initial conditions are specified in Section 8.3.

Furthermore, we consider the spatial dependency of the porosity and the permeability of the porous medium. The permeability can be determined using the Kozeny-Carman equation [136]

$$\kappa(\mathbf{x}, t) = \frac{d_s^2}{180} \frac{\theta(\mathbf{x}, t)^3}{(1 - \theta(\mathbf{x}, t))^2}, \tag{8.4}$$

where $d_s$ is the mean grain size of the soil and the porosity $\theta$ is computed from the displacement vector using the porosity-dilatation relation (see [130])

$$\theta(\mathbf{x}, t) = 1 - \frac{1 - \theta_0}{\exp(\nabla \cdot \mathbf{u})}, \tag{8.5}$$

with $\theta_0$ the initial porosity. As a result of the dependency of the permeability on the displacement vector, Eq. (8.1b) becomes nonlinear.

In this study, we focus on the transport of a tracer during an infiltration process. To describe the solute transport, the advection-dispersion equation in a moving mesh is used (see [146]):

$$\frac{Dc}{Dt} + c(\nabla \cdot \mathbf{v}_{mesh}) + \nabla \cdot \mathbf{J} = 0, \tag{8.6}$$

where $c$ is the concentration of the tracer and $\mathbf{v}_{mesh}$ is the mesh velocity. The material time derivative is given by [77]

$$\frac{Dc}{Dt} = \frac{\partial c}{\partial t} + \mathbf{v}_{mesh} \cdot \nabla c. \tag{8.7}$$

The flux $\mathbf{J}$ is defined as

$$\mathbf{J} = c\mathbf{v} - D\nabla c, \tag{8.8}$$

with $D$ the hydrodynamic dispersion tensor defined in terms of two components: mechanical dispersion and molecular diffusion [67, 86]

$$D = \begin{pmatrix} \alpha_x \frac{v_x}{\theta} + D_{diff} & 0 & 0 \\ 0 & \alpha_y \frac{v_y}{\theta} + D_{diff} & 0 \\ 0 & 0 & \alpha_z \frac{v_z}{\theta} + D_{diff} \end{pmatrix}, \tag{8.9}$$

where $D_{diff}$ is the diffusion coefficient, $\alpha_x$ is the dispersivity in the flow direction, $\alpha_y$ is the transversal dispersivity and $\alpha_z$ is the vertical dispersivity.

## 8.3 Problem formulation

The infiltration of a fluid through a filter into an aquifer is shown in Figure 8.1a. We assume that the flow pattern is axisymmetric, hence for the azimuthal coordinate $\hat{\theta}$ holds $\frac{\partial}{\partial \hat{\theta}}(.) = 0$. Therefore, we determine the solution for a fixed azimuth. The computational domain $\Omega$ is an L-shaped two-dimensional surface with cylindrical coordinates $\mathbf{r} = (r, z)$, as depicted in Figure 8.1b.

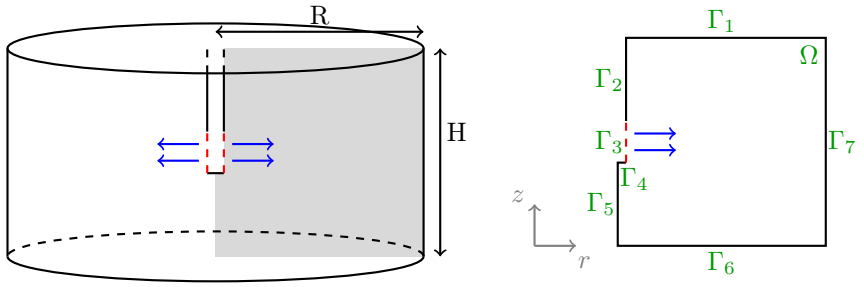


Figure 8.1: *Sketch of the set-up for the aquifer problem: (left) physical problem and (right) numerical discretisation. Taking advantage of the symmetry of geometry and boundary conditions, only the grey region is discretised.*

In order to solve this problem, Biot's consolidation model, as described in Section 8.2, is applied on the computational domain $\Omega$ with radius $R$ and height $H$. The tracer is injected into the soil through a filter placed on boundary segment $\Gamma_3$. Furthermore, the injection tube (boundary segments $\Gamma_2$, $\Gamma_3$ and $\Gamma_4$) is fitted with a casing (boundary segments $\Gamma_2$ and $\Gamma_4$) and a perforated section (boundary segment $\Gamma_3$) to prevent loose material from entering and potentially clogging the injection tube. More precisely, the boundary conditions for this problem are given as follows:

$$p = \rho g(H - z) \quad \text{on} \quad \mathbf{r} \in \Gamma_1 \cup \Gamma_6 \cup \Gamma_7; \tag{8.10a}$$

$$\frac{\kappa}{\eta}(\nabla p + \rho g \mathbf{e}_z) \cdot \mathbf{n} = 0 \quad \text{on} \quad \mathbf{r} \in \Gamma_2 \cup \Gamma_4 \cup \Gamma_5; \tag{8.10b}$$

$$p = \rho g(H - z) + p_{pump} \quad \text{on} \quad \mathbf{r} \in \Gamma_3; \tag{8.10c}$$

$$\boldsymbol{\sigma}'\mathbf{n} = \mathbf{0} \quad \text{on} \quad \mathbf{r} \in \Gamma_1 \cup \Gamma_6; \tag{8.10d}$$

$$(\boldsymbol{\sigma}'\mathbf{n}) \cdot \mathbf{t} = 0 \quad \text{on} \quad \mathbf{r} \in \Gamma_2 \cup \Gamma_3 \cup \Gamma_4 \cup \Gamma_5; \tag{8.10e}$$

$$\mathbf{u} \cdot \mathbf{n} \leq 0 \quad \text{on} \quad \mathbf{r} \in \Gamma_2 \cup \Gamma_3 \cup \Gamma_4; \tag{8.10f}$$

$$\mathbf{u} \cdot \mathbf{n} = 0 \quad \text{on} \quad \mathbf{r} \in \Gamma_5; \tag{8.10g}$$

$$\mathbf{u} = \mathbf{0} \quad \text{on} \quad \mathbf{r} \in \Gamma_7, \tag{8.10h}$$

where $\mathbf{t}$ is the unit tangent vector at the boundary, $\mathbf{n}$ the outward unit normal vector and $p_{pump}$ is a prescribed pump pressure due to the injection of the fluid through a

filter with radius $R_f$ and length $L_f$. Figure 8.1b shows the definition of the boundary segments. Note that the boundary conditions on boundary segment $\Gamma_5$ appear as a result of symmetry. Initially, the following condition is fulfilled:

$$\mathbf{u}(\mathbf{r}, 0) = \mathbf{0} \quad \text{for} \quad \mathbf{r} \in \Omega. \tag{8.11}$$

For the tracer concentration we use the following boundary conditions:

$$c = 0 \quad \text{on} \quad \mathbf{r} \in \Gamma_1 \cup \Gamma_6 \cup \Gamma_7; \tag{8.12a}$$

$$\mathbf{J} \cdot \mathbf{n} = 0 \quad \text{on} \quad \mathbf{r} \in \Gamma_2 \cup \Gamma_4 \cup \Gamma_5; \tag{8.12b}$$

$$c = c_{inj} \quad \text{on} \quad \mathbf{r} \in \Gamma_3, \tag{8.12c}$$

where $c_{inj}$ is the injection concentration of the tracer. The initial condition for the concentration is:

$$c(\mathbf{r}, 0) = 0 \quad \text{for} \quad \mathbf{r} \in \Omega_t. \tag{8.13}$$

In this study, the distribution of the substances of a tracer in the soil profile is simulated in two models: in the first model, the porous medium is homogeneous while the second model has a heterogeneous layered porous medium. A description of these models is given in Section 7.3.

## 8.4 Numerical method

In this section, we outline the numerical procedures used to discretise the poroelastic models coupled with the advection-dispersion equation as presented in Section 8.2 and to solve the resulting coupled fluid-solid-concentration finite-dimensional problem. First, the weak form of the governing equations will be derived and discretised using a continuous Galerkin finite element approach with displacements and fluid pressures as primary variables. Subsequently, the concentration profile of the tracer will be computed using the solutions for $\mathbf{u}$ and $p$ at each time step, by applying the finite element method to Eq. (8.6).

### 8.4.1 Weak formulation

To present the variational formulation of these problems, we first introduce the appropriate function spaces. Let $L^2(\Omega)$ be the Hilbert space of square integrable scalar-valued functions $f$ on $\Omega$ defined in cylinder coordinates $(r, z)$ as $L^2(\Omega) = \{f : \Omega \to \mathbb{R} : \int_\Omega |f|^2 r \, d\Omega < \infty\}$, with inner product $(f, g) = \int_\Omega fgr \, d\Omega$. Let $H^1(\Omega)$ denote the subspace of $L^2(\Omega)$ of functions with first derivatives in $L^2(\Omega)$. We further introduce the function space $\mathscr{Q} = \{q \in H^1(\Omega) : q = \rho g(H - z)$ on $\Gamma_1 \cup \Gamma_6 \cup \Gamma_7$ and $q = \rho g(H - z) + p_{pump}$ on $\Gamma_3\}$. Subsequently, we use the function space $\mathscr{W} = \{\mathbf{w} \in (H^1(\Omega))^2 : \mathbf{w} \cdot \mathbf{n} = 0$ on $\Gamma_5$ and $\mathbf{w} = \mathbf{0}$ on $\Gamma_7\}$. Furthermore, we consider the bilinear forms [100]

$$a(\mathbf{u}, \mathbf{w}) = \lambda(\nabla \cdot \mathbf{u}, \nabla \cdot \mathbf{w}) + 2\mu \sum_{i,j=1}^{2} (\epsilon_{ij}(\mathbf{u}), \epsilon_{ij}(\mathbf{w})); \tag{8.14}$$

$$b(p, q) = \sum_{i=1}^{2} (\frac{\kappa}{\eta} \frac{\partial p}{\partial r_i}, \frac{\partial q}{\partial r_i}). \tag{8.15}$$

The variational formulation in cylinder coordinates $(r, z)$ for problem (8.1) with boundary and initial conditions (8.10)-(8.11), consists of the following, using the notation $\dot{\mathbf{u}} = \frac{\partial \mathbf{u}}{\partial t}$:

For each $t > 0$, find $(\mathbf{u}(t), p(t)) \in (\mathscr{W} \times \mathscr{Q})$ such that

$$a(\mathbf{u}(t), \mathbf{w}) - (p(t), \nabla \cdot \mathbf{w}) + l(p(t), \mathbf{w}) = h(\mathbf{w}) - (\rho g, \mathbf{e}_z \cdot \mathbf{w}) \qquad \forall \mathbf{w} \in \mathscr{W}; \tag{8.16}$$

$$(\nabla \cdot \dot{\mathbf{u}}(t), q) + b(p(t), q) = 0 \qquad \forall q \in \mathscr{Q}_0, \tag{8.17}$$

with the initial condition $\mathbf{u}(0) = \mathbf{0}$, and where

$$l(p, \mathbf{w}) = \int_{\Gamma_2 \cup \Gamma_4} p \ \mathbf{w} \cdot \mathbf{n} \ r \ d\Gamma; \tag{8.18}$$

$$h(\mathbf{w}) = -\int_{\Gamma_3 \cup \Gamma_6} \rho g (H - z) \ \mathbf{w} \cdot \mathbf{n} \ r \ d\Gamma - \int_{\Gamma_3} p_{pump} \ \mathbf{w} \cdot \mathbf{n} \ r \ d\Gamma; \tag{8.19}$$

$$\mathscr{Q}_0 = \{q \in H^1(\Omega) : q = 0 \text{ on } \Gamma_1 \cup \Gamma_3 \cup \Gamma_6 \cup \Gamma_7\}. \tag{8.20}$$

### 8.4.2 Finite element discretisation

Problem (8.16)-(8.20) is solved by applying the finite element method, with triangular Taylor-Hood elements [28, 70, 113]. Let $\mathscr{P}_h^k \subset H^1(\Omega)$ be a function space of piecewise polynomials on $\Omega$ of degree $k$. Hence, we define finite element approximations for $\mathscr{W}$ and $\mathscr{Q}$ as $\mathscr{W}_h^k = \mathscr{W} \cap (\mathscr{P}_h^k \times \mathscr{P}_h^k)$ with basis $\{\boldsymbol{\phi}_i = (\phi_i, \phi_i) \in (\mathscr{W}_h^k \times \mathscr{W}_h^k) : i = 1, \ldots, n_u\}$ and $\mathscr{Q}_h^{k'} = \mathscr{Q} \cap \mathscr{P}_h^{k'}$ with basis $\{\psi_j \in \mathscr{Q}_h^{k'} : j = 1, \ldots, n_p\}$, respectively [2, 100]. Subsequently, we approximate the functions $\mathbf{u}(t)$ and $p(t)$ with functions $\mathbf{u}_h(t) \in \mathscr{W}_h^k$ and $p_h(t) \in \mathscr{Q}_h^{k'}$, defined as

$$\mathbf{u}_h(t) = \sum_{i=1}^{n_u} \mathbf{u}_i(t) \boldsymbol{\phi}_i, \quad p_h(t) = \sum_{j=1}^{n_p} p_j(t) \psi_j, \tag{8.21}$$

in which the Dirichlet boundary conditions are imposed. Then, the semi-discrete Galerkin approximation of problem (8.16)-(8.20) is defined as follows:

For each $t > 0$, find functions $(\mathbf{u}_h(t), p_h(t)) \in (\mathscr{W}_h^k \times \mathscr{Q}_h^{k'})$ such that

$$a(\mathbf{u}_h(t), \mathbf{w}_h) - (p_h(t), \nabla \cdot \mathbf{w}_h) + l(p_h(t), \mathbf{w}_h) = \tag{8.22}$$

$$= h(\mathbf{w}_h) - (\rho g, \mathbf{e}_z \cdot \mathbf{w}_h) \quad \forall \mathbf{w}_h \in \mathscr{W}_h^k;$$

$$(\nabla \cdot \dot{\mathbf{u}}_h(t), q_h) + b(p_h(t), q_h) = 0 \quad \forall q_h \in \mathscr{Q}_{0h}^{k'}, \tag{8.23}$$

and for $t = 0$: $\mathbf{u}_h(0) = \mathbf{0}$.

Simultaneously, discretisation in time is applied using the backward Euler method. Let $\Delta t$ be the time step size and define a time grid $\{t_m = m\Delta t : m \in \mathbb{N}\}$, then the discrete Galerkin scheme of (8.22)-(8.23) is formulated as follows:

For $m \geq 1$, find $(\mathbf{u}_h^m, p_h^m) \in (\mathscr{W}_h^k \times \mathscr{Q}_h^{k'})$ such that

$$a(\mathbf{u}_h^m, \mathbf{w}_h) - (p_h^m, \nabla \cdot \mathbf{w}_h) + l(p_h^m, \mathbf{w}_h) = h(\mathbf{w}_h) - (\rho g, \mathbf{e}_z \cdot \mathbf{w}_h) \quad \forall \mathbf{w}_h \in \mathscr{W}_h^k; \tag{8.24}$$

$$(\nabla \cdot \mathbf{u}_h^m, q_h) + \Delta t \ b(p_h^m, q_h) = (\nabla \cdot \mathbf{u}_h^{m-1}, q_h) \quad \forall q_h \in \mathscr{Q}_{0h}^{k'}, \tag{8.25}$$

while for $m = 0$: $\mathbf{u}_h^0 = \mathbf{0}$.

The discrete Galerkin scheme is solved using triangular Taylor-Hood elements. The displacements are spatially approximated by quadratic basis functions, whereas continuous piecewise linear approximation is used for the pressure field. At each time step, we solve Eqs. (8.24)-(8.25) as a fully coupled system, where we use the permeability from the previous time step. After having obtained the numerical approximations for $\mathbf{u}$ and $p$, we update the porosity using Eq. (8.5). Subsequently, the Kozeny-Carman relation (8.4) is used to calculate the permeability. The new value for the permeability is then used for the next time step.

### 8.4.3 Discretisation of the advection-dispersion equation

After obtaining the solutions for $\mathbf{u}$ and $p$ at each time step, we compute the concentration of the tracer $c$ by applying the finite element method to Eq. (8.6). First we derive the variational formulation, using the continuously deforming domain $\Omega_t$ with $\Omega_0 = \Omega$. Therefore, we introduce the function space $\mathscr{S} = \{s \in H^1(\Omega_t) : s = 0 \text{ on } \Gamma_1 \cup \Gamma_6 \cup \Gamma_7 \text{ and } s = c_{inj} \text{ on } \Gamma_3\}$. Let $s \in \mathscr{S}_0 = \{s \in H^1(\Omega_t) : s = 0 \text{ on } \Gamma_1 \cup \Gamma_3 \cup \Gamma_6 \cup \Gamma_7\}$, then we get

$$\int_{\Omega_t} \left( \frac{Dc}{Dt} + c(\nabla \cdot \mathbf{v}_{mesh}) + \nabla \cdot \mathbf{J} \right) s \; d\Omega = 0. \tag{8.26}$$

For the material time derivative it holds

$$\frac{D}{Dt}(cs) = \frac{Dc}{Dt}s + c\frac{Ds}{Dt} = \frac{Dc}{Dt}s,$$

making use of the transport property (see [47]) for the Lagrangian interpolation functions in $\mathscr{S}_0$:

$$\frac{Ds}{Dt} = 0 \quad \text{on} \quad \Omega_t. \tag{8.27}$$

Hence we get, using the definition of the material time derivative (8.7)

$$\int_{\Omega_t} \left( \frac{\partial}{\partial t}(cs) + \nabla \cdot (cs\mathbf{v}_{mesh}) + (\nabla \cdot \mathbf{J})s \right) \; d\Omega = 0. \tag{8.28}$$

Reynolds' transport theorem [77] reads as follows

$$\int_{\Omega_t} \frac{\partial}{\partial t}(cs) \; d\Omega = \frac{d}{dt} \int_{\Omega_t} cs \; d\Omega - \int_{\Gamma_t} cs \; \mathbf{v}_{mesh} \cdot \mathbf{n} \; d\Gamma. \tag{8.29}$$

This gives, after applying the divergence theorem to the second term in Eq. (8.28)

$$\frac{d}{dt} \int_{\Omega_t} cs \; d\Omega + \int_{\Omega_t} (\nabla \cdot \mathbf{J})s \; d\Omega = 0. \tag{8.30}$$

Rewriting this expression and applying the divergence theorem again yield

$$\frac{d}{dt} \int_{\Omega_t} cs \; d\Omega + \int_{\Gamma_t} (\mathbf{J} \cdot \mathbf{n})s \; d\Gamma - \int_{\Omega_t} \mathbf{J} \cdot \nabla s \; d\Omega = 0. \tag{8.31}$$

From the boundary conditions (8.12) and the definition of the flux (8.8)

$$\frac{d}{dt}\int_{\Omega_t} cs \; d\Omega - \int_{\Omega_t} (c\mathbf{v} - D\nabla c)\cdot\nabla s \; d\Omega = 0. \tag{8.32}$$

The variational formulation in cylinder coordinates $(r, z)$ for Eq. (8.6) with boundary and initial conditions (8.12)-(8.13), consists of the following:

For each $t > 0$ and $\mathbf{r} \in \Omega_t$, find $c(\mathbf{r}, t) \in \mathscr{S}$ such that

$$\frac{d}{dt}\int_{\Omega_t} csr \; d\Omega - \int_{\Omega_t} (c\mathbf{v} - D\nabla c)\cdot\nabla s \; r \; d\Omega = 0 \quad \forall s \in \mathscr{S}_0, \tag{8.33}$$

with the initial condition $c(\mathbf{r}, 0) = 0$.

Subsequently, we define a finite element approximation for $\mathscr{S}$ as $\mathscr{S}_h^1 = \mathscr{S} \cap \mathscr{P}_h^1$ with basis $\{\chi_j \in \mathscr{S}_h^1 : j = 1, \ldots, n_p\}$. Further we approximate the function $c(\mathbf{r}, t)$ with $c_h(\mathbf{r}, t)$ defined as

$$c_h(\mathbf{r}, t) = \sum_{j=1}^{n_p} c_j(t)\chi_j(\mathbf{r}),$$

in which the Dirichlet boundary conditions are imposed. By applying the backward Euler method, we get:

For $m \geq 1$, find $c_h^m \in \mathscr{S}_h^1$ such that

$$\int_{\Omega_t} c_h^m s_h r \; d\Omega - \Delta t \int_{\Omega_t} (c_h^m \mathbf{v} - D\nabla c_h^m)\cdot\nabla s_h \; r \; d\Omega = \int_{\Omega_{t-\Delta t}} c_h^{m-1} s_h r \; d\Omega \quad \forall s_h \in \mathscr{S}_{0h}^1, \tag{8.34}$$

while for $m = 0$: $\quad c_h^0 = 0$.

In this finite element method, the concentration is approximated by linear basis functions.

## 8.5 Numerical results

8

The Galerkin finite element method [113], with triangular Taylor-Hood elements, is employed for the solution of the discretised quasi-two-dimensional problem (8.1) and (8.6). The displacements are spatially approximated by quadratic basis functions, whereas a continuous piecewise linear approximation is used for the pressure field and for the concentration. For the time integration, the backward Euler method is applied. Regarding the concentration, one can use a Streamline Upwind Petrov Galerkin method to preserve monotonicity. This method, however, introduces an additional finite element discretisation error of order $\mathcal{O}(h)$, where $h$ denotes a measure for the mesh size. Alternative better methods based on flux and slope limiting can also be used to preserve monotonicity. This has not (yet) been done in obtaining the preliminary results of this chapter. The numerical investigations are carried out using the matrix-based software package MATLAB (version R2017a).

The computational domain is an L-shaped surface with radius $R = 5.0\,\mathrm{m}$, height $H = 25.0\,\mathrm{m}$, filter radius $R_f = 10.0\,\mathrm{cm}$ and filter length $L_f = 2.0\,\mathrm{m}$. The filter

is placed between $z = 5.5$ and $z = 7.5$. The domain is discretised using a regular triangular grid, with $\Delta r = 0.1$ and $\Delta z = 0.25$. Mesh refinement did not yield any significant changes of the numerical solution. In the generations of the simulation results, the time step size is chosen to be $\Delta t = 0.2$. In addition, values for some model parameters have been chosen based on the literature (see Table 8.1).

Table 8.1: *An overview of the values of the model parameters.*

| Property | Symbol | Value | Unit |
|---|---|---|---|
| Fluid density | $\rho$ | 1000 | $\mathrm{kg/m^3}$ |
| Gravitational acceleration | $g$ | 9.81 | $\mathrm{m/s^2}$ |
| Fluid viscosity | $\eta$ | $1.307 \cdot 10^{-3}$ | $\mathrm{Pa \cdot s}$ |
| Pump pressure | $p_{pump}$ | $0.5 \cdot 10^5$ | Pa |
| Diffusion coefficient | $D_{diff}$ | $1.85 \cdot 10^{-9}$ [78] | $\mathrm{m^2/s}$ |
| Longitudinal dispersivity | $\alpha_r$ | 12 [67] | m |
| Transversal dispersivity | $\alpha_z$ | 1 [67] | m |
| Injection concentration | $c_{inj}$ | 100 | $\mathrm{kg/m^3}$ |

Since we have limited knowledge about the dispersivity coefficients in the different soil layers, we assume in this study that the dispersivity is constant for all layers. In addition, the Lamé coefficients $\lambda$ and $\mu$ are related to Young's modulus $E$ and Poisson's ratio $\nu$ by [2]:

$$\lambda = \frac{\nu E}{(1+\nu)(1-2\nu)} \quad \text{and} \quad \mu = \frac{E}{2(1+\nu)}. \tag{8.35}$$

Young's modulus $E$ and Poisson's ratio $\nu$, that are used to compute the values of the Lamé coefficients, are derived from the book Foundation analysis and design [27] (see Table 8.2).

Table 8.2: *The values of Young's modulus $E$ and Poisson's ratio $\nu$.*

| Type of soil | $E$ [MPa] | $\nu$ |
|---|---|---|
| Loess | 21 | 0.3 |
| Sand | 26 | 0.3 |
| Sand and gravel | 193 | 0.4 |
| Sandy clay | 205 | 0.3 |



### 8.5.1 Numerical results for the homogeneous porous medium

First, the transport of the bromide tracer through a homogeneous porous medium is simulated. Figure 8.2 shows the computed bromide concentration profiles in the soil as a function of the radius, at different times $t$ and at a depth of 18.5 m (i.e. $z = 6.5$). From the results shown in this figure, it can be concluded that the bromide tracer

reaches a maximal distance of 2.5 m after 35 seconds, given a longitudinal dispersivity of 12.0 m, a transversal dispersivity of 1.0 m and a pump pressure of $0.5 \cdot 10^5$ Pa.

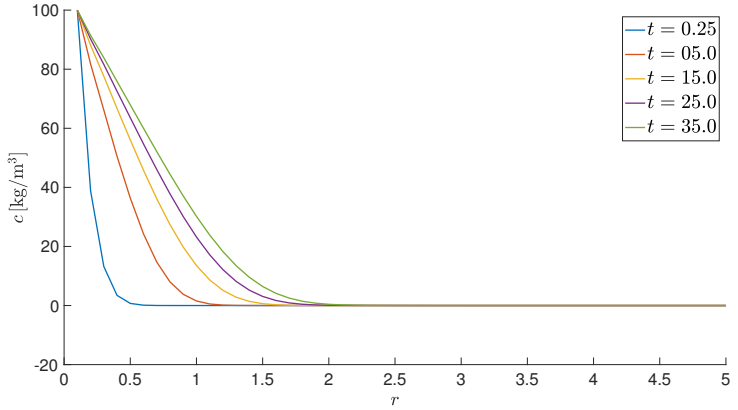


Figure 8.2: *Plots of the concentrations of the bromide tracer $c$ at $z = 6.5$ as function of the radius $r$ in meters, for different times. Given a longitudinal dispersivity of* 12.0 m*, a transversal dispersivity of* 1.0 m *and a pump pressure of* $0.5 \cdot 10^5$ Pa*.*

In Figure 8.3, the results are presented for the computed bromide concentration profiles as a function of the time, at different distances from the injection filter and at a depth of 18.5 m (i.e. $z = 6.5$). These results show that the concentration drop is almost 32% of the injection concentration after 0.4 m from the injection filter. At a distance 0.9 m from the injection filter, the concentration of the bromide tracer is approximately 30 kg/m$^3$.

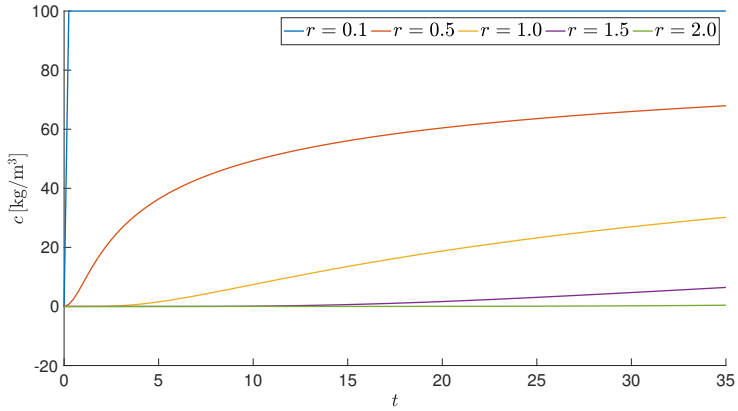


Figure 8.3: *Plots of the concentrations of the bromide tracer $c$ at $z = 6.5$ as function of the time $t$ in seconds. Given a longitudinal dispersivity of* 12.0 m*, a transversal dispersivity of* 1.0 m *and a pump pressure of* $0.5 \cdot 10^5$ Pa*.*

Mechanical dispersion is caused by variations in the flow channels of the porous medium (microscopic heterogeneity). To examine the impact of the longitudinal dispersivity, we doubled the value of $\alpha_r$ in the next simulations. Hence, we assume in these simulations that the porous medium has more variations in the flow channels. In Figure 8.4 the computed concentration profiles of the bromide tracer as a function of the radius is depicted, at different times $t$ and at 18.5 m depth. In these simulations, the longitudinal dispersivity is 24.0 m, the transversal dispersivity is 1.0 m and the pump pressure is $0.5 \cdot 10^5$ Pa. For these parameter values, the bromide tracer reaches a maximal distance of 3.0 m after 35 seconds.

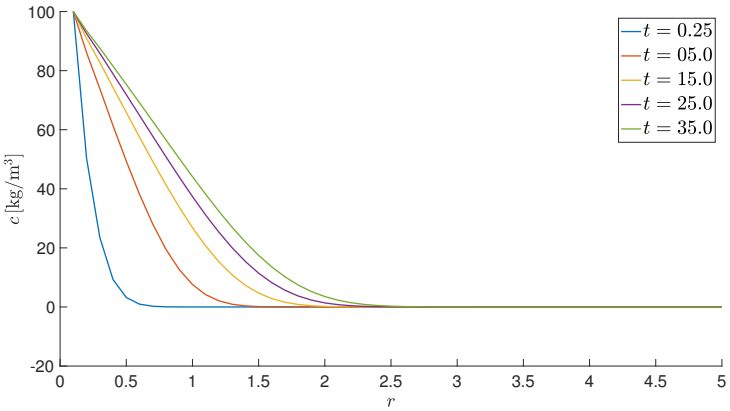


Figure 8.4: *Plots of the concentrations of the bromide tracer $c$ at $z = 6.5$ as function of the radius $r$ in meters, for different times. Using the parameters: $\alpha_r = 24.0$, $\alpha_z = 1.0$ and $p_{pump} = 0.5 \cdot 10^5$.*

In Figure 8.5, the results are presented for the computed concentration profiles of the bromide tracer as a function of the time, at different distances from the injection filter and for $z = 6.5$. At a distance of 0.4 m from the injection filter, the concentration drop is approximately 25% of the injection concentration, as we can see in Figure 8.5. Furthermore, the results indicate that the maximal concentrations after 35 seconds, at the distances of 0.9 m and 1.4 m from the injection filter, are 44 kg/m$^3$ and 17.5 kg/m$^3$ respectively.

Hence, from these results we can conclude that a higher value of the longitudinal dispersivity $\alpha_r$ results in a larger distance that can be reached by the bromide tracer. In addition, higher concentration values are detected in the vicinity of the injection filter, when a higher value of the longitudinal dispersivity is used, as shown in Figure 8.6. Physically, these results mean that the tracer penetrates faster as microscopic heterogeneity increases.

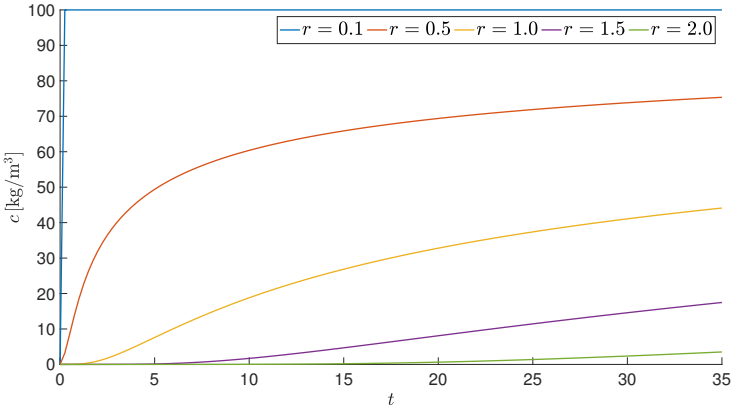


Figure 8.5: *Plots of the concentrations of the bromide tracer $c$ at $z = 6.5$ as function of the time $t$ in seconds. Using the parameters: $\alpha_r = 24.0$, $\alpha_z = 1.0$ and $p_{pump} = 0.5{\cdot}10^5$.*

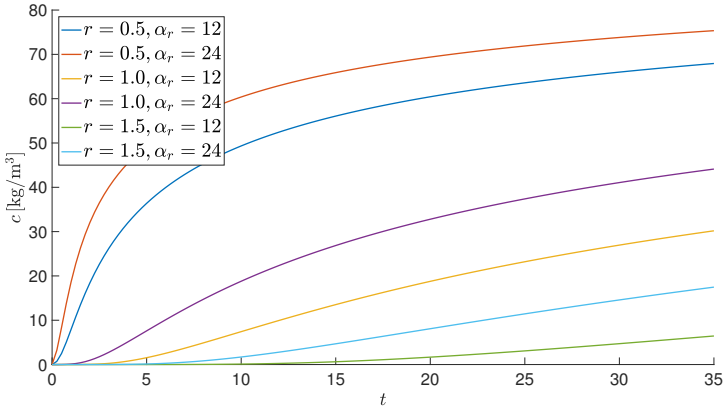


Figure 8.6: *Plots of the concentrations of the bromide tracer $c$ at $z = 6.5$ as function of the time $t$ in seconds.*

8

Since mechanical dispersion is dependent on the fluid velocity $\mathbf{v}$ (see Eq. (8.9)) and advection determines the penetration of the bromide tracer, we will investigate in the following simulations the impact of a higher pump pressure on the concentration profile of the tracer. In these simulations, a pump pressure of $1.0 \cdot 10^5$ Pa is chosen. Furthermore, the longitudinal dispersivity is 12.0 m and the transversal dispersivity is 1.0 m. In Figure 8.7 the computed concentration profiles of the bromide tracer as a function of the radius is depicted, at different times $t$ and at $z = 6.5$. For the chosen parameter values, the bromide tracer reaches a maximal distance of 3.3 m after 35 seconds.

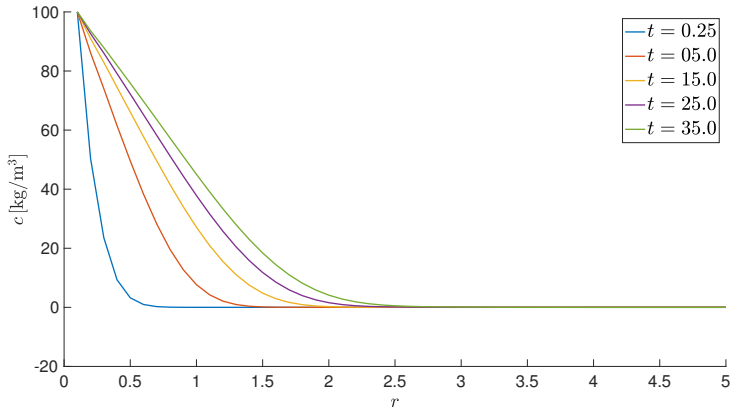


Figure 8.7: *Plots of the concentrations of the bromide tracer c at* $z = 6.5$ *as function of the radius r in meters, for different times. Using the parameters:* $\alpha_r = 12.0$, $\alpha_z = 1.0$ *and* $p_{pump} = 1.0 \cdot 10^5$.

In Figure 8.8, the results are presented for the computed concentration profiles of the bromide tracer as a function of the time, for $z = 6.5$ and at different distances from the injection filter. At a distance of 0.4 m from the injection filter, the concentration drop is approximately 24% of the injection concentration, as we can see in Figure 8.5. Furthermore, the results indicate that the maximal concentrations after 35 seconds, at the distances of 0.9 m and 1.4 m from the injection filter, are 45 $\mathrm{kg/m^3}$ and 18.4 $\mathrm{kg/m^3}$ respectively.

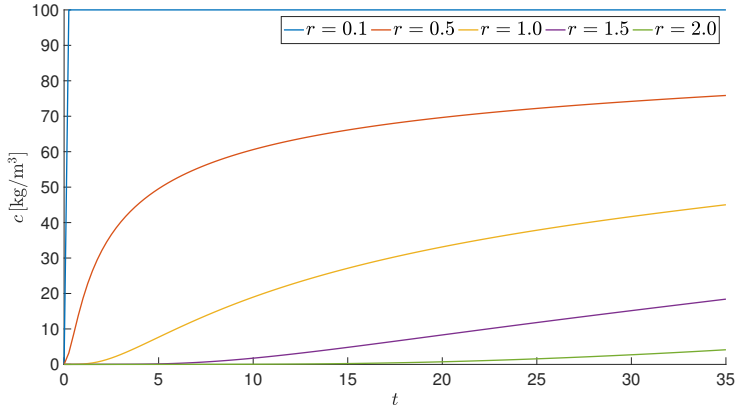


Figure 8.8: *Plots of the concentrations of the bromide tracer c at* $z = 6.5$ *as function of the time t in seconds. Using the parameters:* $\alpha_r = 12.0$, $\alpha_z = 1.0$ *and* $p_{pump} = 1.0{\cdot}10^5$.

From the previous results and from Figure 8.9, we can conclude that doubling either the value of the longitudinal dispersivity or the value of the pump pressure results in almost the same concentration profile. From Eq. (8.9) it is clear that doubling the

value of the flow velocity in the $r$-direction $v_r$ will lead to the same mechanical dispersion as doubling the value of the longitudinal dispersivity. Furthermore, according to Darcy's law (8.3) the flow velocity in the $r$-direction is defined as

$$v_r = -\frac{\kappa}{\eta}\frac{\partial p}{\partial r}, \tag{8.36}$$

from which it follows that doubling the value of the pump pressure results in almost a doubling of the flow velocity. In addition, from these results we can conclude that the rate of solute transport by molecular diffusion is negligibly small in these simulations relative to the rates of solute transport by advection and dispersion. Since the rate of solute transport by mechanical dispersion is in balance with the rate by advection, we can further conclude that for a twice microscopically more homogeneous porous medium it is necessary that the applied pump pressure is twice as high in order to obtain the same penetration of the bromide tracer.

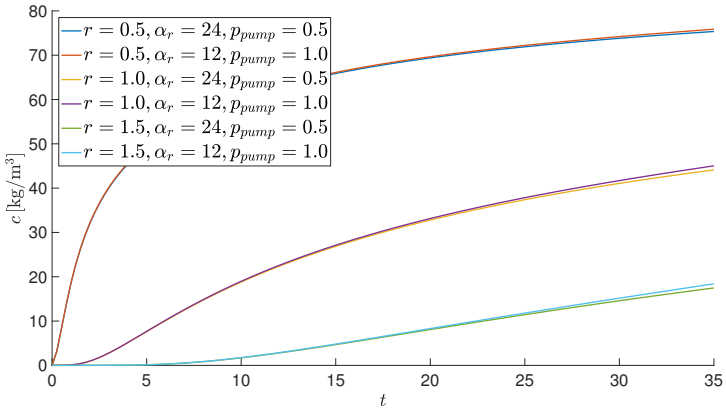


Figure 8.9: *Plots of the concentrations of the bromide tracer $c$ at $z = 6.5$ as function of the time $t$ in seconds. The values of the pump pressure $p_{pump}$ are given in bar.*

8

### 8.5.2 Numerical results of the macroscopic-heterogeneous layered porous medium

Second, we simulated the transport of the bromide tracer through a heterogeneous layered porous medium (see Section 7.3 for a description of this model). The computed bromide concentrations in the soil at different times $t$ and at a depth of 18.5 m (i.e. $z = 6.5$) are plotted in Figure 8.10. Using these parameters, the bromide tracer reaches a distance of 2.5 m in the homogeneous porous medium. While in the heterogeneous layered porous medium, the tracer reaches a maximal distance of 3.1 m after 35 seconds.

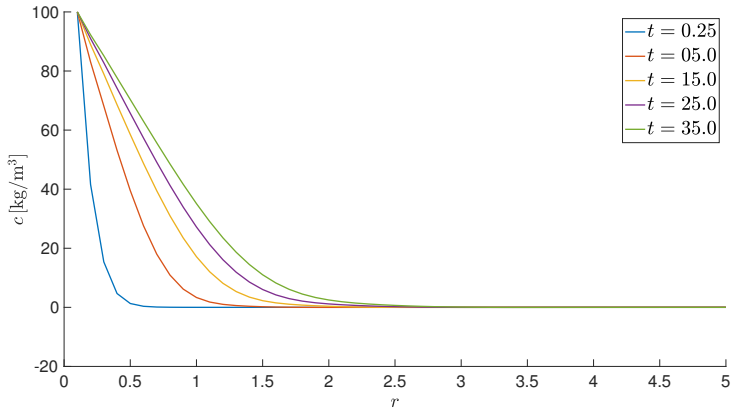


Figure 8.10: *Plots of the concentrations of the bromide tracer $c$ at $z = 6.5$ as function of the radius $r$ in meters, for different times. Given a longitudinal dispersivity of* 12.0 m*, a transversal dispersivity of* 1.0 m *and a pump pressure of* $0.5 \cdot 10^5$ Pa*.*

In Figure 8.11, the numerical results are shown for the computed concentration profiles of the bromide tracer as a function of the time, at different distances from the injection filter and at $z = 6.5$. These results show that the concentration drop is almost 30% of the injection concentration after 0.4 m from the injection filter. At a distance 0.9 m from the injection filter, the concentration of the bromide tracer is approximately 35 kg/m$^3$ in the heterogeneous layered porous medium model.

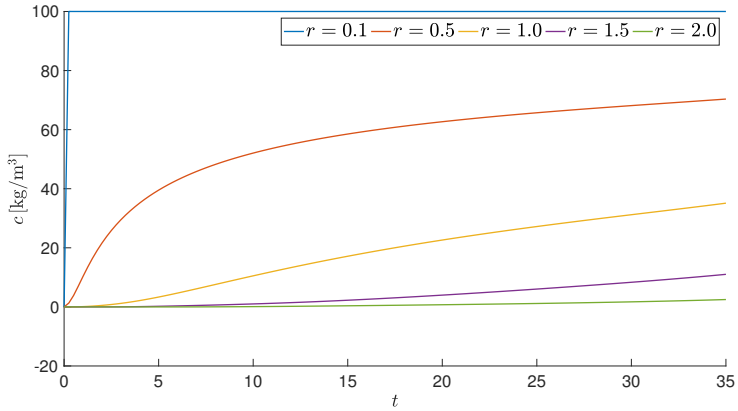


Figure 8.11: *Plots of the concentrations of the bromide tracer $c$ at $z = 6.5$ as function of the time $t$ in seconds. Given a longitudinal dispersivity of* 12.0 m*, a transversal dispersivity of* 1.0 m *and a pump pressure of* $0.5 \cdot 10^5$ Pa*.*

The difference between the numerical results in both models is presented in Figure 8.12, given a longitudinal dispersivity of 12.0 m, a transversal dispersivity of 1.0 m and a pump pressure of $0.5 \cdot 10^5$ Pa. In this figure, the notation $c_h$ is used for the

concentration in the homogeneous model and $c_l$ indicates the concentration in the heterogeneous layered porous medium. It is clear that, for the parameter values chosen, the computed concentration is higher in the heterogeneous layered porous medium than in the homogeneous porous medium, as shown in Figure 8.12. This conclusion is in good agreement with the results mentioned in Chapter 7, where we concluded that water flows faster through heterogeneous layered porous media than through homogeneous porous media.

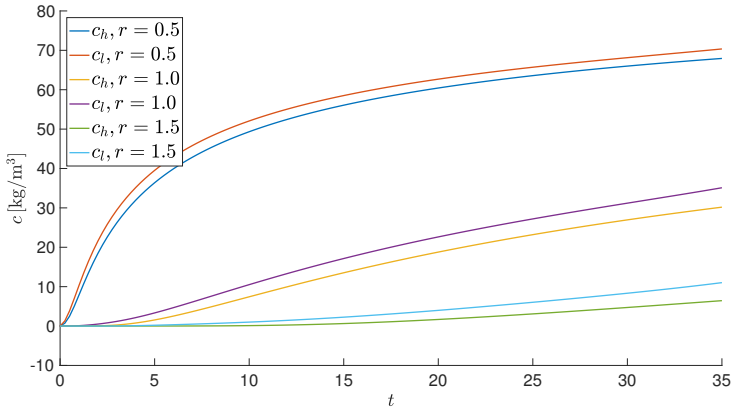


Figure 8.12: *Plots of the concentrations of the bromide tracer $c$ at $z = 6.5$ as function of the time $t$ in seconds, for different distances from the injection filter.*

To investigate the impact of the longitudinal dispersivity, and herewith the microscopic heterogeneity, on the concentration profile in a heterogeneous layered medium, we choose the value of $\alpha_r$ to be twice as large as the value of $\alpha_r$ in the previous simulations. In Figure 8.13 the computed concentration profiles of the bromide tracer as a function of the radius are plotted, at different times $t$ and at 18.5 m depth. In these simulations, the longitudinal dispersivity is 24.0 m, the transversal dispersivity is 1.0 m and the pump pressure is $0.5 \cdot 10^5$ Pa. For these parameter values, the bromide tracer reaches a maximal distance of 3.8 m after 35 seconds, as can be seen in Figure 8.13, while the maximal distance was 3.0 m in the homogeneous porous medium.

In Figure 8.14, the results are presented for the computed concentration profiles of the bromide tracer as a function of the time, at different distances from the injection filter and for $z = 6.5$. At a distance of 0.4 m from the injection filter, the concentration drop is approximately 23.4% of the injection concentration, as we can see in Figure 8.14. Furthermore, the results indicate that the maximal concentrations after 35 seconds, at the distances of 0.9 m and 1.4 m from the injection filter, are 47 $\mathrm{kg/m^3}$ and 22 $\mathrm{kg/m^3}$ respectively.

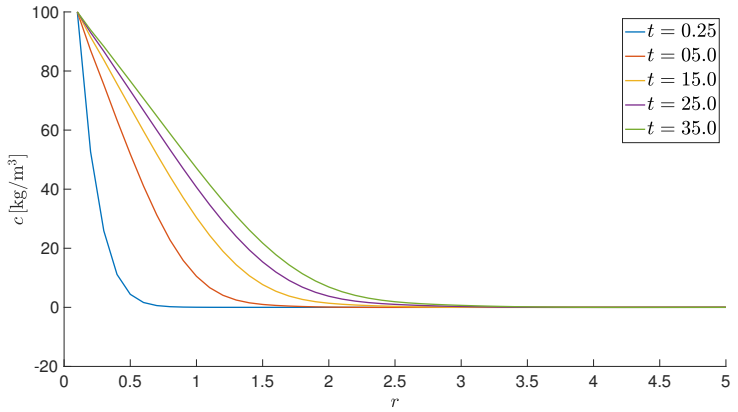


Figure 8.13: *Plots of the concentrations of the bromide tracer $c$ at $z = 6.5$ as function of the radius $r$ in meters, for different times. Using the parameters: $\alpha_r = 24.0$, $\alpha_z = 1.0$ and $p_{pump} = 0.5 \cdot 10^5$.*

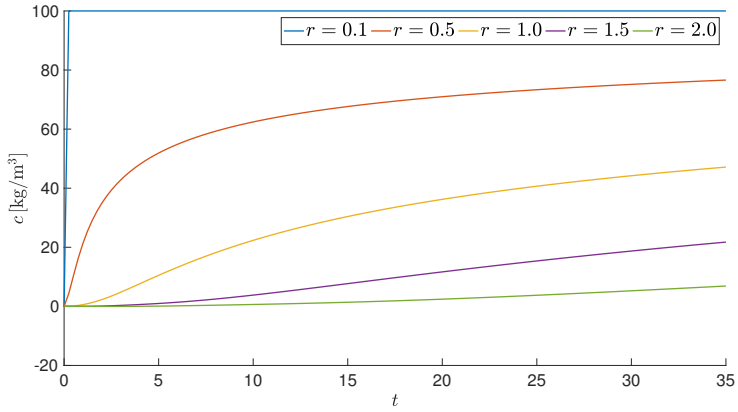


Figure 8.14: *Plots of the concentrations of the bromide tracer $c$ at $z = 6.5$ as function of the time $t$ in seconds. Using the parameters: $\alpha_r = 24.0$, $\alpha_z = 1.0$ and $p_{pump} = 0.5 \cdot 10^5$.*



Hence, from these numerical results we can conclude that a higher value of the longitudinal dispersivity $\alpha_r$ results in a larger distance that can be reached by the bromide tracer. In addition, higher concentration values are detected in the vicinity of the injection filter, when a higher value of the longitudinal dispersivity is used, as shown in Figure 8.15.

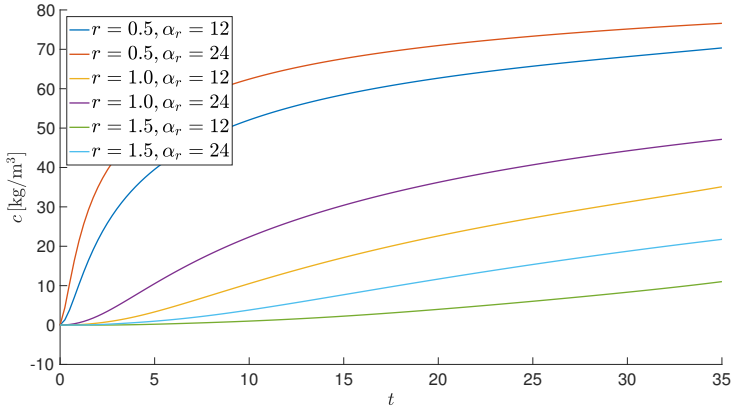


Figure 8.15: *Plots of the concentrations of the bromide tracer* $c$ *at* $z = 6.5$ *as function of the time* $t$ *in seconds. Using the parameters:* $\alpha_z = 1.0$ *and* $p_{pump} = 0.5 \cdot 10^5$.

The impact of a higher pump pressure on the bromide concentration profile is investigated in the following simulations. In these simulations, a pump pressure of $1.0 \cdot 10^5$ Pa is chosen. Furthermore, the longitudinal dispersivity is 12.0 m and the transversal dispersivity is 1.0 m. In Figure 8.16 the computed concentration profiles of the bromide tracer as a function of the radius is depicted, at different times $t$ and at $z = 6.5$. For the chosen parameter values, we notice in Figure 8.16 that the numerical results become unstable and diverge for large times. In Figure 8.17 it is shown that the solution for the concentration becomes unstable for $t > 25$ seconds. The instability may possibly be prevented by using SUPG methods or by using limiters. Moreover, a decrease in the time step size may help to reduce the instabilities, but the problem remains unstable. Another possible strategy could be to make the whole finite element method more implicit by using a monolithic (fully coupled) approach in which a nonlinear problem is solved at each time step in conjunction with the coupled advection-dispersion-Biot problem.

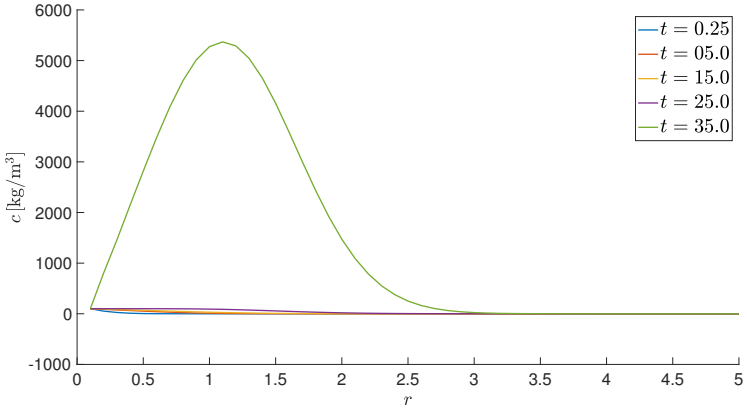


Figure 8.16: *Plots of the concentrations of the bromide tracer $c$ at $z = 6.5$ as function of the radius $r$ in meters, for different times. Using the parameters:* $\alpha_r = 12.0$, $\alpha_z = 1.0$ *and* $p_{pump} = 1.0 \cdot 10^5$.

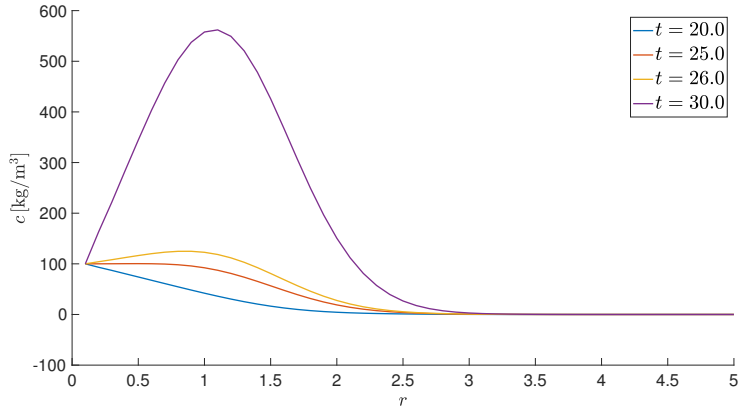


Figure 8.17: *Plots of the concentrations of the bromide tracer $c$ at $z = 6.5$ as function of the radius $r$ in meters, for different times. Using the parameters:* $\alpha_r = 12.0$, $\alpha_z = 1.0$ *and* $p_{pump} = 1.0 \cdot 10^5$.

In Figure 8.18, the results are presented for the computed concentration profiles of the bromide tracer as a function of the time, for $z = 6.5$ and at different distances from the injection filter. With this figure we get a better picture of the instability of the numerical solution for the concentration, when using a higher pump pressure in the heterogeneous layered model. Note that this unstable behaviour did not appear in the homogeneous porous medium in the interval $t \in [0, 35]$ seconds. The reason for these instabilities in the heterogeneous model has not been investigated in this study.

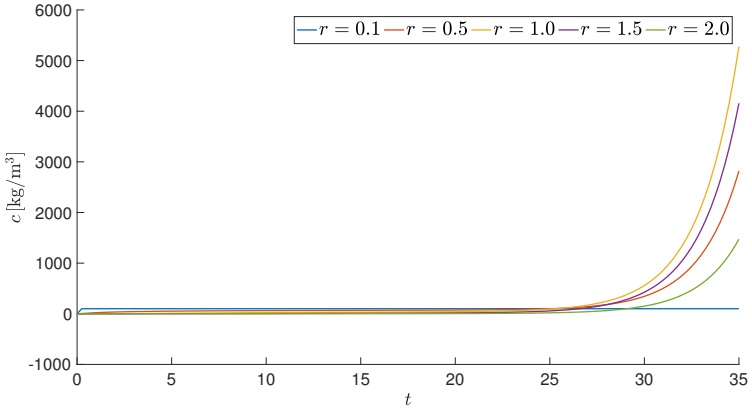


Figure 8.18: *Plots of the concentrations of the bromide tracer $c$ at $z = 6.5$ as function of the time $t$ in seconds. Using the parameters: $\alpha_r = 12.0$, $\alpha_z = 1.0$ and $p_{pump} = 1.0 \cdot 10^5$.*

## 8.6 Discussion and conclusions

The detection of preferential flow paths and the characterisation of their hydraulic properties are important for the development of hydrogeological models in aquifers. Due to lacking information on the aquifer transport behaviour, tracer studies became a prerequisite to obtain reliable transport model predictions and to enhance our understanding of flow paths. Tracer tests offer the possibility to efficiently investigate the aquifer properties and the preferential flow pathways and travel times of the fluid injected into an aquifer.

In this work, we investigated the preferential flow paths of a fluid by injecting a tracer into a heterogeneous layered porous medium and a homogeneous porous medium. For simulating this problem, a tracer model is considered, using bromide ($Br^-$) as a tracer for water flow. Based on the combination of Biot's theory of linear poroelasticity and the advection-dispersion equation, a coupled model describing solute transport in deforming soil is proposed, taking into account nonlinear permeability. The model is discretised by a continuous Galerkin finite element method based on Taylor-Hood elements, combined with the implicit Euler scheme for time stepping.

We started by simulating the transport model of the bromide tracer through homogeneous porous medium. From the simulation results, we can conclude that choosing a higher value for the longitudinal dispersivity (i.e. a larger microscopic heterogeneity) results in a larger distance that can be reached by the bromide tracer. In addition, higher concentration values are computed in the vicinity of the injection filter. The same numerical results could be obtained by using a high value of the pump pressure, which increases the flow velocity and hence leads to a larger mechanical dispersion. Furthermore, from these numerical results we can conclude that the rate of solute transport by molecular diffusion is negligibly small relative to the rates of solute transport by advection and dispersion. Since the rate of solute transport by mechanical dispersion is in balance with the rate by advection, we can further conclude that

for a twice microscopically more homogeneous porous medium it is necessary that the applied pump pressure is twice as high in order to obtain the same penetration of the bromide tracer.

Subsequently, the transport of the bromide tracer through a layered, macroscopic-heterogeneous porous medium is simulated. For the chosen parameter values, the numerical results pointed out that the computed concentration is higher in the heterogeneous layered porous medium than in the homogeneous porous medium. This conclusion is in good agreement with the results mentioned in Chapter 7, where we concluded that water flows faster through heterogeneous layered porous media than through homogeneous porous media. Furthermore, similarly to the homogeneous porous medium model, the simulation results indicated that a higher value of the longitudinal dispersivity results in a larger distance that can be reached by the bromide tracer. In addition, the computed concentrations are higher in the vicinity of the injection filter when a higher value of the longitudinal dispersivity is used. However, high pump pressures resulted in unstable solutions in which the concentration diverges for large times. In contrast, this unstable behaviour did not appear in the homogeneous porous medium in the interval $t \in [0, 35]$ seconds. The instability may possibly be prevented by using a Streamline Upwind Petrov Galerkin method, however, this method introduces an additional finite element discretisation error of order $\mathcal{O}(h)$, where $h$ denotes a measure for the mesh size. Better alternatives are methods based on flux and slope limiting. Another possible strategy could be to make the whole finite element method more implicit by using a monolithic (fully coupled) approach in which a nonlinear problem is solved at each time step in conjunction with the coupled advection-dispersion-Biot problem. This has not yet been done in obtaining the preliminary results of this chapter and we intend to elaborate these possibilities in a future manuscript.

**Acknowledgements** We would like to sincerely thank engineering and consultancy company Fugro GeoServices B.V. for providing us with the measurements of the laboratory tests and the field experiments.

Chapter 9

# Conclusions

*In the present dissertation, four research objectives have been addressed: the construction of a methodology to investigate the impact of mechanical vibrations and pressure pulses on the flow through porous media and to quantify the impact of variation in the input parameters on the model output using Monte Carlo simulations; the investigation of the applicability of the permeability-porosity relation based on the percolation theory on two-dimensional and three-dimensional poroelasticity problems; the development of a finite element solver for linear and nonlinear poroelasticity problems, which is used to compare the predictions of linear poroelasticity with those of large-deformation poroelasticity in the context of a two-dimensional poroelasticity model; and the exploration of the difference between the fluid flow in a model with a homogeneous porous medium and the same fluid flow through a heterogeneous layered porous medium. The conclusions from the findings of each research objective are given in this chapter.*

## 9.1 Uncertainty quantification using Monte Carlo simulations

In the first stage of this research, the quasi-static Biot's poroelasticity system with nonlinear Kozeny-Carman permeability is solved using the continuous Galerkin finite element method based on Taylor-Hood elements, combined with the implicit Euler scheme for time stepping.

The first simulated problem, is an axial flow owing to a pressure difference. In this simulation we consider water injection into a tube filled with a deformable fluid-saturated porous medium (Chapter 2). To begin with, soil vibrations are applied on the casing of the tube as oscillatory displacement boundary condition. Numerical results showed that large amplitudes and high frequencies of the imposed mechanical vibrations lead to high volumetric flow rates for positive values of the phase velocity. On the other hand, for negative values of the phase velocity, the vibrations lead to a decrease in the volumetric flow rate at the right end of the tube. As expected, the water flow, which is directed to the right, is being stimulated by waves travelling in the same direction, while waves travelling in the opposite direction counteract the flow, resulting in negative volumetric flow rates in case the force applied by the oppositely directed waves is larger than the pump pressure. In this dissertation, these effects have been quantified. Subsequently, applying an oscillating load on the casing of the tube showed that water flows faster through porous media with large grain sizes and/or high initial porosities. On the other hand, variation in the values of Young's modulus and Poisson's ratio indicated that these parameters do not have a large impact on the volumetric flow rate. Numerical simulations of pressure pulsing pointed out that injection pulses with small relative pulse times lead to a major increase in the volumetric flow rate, while an increasing pulse period results in a slight increase in the flow rate. Most importantly, we can conclude that pulsed injection has a beneficial effect on the water flow through porous media. In conclusion, pressure pulses and soil vibrations in the direction of the flow increase the amount of water that can be injected into a tube filled with a deformable fluid-saturated porous medium.

The second simulated problem is the injection of water into an aquifer where the fluid flows radially outward owing to a pressure difference (Chapter 3). The study contains Monte Carlo simulations to quantify the impact of variation in the soil characteristics and the injection parameters on the time average of the volumetric flow rate at a particular distance from the injection filter. Furthermore, two different injection methods are tested and compared with each other in order to determine the best infiltration method that can be used for the storage of rainwater in the shallow subsurface. Finally, two different types boundary conditions are considered to describe the fluid injection. To reduce the Monte Carlo error, simulations should be performed with thousands of samples. However, as in our case each sample simulation takes more than one hour, we instead adopted 300 samples. The first boundary condition that we used is a Neumann boundary condition for the pore pressure, where the volumetric flow rate is prescribed at the injection filter. The numerical simulations of pulsed injection pointed out that injection pulses with small pulse periods lead to a major increase in the volumetric flow rate, while an increasing relative pulse time and maximum injection velocity result in a slight increase in the flow rate.

On the other hand, variation in the values of the soil characteristics indicated that these parameters do not have a large impact on the volumetric flow rate. On the contrary, numerical simulations using a Dirichlet boundary condition, in which the boundary pore pressure caused by the injection of the fluid is prescribed, showed that water flows faster through porous media with large mean grain sizes or high initial porosities. However, from these results we could conclude that the volumetric flow rate is invariant under variation in the values of Young's modulus and Poisson's ratio. In addition, pressure pulses with large relative pulse times and maximum injection pressures lead to an increase in the volumetric flow rate. However, the numerical results pointed out that the pulse period does not have a significant impact on the water flow rate. Most importantly, we can conclude that, regardless of the type of soil into which we inject, by applying pulsed injection we can increase the amount of rainwater that can be stored quickly in the underground.

## 9.2 Permeability-porosity relations

Additionally, we investigated the permeability-porosity relation that is used in these poroelasticity simulations. In this research area, the new-developed network-inspired permeability-porosity relation is applied on two two-dimensional poroelasticity problems (Chapter 4) and on a three-dimensional problem (Chapter 5). This numerical experiment is designed in order to analyse the applicability of this microscopic network-inspired relation on the macro-scale. Furthermore, the results obtained with the network-inspired relation are compared to the Kozeny-Carman relation which is often used for these types of physical problems. Starting with the two-dimensional poroelasticity problems: In the first poroelasticity problem, a high pump pressure is imposed in the inlet of a porous medium package. This high pressure forces the grains to move towards the outlet. In the second problem, the poroelastic package is squeezed by applying a load on the middle of the top and bottom edges of the domain. The three-dimensional problem studies the infiltration of a fluid into a porous medium. On a part of the top edge of the domain, a vertical mechanical load is applied. The purpose of considering these poroelasticity problems is to create a large density of the grains in the computational domain which results in a decrease of the porosity. Hence, we can emphasise the difference between the porosity-permeability relations. In these problems, Biot's model for poroelasticity is used to determine the water pressure; and the displacements of the grains that are needed to compute the porosity. From the porosity, the permeability is determined either by the network-inspired relation or by the Kozeny-Carman relation. Depending on the topology, three different percolation thresholds, corresponding with a rectangular network, triangular structured network and triangular unstructured network, are distinguished. However, since the topology of macro-scale porous media is not known, computations are also performed with different values of the percolation threshold to investigate the influence of the percolation threshold (and hence the topology of the porous medium) on the flow rate.

First, the problems are solved with the Kozeny-Carman relation, the network-inspired relation based on the triangular structured network and the relation based on the rectangular network. From the numerical results we conclude that the perme-

ability obtained using the Kozeny-Carman relation exhibits a larger decrease than the permeabilities obtained with the network-inspired relations. In contrast, the porosity profile is not affected significantly by the selected permeability-porosity relation. Second, the time average of the volumetric flow rate was computed for different values of the percolation threshold. For low percolation thresholds, the network-inspired relation results in higher flow rates than the Kozeny-Carman relation. In addition, it is shown that the flow rate changes significantly as a function of the percolation threshold which means that the water flow depends on the topology of the connected pore space. For high percolation thresholds, spurious oscillations appeared due to the violation of the M-matrix property in the discretisation matrix that resulted from the convergence of Biot's problem to the related saddle point problem, as proven in Chapter 4. The results for these percolation thresholds could be improved by using a finer grid.

For the studied problems and the set of parameters chosen, we noticed that the applied permeability-porosity relations result in small changes in the porosity while a major change is realised in the permeability profiles. A possible explanation for this behaviour is that the relation between the velocity field and the change of the displacements in time as stated in the continuity equation, is not strong enough to lead to significant changes in the porosity profile.

## 9.3 Nonlinear poroelasticity equations

In this research topic, we compare the predictions of linear poroelasticity with those of large-deformation poroelasticity in the context of a two-dimensional model problem where flow through elastic, saturated porous media, under applied mechanical oscillations, is considered (Chapter 6). Linear poroelasticity is a good model for very small deformations, besides that it is a simple model to solve and is computationally cheap. On the other hand, the well-known large-deformation theory is more suitable to solve poroelasticity problems with moderate to large deformations. However, adopting this nonlinear mathematical model increases the computational complexity and cost, especially because the basis functions in the finite element code have to be updated in every iteration within the time integration. The suitability of the proposed methodologies to model flow through elastic porous media under finite deformations is demonstrated using an illustrative numerical example. In this example, injection of a fluid into a two-dimensional fully saturated porous medium is considered, assuming that the solid material is subjected to surface mechanical oscillations with different amplitudes. In addition, the impact of introducing a deformation-dependent permeability according to the Kozeny-Carman equation is explored. For solving this physical problem, three different mathematical models are considered: linear poroelasticity combined with constant permeability ($L_C$), linear poroelasticity combined with the Kozeny-Carman equation ($L_{KC}$) and nonlinear poroelasticity combined with the Kozeny-Carman equation ($N_{KC}$).

Firstly, by considering the numerical example without applied oscillations, we have shown that the nonlinearity has more effect on the displacement than on the pressure field. This is a consequence of the nonlinearity in the displacements variable in the large-deformation poroelasticity equations. On the contrary, the impact of including

a deformation-dependent permeability was larger on the pressure field than on the solid deformations. The reason for this behaviour is that the permeability relationship is directly related to the pressure through Darcy's law. Secondly, the impact of the applied mechanical oscillations was investigated by applying standing waves on the top surface of the solid matrix. From the numerical results, we noticed that the oscillatory behaviour was visible in the displacement and pressure profiles. Moreover, the differences between the three models $(L_C)$, $(L_{KC})$ and $(N_{KC})$ are small for small applied oscillations, while these differences become larger by an increasing amplitude of the applied oscillation. Hence, the errors in the simulated displacement and pressure as result of solving the linear poroelasticity model in the finite-deformation range, increase when we choose applied oscillations with large amplitudes. The difference between the linear models can be explained by the impact of the large deformations on the porosity, which in turn has a larger impact on the Kozeny-Carman permeability. Note that this influence is not taken into account in the linear model combined with constant permeability.

In summary, for this particular problem and the chosen parameter values, the use of the linear poroelasticity model for solving physical problems with finite deformations results in errors in the displacement and pressure fields. These errors are mainly the consequence of the lack of the kinematic nonlinearity, in which the geometry of the domain evolves with the deformation resulting in a nonlinear term in the poroelasticity equations. To reduce these errors, especially in the pressure field, the linear poroelasticity model can preferably be combined with a deformation-dependent permeability, such as the Kozeny-Carman relationship. In addition, the kinematic nonlinearity can be incorporated.

## 9.4 Heterogeneous versus homogeneous porous media

In the above-mentioned models, the porous medium is assumed to be homogeneous. However, all natural soils are heterogeneous mixtures of broken rocks and minerals, living organisms, and humus. To determine the composition of soil, laboratory tests and field experiments are needed. However, since these tests and experiments can only been performed on a limited number of locations in the soil, flow through the voids in a soil is usually modelled assuming a homogeneous soil mixture rather than a heterogeneous mixture. In this research area, we investigated whether this simplification is justified by exploring the difference between the flow of water in a model with a heterogeneous layered porous medium and a model with a homogeneous porous medium.



Firstly, this difference is studied by considering two three-dimensional physical problems, describing the infiltration of a fluid through a filter into an aquifer (Chapter 7). In the first simulated problem, the infiltration is stimulated by a constant pump pressure. Furthermore, mechanical oscillations, that are assumed to be induced by the injection of water, are imposed on the infiltration boundary. In the second numerical experiment, the prescribed pump pressure has a pulsing behaviour rather than being constant. To describe this behaviour, rectangular pulse waves are used with different periods and pulse times. These problems are solved using Biot's theory of

linear poroelasticity with single-phase flow, considering nonlinear permeability. We started by performing Monte Carlo simulations to the values of Young's modulus and Poisson's ratio, considering a physical problem without imposing mechanical oscillations nor pressure pulses. The numerical results from these simulations indicated that Young's modulus and Poisson's ratio do not have a large impact on the volumetric flow rate. After applying mechanical oscillations on the infiltration boundary in the form of standing waves with different amplitudes, the numerical results showed that an increase in the amplitude leads to an increase in the volumetric flow rate. Moreover, this impact is larger on the water flow in the heterogeneous layered porous medium than on the water flow in the homogeneous porous medium. However, the change in the volumetric flow rate due to these oscillations is not significant. Finally, numerical simulations of pressure pulsing pointed out that injection pulses does not lead to a higher water flow rate, regardless of the type of soil into which we inject. However, if pressure pulses are preferable to a constant pump pressure, large pulse times must be selected in order to increase the water outflow. More important, water flows twice as fast through heterogeneous layered porous media than through homogeneous porous media, in all problems tested.

Secondly, we investigated the difference between a heterogeneous layered porous medium and a homogeneous porous medium by injecting a bromide tracer for water flow into an aquifer (Chapter 8). Based on the combination of Biot's theory of linear poroelasticity and the advection-dispersion equation, a coupled model describing solute transport in deforming soil is proposed, taking into account nonlinear permeability. The simulation results showed that a larger longitudinal dispersivity (i.e. a larger microscopic heterogeneity) results in a larger distance that can be reached by the bromide tracer. In addition, higher concentration values are computed in the vicinity of the injection filter. In the homogeneous porous medium model, similar results could be obtained by using a high value of the pump pressure, which increases the flow velocity and hence leads to a larger mechanical dispersion. Consequently, from these numerical results follows that the rate of solute transport by molecular diffusion is negligibly small relative to the rates of solute transport by advection and dispersion. However, high pump pressures resulted in unstable solutions of the macroscopic-heterogeneous layered porous medium model. The instability may possibly be prevented by using a Streamline Upwind Petrov Galerkin method, however, this method introduces an additional finite element discretisation error of order $\mathcal{O}(h)$, where $h$ denotes a measure for the mesh size. Better alternatives are methods based on flux and slope limiting. Another possible strategy could be to make the whole finite element method more implicit by using a monolithic (fully-coupled) approach in which a nonlinear problem is solved at each time step in conjunction with the coupled advection-dispersion-Biot problem. Above all, the numerical results pointed out that the computed concentration is higher in the heterogeneous layered porous medium than in the homogeneous porous medium. This conclusion is in good agreement with the results mentioned in Chapter 7, where we concluded that water flows faster through heterogeneous layered porous media than through homogeneous porous media.

# Bibliography


[1] A. C. T. Aarts and G. Ooms. Net flow of compressible viscous liquids induced by travelling waves in porous media. *J. Eng. Math.*, 34:435 – 450, 1998.

[2] G. Aguilar, F. Gaspar, F. Lisbona, and C. Rodrigo. Numerical stabilization of Biot's consolidation model by a perturbation on the flow equation. *Int. J. Numer. Meth. Engng.*, 75:1282 – 1300, 2008.

[3] E. S. Almeida and R. L. Spilker. Finite element formulations for hyperelastic transversely isotropic biphasic soft tissues. *Comput. Methods Appl. Mech. Engrg.*, 151:513 – 538, 1998.

[4] L. Anand. Moderate deformations in extension-torsion of incompressible isotropic elastic materials. *J. Mech. Phys. Solids*, 34(3):293 – 304,, 1986.

[5] L. Auton and C. MacMinn. From arteries to boreholes: steady-state response of a poroelastic cylinder to fluid injection. In *Proc. R. Soc. A*, volume 473, page 20160753, 2017.

[6] S. Badia, A. Quaini, and A. Quarteroni. Coupling Biot and Navier-Stokes equations for modelling fluid-poroelastic media interaction. *J. Comput. Phys.*, 228:7986 – 8014, 2009.

[7] I. Balberg. Recent developments in continuum percolation. *Philosophical Magazine B*, 56(6):991 – 1003, 1987.

[8] M. Bause, F. Radu, and U. Köcher. Space-time finite element approximation of the Biot poroelasticity system with iterative coupling. *Comput. Methods Appl. Mech. Engrg.*, 320:745 – 768, 2017.

[9] J. Bear and M. Corapcioglu. Mathematical model for Regional Land Subsidence Due to Pumping: 1. Integrated Aquifer Subsidence Equations Based on Vertical Displacement Only. *Water Resour. Res.*, 17:937 – 946, 1981.

[10] A. Bensoussan, J.-L. Lions, and G. Papanicolaou. *Asymptotic analysis for periodic structures*. American Mathematical Soc., 2011.

[11] I. A. Beresnev and P. A. Johnson. Elastic-wave stimulation of oil production: A review of methods and results. *Geophysics*, 59:1000 – 1017, 1994.

[12] L. Berger, R. Bordas, K. Burrowes, V. Grau, S. Tavener, and D. Kay. A poroelastic model coupled to a fluid network with applications in lung modelling. *Int. J. Numer. Meth. Biomed. Engng.*, 32(1), 2016.

[13] L. Berger, R. Bordas, D. Kay, and S. Tavener. Stabilized lowest-order finite element approximation for linear three-field poroelasticity. *SIAM J. Sci. Comput.*, 37(5):A2222 – A2245, 2015.

[14] B. Berkowitz and R. P. Ewing. Percolation theory and network modeling applications in soil physics. *Surveys in Geophysics*, 19:23 – 72, 1998.

[15] Y. Bernabe, W. F. Brace, and B. Evans. Permeability, porosity and pore geometry of hot-pressed calcite. *Mechanics of Materials*, 1(3):173 – 183, 1982.

[16] M. A. Biot. General Theory of Three-Dimensional Consolidation. *J. Appl. Phys.*, 12:155 – 164, 1941.

[17] M. A. Biot. Theory of Elasticity and Consolidation for a Porous Anisotropic Solid. *J. Appl. Phys.*, 26(2):182 – 185, 1955.

[18] M. A. Biot. General Solutions of the Equations of Elasticity and Consolidation for a Porous Material. *J. Appl. Mech.*, 78:91 – 96, 1956.

[19] P. B. Bochev, C. R. Dohrmann, and M. D. Gunzburger. Stabilization of low-order mixed finite elements for the Stokes equations. *SIAM J. Numer. Anal.*, 44(1):82 – 101, 2006.

[20] A. Bockelmann, D. Zamfirescu, T. Ptak, P. Grathwohl, and G. Teutsch. Quantification of mass fluxes and natural attenuation rates at an industrial site with a limited monitoring network: a case study. *J. Contam. Hydrol.*, 60:97 – 121, 2003.

[21] D. Boffi, F. Brezzi, and M. Fortin. *Mixed Finite Element Methods and Applications*, volume 44. Springer, 2013.

[22] R. I. Borja, J. Choo, and J. A. White. Rock Moisture Dynamics, Preferential Flow, and the Stability of Hillside Slopes. In *Multi-Hazard Approaches to Civil Infrastructure Engineering*, pages 443 – 464. Springer, 2016.

[23] M. Borregales, K. Kumar, J. M. Nordbotten, and F. A. Radu. Iterative solvers for Biot model under small and large deformation. *arXiv:1905.12996v1 [math.NA]*, 2019.

[24] M. Borregales, F. A. Radu, K. Kumar, and J. M. Nordbotten. Robust iterative schemes for non-linear poromechanics. *Comput. Geosci.*, 22:1021 – 1038, 2018.

[25] J. W. Both, M. Borregales, J. M. Nordbotten, K. Kumar, and F. A. Radu. Robust fixed stress splitting for Biot's equations in heterogeneous media. *Appl. Math. Lett.*, 68:101 – 108, 2017.

[26] A. F. Bower. *Applied Mechanics of Solids*. CRC press, 2010.

[27] J. E. Bowles. *Foundation analysis and design*. McGraw-Hill, 1996.

[28] D. Braess. *Finite elements: Theory, fast solvers, and applications in solid mechanics*. Cambridge University Press, 2001.

[29] D. Braess. *Finite elements: Theory, fast solvers, and applications in solid mechanics*. Cambridge University Press, 2007.

[30] S. C. Brenner and L. R. Scott. *The Mathematical Theory of Finite Element Methods*. Springer Science & Business Media, 2007.

[31] F. Brezzi and J. Pitkäranta. On the stabilization of finite element approximations of the Stokes equations. In *Efficient Solutions of Elliptic Systems*, volume 10, pages 11 – 19. Springer, 1984.

[32] S. R. Broadbent and J. M. Hammersley. Percolation processes: I. Crystals and mazes. In *Mathematical Proceedings of the Cambridge Philosophical Society*, volume 53, pages 629 – 641. Cambridge University Press, 1957.

[33] M. K. Brun, E. Ahmed, I. Berre, J. M. Nordbotten, and F. A. Radu. Monolithic and splitting solution schemes for fully coupled quasi-static thermo-poroelasticity with nonlinear convective transport. *arXiv:1902.05783*, 2019.

[34] C. Callari and A. Abati. Finite element methods for unsaturated porous solids and their application to dam engineering problems. *Comput. Struct.*, 87:485 – 501, 2009.

[35] P. C. Carman. Fluid Flow through Granular Beds. *Trans. Inst. Chem. Eng.*, 15:150 – 166, 1937.

[36] N. Castelletto, J. A. White, and H. A. Tchelepi. Accuracy and convergence properties of the fixed-stress iterative solution of two-way coupled poromechanics. *Int. J. Numer. Anal. Meth. Geomech.*, 39:1593 – 1618, 2015.

[37] M. A. Celia. Geological storage of captured carbon dioxide as a large-scale carbon mitigation option. *Water Resour. Res.*, 53:3527 – 3533, 2017.

[38] R. Chapuis and M. Aubertin. *Predicting the coefficient of permeability of soils using the Kozeny-Carman equation. Report EPM-RT-2003-03*. Département des génies civil, géologique et des mines; École Polytechnique de Montréal, 2003.

[39] A. H. D. Cheng. *Poroelasticity. Theory and Applications of Transport in Porous Media*, volume 27. Springer, 2016.

[40] K. Cliffe, M. Giles, and R. S. A. Teckentrup. Multilevel Monte Carlo methods and applications to elliptic PDEs with random coefficients. *Comput. Visual. Sci.*, 14(1):3 – 15, 2011.

[41] S. C. Cowin. Bone poroelasticity. *J. Biomech.*, 32:217 – 238, 1999.

[42] B. C. Davidson, T. Spanos, and M. B. Dusseault. Laboratory Experiments on Pressure Pulse Flow Enhancement in Porous Media. In *the Proceedings of the CIM Regina Technical Meeting*, 1999.

[43] R. Dean, X. Gai, C. Stone, and S. Minkoff. A Comparison of Techniques for Coupling Porous Flow and Geomechanics. *Spe Journal*, 11(1):132 – 140, 2006.

[44] C. R. Dohrmann and P. B. Bochev. A stabilized finite element method for the Stokes problem based on polynomial pressure projections. *Internat. J. Numer. Methods Fluids*, 46:183 – 201, 2004.

[45] J. Dumais and Y. Forterre. "Vegetable Dynamicks": The Role of Water in Plant Movements. *Annu. Rev. Fluid Mech.*, 44:453 – 478, 2012.

[46] M. Dusseault. Petroleum Geomechanics: Excursions into Coupled Behaviour. *J. Can. Petrol. Technol.*, 38:10 – 14, 1999.

[47] G. Dziuk and C. Elliott. Finite elements on evolving surfaces. *IMA J. Numer. Anal.*, 27:262 – 292, 2007.

[48] A. Ern and J.-L. Guermond. *Theory and Practice of Finite Elements*, volume 159. Springer Science & Business Media, 2013.

[49] M. Ferronato, G. Gambolati, C. Janna, and P. Teatini. Numerical modelling of regional faults in land subsidence prediction above gas/oil reservoirs. *Int. J. Numer. Anal. Meth. Geomech.*, 32:633 – 657, 2008.

[50] G. Franceschini, D. Bigoni, P. Regitnig, and G. Holzapfel. Brain tissue deforms similarly to filled elastomers and follows consolidation theory. *J. Mech. Phys. Solids*, 54:2592 – 2620, 2006.

[51] G. Fu. A high-order HDG method for the Biot's consolidation model. *Comput. Math. Appl.*, 77(1):237 – 252, 2019.

[52] G. Gambolati, P. Teatini, D. Baú, and M. Ferronato. Importance of poroelastic coupling in dynamically active aquifers of the Po river basin, Italy. *Water Resour. Res.*, 36(9):2443 – 2459, 2000.

[53] F. J. Gaspar, F. J. Lisbona, and P. N. Vabishchevich. A finite difference analysis of Biot's consolidation model. *Appl. Numer. Math.*, 44(4):487 – 506, 2003.

[54] F. J. Gaspar, F. J. Lisbona, and P. N. Vabishchevich. Staggered grid discretizations for the quasi-static Biot's consolidation problem. *Appl. Numer. Math.*, 56(6):888 – 898, 2006.

[55] D. Gawin, P. Baggio, and B. A. Schrefler. Coupled heat, water and gas flow in deformable porous media. *Internat. J. Numer. Methods Fluids*, 20:969 – 987, 1995.

[56] Geotechnical parameters. `http://www.geotechdata.info/parameter/parameter.html`. Accessed on 23 May 2017.

[57] J. B. Haga, H. Osnes, and H. P. Langtangen. On the causes of pressure oscillations in low-permeable and low-compressible porous media. *Int. J. Numer. Anal. Meth. Geomech.*, 36(12):1507 – 1522, 2012.

[58] H. Hencky. The law of elasticity for isotropic and quasi-isotropic substances by finite deformations. *J. Rheol.*, 2(2):169 – 176, 1931.

[59] J. Hommel, E. Coltman, and H. Class. Porosity-Permeability Relations for Evolving Pore Space: A Review with a Focus on (Bio-)geochemically Altered Porous Media. *Transp. Porous Med.*, 124(2):589 – 629, 2018.

[60] Homogeneous and heterogeneous mixtures. From Wikipedia, the free encyclopedia. Accessed on 19 November 2019.

[61] L. Hu, P. H. Winterfeld, P. Fakcharoenphol, and Y.-S. Wu. A novel fully-coupled flow and geomechanics model in enhanced geothermal reservoirs. *Journal of Petroleum Science and Engineering*, 107:1 – 11, 2013.

[62] X. Hu, L. Mu, and X. Ye. Weak Galerkin method for the Biot's consolidation model. *Comput. Math. Appl.*, 75:2017 – 2030, 2018.

[63] X. Hu, C. Rodrigo, F. J. Gaspar, and L. T. Zikatanov. A nonconforming finite element method for the Biot's consolidation model in poroelasticity. *J. Comput. Appl. Math.*, 310:143 – 154, 2017.

[64] M. K. Hubbert. Darcy's law and the field equations of the flow of underground fluids. *Hydrolog. Sci. J.*, 2(1):23 – 59, 1957.

[65] T. J. Hughes, G. R. Feijóo, L. Mazzei, and J.-B. Quincy. The variational multiscale method – a paradigm for computational mechanics. *Comput. Methods Appl. Mech. Engrg.*, 166:3 – 24, 1998.

[66] T. J. Hughes, L. P. Franca, and M. Balestra. A new finite element formulation for computational fluid dynamics: V. Circumventing the Babuška-Brezzi condition: A stable Petrov-Galerkin formulation of the Stokes problem accommodating equal-order interpolations. *Comput. Methods Appl. Mech. Engrg.*, 59:85 – 99, 1986.

[67] J. D. Istok. *Groundwater Modeling by the Finite Element Method*, volume 13. American Geophysical Union (AGU), Washington, D.C., 1989.

[68] B. Jha and R. Juanes. A locally conservative finite element framework for the simulation of coupled flow and reservoir geomechanics. *Acta Geotech.*, 2(3):139 – 153, 2007.

[69] R. Juanes, B. Jha, B. Hager, J. Shaw, A. Plesch, L. Astiz, J. Dieterich, and C. Frohlich. Were the May 2012 Emilia-Romagna earthquakes induced? A coupled flow-geomechanics modeling assessment. *Geophys. Res. Lett.*, 43(13):6891 – 6897, 2016.

[70] J. van Kan, A. Segal, and F. Vermolen. *Numerical Methods in Scientific Computing*. VSSD, Delft, 2008.

[71] J. Kim, H. A. Tchelepi, and R. Juanes. Stability, Accuracy and Efficiency of Sequential Methods for Coupled Flow and Geomechanics. In *SPE Reservoir Simulation Symposium*. Society of Petroleum Engineers, 2009.

[72] C. E. Koltermann and S. M. Gorelick. Fractional packing model for hydraulic conductivity derived from sediment mixtures. *Water Resour. Res.*, 31(12):3283 – 3297, 1995.

[73] D. C. Koppenol. *Biomedical implications from mathematical models for the simulation of dermal wound healing*. PhD thesis, DIAM, Delft University of Technology, 2017.

[74] J. Korsawe and G. Starke. A Least-Squares Mixed Finite Element Method for Biot's Consolidation Problem in Porous Media. *SIAM J. Numer. Anal.*, 43(1):318 – 339, 2005.

[75] J. Kozeny. Uber Kapillare Leitung der Wasser in Boden. *Royal Academy of Science, Vienna, Proc. Class I*, 136:271 – 306, 1927.

[76] Z. W. Kundzewicz and P. Döll. Will groundwater ease freshwater stress under climate change? *Hydrolog. Sci. J.*, 54(4):665 – 675, 2009.

[77] L. G. Leal. *Advanced Transport Phenomena: Fluid Mechanics and Convective Transport Processes*, volume 7. Cambridge University Press, 2007.

[78] M. Leistra and J. J. T. I. Boesten. Measurement and Computation of Movement of Bromide Ions and Carbofuran in Ridged Humic-Sandy Soil. *Arch. Environ. Contam. Toxicol.*, 59(1):39 – 48, 2010.

[79] R. W. Lewis and B. Schrefler. A Fully Coupled Consolidation Model of the Subsidence of Venice. *Water Resour. Res.*, 14(2):223 – 230, 1978.

[80] F. List and F. A. Radu. A study on iterative methods for solving Richards' equation. *Comput. Geosci.*, 20:341 – 353, 2016.

[81] P. Longuemare, M. Mainguy, P. Lemonnier, A. Onaisi, C. Gérard, and N. Koutsabeloulis. Geomechanics in Reservoir Simulation: Overview of Coupling Methods and Field Case Study. *Oil & gas science and technology*, 57(5):471 – 483, 2002.

[82] P. Luo. *Multigrid Method for the Coupled Free Fluid Flow and Porous Media System*. PhD thesis, DIAM, Delft University of Technology, 2017.

[83] P. Luo, C. Rodrigo, F. J. Gaspar, and C. W. Oosterlee. Multigrid method for nonlinear poroelasticity equations. *Comput. Visual. Sci.*, 17:255 – 265, 2015.

[84] C. W. MacMinn, E. R. Dufresne, and J. S. Wettlaufer. Large Deformations of a Soft Porous Material. *Phys. Rev. Applied*, 5:044020, 2016.

[85] B. Markert. *Porous Media Viscoelasticity with Application to Polymeric Foams*. PhD thesis, Institut für Mechanik Lehrstuhl II, Universität Stuttgart, 2005.

[86] M. Massabó, R. Cianci, and O. Paladino. An Analytical Solution of the Advection Dispersion Equation in a Bounded Domain and Its Application to Laboratory Experiments. *Journal of Applied Mathematics*, 2011:1 – 14, 2011.

[87] I. Masters, W. Pao, and R. Lewis. Coupling temperature to a double-porosity model of deformable porous media. *Int. J. Numer. Meth. Engng.*, 49(3):421 – 438, 2000.

[88] G. Mavko and A. Nur. The effect of a percolation threshold in the Kozeny-Carman relation. *Geophysics*, 62(5):1480 – 1482, 1997.

[89] A. McCauley, C. Jones, and J. Jacobsen. Basic soil properties. *Soil and water management module 1*, 1:1 – 12, 2005.

[90] A. Mikelić and M. F. Wheeler. Convergence of iterative coupling for coupled flow and geomechanics. *Computational Geosciences*, 17(3):455 – 461, 2013.

[91] S. E. Minkoff, C. M. Stone, S. Bryant, M. Peszynska, and M. F. Wheeler. Coupled fluid flow and geomechanical deformation modeling. *J. Pet. Sci. Eng.*, 38:37 – 56, 2003.

[92] E. Moeendarbary, L. Valon, M. Fritzsche, A. R. Harris, D. A. Moulding, A. J. Thrasher, E. Stride, L. Mahadevan, and G. T. Charras. The cytoplasm of living cells behaves as a poroelastic material. *Nat. Mater.*, 12:253 – 261, 2013.

[93] P. Mostaghimi, M. J. Blunt, and B. Bijeljic. Computations of Absolute Permeability on Micro-CT Images. *Math. Geosci.*, 45(1):103 – 125, 2013.

[94] M. A. Murad and A. F. Loula. On stability and convergence of finite element approximations of Biot's consolidation problem. *Int. J. Numer. Meth. Engng.*, 37:645 – 667, 1994.

[95] S. Na and W. Sun. Computational thermo-hydro-mechanics for multiphase freezing and thawing porous media in the finite deformation range. *Comput. Methods Appl. Mech. Engrg.*, 318:667 – 700, 2017.

[96] D. A. Nield and A. Bejan. *Convection in Porous Media*. Springer International Publishing AG, 2017.

[97] Y. Pan and R. N. Horne. Resonant behavior of saturated porous media. *J. Geophys. Res.*, 105:11021 – 11028, 2000.

[98] P. J. Phillips and M. F. Wheeler. A coupling of mixed and continuous Galerkin finite element methods for poroelasticity I: the continuous in time case. *Comput. Geosci.*, 11(2):131 – 144, 2007.

[99] L. B. Porter, R. W. Ritzi, L. J. Mastera, D. F. Dominic, and B. Ghanbarian-Alavijeh. The Kozeny-Carman Equation with a Percolation Threshold. *Ground Water*, 51(1):92 – 99, 2013.

[100] P. Prokharau and F. J. Vermolen. On Galerkin FEM approximation of 1D and 2D poro-elastic problem. Technical report, DIAM, Delft, 2009.

[101] T. Ptak, M. Piepenbrink, and E. Martac. Tracer tests for the investigation of heterogeneous porous media and stochastic modelling of flow and transport - a review of some recent developments. *J. Hydrol.*, 294:122 – 163, 2004.

[102] M. Rahrah, L. Lopez-Peña, F. Vermolen, and B. Meulenbroek. Network-inspired versus Kozeny-Carman based permeability-porosity relations applied to Biot's poroelasticity model. *Journal of Mathematics in Industry*, 10:19, 2020.

[103] M. Rahrah and F. Vermolen. Monte Carlo Assessment of the Impact of Oscillatory and Pulsating Boundary Conditions on the Flow Through Porous Media. *Transp. Porous Med.*, 123(1):125 – 146, 2018.

[104] M. Rahrah and F. Vermolen. Uncertainty Quantification in Injection and Soil Characteristics for Biot's Poroelasticity Model. In *European Conference on Numerical Mathematics and Advanced Applications ENUMATH 2017*, pages 645 – 652. Springer, 2019.

[105] M. Rahrah and F. Vermolen. A moving finite element framework for fast infiltration in nonlinear poroelastic media. *Comput. Geosci.*, 2020.

[106] M. Rahrah, F. J. Vermolen, L. A. Lopez-Peña, and B. J. Meulenbroek. A Poroelasticity Model Using a Network-Inspired Porosity-Permeability Relation. In *Progress in Industrial Mathematics at ECMI 2018*, pages 83 – 88. Springer, 2019.

[107] A. Richey, B. Thomas, M.-H. Lo, J. Reager, J. Famiglietti, K. Voss, S. Swenson, and M. Rodell. Quantifying renewable groundwater stress with GRACE. *Water Resour. Res.*, 51(7):5217 – 5238, 2015.

[108] C. Rodrigo, F. Gaspar, X. Hu, and L. Zikatanov. Stability and monotonicity for some discretizations of the Biot's consolidation model. *Comput. Methods Appl. Mech. Engrg.*, 298:183 – 204, 2016.

[109] J. Rutqvist. The Geomechanics of $CO_2$ Storage in Deep Sedimentary Formations. *Geotech. Geol. Eng.*, 30(3):525 – 551, 2012.

[110] M. Sahimi. *Flow and Transport in Porous Media and Fractured Rock.* VCH, Weinheim, 1995.

[111] B. Schrefler. Computer modelling in environmental geomechanics. *Comput. Struct.*, 79:2209 – 2223, 2001.

[112] R. Schulz, N. Ray, S. Zech, A. Rupp, and P. Knabner. Beyond Kozeny-Carman: Predicting the permeability in porous media. *Transp. Porous Med.*, 130:487 – 512, 2019.

[113] A. Segal. *Finite element methods for the incompressible Navier-Stokes equations.* Delft Institute of Applied Mathematics, Delft, 2012.

[114] M. Sharifi and M. Kelkar. Novel permeability upscaling method using Fast Marching Method. *Fuel*, 117:568 – 578, 2014.

[115] R. E. Showalter. Diffusion in Poro-Elastic Media. *J. Math. Anal. Appl.*, 251:310 – 340, 2000.

[116] K. Soga, E. Alonso, A. Yerro, K. Kumar, and S. Bandara. Trends in large-deformation analysis of landslide mass movements with particular emphasis on the material point method. *Géotechnique*, 66(3):248 – 273, 2016.

[117] Soil properties. `http://structx.com/Soil_Properties.html`. Accessed on 23 May 2017.

[118] M. Spiegelman. Flow in deformable porous media. Part 1. Simple analysis. *J. Fluid Mech.*, 247:17 – 38, 1993.

[119] C. Stover and E. W. Weisstein. Percolation threshold. From MathWorld - A Wolfram Web Resource. Accessed on 04 February 2019.

[120] K. H. Støverud, M. Darcis, R. Helmig, and S. M. Hassanizadeh. Modeling Concentration Distribution and Deformation During Convection-Enhanced Drug Delivery into Brain Tissue. *Transp. Porous Med.*, 92(1):119 – 143, 2012.

[121] M. Sun and H. Rui. A coupling of weak Galerkin and mixed finite element methods for poroelasticity. *Comput. Math. Appl.*, 73:804 – 823, 2017.

[122] W. Sun, Q. Chen, and J. T. Ostien. Modeling the hydro-mechanical responses of strip and circular punch loadings on water-saturated collapsible geomaterials. *Acta Geotech.*, 9:903 – 934, 2014.

[123] W. Sun, J. T. Ostien, and A. G. Salinger. A stabilized assumed deformation gradient finite element formulation for strongly coupled poromechanical simulations at finite strain. *Int. J. Numer. Anal. Meth. Geomech.*, 37(16):2755 – 2788, 2013.

[124] M. L. Szulczewski, C. W. MacMinn, H. J. Herzog, and R. Juanes. Lifetime of carbon capture and storage as a climate-change mitigation technology. In *Proc. Natl. Acad. Sci. U.S.A.*, volume 109, pages 5185 – 5189, 2012.

[125] C. Taylor and P. Hood. A numerical solution of the Navier-Stokes equations using the finite element technique. *Computers & Fluids*, 1(1):73 – 100, 1973.

[126] M. Tchonkova, J. Peters, and S. Sture. A new mixed finite element method for poro-elasticity. *Int. J. Numer. Anal. Meth. Geomech.*, 32(6):579 – 606, 2008.

[127] P. Teatini, M. Ferronato, G. Gambolati, and M. Gonella. Groundwater pumping and land subsidence in the Emilia-Romagna coastland, Italy: Modeling the past occurrence and the future trend. *Water Resour. Res.*, 42(1):W01406, 2006.

[128] K. Terzaghi. *Theoretical soil mechanics*. Chapman And Hall, Limited.; London, 1951.

[129] A. Truty and T. Zimmermann. Stabilized mixed finite element formulations for materially nonlinear partially saturated two-phase media. *Comput. Methods Appl. Mech. Engrg.*, 195:1517 – 1546, 2006.

[130] T.-L. Tsai, K.-C. Chang, and L.-H. Huang. Body force effect on consolidation of porous elastic media due to pumping. *J. Chin. Inst. Eng.*, 29(1):75 – 82, 2006.

[131] United Nations Committee on Economic, Social and Cultural Rights. *General Comment No. 15. The Right to Water.* U. N. Econ. and Soc. Counc., Geneva, Switzerland, 2003.

[132] P. A. Vermeer and A. Verruijt. An accuracy condition for consolidation by finite elements. *Int. J. Numer. Anal. Meth. Geomech.*, 5(1):1 – 14, 1981.

[133] A.-T. Vuong, L. Yoshihara, and W. Wall. A general approach for modeling interacting flow through porous media under finite deformations. *Comput. Methods Appl. Mech. Engrg.*, 283:1240 – 1259, 2015.

[134] J. Wan. *Stabilized finite element methods for coupled geomechanics and multiphase flow.* PhD thesis, Stanford University, 2003.

[135] H. F. Wang. *Theory of Linear Poroelasticity with Applications to Geomechanics and Hydrogeology.* Princeton University Press, 2000.

[136] S.-J. Wang and K.-C. Hsu. Dynamics of deformation and water flow in heterogeneous porous media and its impact on soil properties. *Hydrol. Process.*, 23:3569 – 3582, 2009.

[137] What is soil? `http://lifeunderyourfeet.org/en/soileco/intro/whatis.asp`. Accessed on 19 November 2019.

[138] M. Wheeler, G. Xue, and I. Yotov. Coupling multipoint flux mixed finite element methods with continuous Galerkin methods for poroelasticity. *Comput. Geosci.*, 18:57 – 75, 2014.

[139] S. Whitaker. *The method of volume averaging*, volume 13. Springer Science & Business Media, 2013.

[140] J. White, L. Chiaramonte, S. E. W. Foxall, Y. Hao, A. Ramirez, and W. McNab. Geomechanical behavior of the reservoir and caprock system at the In Salah $CO_2$ storage project. In *Proc. Natl. Acad. Sci.*, volume 111, pages 8747 – 8752, 2014.

[141] J. A. White and R. I. Borja. Stabilized low-order finite elements for coupled solid-deformation/fluid-diffusion and their application to fault zone transients. *Comput. Methods Appl. Mech. Engrg.*, 197:4353 – 4366, 2008.

[142] M. van Wijngaarden. *Mathematical Modelling and Simulation of Biogrout.* PhD thesis, DIAM, Delft University of Technology, 2015.

[143] P.-Z. Wong. The Statistical Physics of Sedimentary Rock. *Physics Today*, 41:24 – 32, 1988.

[144] L. You and H. Liu. A two-phase flow and transport model for the cathode of PEM fuel cells. *Int. J. Heat Mass Transfer*, 45:2277 – 2287, 2002.

[145] A. Ženíšek. The existence and uniqueness theorem in Biot's consolidation theory. *Aplikace Matematiky*, 29(3):194 – 211, 1984.

[146] Z. Zhi-hong, F. Yuan-fang, and D. Xiu-li. 3D Transport of Solute in Deformable Soils with Different Adsorption Modes. *Soil Mech. Found. Eng.*, 54(2):128 – 136, 2017.

[147] O. C. Zienkiewicz and J. Z. Zhu. The superconvergent patch recovery and a posteriori error estimates. Part 1: The recovery technique. *Int. J. Numer. Meth. Engng.*, 33(7):1331 – 1364, 1992.

# Acknowledgements

"*He who does not thank the people, is not thankful to Allah.*"
Prophet Mohammed (Peace and blessings be upon him)

This dissertation contains the main results of the PhD project that I have been working on during the past few years. It has been a very interesting and valuable experience for me to conduct this research. Here, I would like to take the opportunity to thank a number of people who made the realisation of this dissertation possible.

First and foremost, I would like to extend my sincere gratitude to Fred Vermolen for giving me the opportunity to work on this interdisciplinary project and for his guidance, support and encouragement throughout the research process. It was a great pleasure to collaborate with you. Your mathematical input has been extremely important to me over the years and you have helped me a lot with scientific writing. You were always positive about every (baby) step I made and supportive during all the ups and downs. Your endless enthusiasm and constructive criticism made it a real pleasure to work with you. Therefore, I look forward to hopefully continuing our scientific collaboration in the future. I would also like to thank you for the informal and friendly atmosphere during our meetings and for the many conversations we have had over the years. All I want to say is that I learned a lot from you, not only in the field of mathematics, but also about life.

I would also like to thank Kees Vuik. As head of our Numerical Analysis group, he created a pleasant and friendly academic environment and atmosphere where it was a pleasure to work. Thank you Kees for always being there for your PhD students whenever they need your help, despite your busy schedule. You are very supportive and a real father figure to all your colleagues in the group.

In addition to my supervisors, I would like to thank the rest of the committee members for participating in my doctoral committee, reading my dissertation and accepting the invitation to my defence.

This work has been made possible thanks to the financial support of NWO and the members of the O2DIT foundation: Fugro GeoServices, Theo van Velzen, Henk van Tongeren, BoutenGeotron, De Vet en Zonen Mill and Hölscher Wasserbau. I would like to thank all industrial partners for the opportunities to visit their companies and fieldwork. These visits provided us with new insights from an experimental perspective in order to improve our mathematical models. I would like to express my gratitude to my advisors at Fugro, Herman Wolfs and Barbara Snacken, for their guidance and for the suggestions they made during our progress meetings.

This PhD journey would not be a great and unforgettable experience without the company of many wonderful people in the Numerical Analysis group, to whom

I express my gratitude. I owe a great deal of appreciation to my office mates: Guido, Joost and Manuel, for the joyful moments and for making the working environment a pleasant place to be. My special gratitude goes to Joost who helped me whenever I needed some support. I want to acknowledge Luis Lopez-Peña for the successful collaboration that resulted in two papers. I really enjoyed working with you Luis and I am very happy with the results we have achieved. Many more colleagues and friends made my PhD life very special. Thank you: Alice, Baljaa, Behrouz, Berna, Fahim, Ginger, Jiao, Jing, Jochen, Lisa, Marieke, Merel, Mohamed, Mousa, Owen, Peiyao, Prajakta, Reinaldo, Roel, Shuaiqiang, Vandana and Xiujie, it was really fun meeting you and I have many memorable moments with all of you. I also want to thank Anne for the amazing trip to the US and for the nice conversations we had every day until late at night. Thank you Gaby for an unforgettable ECMI and for so many great moments together. I look forward to visiting you and Luis in Mexico someday. I enjoyed the many conversations we had Daniël, thank you for your advices and for sharing your experiences with me. I would also like to express my gratitude to the senior researchers in our group: Domenico, Duncan, Kees Oosterlee, Kristof, Martin, Matthias and Neil, for sharing your experiences with us and for creating a friendly atmosphere in the department. Regarding official affairs and technical support, my appreciation goes to Deborah and all secretaries, Kees Lemmens, Xiwei and Carl.

In truth, I could not have achieved my current level of success without a strong support group of family and friends. Allereerst wil ik mijn familie, en vooral mijn ouders, bedanken voor hun eindeloze en onvoorwaardelijke liefde, hun steun en hun nooit afnemende vertrouwen tijdens dit doctoraatswerk. Dit heeft mij de afgelopen jaren enorm geholpen. Mama, ik wil je bedanken voor alle steun die je me de afgelopen jaren hebt gegeven. Je hebt me vaak een luisterend oor geboden en advies gegeven. Jouw troostende woorden hielpen me door de donkere tijden heen en dankzij jouw aanmoediging heb ik dit onderzoeksproject kunnen voltooien. Ik ben je hiervoor zeer dankbaar en mijn waardering is niet in woorden uit te drukken.

Ik wil Thea ook heel erg bedanken voor haar oprechte steun, haar luisterend oor en de tijd die we samen hebben doorgebracht. Je hebt me door verschillende uitdagingen in mijn leven heen geholpen en ik heb veel van je geleerd. Ik hoop dat we nog vele jaren beste vriendinnen blijven. Iman, ondanks de afstand tussen ons ben je altijd mijn hartsvriendin geweest en bij elk contact voelt het alsof we nooit gescheiden zijn geweest. Bedankt voor jouw steun en voor jouw waardevolle adviezen. De plus, je suis très reconnaissante à Safae, Hatim, Choayb et Rafik d'être ma deuxième famille en France. Leur présence et leur bonne humeur m'ont beaucoup soulagé du mal du pays. J'ai vraiment apprécié notre temps ensemble lors des beaux voyages que nous avons faits et j'ai hâte d'en voir beaucoup d'autres à venir!

Last but not least, I would like to extend my deepest gratitude to my beloved husband Makrem for his encouragement and for his patience in putting off so many plans we had until I finished my research. It takes a special person to make such difficult and selfless decisions while remaining wholeheartedly caring and supportive. I also want to thank you for your understanding and for putting up with my stressful periods. I am extremely happy to share my life with you and I look forward to our further life together and especially to our little miracle that we are expecting soon.

Menel Rahrah
Paris, August 2020

# List of scientific activities

## Journal publications

- M. Rahrah and F. Vermolen. Monte Carlo Assessment of the Impact of Oscillatory and Pulsating Boundary Conditions on the Flow Through Porous Media. *Transp. Porous Med.*, 123(1):125 – 146, 2018.

- M. Rahrah and F. Vermolen. A moving finite element framework for fast infiltration in nonlinear poroelastic media. *Comput. Geosci.*, 2020.

- M. Rahrah, L. Lopez-Peña, F. Vermolen, and B. Meulenbroek. Network-inspired versus Kozeny-Carman based permeability-porosity relations applied to Biot's poroelasticity model. *Journal of Mathematics in Industry*, 10:19, 2020.

## Peer-reviewed conference proceedings

- M. Rahrah and F. Vermolen. Uncertainty Quantification in Injection and Soil Characteristics for Biot's Poroelasticity Model. In *European Conference on Numerical Mathematics and Advanced Applications ENUMATH 2017*, pages 645 – 652. Springer, 2019.

- M. Rahrah, F. J. Vermolen, L. A. Lopez-Peña, and B. J. Meulenbroek. A Poroelasticity Model Using a Network-Inspired Porosity-Permeability Relation. In *Progress in Industrial Mathematics at ECMI 2018*, pages 83 – 88. Springer, 2019.

## Contributions at international conferences

### Oral presentations

- *Modelling and uncertainty quantification in Biot's poro-elasticity with pulsating and oscillatory boundary conditions.* Presented at: SIAM Annual Meeting, Pittsburgh, United States, July 12, 2017.

- *Monotonicity analysis and uncertainty quantification in Biot's poroelasticity model using finite element methods.* Presented at: ENUMATH Conference, Bergen, Norway, September 26, 2017.

- *Uncertainty quantification of a poroelasticity model using a network-inspired porosity-permeability relation.* Presented at: ECMI Conference, Budapest, Hungary, June 19, 2018.
- *Mathematical modelling of Fast, High Volume Infiltration in poroelastic media using finite elements.* Presented at: Seminar of the project-team Serena of research institute Inria, Paris, France, April 12, 2019.

### Scientific posters

- *Mathematical Modeling of Fast, High Volume Infiltration near Building Sites.* Presented at: Thirty-ninth SCS Woudschoten conference, Zeist, The Netherlands, October 8-10, 2014.
- *Fast, High Volume Infiltration.* Presented at: Fortieth SCS Woudschoten conference, Zeist, The Netherlands, October 7-9, 2015.
- *Mathematical modelling of Fast, High Volume Infiltration.* Presented at: Forty-first SCS Woudschoten conference, Zeist, The Netherlands, October 5-7, 2016.
- *The impact of oscillatory and pulsating BC's on the flow through porous media.* Presented at: Forty-second SCS Woudschoten conference, Zeist, The Netherlands, October 4-6, 2017.
- *Monte Carlo assessment of the impact of oscillatory and pulsating BC's on the flow through porous media.* Presented at: Lorentz workshop: The Computational Mathematics Aspects of Porous Media, and Fluid Flow, Leiden, The Netherlands, May 22-25, 2018.

## Academic theses

- M. Rahrah. Energieverlies bij warmwaterleidingen. Bachelor thesis in Applied Mathematics, Delft University of Technology. Scientific supervision: Prof.dr.ir. C. Vuik. 2010.
- M. Rahrah. Modeling interactions between turbulence induced mechanical vibrations and subsurface flow of water. Master thesis in Applied Mathematics, Delft University of Technology. Scientific supervision: Dr.ir. F.J. Vermolen and prof.dr.ir. C. Vuik. 2012.

# Curriculum Vitæ

Menel Rahrah was born in The Hague, The Netherlands.

Between 2001 and 2007, she received secondary education at the Johan de Witt College (The Hague) and graduated Cum Laude with a 9.75/10 for mathematics. In her final year, she received the Graduation Award of the Johan de Witt Scholengroep (a group of five schools in The Hague).

In 2007, she started her academic career in Applied Mathematics at Delft University of Technology. After completing the first year of her studies, she was awarded the Kartini Prize 2008 from the Royal Dutch Society of Sciences and Humanities for the best female ethnic minority student of the exact sciences in The Netherlands. In 2010, she finished her bachelor's degree (Cum Laude), and in 2012, she obtained her MSc diploma with a specialisation in Computational Science and Engineering. Her master's thesis: "Modeling interactions between turbulence induced mechanical vibrations and subsurface flow of water", formed the basis for her PhD project.

From 2012 to 2014, Menel worked as a computational engineer at Fugro GeoServices B.V. (as part of foundation O2DIT) in Leidschendam.

Her PhD project started in July 2014, after receiving a grant from the Netherlands Organisation for Scientific Research NWO. In her research, she focused primarily on mathematical modelling of fluid flow through poroelastic porous media and on developing and programming numerical methods for the simulation of poroelasticity problems. In 2019, she was ranked in the top 15 of the best contributions to the Proceedings of the conference ECMI 2018 and she was invited to submit a paper for publication in a special issue of Journal of Mathematics in Industry. Next to her research, Menel was the treasurer of the SIAM Student Chapter Delft (2016 - 2017) and she was a teaching assistant in the lab sessions of the courses Numerical Mathematics, Linear Algebra and Differential Equations. She also helped with grading exams and writing project manuals.